



**UNIVERSITY OF  
BIRMINGHAM**

**ANTENNA DESIGNS BASED ON  
METAMATERIAL-INSPIRED STRUCTURES**

By

**XIANG GAO**

A thesis submitted to the College of  
Engineering and Physical Sciences,  
University of Birmingham, for the degree of  
**DOCTOR OF PHILOSOPHY**

School of Electronic, Electrical and  
Systems Engineering  
College of Engineering and Physical  
Sciences  
University of Birmingham  
September 2016

UNIVERSITY OF  
BIRMINGHAM

**University of Birmingham Research Archive**

**e-theses repository**

This unpublished thesis/dissertation is copyright of the author and/or third parties. The intellectual property rights of the author or third parties in respect of this work are as defined by The Copyright Designs and Patents Act 1988 or as modified by any successor legislation.

Any use made of information contained in this thesis/dissertation must be in accordance with that legislation and must be properly acknowledged. Further distribution or reproduction in any format is prohibited without the permission of the copyright holder.

# Abstract

The research presented in this thesis concerns antenna designs based on metamaterial-inspired structures. Based on a review of the existing literature and understanding of the background theories, different metamaterial-inspired structures are applied to designs of resonant antennas (RAs) and leaky wave antennas (LWAs) for improved antenna characteristics. Extended composite right/left-handed (ECRLH) unit cell structures enable the RA designs with multiband or wideband properties; the novel metamaterial-inspired supercell structures enable the LWA designs with the dual-passband property and the backward-to-forward leaky-wave radiation characteristics in each passband. In addition, two tunable antennas are presented to mainly achieve the frequency reconfigurability and possibly the pattern reconfigurability by electronically controlling surface-mounted semiconductor varactors or discrete ferroelectric barium strontium titanium (BST) thin-film varactors. Furthermore, the uncertainty analysis in determination of permittivity of BST film materials from the characterization process is discussed in this thesis, in order to provide the design clues when the antenna with BST materials is designed. The conclusions are drawn and the possible future research directions are explained as well.

*To my parents, my wife and my families*

# Acknowledgements

First of all, I would like to express my deepest gratitude and greatest respects to my supervisor Professor Peter Gardner, Dr. Timothy J. Jackson, and Professor Peter S. Hall for valuable guidance, fruitful advice and excellent supports throughout my PhD period. I would also appreciate them for their encouragement and share in their knowledge and experience.

I would also express my gratitude to all members of the Communication Engineering Research Group, especially my nice colleagues and friends – Dr. Zhengpeng Wang, Dr. Bin Liang, Dr. Kai Lu, Dr. Xiaolei Sun, Dr. Liang Wan, Dr. Jinsong Song, Dr. Sampson Hu, Dr. M. M. Awang Kechik, Dr. Xiao Li, Dr. Konstantinos Konstantinidis, Dr. Yasin Kabiri, and Mr. Yineng Wang. Their help and supports enable me to have a happy and knowledgeable PhD period. I also want to express my special thanks to Dr. Alexandros Feresidis for his fruitful guidance in antenna designs and Mr. Alan Yates for his technical supports in the antenna fabrication and the usage of measurement equipment.

Finally, I would like to express my deepest love to my parents, my wife and all my families for their generous supports, endless love, and deep understanding. Their love means too much to me.

# Contents

<b>Abstract</b> .....	<b>I</b>
<b>Acknowledgement</b> .....	<b>III</b>
<b>List of Figures</b> .....	<b>VII</b>
<b>List of Tables</b> .....	<b>XVI</b>
<b>List of Abbreviations</b> .....	<b>XVIII</b>
<b>List of Publications</b> .....	<b>XX</b>
<b>Chapter I Introduction</b> .....	<b>1</b>
1.1 Background.....	1
1.2 Motivations and Objectives.....	2
1.2.1 Motivations .....	2
1.2.2 Objectives.....	4
1.3 Outline of Thesis.....	5
1.4 Contributions.....	7
<b>Chapter II Background Theory</b> .....	<b>10</b>
2.1 Introduction.....	10
2.2 Theory of Conventional Leaky Wave Antennas.....	10
2.2.1 Uniform or Quasi-Uniform LWAs .....	12
2.2.2 Periodic LWAs .....	13
2.3 Theory of Composite Right/Left Handed Transmission Line Structure.....	15
2.4 Theory of Metamaterial-Inspired Resonant Antenna .....	20
2.5 Theory of Extended Composite Right/Left Handed Transmission Line Structure.....	25
2.6 Summary .....	30
<b>Chapter III Review of Artificial Electromagnetic Structures And Barium Strontium Titanium Materials Applied to Antenna Designs</b> .....	<b>31</b>
3.1 Introduction.....	31
3.2 Literature of Metamaterial-Inspired RAs.....	32
3.3 Literature of Metamaterial-Inspired LWAs .....	41
3.3.1 Literature of LWA Designs Based On CRLH Structures .....	42
3.3.2 Literature of LWA Designs Based On Metamaterial-Inspired Structures .....	51
3.4 Literature of Component Designs with BST Materials.....	56
3.5 Literature of Antenna Designs with Different Tuning Techniques.....	64
3.6 Summary .....	68
<b>Chapter IV Open-Ended Resonant Antennas Based On Extended Composite Right/Left Handed Transmission-Line Unit Cell Structure</b> .....	<b>69</b>
4.1 Introduction.....	69
4.2 Resonant Theory of ECRLH Structure .....	72
4.3 Passive RA Design with SMD Capacitors .....	75

4.3.1 Measurement and Simulation.....	77
4.3.2 Analysis of passive RA with SMD chip capacitors.....	81
4.4 Passive RA Design with IDSs.....	85
4.4.1 Measurement and Simulation.....	87
4.4.2 Analysis of passive RA with IDSs.....	90
4.4.3 Comparison with A Conventional Monopole Antenna.....	93
4.5 Tunable RA Design with One Semiconductor Varactor.....	95
4.5.1 Simulation and Measurement.....	98
4.5.2 Loss Analysis of Varactor.....	103
4.6 Summary.....	104

**Chapter V Dual-band Leaky Wave Antennas Based On Metamaterial-Inspired Transmission-Line Structures ..... 106**

5.1 Introduction.....	106
5.2 Passive LWA Design Based On ECRLH Structure.....	109
5.2.1 Measurement Results.....	111
5.2.2 Analysis of One ECRLH TL Unit Cell.....	115
5.2.3 Loss of SMD Chip Capacitors.....	118
5.3 Passive LWA Design Based On Supercell_v1 Structure.....	119
5.3.1 Analysis Using TL Approach.....	119
5.3.2 Antenna Design.....	122
5.3.3 Analysis of Supercell_v1 Structure.....	124
5.3.4 Measurement Results of LWA.....	125
5.3.5 Loss of SMD Chip Capacitors.....	128
5.4 LWA Designs Based On Supercell_v2 Structure.....	130
5.4.1 Analysis of Supercell_v2 Structure Using TL Approach.....	130
5.4.2 Passive LWA Design Based On Supercell_v2 Structure.....	132
5.4.2.1 Passive antenna design.....	132
5.4.2.2 Analysis of Supercell_v2 structure.....	134
5.4.2.3 Measurement results.....	136
5.4.2.4 Loss of SMD chip capacitors.....	139
5.4.2.5 Influence of capacitors on dispersion relation of Supercell_v2 structure.....	140
5.4.3 Tunable LWA Design Based On Supercell_v2 Structure.....	142
5.4.3.1 Tunable antenna design.....	142
5.4.3.2 Frequency responses.....	144
5.4.3.3 Dispersion relations.....	149
5.4.3.4 Farfield patterns.....	151
5.4.3.5 Gains and directivities.....	153
5.4.3.6 Losses of varactors and chip capacitors.....	155
5.5 Summary.....	157

**Chapte VI Uncertainty Analysis of Determination in Permittivity of Ferroelectric Materials And Implications For Design of A CRLH-Based Leaky Wave Antenna ..... 159**

6.1 Introduction.....	159
6.2 Background of BST Material.....	160

6.3 CRLH-Based LWA with BST Varactors.....	163
6.4 Uncertainty Analysis .....	172
6.5 Summary .....	180
<b>Chapter VII Conclusions And Future Research .....</b>	<b>182</b>
7.1 Conclusions.....	182
7.1.1 Class of Metamaterial-Inspired RAs .....	183
7.1.2 Class of Dual-Passband LWAs .....	183
7.1.3 Class of BST-Based Antennas .....	184
7.2 Future Research.....	185
<b>Appendix A Brief Datasheet of MURATA 0402 Chip Capacitor.....</b>	<b>192</b>
<b>Appendix B Datasheet of MICROSEMI MV34002 Semiconductor Varactor....</b>	<b>196</b>
<b>Appendix C Datasheet of SKYWORKS SMV1234-040LF Silicon Semiconductor Varactor.....</b>	<b>197</b>
<b>Appendix D MATLAB Functions.....</b>	<b>200</b>
<b>References.....</b>	<b>205</b>

# List of Figures

Figure 2.1 Examples of conventional LWAs.....	11
Figure 2.2 Equivalent models of different unit cell structure, (a) one conventional RH unit cell structure; (b) one LH unit cell structure; (c) one asymmetric CRLH unit cell structure.....	15
Figure 2.3 Dispersion diagrams of the CRLH structure, (a) the unbalanced condition; (b) the balanced condition.....	20
Figure 2.4 Resonance spectrums of the CRLH structure, (a) the unbalanced condition; (b) the balanced condition.....	22
Figure 2.5 Equivalent circuit model of the ECRLH structure.....	25
Figure 2.6 Equivalent circuit model of the DCRLH structure.....	26
Figure 2.7 Dispersion diagrams of the ECRLH structure, (a) the unbalanced condition; (b) the balanced condition.....	30
Figure 3.1 Configuration of four-cell ZOR antenna [14].....	33
Figure 3.2 Configurations of the proposed ZOR antennas, (a) ENG; (b) DNG [16]...34	
Figure 3.3 Configuration of the proposed ZOR antenna using mushroom structure [17].....	35
Figure 3.4 Configuration of the proposed antenna with bandwidth extension [18]....35	
Figure 3.5 Configurations of the proposed ZOR antenna, (a) top view; (b) rear view [19].....	36
Figure 3.6 Configuration of the proposed CPW ZOR antenna [20].....	37
Figure 3.7 (a) Top view and side view of the antenna configuration; (b) top view and side view of the designed CRLH-based elements [21] .....	37
Figure 3.8 Configurations of the proposed asymmetric ZOR antenna, (a) top view; (b) rear view [22].....	39
Figure 3.9 Configuration of the proposed CPW ZOR antenna [23].....	39
Figure 3.10 Configuration of the first CRLH-based 1-D LWA, (a) unit cell structure; (b) fabricated LWA [25].....	43
Figure 3.11 (a) Layout and equivalent circuits of the proposed active CRLH unit cell structure; (b) the fabricated tunable LWA with 30 cascaded CRLH unit cells. [28].....	44
Figure 3.12 Configuration of this active LWA with 48 CRLH unit cells and 7 amplifiers, (a) top view; (b) rear view [29].....	46

Figure 3.13 Configuration of this non-uniform CRLH-based LWA [30].....	47
Figure 3.14 Configurations of this CRLH-based LWA, (a) cross-sectional view; (b) top view [31].....	47
Figure 3.15 Configurations of this CRLH-based LWA with SRRs [32].....	48
Figure 3.16 Prototype of the fabricated LWA based on the SIW CRLH structure [33].....	48
Figure 3.17 Prototype of the fabricated HMSIW LWA with CP [34].....	49
Figure 3.18 (a) Layout of the single CRLH unit cell structure; (b) configuration of the fabricated LWA with 1-D multiple periodic unit cells [35].....	49
Figure 3.19 (a) Equivalent circuit of one ECRLH unit cell; (b) photograph of the fabricated LWA based on the ECRLH structure [36].....	52
Figure 3.20 (a) Equivalent circuit of one DP-CRLH unit cell; (b) photograph of the fabricated LWA based on the DP-CRLH structure [37].....	52
Figure 3.21 (a) Equivalent circuit of one metamaterial-inspired supercell; (b) photograph of the fabricated half-width microstrip LWA [38].....	53
Figure 3.22 (a) Layout of one dual-band CRLH unit cell structure; (b) photograph of the fabricated SIW LWA [39].....	54
Figure 3.23 (a) Layout of one MNG unit cell structure; (b) photograph of the fabricated LWA based on the MNG structure [40].....	55
Figure 3.24 (a) Photograph of the fabricated phased array antenna; (b) layout of the loaded-line phase shifter with MIM BST varactors [44].....	58
Figure 3.25 (a) Photograph of one BST varactor; (b) top view of the active FSS with BST varactors; (c) photograph of the fabricated antenna [45] .....	59
Figure 3.26 Configurations of the antenna with the BST layer, (a) side view; (b) top view [46].....	60
Figure 3.27 Antenna layout, (a) top view of the antenna; (b) side view of the BST varactor; (c) top view of the BST varactor [47]. .....	60
Figure 3.28 Configuration of the interdigital capacitor [48].....	61
Figure 3.29 Configuration of a patch antenna on the liquid crystal substrate [52].....	65
Figure 3.30 Configurations of a RF-MEMS-based antenna, (a) bottom view; (b) top view [53].....	66
Figure 3.31 Configuration of a ferrite loaded antenna [54].....	66
Figure 4.1 Equivalent circuit model of one ECRLH unit cell structure.....	72
Figure 4.2 Resonance spectrums of one ECRLH unit cell structure in different operation conditions, (a) the unbalanced condition; (b) the balanced condition.....	74
Figure 4.3 Configurations of the passive RA with SMD capacitors, (a) top view;	

(b) rear view.....	75
Figure 4.4 Photographs of the fabricated passive RA with SMD capacitors, (a) top view; (b) rear view.....	76
Figure 4.5 Full-wave simulated, circuit-model simulated and measured S11 results of the proposed RA.....	78
Figure 4.6 Full-wave simulated and measured gains of the proposed RA with SMD capacitors. ....	78
Figure 4.7 Current distributions of this RA, (a) 0.707 GHz; (b) 5.5 GHz. ....	78
Figure 4.8 Measured and simulated normalized farfield patterns of the RA for co-polarization and cross-polarization, (a) YOZ plane at 0.707 GHz; (b) XOY plane at 0.707 GHz; (c) YOZ plane at 2.4 GHz; (d) XOY plane at 2.4 GHz; (e) YOZ plane at 5.5 GHz; (f) XOY plane at 5.5 GHz. ....	79
Figure 4.9 Equivalent circuit model of the proposed RA with SMD capacitors.....	81
Figure 4.10 Effects of the dimension changing of the part of the antenna structure on the frequency response of this RA, (a) $C_{hs}$ ; (b) $C_{hp}$ ; (c) $C_{vs}$ ; (d) $L10$ ; (e) $L9$ ; (f) $L6$ ; (g) $L7$ ; (h) $L1$ ; (i) $L3$ . ....	84
Figure 4.11 Configurations of the passive RA with IDSs, (a) top view; (b) rear view.....	85
Figure 4.12 IDSs in the proposed antenna structure, (a) $C_{hp}$ ; (b) $C_{hs}$ ; (c) $C_{vs}$ . ....	85
Figure 4.13 Prototypes of the fabricated RA with IDSs, (a) front view; (b) rear view.....	87
Figure 4.14 Full-wave simulated, circuit-model simulated and measured S11 results of the proposed RA with the IDSs. ....	87
Figure 4.15 Simulated and measured gains of the proposed RA at resonant frequencies.....	87
Figure 4.16 Current distributions of this RA, (a) 0.887 GHz; (b) 5.5 GHz.....	88
Figure 4.17 Measured and simulated normalized farfield patterns of this RA for co-polarization and cross-polarization, (a) YOZ plane at 0.887 GHz; (b) XOY plane at 0.887 GHz; (c) YOZ plane at 2.4 GHz; (d) XOY plane at 2.4 GHz; (e) YOZ plane at 5.5 GHz; (f) XOY plane at 5.5 GHz. ....	89
Figure 4.18 Effects of the dimension changing of the part of the antenna structure on the frequency response of the antenna, (a) $Wf1$ ; (b) $Wf2$ ; (c) $Wf3$ ; (d) $W3$ ; (e) $W2$ ; (f) $L6$ ; (g) $L7$ ; (h) $L1$ ; (i) $L3$ . ....	92
Figure 4.19 Configuration of a conventional monopole antenna. ....	94
Figure 4.20 Comparison of S11 results between the RA with IDSs and this monopole antenna. ....	94
Figure 4.21 Configurations of the active RA with one varactor, (a) top view; (b) rear view.....	94

view; (c) the IDS for $C_{hs}$ ; (d) the IDS for $C_{vs}$ . .....	95
Figure 4.22 Equivalent circuit model of <i>MICROSEMI MV34002</i> semiconductor varactor.....	96
Figure 4.23 Configurations of this tunable RA with one varactor, (a) top view; (b) rear view.....	96
Figure 4.24 Simulated S11 of the RA with different capacitance of $C_{hp}$ .....	98
Figure 4.25 Measured S11 of the RA by applying different DC bias voltages to the varactor. ....	98
Figure 4.26 Measured and simulated normalized patterns of the tunable RA for co-polarization and cross-polarization, (a) YOZ plane at 0.7 GHz with 1.5 V; (b) XOY plane at 0.7 GHz with 1.5 V; (c) YOZ plane at 0.85 GHz with 2.85 V; (d) XOY plane at 0.85 GHz with 2.85 V; (e) YOZ plane at 0.96 GHz with 4.37 V; (f) XOY plane at 0.96 GHz with 4.37 V. ....	100
Figure 4.27 Measured and simulated normalized patterns of the tunable RA with 2.85 V bias voltage for co-polarization and cross-polarization, (a) YOZ plane at 2.4 GHz; (b) XOY plane at 2.4 GHz; (c) YOZ plane at 5.5 GHz; (d) XOY plane at 5.5 GHz..	101
Figure 4.28 Simulated and measured gains of the tunable RA with different bias voltages at 0.7 GHz, 0.85 GHz, and 0.96 GHz. ....	101
Figure 4.29 Simulated and measured gains of the tunable RA over 1.7-6 GHz with 2.85 V DC bias voltages. ....	102
Figure 4.30 Comparison of the simulated gains of the tunable RA with a lossy and lossless equivalent circuit models of the varactor with $C_{hp}$ of 2.5 pF.....	103
Figure 5.1 Simplified equivalent circuit model of one <i>Supercell_v1</i> structure. ....	108
Figure 5.2 Simplified equivalent circuit model of one <i>Supercell_v2</i> structure. ....	108
Figure 5.3 Configuration of one asymmetric ECRLH unit cell structure.....	110
Figure 5.4 Photograph of the fabricated LWA with 14 ECRLH unit cells.....	110
Figure 5.5 Simulated and measured S11 and S21 of the passive LWA with 14 ECRLH unit cells.....	111
Figure 5.6 Co-polarized simulated and measured normalized farfield leaky-wave radiation patterns at the XOZ plane within two passbands, (a) 0.9-1.25 GHz; (b) 3.1-3.6 GHz; (c) 5.7-6.2 GHz.....	113
Figure 5.7 Simulated and measured gains in dBi of this passive LWA at the leaky-wave regions. ....	114
Figure 5.8 Leakage rates of this LWA at the leaky-wave regions, (a) 0.9-1.25 GHz; (b) 3.1-3.6 GHz; (c) 5.7-6.2 GHz. ....	114
Figure 5.9 Simulated directivities of this LWA at the leaky-wave regions within both passbands. ....	114

Figure 5.10 Equivalent circuit model of one ECRLH unit cell structure.....	115
Figure 5.11 Full-wave and circuit-model simulated performances of one ECRLH unit cell in the antenna structure, (a) the frequency response; (b) the dispersion diagram. ....	116
Figure 5.12 Comparison of the simulated gains of this passive LWA at the leaky-wave regions in the lossy and lossless case.....	118
Figure 5.13 Comparison of the simulated total efficiencies of this passive LWA at the leaky-wave regions in the lossy and lossless case.....	118
Figure 5.14 Dispersion diagrams of a <i>Supercell_v1</i> structure in different conditions, (a) the unbalanced condition; (b) the balanced condition. ....	120
Figure 5.15 Configuration of one <i>Supercell_v1</i> structure. ....	122
Figure 5.16 Equivalent circuit model of one <i>Supercell_v1</i> structure. ....	122
Figure 5.17 Photograph of the fabricated LWA with 6 <i>Supercell_v1</i> structures. ....	124
Figure 5.18 Full-wave and circuit-model simulated performances of a <i>Supercell_v1</i> structure, (a) the frequency response; (b) the dispersion diagram. ....	124
Figure 5.19 Full-wave simulated and measured S11 and S21 of the passive LWA with 6 <i>Supercell_v1</i> structures. ....	125
Figure 5.20 Co-polarized simulated and measured normalized farfield leaky-wave radiation patterns at the XOZ plane within two passbands, (a) 0.88-1.25 GHz; (b) 3.7-5.3 GHz. ....	126
Figure 5.21 Simulated and measured gains at the leaky-wave regions within both passbands.....	127
Figure 5.22 Leakage rates of this LWA at the leaky-wave regions, (a) 0.8-1.25 GHz; (b) 3.7-5.3 GHz. ....	128
Figure 5.23 Simulated directivities of this LWA at the leaky-wave regions within both passbands.....	128
Figure 5.24 Comparison of the simulated gains of this passive LWA at the leaky-wave regions in the lossy and lossless case.....	129
Figure 5.25 Comparison of the simulated total efficiencies of this passive LWA at the leaky-wave regions in the lossy and lossless case.....	129
Figure 5.26 Dispersion diagrams of one <i>Supercell_v2</i> structure in different conditions, (a) the unbalanced condition; (b) the balanced condition. ....	132
Figure 5.27 Configuration of a <i>Supercell_v2</i> structure. ....	132
Figure 5.28 Detailed equivalent circuit model of one <i>Supercell_v2</i> structure. ....	133
Figure 5.29 Photograph of the passive LWA with 7 cascaded <i>Supercell_v2</i> structures.....	134
Figure 5.30 Full-wave and circuit-model simulated performances of a <i>Supercell_v2</i>	

structure, (a) the frequency response; (b) the dispersion diagram. ....	135
Figure 5.31 Measured and simulated S11 and S21 of the passive LWA with 7 <i>Supercell_v2</i> structures. ....	136
Figure 5.32 Co-polarized simulated and measured normalized farfield leaky-wave radiation patterns at the XOZ plane within two passbands, (a) 1.0-1.3 GHz; (b) 3.8-5.7 GHz.....	137
Figure 5.33 Simulated and measured gains of this passive LWA at the leaky-wave regions. ....	137
Figure 5.34 Leakage rates of this LWA at the leaky-wave regions, (a) 1.0-1.3 GHz; (b) 3.8-5.7 GHz. ....	138
Figure 5.35 Simulated directivities of this LWA at the leaky-wave regions within both passbands.....	138
Figure 5.36 Comparison of the simulated gains of this passive LWA at the leaky-wave regions in the lossy and lossless case.....	139
Figure 5.37 Comparison of the simulated total efficiencies of this passive LWA at the leaky-wave regions in the lossy and lossless case.....	139
Figure 5.38 Comparison of dispersion diagrams with different capacitances of each capacitor, (a) $C_{hs}$ ; (b) $C_{se}$ ; (c) $C_{vs}$ ; (d) $C_{vp}$ ; (e) $C_{st}$ . ....	141
Figure 5.39 Configuration of a tunable <i>Supercell_v2</i> structure.....	142
Figure 5.40 Photograph of this tunable LWA with 7 cascaded <i>Supercell_v2</i> structures.....	144
Figure 5.41 Measured and simulated results of S11 and S21 of this tunable LWA in the initial state.....	145
Figure 5.42 Comparison of the measured results of S11 and S21 of the low CRLH passband between the initial state and the tuning states. ....	146
Figure 5.43 Comparison of the measured results of S11 and S21 of the high CRLH passband between the initial state and the tuning states. ....	146
Figure 5.44 Comparison of the measured results of S11 and S21 of the low CRLH passband between the initial state and the controlling states. ....	148
Figure 5.45 Comparison of the measured results of S11 and S21 of the high CRLH passband between the initial state and the controlling states. ....	148
Figure 5.46 Comparison of the simulated dispersion diagrams of the single tunable <i>Supercell_v2</i> structure between the initial state and the 4th states. ....	150
Figure 5.47 Comparison of the simulated dispersion diagrams of the single tunable <i>Supercell_v2</i> structure between the initial state and the 6th states. ....	150
Figure 5.48 Co-polarized normalized farfield patterns of this tunable LWA at the XOZ plane, (a) the measured results at 1.08 GHz in the initial, 3rd, and 4th states; (b) the	

measured and simulated results over 2.8-4.3 GHz in the initial state; (c) the measured results over 3.0-4.3 GHz in the 3rd state; (d) the measured results over 3.0-4.3 GHz in the 4th state. ....	152
Figure 5.49 Gains of this tunable LWA, (a) the simulated and measured results in the initial state; (b) the measured results in the 3rd and 4th states.....	153
Figure 5.50 Simulated directivities of this LWA at the leaky-wave regions within both passbands.....	154
Figure 5.51 Leakage rates of this tunable LWA in the initial state at the leaky wave regions with both CRLH passbands, (a) 0.9-1.3 GHz; (b) 2.8-4.3 GHz.....	154
Figure 5.52 Comparison of the simulated gains of this tunable LWA within the leaky-wave regions in the lossy, and the 1st and 2nd lossless scenarios.....	156
Figure 5.53 Comparison of the simulated total efficiencies at the leaky-wave regions within both CRLH passbands in the lossy, and the 1st and 2nd lossless scenario...	156
Figure 6.1 Types of the BST varactors, (a) parallel type; (b) coplanar type. ....	162
Figure 6.2 Expanded views of the CRLH unit cell with and without BST varactors, (a) top view without BST varactors; (b) top view with BST varactors; (c) perspective view without BST varactors; (d) perspective view with BST varactors. ....	163
Figure 6.3 Expanded views of the discrete BST varactors, (a) top view of <i>BST_varactor_1</i> ; (b) top view of <i>BST_varactor_2</i> ; (c) perspective view of <i>BST_varactor_1</i> ; (d) perspective view of <i>BST_varactor_2</i> . ....	164
Figure 6.4 Simulated S11 and S21 of the CRLH unit cell in the initial and final state. ....	166
Figure 6.5 Simulated dispersion diagram of the CRLH unit cell in the initial and final state. ....	166
Figure 6.6 Configurations of the unit cell with feeding lines and bias lines, (a) without BST varactors; (b) with BST varactors. ....	167
Figure 6.7 Complete configuration of the LWA with BST varactors. ....	168
Figure 6.8 Simulated S parameters of the LWA in the initial state. ....	168
Figure 6.9 Simulated farfield patterns of the LWA over 2.2-2.6 GHz in the initial state. ....	168
Figure 6.10 Simulated gains in dBi of the LWA over 2.1-2.6 GHz in the initial state.....	169
Figure 6.11 Simulated S parameters of the LWA in the final state. ....	169
Figure 6.12 Simulated farfield patterns of the LWA over 2.4-2.8 GHz in the final state. ....	170
Figure 6.13 Simulated gains in dBi of the LWA over 2.2-3.0 GHz in the final state.....	170

Figure 6.14 Comparison of the simulated gains in dBi of the LWA in the lossy and lossless cases under 0 V DC bias voltages. ....	171
Figure 6.15 Two-layer CPW TL model. ....	173
Figure 6.16 Two-port network in the transmission ABCD matrix. ....	174
Figure 6.17 Equivalent circuit model of the CPW TL structure. ....	174
Figure 6.18 Equivalent models, (a) the equivalent CPW with air filling, i.e., $\epsilon_r = 1$ ; (b) the equivalent CPW model with permittivity of $(\epsilon_{r\_sub} - 1)$ ; (c) the equivalent CPW model with permittivity of $(\epsilon_{r\_BST} - \epsilon_{r\_sub})$ . ....	176
Figure 6.19 Distribution of uncertainties in BST permittivity in the first case. ....	178
Figure 6.20 Distribution of uncertainties in BST permittivity in the second case....	179

## List of Tables

Table 3.1 Summary of the metamaterial-inspired RAs in [15]-[23].....	40
Table 3.2 Summary of the CRLH-based LWAs in [25], [28]-[34] .....	51
Table 3.3 Summary of the multiband LWAs in [36]-[40] .....	56
Table 3.4 Summary of the BST material in [44]-[49] .....	63
Table 3.5 Summary of the tuning techniques for tunable antenna designs in [44], [28], [52]-[54].....	67
Table 4.1 Dimensions of the proposed passive RA with SMD chip capacitors and the capacitances of the SMD capacitors in this RA.....	76
Table 4.2 Component values in the equivalent circuit model of this RA with SMD chip capacitors.....	81
Table 4.3 Some parts of the RA with SMD chip capacitors and the operating resonances correspondingly controlled by each part.....	83
Table 4.4 Dimensions of the proposed passive RA with IDSs.....	85
Table 4.5 Component values in the equivalent circuit model of this RA with IDSs...	90
Table 4.6 Some parts of the RA with IDSs and the operating resonances correspondingly controlled by each part.....	91
Table 4.7 Dimensions of a conventional monopole antenna.....	94
Table 4.8 Dimensions of the active antenna with one varactor.....	96
Table 4.9 Summary of the RAs in this chapter.....	104
Table 5.1 Dimensions of one asymmetric ECRLH unit cell structure.....	111
Table 5.2 Component values used in the equivalent circuit model of one ECRLH unit cell structure.....	116
Table 5.3 Component values in the equivalent circuit model of one <i>Supercell_v1</i> structure.....	123
Table 5.4 Dimensions of one <i>Supercell_v1</i> structure.....	123
Table 5.5 Component values in the equivalent circuit model of one <i>Supercell_v2</i> structure.....	133
Table 5.6 Dimensions of one <i>Supercell_v2</i> structure.....	133
Table 5.7 Dimensions of one tunable <i>Supercell_v2</i> structure.....	142
Table 5.8 List of all states with different sets of DC bias voltages.....	145
Table 5.9 Summary of the LWAs in this chapter.....	157

Table 6.1 Comparison of BST with GaAs and MEMS techniques [43].	162
Table 6.2 Dimensions of one CRLH TL unit cell and BST varactors.	165
Table 6.3 Some parameters of the BST varactors in the LWA design in the simulation.	165
Table 6.4 Dimensions of the feeding lines and bias lines.	167
Table 6.5 Some parameters used in the uncertainty analysis.	172
Table 6.6 The first case of the key parameters with corresponding standard deviation.	178
Table 6.7 The second case of the key parameters with corresponding standard deviation.	179
Table 7.1 Summary of the antenna characteristics, achievements and meanings of three classes of antennas in this thesis.	185

# List of Abbreviations

**LWA** – Leaky Wave Antenna

**RA** – Resonant Antenna

**CRLH** – Composite Right/Left Handed

**TL** – Transmission Line

**1-D** – One-Dimension

**ECRLH** – Extended Composite Right/Left Handed

**FE** – Ferroelectric

**BST** – Barium Strontium Titanium

**SMD** – Surface Mounted

**IDS** – Interdigital Structure

**GaAs** – Gallium Arsenide

**ZOR** – Zeroth-Order Resonant

**IDC** – Interdigital Capacitor

**GP** – Ground Plane

**ENG** – Epsilon Negative

**MTL** – Meta-structured Transmission Line

**DNG** – Double Negative

**CPW** – Coplanar Waveguide

**MNG** – Mu-Negative

**MIM** – Metal-Insulator-Metal

**SIW** – Substrate Integrated Waveguide

**LTE** – Long Term Evolution

**GSM** – Global Systems for Mobile Communications

**UMTS** – Universal Mobile Telecommunications System

**WLAN** – Wireless Local Area Network

**DCS** – Digital Cellular System

**PCS** – Personal Communication Service

**2-D** – Two-Dimension

**LH** – Left Handed

**RH** – Right Handed

**GPS** – Global Positioning System

**HMSIW** – Half-Mode Substrate Integrated Waveguide

**CP** – Circular Polarization

**SSR** – Split-Ring Resonator

**DP-CRLH** – Double Periodic Composite Right/Left Handed

**FSS** – Frequency Selective Surface

**PBC** – Periodic Boundary Condition

**NRI** – Negative Refractive Index

**DCRLH** – Dual Composite Right/Left Handed

**PCB** – Printed Circuit Board

**CQF** – Commutation Quality Factor

# List of Publications

## Journal Papers in Progress

1. X. Gao, T. J. Jackson, and P. Gardner, "Multiband Open-Ended Resonant Antenna Based On One ECRLH Unit Cell Structure", *IEEE Antenna and Wireless Propag. Lett.*, DOI:10.1109/LAWP.2016.2632299, accepted, 2016.
2. X. Gao, T. J. Jackson, and P. Gardner, "Radiation Characteristics of Microstrip Leaky-Wave Antenna Based On Extended Right/Left-Handed Transmission-Line Structure", *IEEE Antenna and Wireless Propag. Lett.*, submitted, 2017.
3. X. Gao, T. J. Jackson, and P. Gardner, "Dual-band Leaky Wave Antenna Based on Novel Metamaterial-Inspired Supercell Structure", to be submitted to *IEEE Antenna and Wireless Propagation Letters*, 2017.
4. X. Gao, T. J. Jackson, and P. Gardner, "Analysis of Open-Ended Resonant Antennas with One ECRLH Unit Cell Structure", to be submitted to *IEEE Transactions on Antennas and Propagation*, 2017.
5. X. Gao, T. J. Jackson, and P. Gardner, "Analysis of Dual-Band Leaky Wave Antenna Using New Supercell Structures", to be submitted to *IEEE Transactions on Antennas and Propagation*, 2017.

## Conference Papers

1. X. Gao, T. J. Jackson, P. Gardner, M. M. Kechik, and B. Jancar, "Influence of Uncertainty in Dielectric Properties on Design Performance of a Tunable CRLH LWA," *Applications of Ferroelectric, International Symposium on Integrated Functionalities and Piezoelectric Force Microscopy Workshop (ISAF/ISIF/PFM), 2015 Joint IEEE International Symposium on the*, pp. 182-185, 2015.
2. P. Gardner, A. Feresidis, P. S. Hall, T. J. Jackson, O. Tade, M. Mavridou, Y. Kabiri and X. Gao, "Frequency Reconfiguration in Single and Dual Antenna Modules", *7th European Conference on Antennas and Propagation (EUCAP)*, 2013.

# CHAPTER I

## INTRODUCTION

### **1.1 Background**

As important components in wireless communication systems, antennas have attracted a lot of research interest for many decades. Antennas with good performance can always facilitate the improvement of the final communication quality and simplification of the entire communication system architecture.

In the last decade, due to the unusual and interesting properties of artificial electromagnetic metamaterial structures, such as simultaneously negative permittivity and negative permeability, an increasing number of antennas based on different metamaterial-inspired structures have been designed and investigated to achieve interesting antenna characteristics. As two major fields of the metamaterial-inspired antennas, resonant antennas (RAs) and leaky wave antennas (LWAs) have attracted a lot of research interest. The combination of the antenna design with the artificial electromagnetic metamaterial structure can enable the RA or LWA to have some novel antenna characteristics. For example, the classic metamaterial composite

right/left-handed (CRLH) transmission line (TL) structure may be used to enhance the bandwidth of some metamaterial-inspired RAs; new metamaterial-inspired supercell structures may enable multi-passband leaky-wave radiation characteristics for one-dimension (1-D) LWAs.

Evidently, the research fields of artificial electromagnetic metamaterial structures and their applications are still in progress and have great potentials and values to be further explored. The antenna designs based on new artificial electromagnetic metamaterial structures can exhibit some improvements in antenna performance, such as the frequency response, radiation pattern, gain or polarization. Due to the possible improvements of the antenna performance, antenna designs based on new artificial electromagnetic metamaterial structures with novel antenna characteristics are a very important and interesting research direction.

## **1.2 Motivations and Objectives**

### **1.2.1 Motivations**

Multiband or frequency-agile antennas are very important and useful in modern wireless communication systems, e.g., the cellular communication system, because they can support a variety of wireless frequency bands using their multiband or frequency tunable characteristics at microwave frequencies. The increasing demands of multiband or frequency-agile antennas have enabled a lot of antenna designs with multiband or frequency tunable characteristics. The artificial electromagnetic

metamaterial-inspired structures can provide a good way to help antennas achieve the expected multiband or frequency tunable characteristics. For example, a metamaterial-inspired monopole antenna loaded with one CRLH unit cell can be used for tri-band applications [1]; an internal antenna with an epsilon negative resonator can realize the frequency tunability from 474 MHz to 702 MHz for digital video broadcasting-handheld services [2]. In artificial electromagnetic metamaterial structures, the extended CRLH (ECRLH) structure and some metamaterial-inspired supercell structures exhibit multiband properties. They can be applied to antenna designs, such as RAs and LWAs, in order to enable antennas to have multiband or frequency tunable characteristics. For example, a substrate integrated waveguided (SIW) LWA based on one ECRLH structure can achieve the backward-to-forward leaky-wave radiation characteristics within both passbands [3]; an SIW LWA based on the cascaded metamaterial-inspired supercell structures can achieve the forward-only and backward-to-forward leaky-wave radiation characteristics within two passbands, respectively [4].

Based on these considerations and motivations above, in order to design novel antennas with multiband or frequency tunable characteristics and simultaneously explore the applications of artificial electromagnetic metamaterial structures, the RAs and LWAs based on the ECRLH structures or the metamaterial-inspired supercell structures are carefully designed for multiband operations. For metamaterial-inspired RAs, a class of the RAs based on one ECRLH unit cell structure is designed for multiband or frequency-agile applications. For metamaterial-inspired LWAs,

according to the observation that the LWA based on the ECRLH structure does not have the backward-to-forward leaky-wave radiation characteristics within its high passband, the LWAs based on two novel metamaterial-inspired supercell structures are proposed to achieve the backward-to-forward leaky-wave radiation within its both passbands. In addition, an electronically tunable LWA with semiconductor varactors is presented in order to investigate the frequency tunability of its balanced points within both passbands.

### **1.2.2 Objectives**

In this thesis, the main objectives are summarized as followings:

- (1) To design RAs and LWAs based on the metamaterial ECRLH structures based on the background theory of the ECRLH structure, and to further investigate their antenna characteristics.
- (2) To design dual-passband LWAs based on two metamaterial-inspired supercell structures, in order to achieve the backward-to-forward leaky-wave radiation within both passbands.
- (3) To develop an electronically tunable LWA with discrete ferroelectric (FE) barium strontium titanium (BST) thin-film varactors, and to further analyze the uncertainty in the determination of the BST permittivity from the characterization process.

### **1.3 Outline of Thesis**

The focus of this thesis is novel RA and LWA designs based on different metamaterial-inspired structures at microwave frequencies. A brief introduction to the background and a description of motivations, objectives, and contributions have been presented in this chapter. The content of the remaining chapters in this thesis is briefly explained as follows:

In Chapter II, the background theories of conventional LWAs, the CRLH structure, the metamaterial-inspired RA based on the CRLH structure, and the ECRLH structure with multiband properties are briefly introduced and explained. The antenna designs in this thesis are based on these background theories.

In Chapter III, the existing designs of the metamaterial-inspired RAs, the 1-D LWAs based on different CRLH TL structures, the 1-D LWAs based on different metamaterial-inspired supercell structures, the antennas with FE BST materials are briefly reviewed. In addition, the tuning techniques used in existing antenna designs at microwave frequencies are reviewed as well. The reported antenna designs in these five fields are compared and summarized in five tables, respectively.

In Chapter IV, a class of the metamaterial-inspired RAs based on one ECRLH unit cell structure is proposed. As an extension of conventional metamaterial-inspired ones based on the CRLH unit cell structure, the resonant theory of a resonant structure based on the ECRLH unit cell structure is developed. Three open-ended RAs based on one ECRLH unit cell structure are proposed for multiband or frequency-agile

applications. The first design is incorporated with surface-mounted (SMD) chip capacitors for initial theoretical realization. In order to avoid the losses from these chip capacitors, the second design is realized using interdigital structures (IDSs). The third design using one SMD GaAs semiconductor varactor is further proposed to achieve the frequency tunability of one operating resonance at the low frequency while maintaining the wideband coverage formed by the other operating resonances.

In Chapter V, 1-D dual-passband LWAs based on the ECRLH TL structure and the metamaterial-inspired supercell structures are proposed to achieve different leaky-wave radiation characteristics. The first dual-passband LWA based on the ECRLH TL structure is analyzed in terms of its leaky-wave radiation characteristics. Due to the fact that the first LWA does not have the backward-to-forward leaky-wave radiation characteristics within its high passband, two metamaterial-inspired supercell structures, i.e., *Supercell\_v1* and *Supercell\_v2*, are developed and applied to the second and third LWA designs, in order to achieve the backward-to-forward leaky-wave radiation characteristics within both passbands. *Supercell\_v1* and *Supercell\_v2* are the given names of these two proposed metamaterial-inspired supercells. The *Supercell\_v2* structure is developed from the *Supercell\_v1* structure. In addition, the fourth design is an electronically tunable LWA based on the *Supercell\_v2* structure, which can achieve the relatively independent tunability of the low balanced point while keeping the frequency position of the high balanced point and maintaining the backward-to-forward leaky-wave radiation characteristics within the high passband.

In Chapter VI, the additional research related to the FE BST material is presented. Firstly, an electronically tunable 1-D LWA incorporated with discrete BST thin-film varactors is designed and its frequency tunability is also demonstrated in the simulation. Due to the importance of knowledge of the BST permittivity used as an input quantity in the antenna design, the uncertainty analysis in determination of the permittivity of the FE BST material is also included in this chapter.

In Chapter VII, the conclusions of the works are presented, and the possible research directions of the future work are discussed.

## **1.4 Contributions**

The main contributions of the research in this thesis are summarized as followings:

- (1) A class of microstrip-fed open-ended metamaterial-inspired RAs based on one asymmetric ECRLH unit cell structure for multiband or frequency-agile applications will be presented in Chapter IV. The RAs in this class can provide new ideas for future small antenna designs in mobile devices. The investigation of the ECRLH structure in these RA designs may enable new structures of small antenna design for multiband or frequency-agile applications. Most existing RA designs based on the CRLH structure only generate a few operating resonances to cover a few frequency bands. Compared to them, the proposed RAs generate more operating resonances working at the chosen frequency bands. The passive RAs can achieve the multiband coverage over 0.5-6.0 GHz, while a tunable one

can achieve the frequency tunability of one operating resonance at the low frequency to cover 0.7-0.96 GHz and keeping the wideband coverage over 1.7-6.0 GHz.

(2) The LWAs based on the ECRLH and novel metamaterial-inspired supercell structures (i.e., *Supercell\_v1* and *Supercell\_v2*) are mainly designed for dual-passband applications with different leaky-wave radiation characteristics, which will be presented in Chapter V. According to the observation that a microstrip LWA based on the ECRLH structure does not present the conventional backward-to-forward leaky-wave radiation characteristics within its high passband, the LWAs based on the *Supercell\_v1* and *Supercell\_v2* structures can achieve the backward-to-forward leaky-wave radiation characteristics within both passbands. Most existing LWA designs based on the CRLH structures mainly focus on the performance improvement within its single operating band. Most existing LWA designs based on metamaterial-inspired structures are mainly designed based on the passive SIW structure, which may lose the tunability or control for the operation bands or the beam patterns. These dual-passband LWA designs are suitable for dual-band high-directivity applications. The investigation of these supercell structures may be used as references to design other kinds of antennas.

(3) An LWA design with discrete FE BST varactors presented in Chapter VI provides a good way to integrate the antenna structure with BST materials. Most existing BST-based antennas mainly use an entire piece of the BST layer, which may

introduce unnecessary losses to degrade the antenna radiation performance. The proposed LWA uses discrete BST varactors on the necessary positions, which may be very helpful to reduce the losses from the BST varactors. Furthermore, the uncertainty analysis in the determination of the BST permittivity from the characterization process can provide design clues and can be very helpful to optimize the antenna design process.

# CHAPTER II

## BACKGROUND THEORY

### **2.1 Introduction**

This chapter introduces the relevant background theories for the proposed antenna designs in this thesis. These theories lay the solid bases for the antenna research in this thesis. In section 2.2, the background theory of conventional LWAs is introduced. The basic theory of the CRLH structure is presented in Section 2.3. Furthermore, the resonant theory of a resonant structure based on the CRLH unit cell structure is presented in Section 2.4. In Section 2.5, the background theory of the ECRLH structure with multiband properties is introduced.

### **2.2 Theory of Conventional Leaky Wave Antennas**

Generally, an LWA is designed based on a wave-guiding structure which has some power leakage from this structure during wave propagation. The LWAs can achieve different leaky-wave characteristics, depending on structural forms (i.e., 1-D or 2-D)

and excitation positions (i.e., end excitation or center excitation) [5]. The 1-D LWAs with an end excitation are a major research field of interest in this thesis, so the discussion of 1-D LWAs with an end excitation will be presented in this section.

Generally, the background theory can be briefly explained as following: the energy of a guided wave flows through the guiding structure for an LWA, and the branches for perturbation in the guiding structure will interrupt the smooth wave propagation along this guiding structure. The energy can be mainly radiated or leaked at these perturbation branches from the guiding structure, which can be used for leaky-wave applications. The energy radiation from uniform or periodic perturbation branches can result in a fan beam with high directivity. One distinct characteristic of the LWA is that the main beam direction changes with frequency, which can be used for high-directivity applications. Figure 2.1 shows some LWA examples.

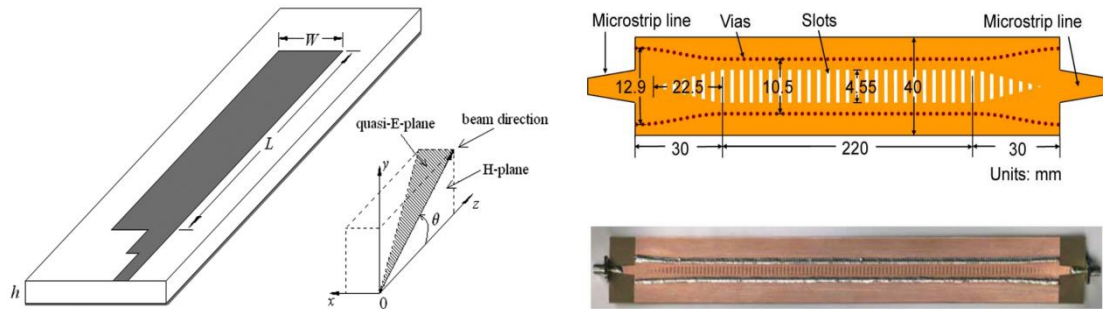


Figure 2.1 Examples of conventional LWAs.

For an LWA, its leaky-wave radiation is dependent on its complex propagation constant  $\gamma = \alpha + j\beta$  [6], where  $\alpha$  is the attenuation constant and  $\beta$  is the phase constant. Notably,  $\alpha$  and  $\beta$  are two critical parameters for a leaky-wave structure, which can determine the main beamwidth, radiation efficiency and radiation angle,

respectively [6]. The radiated power from the beginning of a guiding structure to the end generally follows an exponentially decreasing function. As the parameter for the power attenuation or leakage, a larger  $\alpha$  can result in a shorter effective aperture with less power leakage for radiation and wider beamwidth [6]. In contrast, a smaller  $\alpha$  can lead to a longer effective aperture with more power leakage for radiation and narrower beamwidth [6]. Generally, one LWA should be designed to achieve desirably around 90% of the accepted power along its guiding structure being radiated when the wave reached the antenna end [6]. With a matched load at the end of the guiding structure, the remaining power can be absorbed totally. The phase constant  $\beta$  changes as the operating frequency changes, which can further result in the change of the beam direction [6]. The intrinsic space harmonics of the antenna structure can be expressed in Eq. (2-1), in terms of  $\beta$ :

$$\beta_n = \beta_0 + \frac{2n\pi}{d} \quad \text{Eq. (2-1)}$$

where  $\beta_0$  is the phase constant of the lowest order space harmonic,  $\beta_n$  is the phase constant of the  $n$ th-order space harmonic,  $d$  is the period, and  $n$  is the number of space harmonics [5].

In general, 1-D LWAs can be mainly divided into two types – uniform (or quasi-uniform) and periodic. The radiation mechanisms of LWAs in these two types are different, which are respectively explained below.

### **2.2.1 Uniform or Quasi-Uniform LWAs**

For LWAs in uniform or quasi-uniform type, the guiding structure is either of uniform

structure or is composed of multiple cascaded periodic unit cells in which the period is much less than one guided wavelength (i.e.,  $d \ll \lambda_g$ ). This type of LWAs uses a fast wave for radiation. The fast wave is with respect to the wave velocity in free space, and the complex wave-number of the leaky mode  $k_z = \beta_n - j\alpha$  with  $0 < \beta_n < k_0$ , where  $k_0$  the wave-number in free space [5]. The beam direction and beamwidth of the LWA of this type can be expressed in Eq. (2-2) and Eq. (2-3) [6]:

$$\sin \theta_m \approx \beta_n / k_0 \quad \text{Eq. (2-2)}$$

$$\Delta\theta \approx \frac{1}{(L/\lambda_0) \cdot \cos\theta_m} \quad \text{Eq. (2-3)}$$

where  $\theta_m$  is the radiation angle of the main beam,  $L$  is the physical length of the guiding structure of the LWA,  $\lambda_0$  is the wavelength in free space,  $\Delta\theta$  is the beamwidth of the main beam and  $k_0 = (2\pi)/\lambda_0$  [6]. From Eq. (2-3), the physical length  $L$  of an LWA can affect the beamwidth  $\Delta\theta$  of its main beam. The relationship between the physical length  $L$  and the attenuation constant  $\alpha$  can be approximately expressed in Eq. (2-4) [6]:

$$\frac{L}{\lambda_0} \approx \frac{0.18}{\alpha} \cdot k_0 \quad \text{Eq. (2-4)}$$

### 2.2.2 Periodic LWAs

For periodic LWAs, the radiation mechanism of an LWA in this type is different from the one in uniform or quasi-uniform type. This type of LWAs supports a slow wave. The slow wave is with respect to free space, i.e.,  $\beta_n > k_0$ . The fundamental mode of a periodic LWA is slow with respect to the free-space velocity [5]. The periodic modulation is introduced to the wave-guiding structure in order to produce

leaky-wave radiation using proper harmonic modes. For a periodic LWA, the intrinsic space harmonics can be expressed using Eq. (2-2) as well.

As mentioned above, there are two major regions – fast-wave region (i.e.,  $0 < \beta_n < k_0$ ) and slow-wave region (i.e.,  $\beta_n > k_0$ ). Due to the non-radiation property of the fundamental mode space harmonic, a periodic LWA mainly uses the negative-order-mode ( $m = -1, -2, -3\dots$ ) space harmonics to operate within the fast-wave region for leaky wave radiation [6]. A periodic LWA usually uses the first-negative-order ( $m = -1$ ) harmonic mode for leaky-wave radiation, which is different from a uniform or quasi-uniform one that usually uses the fundamental mode ( $m = 0$ ) for radiation. Conventional LWAs usually suffer from the open stopband problem, which will be explained in Chapter III. An effective technique to suppress or even eliminate the open stopband region near broadside for a periodic LWA has been proposed in [7]. The radiation angle of the main beam in a periodic LWA can be expressed [5]:

$$\sin \theta_m \approx \beta_{-1} / k_0 \quad \text{Eq. (2-5)}$$

where  $\beta_{-1}$  is the phase constant of the first-negative-order harmonic, i.e.,

$$\beta_{-1} = \beta_0 - \frac{2\pi}{d} \quad \text{Eq. (2-6)}$$

where  $d$  is the period of the unit cell. For the beamwidth, Eq. (2-3) is still applicable to a periodic LWA. For the relationship between the physical length  $L$  of the guiding structure and its attenuation constant  $\alpha$ , Eq. (2-4) is applicable to the LWAs in the periodic type as well.

## 2.3 Theory of Composite Right/Left Handed Transmission Line Structure

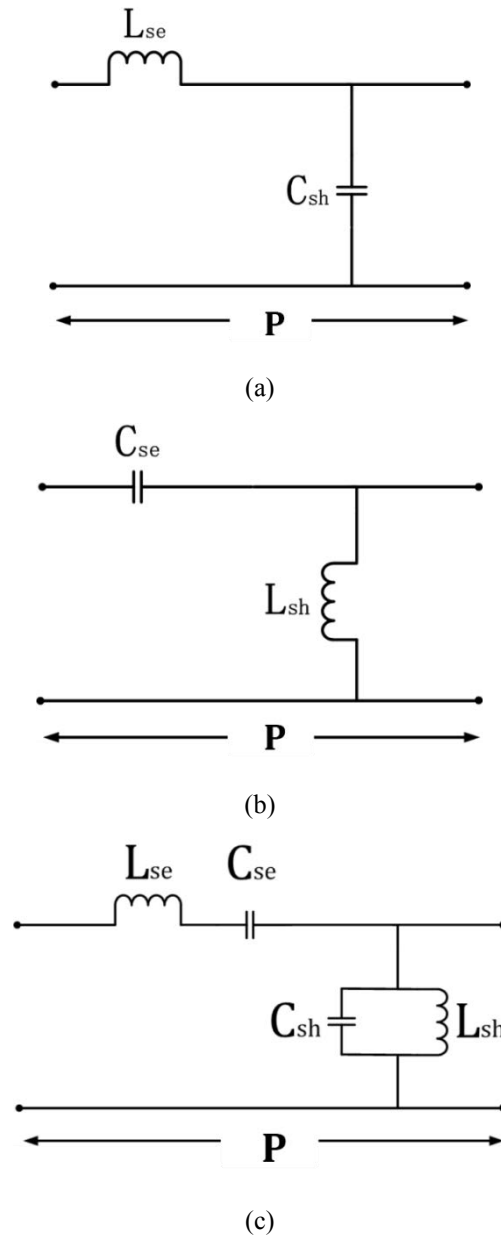


Figure 2.2 Equivalent models of different unit cell structure, (a) one conventional RH unit cell structure; (b) one LH unit cell structure; (c) one asymmetric CRLH unit cell structure.

The CRLH structure, as a classic artificial electromagnetic metamaterial structure, can be used to model the equivalent TL structure using multiple cascaded CRLH unit cells, if the condition for the effectively homogeneous medium can be satisfied. The CRLH

structure can be viewed as a combination of the conventional RH and LH structure. The equivalent models of the RH and LH unit cell structure are shown in Figure 2.2(a) and Figure 2.2(b), respectively.

The equivalent model of one CRLH unit cell structure is shown in Figure 2.2(c). The physical length of one unit cell is  $P$ , which is also the period of unit cells. When  $P \ll \lambda_g$ , these cascaded CRLH unit cell structures can be used to effectively model a TL structure;  $\lambda_g$  is the guided wavelength [8]. As shown in Figure 2.2(c), the equivalent model consists of an inductance  $L_{se}$  in series with a capacitance  $C_{se}$  in the horizontal branch and a shunt inductance  $L_{sh}$  in parallel with a capacitance  $C_{sh}$  in the vertical branch. The impedance of the horizontal branch and the admittance of the vertical branch are shown respectively as below:

$$Z(\omega) = j\omega L_{se} + \frac{1}{j\omega C_{se}} \quad \text{Eq. (2-7)}$$

$$Y(\omega) = j\omega C_{sh} + \frac{1}{j\omega L_{sh}} \quad \text{Eq. (2-8)}$$

The propagation constant of this CRLH structure is expressed in Eq. (2-9):

$$\gamma = \alpha + j\beta = \sqrt{Z(\omega)Y(\omega)} \quad \text{Eq. (2-9)}$$

where  $\alpha$  is the attenuation constant and  $\beta$  is the phase constant. The characteristic impedance of the CRLH structure is expressed in Eq. (2-10):

$$Z_c(\omega) = \frac{Z(\omega)}{\gamma} = \sqrt{\frac{Z(\omega)}{Y(\omega)}} \quad \text{Eq. (2-10)}$$

The resonant frequencies of the series and shunt  $L$ - $C$  resonators can be expressed in Eq. (2-11) and Eq. (2-12), respectively [8]:

$$\omega_{se} = \frac{1}{\sqrt{L_{se}C_{se}}} \quad \text{Eq. (2-11)}$$

$$\omega_{sh} = \frac{1}{\sqrt{L_{sh}C_{sh}}} \quad \text{Eq. (2-12)}$$

The center operation frequency of the CRLH structure is obtained as below [8]:

$$\omega_0 = \frac{1}{\sqrt[4]{L_{se}C_{se}L_{sh}C_{sh}}} \quad \text{Eq. (2-13)}$$

As mentioned above, the CRLH structure can be considered as a combination of the RH and LH structure, thus the resonant frequencies of the corresponding RH and LH  $L$ - $C$  resonators in the CRLH structure can be expressed [8]:

$$\omega_{RH} = \frac{1}{\sqrt{L_{se}C_{sh}}} \quad \text{Eq. (2-14)}$$

$$\omega_{LH} = \frac{1}{\sqrt{L_{sh}C_{se}}} \quad \text{Eq. (2-15)}$$

The impedances of the RH and LH structure can be expressed in Eq. (2-16) and Eq. (2-17), respectively [8]:

$$Z_{RH} = \sqrt{\frac{L_{se}}{C_{sh}}} \quad \text{Eq. (2-16)}$$

$$Z_{LH} = \sqrt{\frac{L_{sh}}{C_{se}}} \quad \text{Eq. (2-17)}$$

Through transformations, the propagation constant can be re-written as below [8]:

$$\gamma = \alpha + j\beta = js(\omega)\sqrt{\left(\frac{\omega}{\omega_{RH}}\right)^2 + \left(\frac{\omega_{LH}}{\omega}\right)^2 - (L_{se}C_{se} + L_{sh}C_{sh})\omega_{LH}^2} \quad \text{Eq. (2-18)}$$

where  $s(\omega)$  can be either negative or positive as a sign function,

$$s(\omega) = \begin{cases} -1, & \text{if } \omega < \min(\omega_{se}, \omega_{sh}), \text{ LH Range} \\ +1, & \text{if } \omega > \max(\omega_{se}, \omega_{sh}), \text{ RH Range} \end{cases} \quad \text{Eq. (2-19)}$$

The propagation constant  $\gamma$  can be purely real or purely imaginary, which is dependent on the operating band characteristics. The propagation constant is purely imaginary within the passband, i.e.,  $\gamma = j\beta$ , while it is purely real within the stopband, i.e.,  $\gamma = \alpha$  [8].

The dispersion relation of the CRLH unit cell can be derived in Eq. (2-20) by applying the periodic boundary conditions (PBCs) according to the Bloch-Floquet Theorem [8]:

$$\beta(\omega) = \frac{1}{P} \cos^{-1} \left( 1 + \frac{ZY}{2} \right) \quad \text{Eq. (2-20)}$$

where  $Z$  and  $Y$  are the total impedance of the series branch and the total admittance of the shunt branch. Due to the small electrical length of the unit cell, Eq. (2-21) can be approximately obtained using the Taylor approximation [8]:

$$\beta(\omega) = \frac{s(\omega)}{P} \sqrt{\omega^2 L_{se} C_{sh} + \frac{1}{\omega^2 L_{sh} C_{se}} - \left( \frac{L_{se}}{L_{sh}} + \frac{C_{sh}}{C_{se}} \right)} \quad \text{Eq. (2-21)}$$

Without considering the inter-cell coupling effects, the TL approach can also be used as a simple and useful way to analyze the characteristics and performance of the CRLH structure. The transmission ABCD matrix of one single asymmetric CRLH unit cell can be expressed [8]:

$$\begin{bmatrix} A & B \\ C & D \end{bmatrix}_{asym} = \begin{bmatrix} 1 & Z \\ 0 & 1 \end{bmatrix} \begin{bmatrix} 1 & 0 \\ Y & 1 \end{bmatrix} = \begin{bmatrix} 1 + ZY & Z \\ Y & 1 \end{bmatrix} \quad \text{Eq. (2-22)}$$

where  $Z$  and  $Y$  are the total impedance of the series branch and the total admittance of the shunt branch. By translating Eq. (2-7), Eq. (2-8), Eq. (2-11), and Eq. (2-12) into Eq. (2-22), the transmission ABCD matrix can be re-written as below [8]:

$$\begin{bmatrix} A & B \\ C & D \end{bmatrix}_{asym} = \begin{bmatrix} 1 - \xi & j \frac{(\omega/\omega_{se})^2 - 1}{\omega C_{se}} \\ j \frac{(\omega/\omega_{sh})^2 - 1}{\omega L_{sh}} & 1 \end{bmatrix} \quad \text{Eq. (2-23)}$$

where

$$\xi = ZY = \left( \frac{\omega}{\omega_{RH}} \right)^2 + \left( \frac{\omega_{LH}}{\omega} \right)^2 - \epsilon \omega_L^2 \quad \text{Eq. (2-24)}$$

$$\epsilon = L_{se} C_{se} + L_{sh} C_{sh} \quad \text{Eq. (2-25)}$$

Thus, the dispersion relation and the characteristic impedance of the CRLH structure can be respectively re-written in Eq. (2-26) and Eq. (2-27), respectively, in terms of the elements of the transmission ABCD matrix

$$\beta = \frac{1}{p} \cos^{-1}\left(\frac{A+D}{2}\right) \quad \text{Eq. (2-26)}$$

$$Z_c = \sqrt{\frac{B}{C}} \quad \text{Eq. (2-27)}$$

The CRLH structure can work under two different operating conditions – unbalanced condition and balanced condition [8]. Under the unbalanced condition, there is an open stopband existing from the LH band to the RH band, due to the difference between the resonant frequencies of the series branch and the shunt branch, i.e.,  $\omega_{se} \neq \omega_{sh}$  [8]. This open stopband will be explained in Section 3.3 of Chapter III. Under the balanced condition, the open stopband is closed and a balanced point is formed at the transition frequency from the LH band to the RH band. In this condition, the resonant frequencies of the series branch and the shunt branch are equal, i.e.,  $\omega_{se} = \omega_{sh}$ .

Generally, the leaky-wave characteristics of an LWA are analyzed and investigated using the dispersion diagram. A dispersion diagram is a graphical representation for the phase constant of the space harmonic modes with different velocities as a function of the angular frequency [9]. From the dispersion diagram, the characteristics of the passbands, stopbands and propagation space harmonic modes for the LWA can be observed and studied. The dispersion diagrams of the CRLH structure under the unbalanced and balanced condition are shown in Figure 2.3(a) and Figure 2.3(b),

respectively.

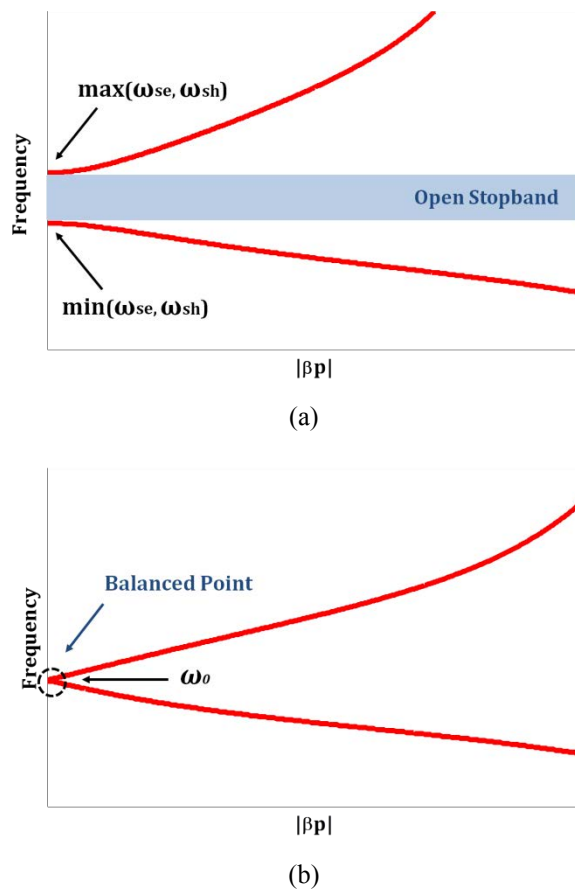


Figure 2.3 Dispersion diagrams of the CRLH structure, (a) the unbalanced condition; (b) the balanced condition.

## 2.4 Theory of Metamaterial-Inspired Resonant Antennas

The concept of the metamaterial-inspired structure brings novel ideas to RA designs. Most existing metamaterial-inspired RA designs are mainly based on the CRLH structure. For metamaterial-inspired RAs, a metamaterial-inspired structure is generally terminated with a short or an open end. Take the class of RAs based on the CRLH structure as one example for analysis and explanation. These RAs include one

or multiple CRLH unit cell structures as the major resonant structures. With a proper feeding approach, the intrinsic resonant modes can be excited for radiation. The resonant modes of a CRLH resonant structure with the total physical length  $L$ , which is composed of  $N$  unit cells with the period  $P$ , are expressed as Eq. (2-28) [10]:

$$\beta_m \cdot L = m \cdot \pi, \quad m = (0, \pm 1, \pm 2, \dots) \quad \text{Eq. (2-28)}$$

where  $\beta_m$  is the phase constant of the  $m$ th-order resonant mode,  $L = N \cdot P$ , and  $m$  is the sequence number of one specific resonant mode. Specifically, for the resonant modes,  $m$  can be both positive for RH bands (i.e.,  $m = +1, +2, \dots$ ) and negative for LH bands (i.e.,  $m = -1, -2, \dots$ ) and even zero ( $m = 0$ ) which exists at the transition frequency area [10]. A CRLH-based resonant structure consisting of  $N$  unit cells can be excited to generate a finite number of  $2N$  (under the unbalanced condition) or  $2N-1$  (under the balanced condition) resonances [10]. The corresponding resonant modes can be expressed in Eq. (2-29) [10]:

$$\beta_m \cdot P = \beta_m \cdot \left(\frac{L}{N}\right) = m \cdot \pi/N, \quad m = (0, \pm 1, \pm 2, \dots) \quad \text{Eq. (2-29)}$$

In terms of the dispersion relation, each resonant mode can have its corresponding axis of the phase constant ( $\beta_m$ ) and its corresponding operating frequency ( $\omega_m$ ). As mention above, the CRLH structure mainly has two operating conditions – unbalanced condition and balanced condition [8]. The resonance spectrums of a resonant structure based on the CRLH structure under the unbalanced and balanced condition are presented in Figure 2.4(a) and Figure 2.4(b), respectively.

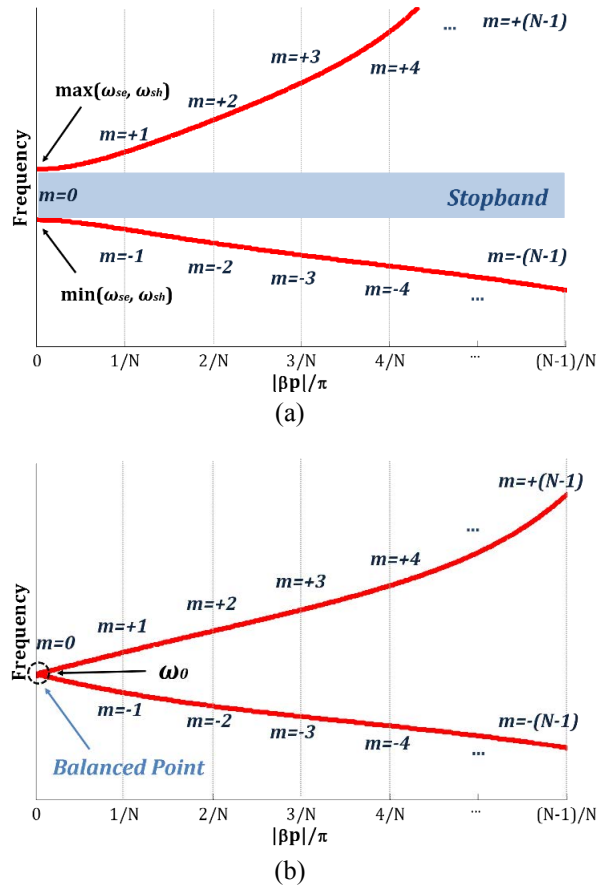


Figure 2.4 Resonance spectrums of the CRLH structure, (a) the unbalanced condition; (b) the balanced condition.

Generally, CRLH-based RAs can mainly be divided into two types – short-ended and open-ended [10]. For short-ended RAs, one or multiple CRLH unit cells are integrated together as a major resonant structure, and the termination of the antenna is directly connected to the ground plane or connected to a virtual ground plane. With a proper excitation, the multiple operating resonances of the resonant structure can be generated using the zeroth-order mode ( $m = 0$ ), negative-order modes ( $m = -1, -2, \dots$ ) and positive-order modes ( $m = +1, +2, \dots$ ). Thus, the RAs with a short end can achieve multi-band or wideband operations using these operating resonances. The other type is open-ended RAs. In this type, the RAs are usually realized by either

of one conventional open-ended antenna (e.g., monopole antenna) loaded with one or multiple metamaterial-based CRLH unit cells, or one or multiple open-ended unit cells excited directly by a proper feeding approach. Two major advantages of the metamaterial-inspired open-ended RAs can be summarized in comparison with conventional open-ended antennas [1]: (1) more operating resonances for multiband or wideband operations; (2) at least one operating resonance working at lower frequency than conventional monopole antennas. These advantages have attracted a lot of research interest on the metamaterial-inspired RAs and have enabled the antenna performance improvement.

Most metamaterial-inspired RAs are usually designed to use the zeroth-order mode ( $m = 0$ ) as the major radiated resonance. The utilization of the zeroth-order mode might enable the electrically small antenna designs [10]. This kind of RAs is also called the ZOR antennas. The resonant modes can be derived from Eq. (2-21). When  $m = 0$ , the phase constant of the zeroth-order mode is close to zero, i.e.,  $\beta_0 \rightarrow 0$ . The resonant frequency of the zeroth-order mode is independent of the physical length of the antenna, but is determined by inductance and capacitance values in the unit cell [11]. The input impedance ( $Z_{in}$ ) of the lossless CRLH structure ( $\alpha = 0$ ) can be expressed in Eq. (2-30) in terms of the TL theory:

$$Z_{in} = Z_c \left[ \frac{Z_L + jZ_c \tan(\beta L)}{Z_c + jZ_L \tan(\beta L)} \right] \quad \text{Eq. (2-30)}$$

where  $Z_c$  is the characteristic impedance of the CRLH structure,  $Z_L$  is the impedance of the load at the end,  $\beta$  is the phase constant, and  $L$  is the total physical length of the CRLH structure.

For the zeroth-order resonant mode, i.e.,  $m = 0$ ,  $\beta \rightarrow 0$ , of an open-ended RA, i.e.,  $Z_L = \infty$ , Eq. (2-31) can be re-written as:

$$Z_{in}^{open} = -jZ_c \cot(\beta L) \approx -\frac{jZ_c}{\beta L} = -j\sqrt{\frac{Z}{Y}} \left( \frac{1}{-j\sqrt{ZY}L} \right) = \frac{1}{YNP} \quad \text{Eq. (2-31)}$$

where  $Y$  is the shunt admittance,  $Z$  is the series impedance,  $N$  is the number of unit cells in the CRLH resonant structure, and  $P$  is the period of the unit cell. In this case, the zeroth-order resonant frequency  $\omega_{ZOR}$  of this CRLH-based resonant structure with an open end can be written as below:

$$\omega_{ZOR} = \omega_{sh} = \frac{1}{\sqrt{L_{sh}C_{sh}}} \quad \text{Eq. (2-32)}$$

where  $\omega_{sh}$  is the resonant frequency of the shunt branch in the CRLH unit cell structure, and  $L_{sh}$  and  $C_{sh}$  are the inductance and the capacitance in the shunt branch. From Eq. (2-31) and Eq. (2-32), it is obvious that the resonant frequency of the zeroth-order mode ( $m = 0$ ) for the open-ended case is primarily determined by the inductance and capacitance in the shunt branch of the CRLH unit cell structure.

Similarly, for the zeroth-order resonant mode, i.e.,  $m = 0$ ,  $\beta \rightarrow 0$ , and the RA is short-ended, i.e.,  $Z_L = 0$ , Eq. (2-30) can be re-written as:

$$Z_{in}^{short} = jZ_c \tan(\beta L) \approx jZ_c \beta L = \sqrt{\frac{Z}{Y}} \sqrt{ZY}L = ZNP \quad \text{Eq. (2-33)}$$

Correspondingly, in this case, the zeroth-order resonant frequency  $\omega_{ZOR}$  of a CRLH-based resonant structure with a short end can be written as below:

$$\omega_{ZOR} = \omega_{se} = \frac{1}{\sqrt{L_{se}C_{se}}} \quad \text{Eq. (2-34)}$$

where  $\omega_{se}$  is the resonant frequency of the shunt branch in the CRLH unit cell structure, and  $L_{se}$  and  $C_{se}$  are the inductance and the capacitance in the series branch. From Eq. (2-33) and Eq. (2-34), it is obvious that the resonant frequency of

the zeroth-order mode for the short-ended case is primarily determined by the inductance and capacitance in the series branch of the CRLH unit cell structure.

## 2.5 Theory of Extended Composite Right/Left Handed Transmission Line Structure

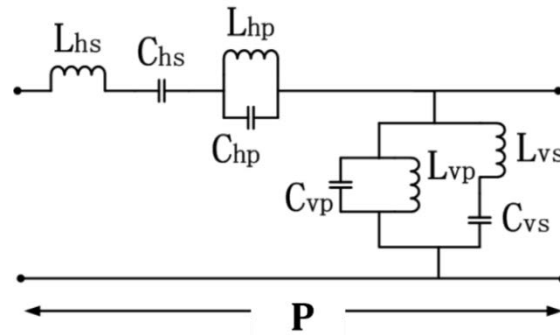


Figure 2.5 Equivalent circuit model of one ECRLH unit cell structure.

The metamaterial ECRLH structure was introduced in [12] as a generalized extension of the conventional CRLH structure, which is also called the generalized negative-refractive-index (GNRI) structure [13]. The equivalent circuit model of the ECRLH unit cell structure is shown in Figure 2.5.  $P$  is the physical length of the ECRLH unit cell. By inserting one parallel L-C resonator into the series branch and one series L-C resonator into the shunt branch in the equivalent model of the conventional CRLH structure, there are four L-C resonators in the equivalent model. The ECRLH structure can be seen as a combination of the conventional CRLH structure and the dual CRLH (DCRLH) structure. The equivalent model of the DCRLH unit cell structure is shown in Figure 2.6. The ECRLH structure yields two pairs of left-handed (LH) backward-wave and right-handed (RH) forward-wave bands,

instead of one pair in the conventional CRLH structure [12]. There is one middle bandgap existing between these two pairs of the LH and RH bands.

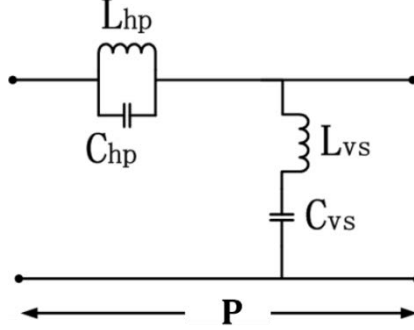


Figure 2.6 Equivalent circuit model of the DCRLH unit cell structure.

The impedance for the series resonator and the admittance of the parallel resonator in the horizontal branch can be respectively written as:

$$Z_{hs} = j\omega L_{hs} + \frac{1}{j\omega C_{hs}} \quad \text{Eq. (2-35)}$$

$$Y_{hp} = j\omega C_{hp} + \frac{1}{j\omega L_{hp}} \quad \text{Eq. (2-36)}$$

In the same way, the impedance for the series resonator and the admittance for the parallel resonator in the vertical branch can be respectively written as:

$$Z_{vs} = j\omega L_{vs} + \frac{1}{j\omega C_{vs}} \quad \text{Eq. (2-37)}$$

$$Y_{vp} = j\omega C_{vp} + \frac{1}{j\omega L_{vp}} \quad \text{Eq. (2-38)}$$

Each of four resonators in the circuit model has its own resonant frequency.  $\omega_{hs}$ ,  $\omega_{hp}$ ,  $\omega_{vs}$  and  $\omega_{vp}$  are used to represent the resonant frequencies of the horizontal series and parallel resonators and the vertical series and parallel resonators respectively, and can be written [13]:

$$\omega_{hs} = \frac{1}{\sqrt{L_{hs}C_{hs}}} \quad \text{Eq. (2-39)}$$

$$\omega_{hp} = \frac{1}{\sqrt{L_{hp}C_{hp}}} \quad \text{Eq. (2-40)}$$

$$\omega_{vs} = \frac{1}{\sqrt{L_{vs}C_{vs}}} \quad \text{Eq. (2-41)}$$

$$\omega_{vp} = \frac{1}{\sqrt{L_{vp}C_{vp}}} \quad \text{Eq. (2-42)}$$

The total impedance of the horizontal branch ( $Z_H$ ) and the total admittance of the vertical branch ( $Y_V$ ) are expressed in Eq. (2-43) and Eq. (2-44), respectively:

$$Z_H = Z_{hs} + \frac{1}{Y_{hp}} = j\omega L_{hs} + \frac{1}{j\omega C_{hs}} + 1/(j\omega C_{hp} + \frac{1}{j\omega L_{hp}}) \quad \text{Eq. (2-43)}$$

$$Y_V = Y_{vp} + \frac{1}{Z_{vs}} = j\omega C_{vp} + \frac{1}{j\omega L_{vp}} + 1/(j\omega L_{vs} + \frac{1}{j\omega C_{vs}}) \quad \text{Eq. (2-44)}$$

The resonant frequencies of the horizontal and vertical branches are expressed in Eq. (2-45) and Eq. (2-46) [13]:

$$\omega_{hshp} = \frac{1}{\sqrt{L_{hs}C_{hp}}} \quad \text{Eq. (2-45)}$$

$$\omega_{vsvp} = \frac{1}{\sqrt{L_{vs}C_{vp}}} \quad \text{Eq. (2-46)}$$

In order to use multiple cascaded ECRLH unit cells to model an effectively homogenous TL structure, the period  $P$  of the unit cell should meet the homogeneity condition [8]; the period of the unit cell should be much smaller than one guided wavelength, i.e.,  $P \ll \lambda_g$ . The propagation constant ( $\gamma$ ) of one ideal ECRLH structure is expressed in Eq. (2-47):

$$\gamma = \alpha + j\beta = \sqrt{Z_H Y_V} \quad \text{Eq. (2-47)}$$

where  $\alpha$  and  $\beta$  are the attenuation constant and the propagation constant, respectively.

The characteristic impedance of the proposed ECRLH is expressed in Eq. (2-48) [12]:

$$Z_c = \sqrt{\frac{Z_H}{Y_V}} = \sqrt{\frac{L_{hs}}{C_{vp}}} \sqrt{\frac{1 - (\omega_{hs}/\omega)^2 + (L_{hp}/L_{hs})/[1 - (\omega/\omega_{hp})^2]}{1 - (\omega_{vp}/\omega)^2 + (C_{vs}/C_{vp})/[1 - (\omega/\omega_{vs})^2]}} \quad \text{Eq. (2-48)}$$

The dispersion characteristic of the ECRLH unit cell is obtained from the PBCs related to the Bloch-Floquet theorem [8]:

$$\beta \cdot P = \cos^{-1}\left(1 + \frac{Z_H Y_V}{2}\right) \quad \text{Eq. (2-49)}$$

where  $\beta \cdot P$  is the phase shift of the ECRLH unit cell of the physical length of  $P$ , and  $\beta$  is the phase constant or propagation constant of the ECRLH unit cell.

The ABCD transmission matrix of the proposed asymmetric ECRLH unit cell is written in Eq. (2-50)

$$\begin{bmatrix} A & B \\ C & D \end{bmatrix} = \begin{bmatrix} 1 & Z_H \\ 0 & 1 \end{bmatrix} \begin{bmatrix} 1 & 0 \\ Y_V & 1 \end{bmatrix} = \begin{bmatrix} 1 + Z_H Y_V & Z_H \\ Y_V & 1 \end{bmatrix} \quad \text{Eq. (2-50)}$$

Thus, based on the analysis using the transmission line approach [8], Eq. (2-49) can also be re-written as

$$\beta \cdot P = \cos^{-1}\left(\frac{A+D}{2}\right) \quad \text{Eq. (2-51)}$$

Eq. (2-48) can also be re-written in terms of the transmission matrix elements of  $B$  and  $C$ :

$$Z_c = \sqrt{B/C} \quad \text{Eq. (2-52)}$$

Similar as the conventional CRLH structure, the ECRLH structure also has two operating conditions – unbalanced condition and balanced condition. Under the unbalanced condition, within each pair of the LH and RH band, one open stopband exists between the LH and RH band. These two open stopbands are called the low open stopband and high open stopband, respectively. The background theory of the open stopband is same for the phenomenon of the CRLH structure in the unbalanced condition. In the balanced condition, the ECRLH structure, the open stopband within each pair of the LH and RH band can be closed to form the balanced point at the transition frequency from the LH band to the RH band, thereby forming two entire

passbands with separation by one middle bandgap. These two balanced points are represented by low balanced point and high balanced point, respectively. The ECRLH structure can be used for dual-band, tri-band, quad-band or even multiband applications, depending on different operating conditions and different designs. In the balanced condition, one operating frequency within the middle bandgap area is denoted by  $\omega_0$ . At  $\omega_0$ , the horizontal branch becomes short circuited and the vertical branch is open circuited [13].

In order to derive the equations for the balanced and unbalanced condition, Eq. (2-43) and Eq. (2-44) can be re-written as below, in terms of the resonant frequencies [13]:

$$Z_H = j\omega L_{hs} \left(1 - \frac{\omega_{hs}^2}{\omega^2}\right) - \frac{j}{\omega C_{hp}(1 - \omega_{hp}^2/\omega^2)} \quad \text{Eq. (2-52)}$$

$$Y_V = j\omega C_{vp} \left(1 - \frac{\omega_{vp}^2}{\omega^2}\right) - \frac{j}{\omega L_{vs}(1 - \omega_{vs}^2/\omega^2)} \quad \text{Eq. (2-53)}$$

For  $\beta = 0$ , Eq. (2-54) and Eq. (2-55) can be derived by setting  $Z_H = Y_V = 0$  [13]:

$$\omega_{H,zero}^2 = 0.5(\omega_{hp}^2 + \omega_{hs}^2 + \omega_{hshp}^2) \pm 0.5\sqrt{(\omega_{hp}^2 + \omega_{hs}^2 + \omega_{hshp}^2)^2 - 4\omega_{hp}^2\omega_{hs}^2} \quad \text{Eq. (3-54)}$$

$$\omega_{V,zero}^2 = 0.5(\omega_{vp}^2 + \omega_{vs}^2 + \omega_{vsvp}^2) \pm 0.5\sqrt{(\omega_{vp}^2 + \omega_{vs}^2 + \omega_{vsvp}^2)^2 - 4\omega_{vp}^2\omega_{vs}^2} \quad \text{Eq. (3-55)}$$

The balanced condition can be determined by setting  $\omega_{H,zero} = \omega_{V,zero} = 0$ , thereby yielding Eq. (2-56), Eq. (2-57), and Eq. (2-58) for the balanced condition [13]:

$$\omega_{hs} = \omega_{vp} \quad \text{Eq. (2-56)}$$

$$\omega_{hp} = \omega_{vs} = \omega_0 \quad \text{Eq. (2-57)}$$

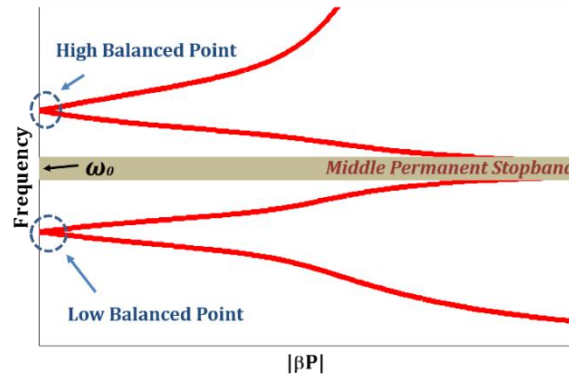
$$\omega_{hshp} = \omega_{vsvp} \quad \text{Eq. (2-58)}$$

The dispersion diagrams of the ECRLH structure in the unbalanced and balanced condition are respectively shown in Figure 2.7(a) and Figure 2.7(b). In this condition, the characteristic impedance can be expressed as below [13]:

$$Z_{c,balanced} = \sqrt{\frac{L_{hs}}{C_{vp}}} = \sqrt{\frac{L_{vp}}{C_{hs}}} = \sqrt{\frac{L_{hp}}{C_{vs}}} = \sqrt{\frac{L_{vs}}{C_{hp}}} \quad \text{Eq. (2-59)}$$



(a)



(b)

Figure 2.7 Dispersion diagrams of the ECRLH structure, (a) the unbalanced condition; (b) the balanced condition.

## 2.6 Summary

This chapter introduces the background theory of the conventional LWAs, the metamaterial CRLH structure, the resonant theory for the CRLH-based resonant structure, and the metamaterial ECRLH structure. These background theories provide important theoretical tools and supports for design and analysis of antennas in the following chapters.

# CHAPTER III

## REVIEW OF ARTIFICIAL ELECTROMAGNETIC STRUCTURES AND BARIUM STRONTIUM TITANIUM MATERIALS APPLIED TO ANTENNA DESIGNS

### **3.1 Introduction**

Since the concept of the metamaterial CRLH structure was firstly proposed in 2004 [14], this novel artificial electromagnetic structure has attracted a lot of research interest and has been applied to many different designs of components and antennas from microwave to optical frequencies, due to its unusual and interesting properties, such as simultaneously negative permittivity and negative permeability. With inspirations from the CRLH structure, many metamaterial-inspired structures have been proposed and applied to antenna designs for microwave, millimeter-wave or even optical applications. Generally, antennas based on metamaterial-inspired

structures can be mainly divided into two categories – metamaterial-inspired RAs and metamaterial-inspired LWAs.

The antenna designs in this thesis can be mainly divided into three parts. The first part is the metamaterial-inspired RA designs based on the ECRLH unit cell structure, which will be presented in Chapter IV. The second part is the dual-passband LWA designs based on the metamaterial-inspired supercell structures, which will be presented in Chapter V. The third part is an electronically tunable LWA design based on the CRLH structure with discrete BST thin-film varactors and the uncertainty analysis in the determination of the FE BST permittivity, which will be introduced in Chapter VI. Therefore, corresponding to this arrangement of the content in this thesis, literature reviews in this chapter is organized as follows. In Section 3.2, the literature of some existing RAs based on metamaterial-inspired structures is introduced. In Section 3.3, a literature review of some existing LWAs based on the CRLH structure is presented. Most existing multiband LWAs based on different metamaterial-inspired structures are reviewed in Section 3.3 as well. In Section 3.4, antenna and component designs using BST materials are introduced and reviewed. In addition, some existing antenna designs using different tuning techniques are reviewed and compared in Section 3.5. The summary is given in Section 3.6.

## **3.2 Literature of Metamaterial-Inspired RAs**

Metamaterial-inspired RAs are an interesting category of resonant antennas. With a

proper excitation, antennas in this category can generate one or multiple operating resonances for radiation using its intrinsic resonant modes. Most existing RAs are designed based on metamaterial structures, especially the CRLH structure. The background theory of a resonant structure based on the CRLH unit cell structure has been presented in Section 2.4 of Chapter II.

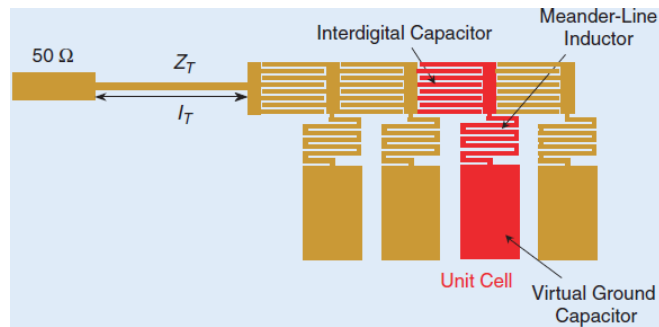


Figure 3.1 Configuration of four-cell ZOR antenna [14].

The first design of the RA in this category was proposed in 2003 [15]. This RA is designed based on the CRLH structure. The resonant structure of this antenna consists of four cascaded microstrip-based CRLH unit cells. Each unit cell has an interdigital capacitor (IDC) and a shunt meander line connected to a rectangular patch [14]. Each rectangular patch is modeled as a virtual ground plane (GP). The configuration of this antenna is shown in Figure 3.1. By exciting this resonant structure through a microstrip line, this antenna can generate multiple operating resonances resulting from its intrinsic resonant modes (e.g., the zeroth-order mode) to work at different frequencies. The zeroth-order mode ( $m = 0$ ) resonance operates at 4.88 GHz. The resonant frequencies resulting from the negative-order modes ( $m < 0$ ) resonances work below the ZOR resonant frequency, while the positive-order modes ( $m > 0$ )

resonances work above the bandgap around 11.8 GHz. In [15], the authors also compare the proposed antenna to a reference conventional patch antenna, in order to demonstrate the antenna size reduction. When this RA and the referenced patch antenna work at the same frequency, the RA achieves a smaller size. In comparison with this reference patch antenna, this ZOR antenna can achieve 75% footprint area reduction.

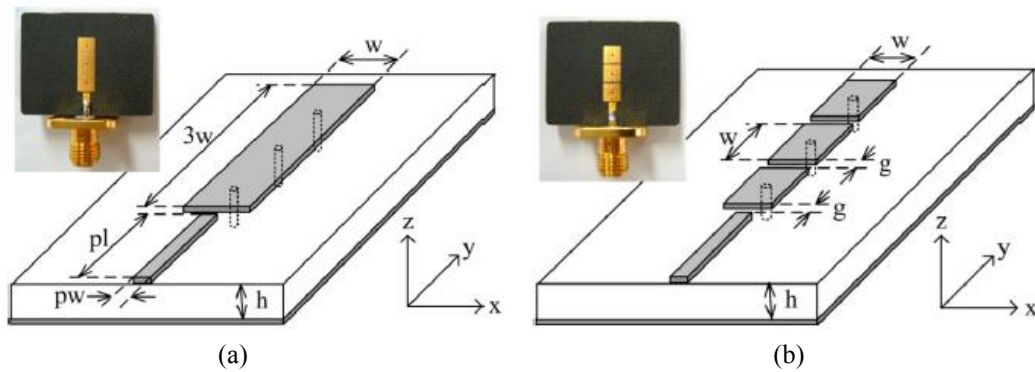


Figure 3.2 Configurations of the proposed ZOR antennas, (a) ENG; (b) DNG [16].

In [16], a novel ZOR antenna is presented based on the epsilon negative (ENG) meta-structured TL (MTL) structure. The equivalent model of the ENG MTL structure is composed of the series inductance, the shunt inductance and shunt capacitance. According to the feature that the ENG MTL structure supports the zeroth-order ( $m = 0$ ) operating resonance which is same as the CRLH TL structure, the proposed ZOR antenna is designed with three ENG MTL unit cells to generate a zeroth-order mode resonance for radiation. The configuration of this antenna based on the ENG MTL structure is shown in Figure 3.2(a). In comparison, a ZOR antenna, based on the double negative (DNG) MTL which is also the CRLH TL structure, is also designed in [16] to work at the same zeroth-order mode resonant frequency of 10 GHz. The

configuration of this RA based on the DNG MTL structure is shown in Figure 3.2(b). The measured results show that the ENG ZOR antenna has wider bandwidth of the zeroth-order mode resonance compared to the DNG ZOR antenna. However, these two RAs have similar radiation patterns at the zeroth-order mode resonant frequency of 10 GHz.

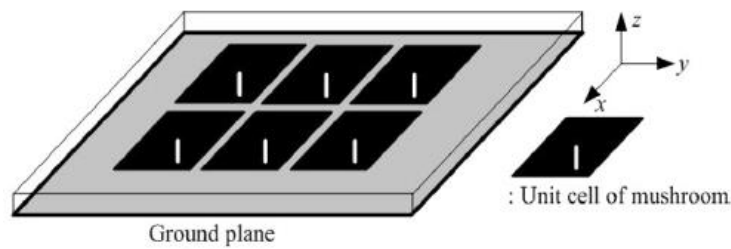


Figure 3.3 Configuration of the proposed ZOR antenna using mushroom structure [17].

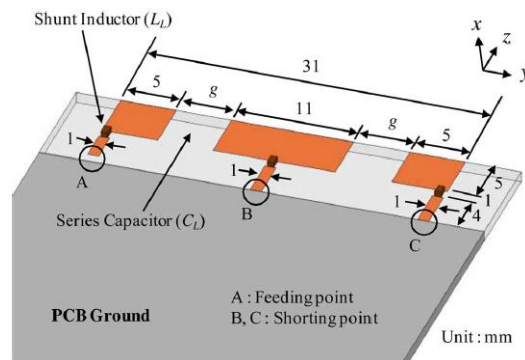


Figure 3.4 Configuration of the proposed antenna with bandwidth extension [18].

In [17], a low-profile RA is presented using the CRLH-based mushroom structure. The antenna configuration with six mushroom structures is shown in Figure 3.3. The mushroom structure can be used to model the CRLH structure. With an excitation on one mushroom structure, the magnetic current flows through these six mushroom structures and forms a closed loop trajectory. Thus, this antenna can also be recognized as a loop RA. The zeroth-order mode ( $m = 0$ ) resonant frequency of this loop RA is 7.9 GHz. This proposed RA, which is a loop ZOR antenna, can be used for

multiband applications.

In [18], a CRLH-based RA with bandwidth extension is presented. The configuration of this RA is shown in Figure 3.4. This antenna is realized using a planar CRLH unit cell structure. This antenna supports the zeroth-order mode resonance for radiation and also has wideband characteristics. By merging the zeroth-order mode ( $m = 0$ ) resonance at 2.24 GHz and the first-negative-order mode ( $m = -1$ ) resonance at 1.99 GHz together, this CRLH-based RA achieves a wideband coverage from 1.9 GHz to 2.35 GHz. This method of bandwidth extension can be considered as an efficient way to improve bandwidth of antenna designs for mobile devices.

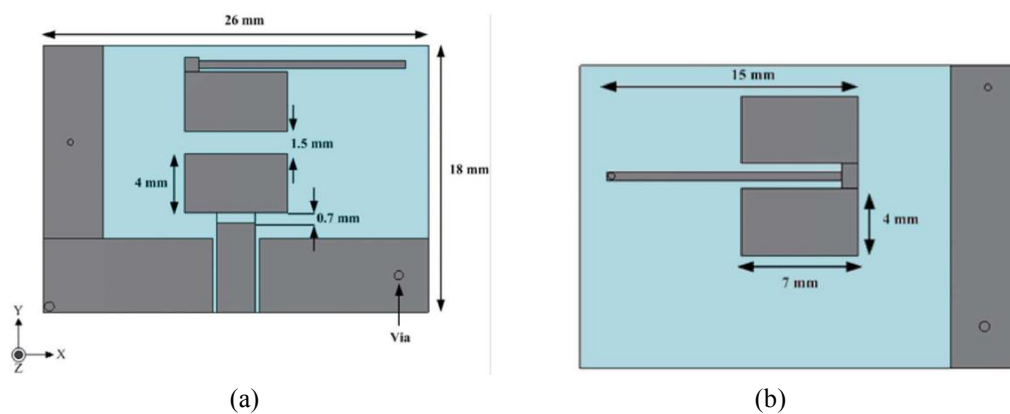


Figure 3.5 Configurations of the proposed ZOR antenna, (a) top view; (b) rear view [19].

In [19], a compact ZOR antenna with two cascaded CRLH unit cells is presented. The configurations of this antenna are shown in Figure 3.5, in terms of the top view and rear view. In this antenna structure, two asymmetrical straight meta-strip lines with via-holes, metal-insulator-metal (MIM) parallel-plate capacitors and the gap capacitor between unit cells are used to model the shunt inductors, series capacitances and shunt capacitances, respectively, in order to achieve good impedance matching and improve

antenna efficiencies. This ZOR antenna exhibits a linear polarization with an enhanced peak gain of 2.3 dB and efficiency of 79%, at the zeroth-order mode ( $m = 0$ ) resonant frequency of 2.3 GHz.

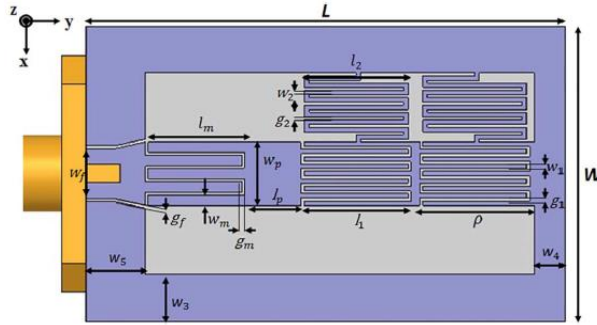


Figure 3.6 Configuration of the proposed CPW ZOR antenna [20].

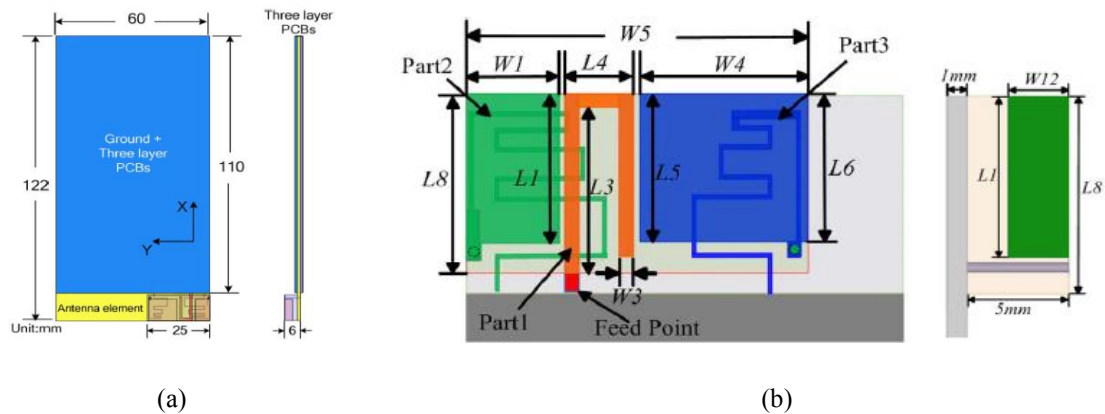


Figure 3.7 (a) Top view and side view of the antenna configuration; (b) top view and side view of the designed CRLH elements [21].

In [20], a compact vialess asymmetric coplanar waveguided (CPW) ZOR antenna with bandwidth improvement is presented. The antenna configuration is shown in Figure 3.6. Two cascaded CRLH unit cell are used to form a major resonant structure. Interdigital structures are used to model the series capacitor and inductor, and the meander-line structures are used to model the shunt inductor. The interdigital structures are very helpful to decrease the quality factor of the resonator and improve

the working bandwidth. This antenna works at 0.75 GHz for the first-negative order mode ( $m = -1$ ) resonance and 2.16 GHz for the zeroth-order mode ( $m = 0$ ) resonance. For the zeroth-order mode resonance, this antenna has an improved bandwidth from 2.05 GHz to 2.35 GHz.

In [21], a dual-band ZOR antenna based on the CRLH structure is presented for compact multiband smart phone applications. The configuration of this proposed antenna is shown in Figure 3.7. Through an excitation of a monopole antenna, with two parasitic metal-strip elements connected to the GP in different dimensions, this proposed antenna can form dual bands using the zeroth-order mode ( $m = 0$ ) resonances of two CRLH unit cells for proper radiation. This antenna can work at 0.9 GHz with the measured antenna gain of 0.09 dBi and 2.0 GHz with the gain of 2.2 dBi. Thus, this antenna can be used for mobile handset applications to work at GSM850/900 (824-960MHz) and DCS1800/PCS1900/UTMS (1710-2170 MHz). Furthermore, this antenna design has great potentials for future wireless mobile terminals.

In [22], a compact asymmetric CPW antenna is presented for dual-band applications. The antenna configurations are shown in Figure 3.8. In this antenna structure, the major resonant structure consists of two asymmetric cascaded CRLH unit cells with a short end at the termination, and the GP is also modified to be asymmetric. This CPW RA forms a dual-band frequency response with one narrow band at 1.5 GHz for the first-negative order ( $m = -1$ ) resonance and one broad band of 2.69-9.15 GHz. The zeroth-order mode ( $m = 0$ ) and the first-positive order ( $m = +1$ ) resonances of the

CRLH-based resonant structure and a half-wavelength and a one-wavelength resonance of the modified GP work together to form a wide band coverage with -10 dB bandwidth of 6.46 GHz.

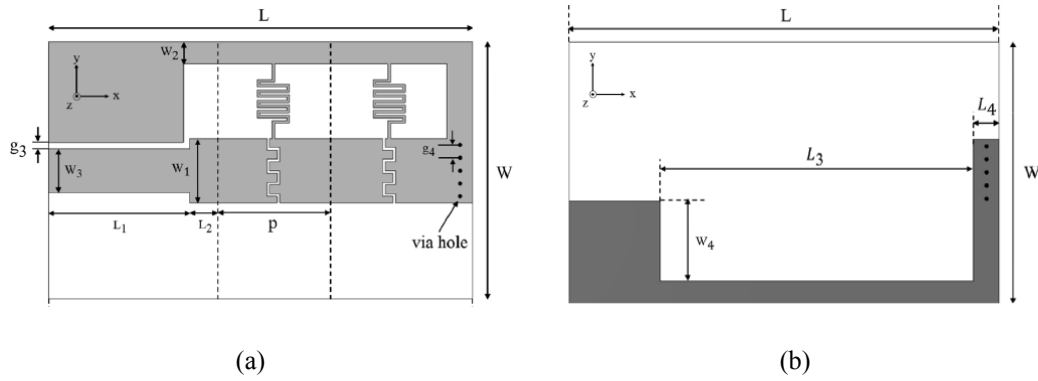


Figure 3.8 Configurations of the asymmetric CPW antenna, (a) top view; (b) rear view [22].

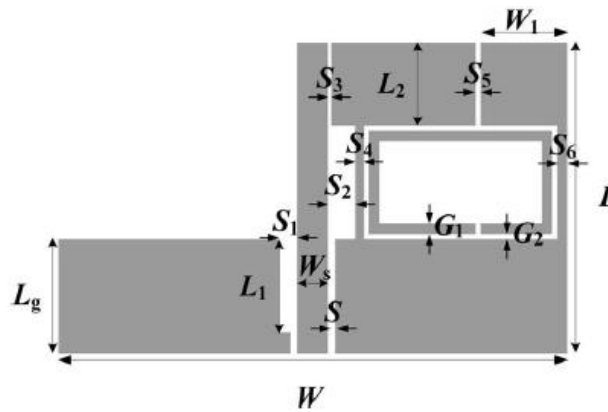


Figure 3.9 Configuration of the proposed CPW ZOR antenna. [23]

In [23], a novel CRLH-based CPW ZOR antenna with bandwidth improvement is presented. The configuration of this antenna is shown in Figure 3.9. The antenna structure is designed with one CRLH unit cell structure. With an excitation of one conventional monopole, this ZOR antenna can radiate properly using its zeroth-order mode ( $m = 0$ ) resonance. A split-ring resonant structure is included in the antenna structure to generate a new operating resonance, in order to improve the operating

bandwidth of this antenna. According to the measurement, this antenna works at 1.75 GHz using the zeroth-order mode resonance and has a wide band of 1.67-2.51 GHz. This antenna is a good candidate for GSM/UMTS/LTE/WLAN applications.

The metamaterial-inspired RAs introduced above are designed mainly based on one or multiple metamaterial unit cells, e.g., the CRLH unit cell. The features of these RAs in this category include planar configurations, multi-band applications, the zeroth-order mode ( $m = 0$ ) resonance for radiation, usually with multiple cascaded unit cells. The brief information and advantageous features of these antennas in [15]-[23] are summarized in Table 3.1.

Table 3.1 Summary of the metamaterial-inspired RAs in [15]-[23].

	Technology	Antenna Electrical Size	ZOR Frequency	Antenna Bandwidth (MHz)	Peak Gain of ZOR Mode (dBi)	Description of Advantageous Features
Ref. [15]	CRLH	About $0.16\lambda_0 \times 0.16\lambda_0$	4.88 GHz	10	Not Specify	Size reduction compared with a patch antenna
Ref. [16]	ENG	$0.11\lambda_0 \times 0.35\lambda_0$	10 GHz	250	4.2	Antenna miniaturization
Ref. [17]	CRLH	$0.31\lambda_0 \times 0.2\lambda_0$	7.9 GHz	50	2.6	Loop current distribution
Ref. [18]	CRLH	$0.2\lambda_0 \times 0.067\lambda_0$	2.27 GHz	430	3.31	Bandwidth enhancement
Ref. [19]	CRLH	$0.2\lambda_0 \times 0.14\lambda_0$	2.3 GHz	100	2.3	(1) Gain improvement (2) Efficiency improvement
Ref. [20]	CRLH	$0.14\lambda_0 \times 0.22\lambda_0$	2.16 GHz	320	1.62	Bandwidth enhancement
Ref. [21]	CRLH	Not Specify	0.87 GHz; 2.05 GHz	140; 500	0.09; 2.2	Multiband operation
Ref. [22]	CRLH	$0.087\lambda_0 \times 0.19\lambda_0$ $\times 0.015\lambda_0$	2.9 GHz	6460	2.59	(1) Asymmetric structure (2) Bandwidth enhancement
Ref. [23]	CRLH	$0.54\lambda_0 \times 0.32\lambda_0$	1.73 GHz	840	3.4	Bandwidth enhancement with one resonant ring

However, most of these RAs only generate a few operating resonances using the intrinsic resonant modes to cover a few frequency bands. In terms of modern commercial frequency bands, most of these RA designs are not capable of a sufficient number of operating resonances for multiband or wideband applications. The metamaterial-inspired RAs presented in Chapter IV have two major advantages

compared to most existing ones: (1) more operating resonances (e.g., six or ten operating resonances) working at the chosen frequency bands for the passive designs; (2) frequency tunability over 0.7-0.96 GHz of one operating resonance at the low frequency while keeping the wideband coverage over 1.7-6.0 GHz formed by the other operating resonances. The proposed RAs can be used for multiband or frequency-agile applications.

### **3.3 Literature of Metamaterial-Inspired LWAs**

In 1940, the first LWA was proposed in the form of a rectangular waveguide with periodic slots [24]. During these decades, LWAs have attracted a lot of research interest and industrial applications. In recent twenty years, LWAs have a rapid and steady development in terms of the structural design and antenna theory. In this thesis, 1-D LWAs with an end excitation are the major research field of interest. The background theory of conventional LWAs has been explained in Section 2.2 of Chapter II.

It is worthy to note here that conventional LWAs usually suffer from a stopband region for the radiation degradation around broadside. This problem is known as the open stopband problem [7]. The open stopband region around broadside results from the coupling of a pair of space harmonics in the radiation region of an open guiding structure [7]. The coupling mechanism in this open stopband region can be briefly explained as following: It is very similar as the one of closed stopbands, and the

difference is the effects on the dispersion curve [7]. In an open stopband region, the propagation wavenumber is complex and the slope of the dispersion curve is around zero within a frequency range of the open stopband region [7]. Due to the coupling between the radiated space harmonics, the amplitude drops dramatically and the amount of the radiated power is decreased either [7]. Besides, the pertinent pair of oppositely-directed space harmonics is equal in terms of the amplitude, thereby leading to a standing-wave effect and the complex Bloch impedance around broadside [7]. One effective approach has been proposed for a periodic LWA to suppress or eliminate the open stopband region [7].

In [7], based on a review of negative effects of an open stopband region on the broadside radiation in a 1-D periodic LWA in terms of its dispersion relation and the scanning capability, a novel and effective technique to completely eliminate the open stopband region around broadside is proposed. With integration of quarter-wave transformers or alternatively matching stubs into each unit cell structure, the Bloch-wave impedance of the antenna remains real and non-zero around broadside. Furthermore, with incorporation of two stubs into each unit cell structure, the open stopband problem is mitigated around broadside.

### **3.3.1 Literature of LWA Designs Based On CRLH Structures**

The concept of the metamaterial CRLH structure brings novel ideas to 1-D LWA designs. If the period of one CRLH unit cell can be much less than one guided wavelength and the condition to model an effective transmission medium for

electromagnetic homogeneity [8] can be satisfied, multiple CRLH unit cells can be cascaded together to model the guiding structure of a 1-D LWA. Thus, many different 1-D LWAs based on the CRLH structure have been designed and investigated in terms of the antenna performance and background theories.

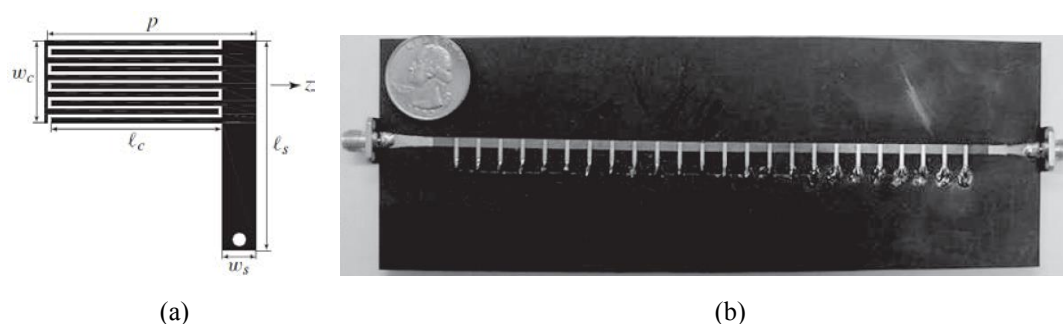


Figure 3.10 Configurations of the first CRLH-based 1-D LWA, (a) unit cell structure; (b) fabricated LWA [25].

The first 1-D LWA based on the CRLH structure was proposed in 2003 [25]. Based on the background theory of the CRLH structure [8], a microstrip 1-D LWA can be designed with multiple cascaded CRLH unit cells. The CRLH unit cell structure is shown in Figure 3.10(a), while the configuration of the fabricated LWA with 24 cascaded CRLH unit cells is shown in Figure 3.10(b). The period of each unit cell is much less than one guided wavelength, thus the multiple cascaded unit cells can be used to model the guiding structure of this LWA, because the effective-medium condition [8] for electromagnetic homogeneity can be successfully satisfied. The major characteristics of this 1-D LWA can be summarized as follows: (1) the main beam of this LWA can scan from backward to forward through broadside smoothly without suffering the open stopband problem around broadside in the balanced condition; (2) because the period of each unit cell is much less than one operating

wavelength, the antenna mainly radiates from its fundamental mode space harmonic, thus this antenna can be classified as quasi-uniform [5].

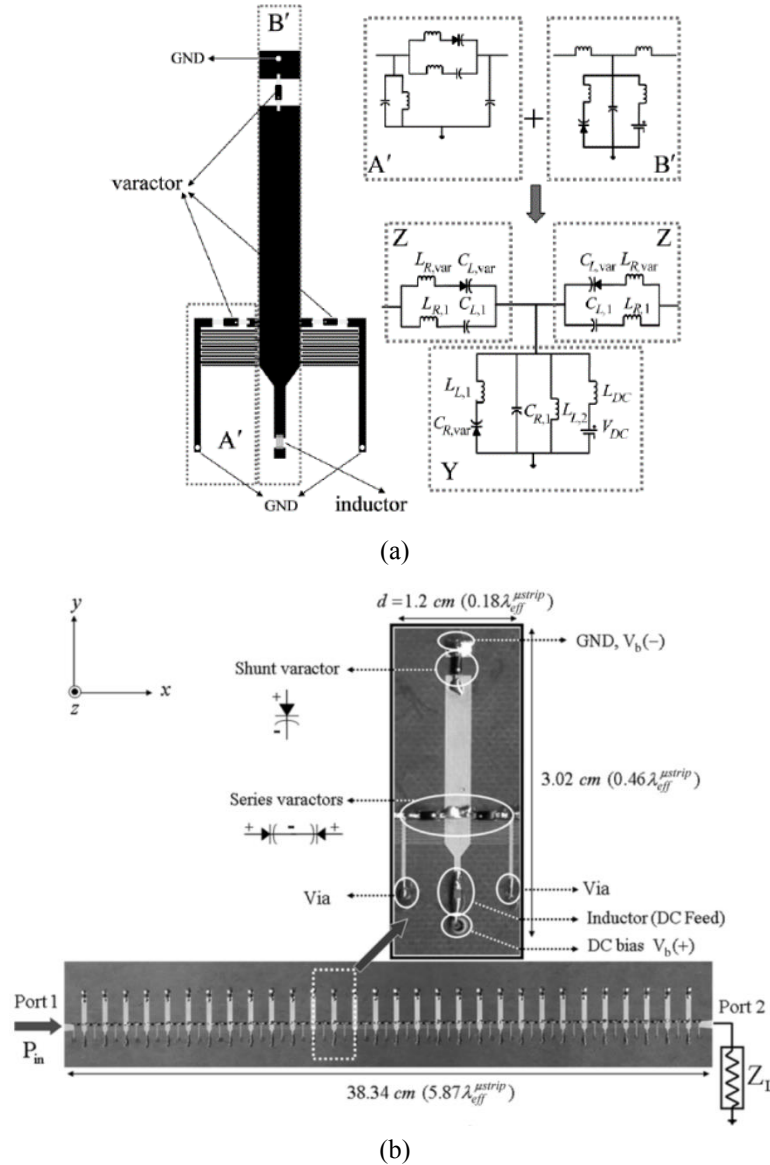


Figure 3.11 (a) Layout and equivalent circuits of the proposed tunable CRLH unit cell structure; (b) the fabricated tunable LWA with 30 cascaded CRLH unit cells [28].

In [26], based on the dispersion analysis of a planar microstrip CRLH-based LWA (e.g., the LWA design in [25]) using a full-wave modal approach [27], with consideration of all the proper and improper space harmonics, it is confirmed that the balanced condition is very useful for the LWA to eliminate the open stopband region

around broadside, and achieve the frequency scanning from backward to forward through broadside smoothly without suffering the open stopband problem. In the balanced condition, the open stopband between the LH and RH band can be closed due to mutual cancellation of the generated operating resonances, which can result in a continuous transition from the LH band to the RH band. By comparing the results of three different analysis approaches (i.e., the full-wave modal approach, the artificial transmission-line approach and the Bloch-wave analysis approach), the full-wave modal approach is selected to analyze and optimize the microstrip CRLH LWA for elimination of the open stopband region.

In [28], an electronically controlled tunable LWA is presented based on the CRLH structure. Due to incorporation of silicon semiconductor varactors into the antenna structure, this LWA can operate at two different modes – the mode of tunable radiation angle and the mode of tunable beamwidth. The layout and equivalent models of a microstrip CRLH unit cell is shown in Figure 3.11(a), and the fabricated LWA with 30 unit cells is shown in Figure 3.11(b). For the mode of tunable radiation angle, when all the varactors are uniformly biased, this antenna can achieve the beam scanning at a fixed frequency. However, if all the semiconductor varactors are non-uniformly biased, the antenna beamwidth can be continuously controlled. The proposed functions of this antenna have been experimentally demonstrated at different modes.

In [29], a high-gain active LWA is presented based on the CRLH structure. With integration of power amplifiers into the antenna structure, the amplitude of the signal can be re-amplified repeatedly in the radiation process. The antenna configurations

are shown in Figure 3.12. The proposed active LWA can achieve a strongly improved gain of 17.8 dB at its center operation frequency of 3.7 GHz, due to the power concomitance and matching regeneration from the amplifiers. This proposed LWA concept can also be used for static and dynamic beam forming [29].

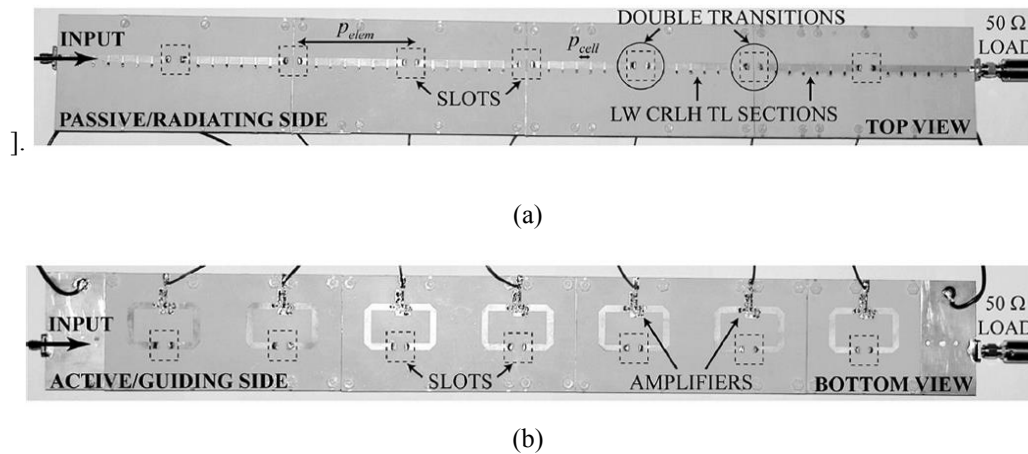


Figure 3.12 Configurations of the active LWA with 48 CRLH unit cells and 7 amplifiers, (a) top view; (b) rear view [29].

In [30], a novel non-uniform tapered LWA was presented based on the CRLH structure. The configuration of the proposed LWA is shown in Figure 3.13. The major advantage of this LWA is that the sidelobes of this antenna can be minimized to a lower level. Based on experiments on this antenna at its operating frequency of 2.45 GHz, an 8 dB reduction of the sidelobe level can be achieved in comparison with a uniform CRLH-based LWA with 12 unit cells which has the same gain. It is also noted here that this LWA is designed using an automatic co-simulation approach based on a genetic algorithm optimization.

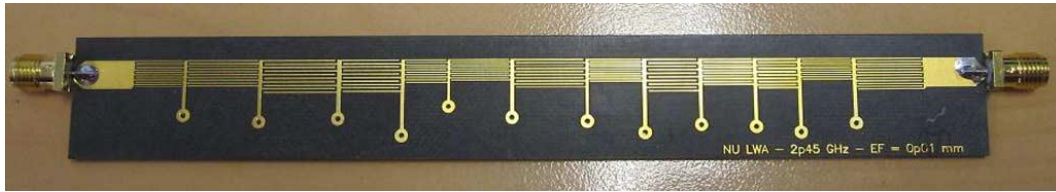


Figure 3.13 Configuration of this non-uniform CRLH-based LWA [30].

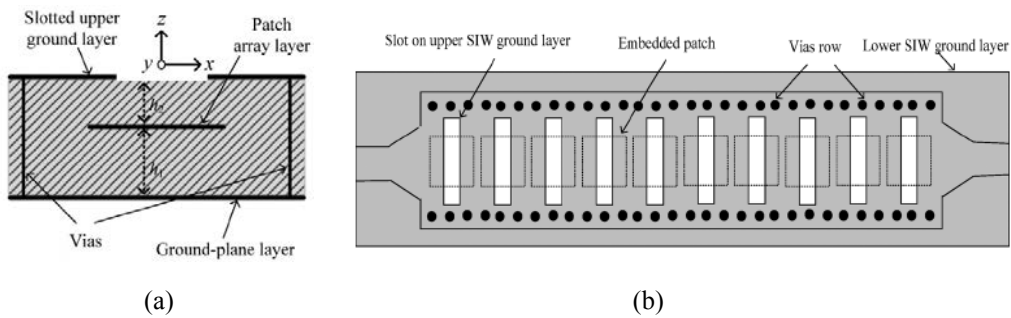


Figure 3.14 Configurations of this CRLH-based LWA, (a) cross-sectional view; (b) top view [31].

In [31], a multilayered SIW LWA based on the CRLH structure is presented, in order to achieve consistent gains within the beam continuous scanning region from backward to forward. The cross-sectional view of one CRLH unit cell is shown in Figure 3.14(a), and the top view of the LWA layout is shown in Figure 3.14(b). Each CRLH unit cell consists of a slot on the upper ground layer of the SIW structure and a patch beneath the slot. In the balanced condition, a full upper half-spherical beam of this antenna can be scanned with consistent realized gains from backward to the forward. This antenna can work from 8.25 GHz to 12.8 GHz with consistent gains of around 12.8 dBi.

In [32], a planar slot-line LWA is presented based on the CRLH structure. The configuration of this LWA with 17 CRLH unit cells is shown in Figure 3.15. In this antenna structure, the split-ring resonators (SRRs) are used to provide the CRLH characteristics. This planar LWA can achieve the continuous beam scanning using its

fundamental mode from the LH band to the RH band with the balanced transition frequency point of 2.5 GHz. In experiments, the presented LWA can achieve the maximum measured gains of 7.1 dBi and 11.3 dBi for the LH and RH band, respectively.

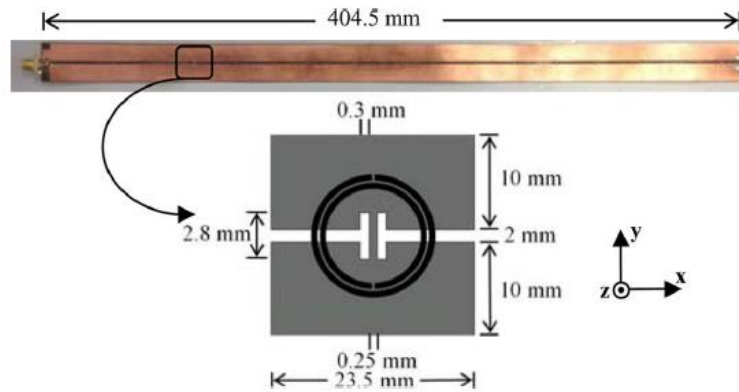


Figure 3.15 Configuration of this CRLH-based LWA with SRRs [32].

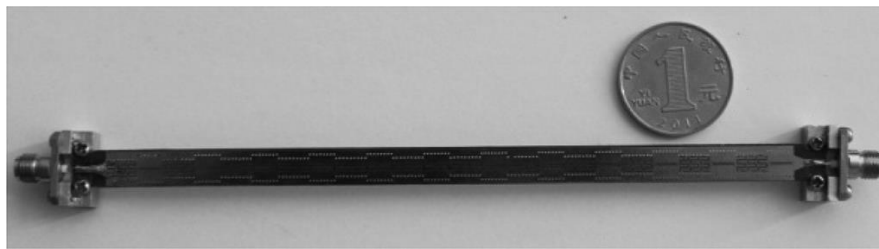


Figure 3.16 Prototype of the fabricated LWA based on the SIW CRLH structure [33].

In [33], an SIW LWA based on the CRLH structure is presented with an improved frequency beam-scanning capability. The fabricated antenna configuration is shown in Figure 3.16. The proposed SIW LWA is composed of 12 CRLH unit cells with the etched slots on the surface metal. In experiments, the fabricated LWA can work from 23.95 GHz to 27.725 GHz. The LWA can scan from  $-17^\circ$  to  $+13^\circ$  within the frequency range of 24-27 GHz. In comparison with some conventional SIW CRLH-based LWAs, this LWA has good radiation performance with less gain

variation, which makes this antenna very suitable for automotive communications or radar applications.

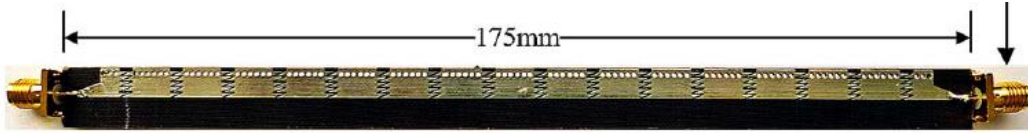


Figure 3.17 Prototype of the fabricated HMSIW LWA with CP [34].

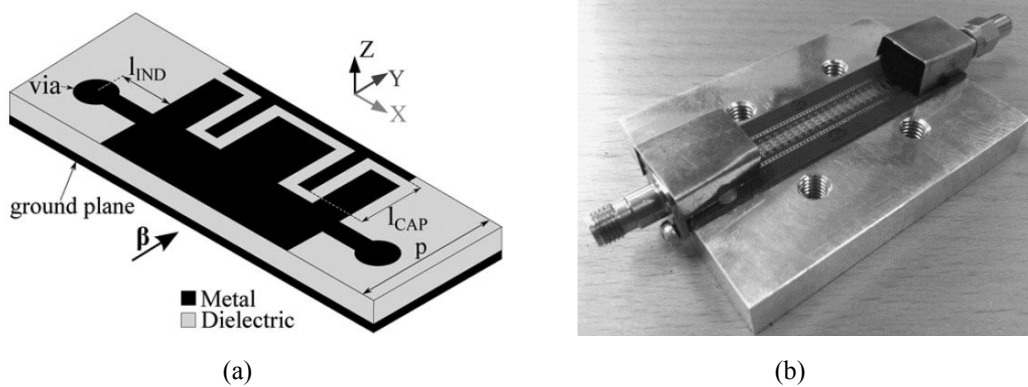


Figure 3.18 (a) Layout of the single CRLH unit cell structure; (b) configuration of the fabricated LWA with 1-D multiple cascaded unit cells [35].

In [34], a miniaturized LWA with circular polarization (CP) is presented for frequency scanning applications. In this antenna structure, interdigital structures (IDSs) are used in the half-mode SIW (HMSIW) to model the CRLH unit cell structure. The configurations of this LWA using the HMSIW structure are shown in Figure 3.17. In the balanced condition, this LWA can work from 7.4 GHz to 13.5 GHz with continuous frequency scanning from  $-70^\circ$  to  $+70^\circ$  and with the measured realized gains of 7.8-12.0 dBi. The axial ratio of lower than 3.1 in the direction of the main beam can be obtained in experiments, which can verify the CP of this LWA.

In [35], a systematic method is introduced to design the planar CRLH TL structure.

This method is demonstrated at 26 GHz in experiments for the frequency response and the structural design. The layout of the proposed CRLH unit cell structure is shown in Figure 3.18(a), and a fabricated LWA with 1-D multiple cascaded CRLH unit cells is shown in Figure 3.18(b). It should be noted that the effect from the inter-cell coupling is further investigated. It can be found that the inter-cell coupling can generate the parasitic components and change the original values of the components, based on analysis of the corresponding coupling coefficients. However, when the number of the cascaded unit cell is larger than 12, the component values reach their saturation points and achieve relatively stable levels. A scheme for compensation of the component values is introduced for the design, which is an efficient approach for the LWA design and optimization. In addition, this paper summarizes the design steps for a TL structure of 1-D multiple cascaded CRLH unit cells, which can be used as a reference for future designs.

The concept of the CRLH structure has brought inspirations to LWA designs. Based on different CRLH structures, LWAs can be designed to achieve different characteristics. The brief information and advantageous features of the antennas in [25], [28]-[34] are further summarized in Table 3.2.

However, these CRLH-based LWAs mainly focus on the antenna performance improvement within one single operating band. For comparison, the LWAs with the multiband feature can bring more flexibility and more potential to applications. Thus, multiband LWAs with novel metamaterial-inspired structures are a new research topic and have attracted a lot of research interest so far. The proposed passive

metamaterial-inspired LWAs in Chapter V have two major advantages over most existing LWA designs based on the CRLH structure: (1) two distinct passbands separated by a middle separation area; (2) the CRLH backward-to-forward leaky-wave radiation characteristics within each passband. These two advantages make the proposed LWAs suitable for dual-band applications.

Table 3.2 Summary of the CRLH-based LWAs in [25], [28]-[34].

	Technology	No. of Unit Cells	Operating Frequency	Antenna Feature	Description of Advantageous Characteristics
Ref. [25]	CRLH	10	3.1 – 6 GHz	Microstrip	(1) Fundamental mode harmonic for scanning radiation (2) Smooth scanning at broadside under balanced condition
Ref. [28]	CRLH	30	2.7 – 3.9 GHz	(1) Microstrip (2) Active	(1) Tunable radiation under uniform bias voltages (2) Tunable beamwidth under non-uniform bias voltages
Ref. [29]	CRLH	N/A	5.5 – 6.5 GHz	(1) Ferrite-loaded (2) Waveguide	(1) Uniform ferrite-loaded open waveguide structure (2) Tunable radiation under bias magnetic field
Ref. [30]	CRLH	12	2.3 – 2.7 GHz	(1) Microstrip (2) Non-uniform	Non-uniform taper TL structure for minimized sidelobe level
Ref. [31]	CRLH	15	8 – 13 GHz	(1) SIW (2) Consistent gain	Multilayered SIW TL structure for the consistent gain
Ref. [32]	CRLH	17	2.3 – 3.3 GHz	(1) CPW (2) Double-side	Fundamental-mode harmonic for scanning radiation with a slotline with split-ring resonators
Ref. [33]	CRLH	12	24 – 27 GHz	SIW	Novel SIW TL structure with slots for scanning-angle enhancement and gain flatness
Ref. [34]	CRLH	15	7 – 13 GHz	(1) Half-mode SIW (2) Circular polarization	Half-mode SIW CRLH TL structure with interdigital capacitors for wide bandwidth and circular polarization

### 3.3.2 Literature of LWA Designs Based On Metamaterial-Inspired Structures

LWAs with multiband properties have attracted a lot of research interest in recent years. Many metamaterial-inspired structures have been proposed and applied to LWA designs. These structures can enable LWAs to have multiband properties and different leaky-wave radiation characteristics for different applications. Some existing LWA designs with multiband leaky wave radiation characteristics are introduced as follows.

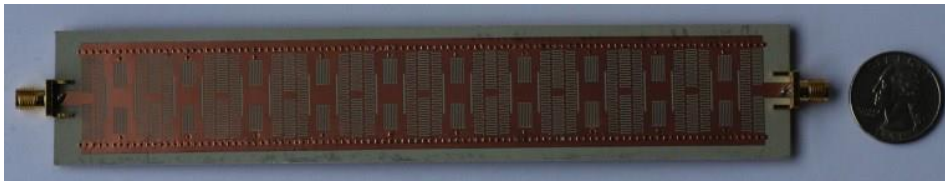
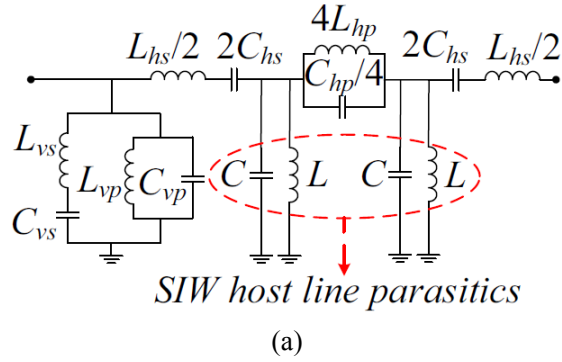


Figure 3.19 (a) Equivalent circuit of one ECRLH unit cell; (b) photograph of the fabricated LWA based on the ECRLH structure [36].

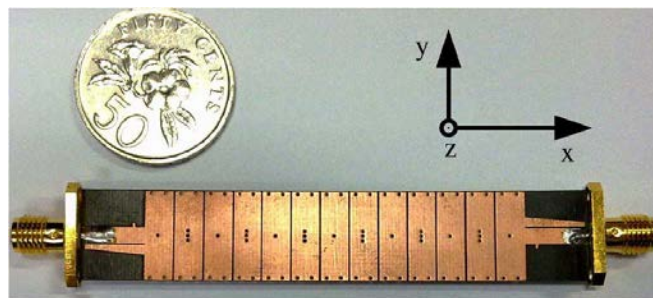
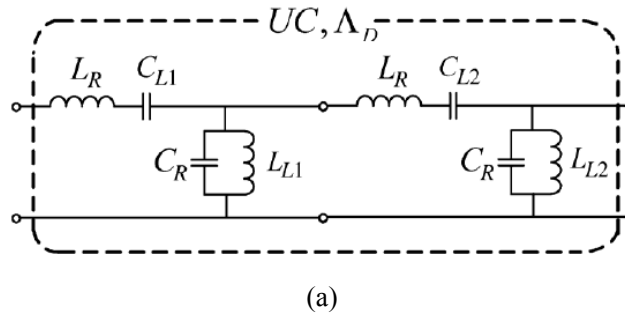


Figure 3.20 (a) Equivalent circuit of one DP-CRLH unit cell; (b) photograph of the fabricated LWA based on the DP-CRLH structure [37].

In [36], a dual-band SIW LWA is presented based on the ECRLH TL structure. This LWA consists of 1-D multiple cascaded ECRLH unit cells. The equivalent circuit of

one ECRLH unit cell is shown in Figure 3.19(a), and the photograph of the fabricated LWA is shown in Figure 3.19(b). This LWA has two distinct passbands with the CRLH leaky-wave radiation characteristic within both passbands. One middle bandgap exists between these two passbands.

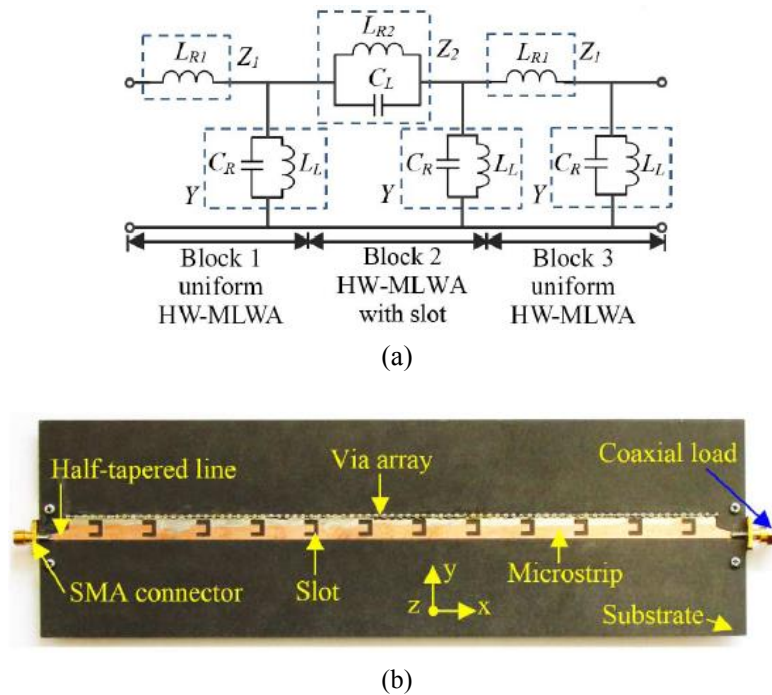


Figure 3.21 (a) Equivalent circuit of one metamaterial-inspired supercell; (b) photograph of the fabricated half-width microstrip LWA [38].

An SIW LWA based on a double periodic CRLH (DP-CRLH) structure is proposed in [37]. One DP-CRLH unit cell structure is composed of two different CRLH unit cells. The equivalent circuit of the DP-CRLH unit cell structure is shown in Figure 3.20(a), and the photograph of the fabricated LWA based on the DP-CRLH structure is presented in Figure 3.20(b). This LWA has a RH leaky-wave band at low frequencies over 5.9-6.2 GHz and a conventional CRLH leaky-wave band at high frequencies over 11.9-17.9 GHz.

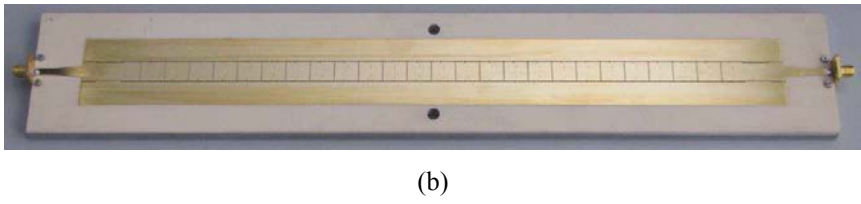
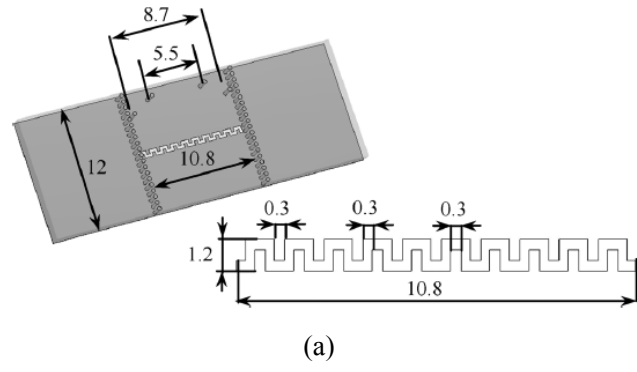


Figure 3.22 (a) Layout of one dual-band CRLH unit cell structure; (b) photograph of the fabricated SIW LWA [39].

In [38], a half-width microstrip LWA based on a metamaterial-inspired TL structure is proposed for dual-band applications. This metamaterial-inspired TL structure is composed of 1-D multiple periodic U-shaped slots. The equivalent circuit of one metamaterial-inspired supercell structure is shown in Figure 3.21(a), and the fabricated half-width microstrip LWA is shown in Figure 3.21(b). Figure 3.21(a) shows that one supercell consists of three CRLH unit cells in series connection. This LWA can achieve one RH band of 5.24-6.37 GHz and one LH band of 7.9-9.02 GHz, respectively.

In [39], an SIW LWA based on a dual-band CRLH structure is presented for dual-band applications. The dual-band CRLH unit cell structure is realized by the SIW periodic meander slot structure. The layout of the SIW meander slot unit cell structure is shown in Figure 3.22(a), and the photograph of the fabricated SIW LWA is presented

in Figure 3.22(b). This dual-band LWA can achieve the CRLH leaky-wave radiation characteristics in both passbands.

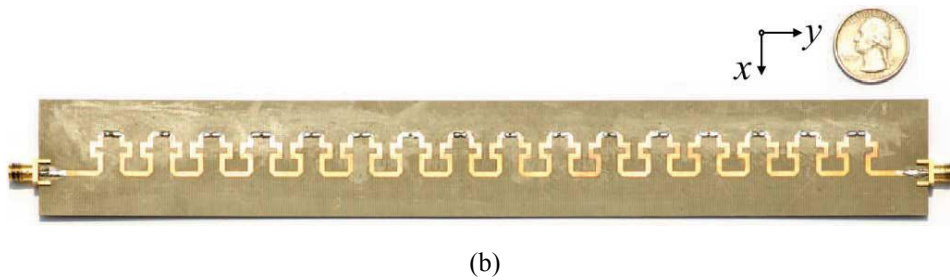
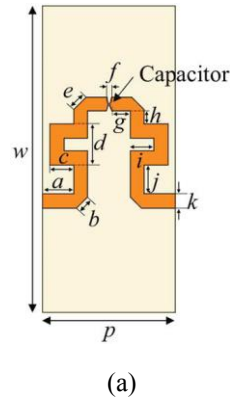


Figure 3.23 (a) Layout of one MNG unit cell structure; (b) photograph of the fabricated LWA based on the MNG structure [40].

In [40], an LWA based on the MNG TL structure is presented for dual-band applications. This MNG TL structure is composed of 1-D multiple cascaded MNG unit cells. The layout of one MNG unit cell is shown in Figure 3.23(a), and the photograph of the fabricated LWA based on the MNG TL structure is shown in Figure 3.23(b). This LWA has two CRLH bands of 3.7-5.5 GHz and 6.7-10 GHz.

The metamaterial-inspired structures have enabled many multiband LWA designs. These LWAs can achieve different frequency responses and different leaky-wave radiation characteristics. The brief information and advantageous features of the multiband LWAs in [36]-[40] are summarized in Table 3.3.

Table 3.3 Summary of the multiband LWAs in [36]-[40].

	Technology	No. of Units	Antenna Feature	Radiation Characteristics & Operating Bands	Peak Gains in Operating Bands	Scanning Angle
Ref. [36]	ECRLH	10	(1) SIW; (2) Passive	(1) CRLH Band: 3.63-4.16 GHz; (2) CRLH Band: 5.1-5.67 GHz	(1) 15.7 dBi (Low CRLH Band); (2) 9.8 dBi (High CRLH Band)	(1) -63° to +63° (Low CRLH Band); (2) -50° to +50° (High CRLH Band);
Ref. [37]	DP-CRLH	6	(1) SIW; (2) Passive	(1) RH Band: 5.2-5.8 GHz; (2) CRLH Band: 12.6-18.7 GHz	(1) 6.5 dBi (RH Band); (2) 8.2 dBi (CRLH Band)	(1) +33° to +37° (RH Band); (2) -42° to +40° (CRLH Band);
Ref. [38]	CRLH-based U-shaped slots	12	(1) SIW; (2) Passive	(1) RH Band: 5.24-6.37 GHz; (2) LH Band: 7.9-9.02 GHz	(1) 12.2 dBi (RH Band); (2) 14.1 dBi (LH Band)	(1) +30° to +65° (RH Band); (2) -46° to -10° (LH Band);
Ref. [39]	CRLH-based meander slots	25	(1) SIW; (2) Passive	(1) CRLH Band: 3.63-4.16 GHz; (2) CRLH Band: 5.1-5.67 GHz	(1) 6.5 dBi (Low CRLH Band); (2) 16 dBi (High CRLH Band)	(1) -25° to +35° (Low CRLH Band); (2) -25° to +15° (High CRLH Band);
Ref. [40]	MNG	16	(1) Microstrip; (2) Passive	(1) CRLH Band: 3.7-5.5 GHz; (2) CRLH Band: 6.7-10 GHz	(1) 9.5 dBi (Low CRLH Band); (2) 15.5 dBi (High CRLH Band)	(1) -43° to +73° (Low CRLH Band); (2) -80° to +83° (High CRLH Band);

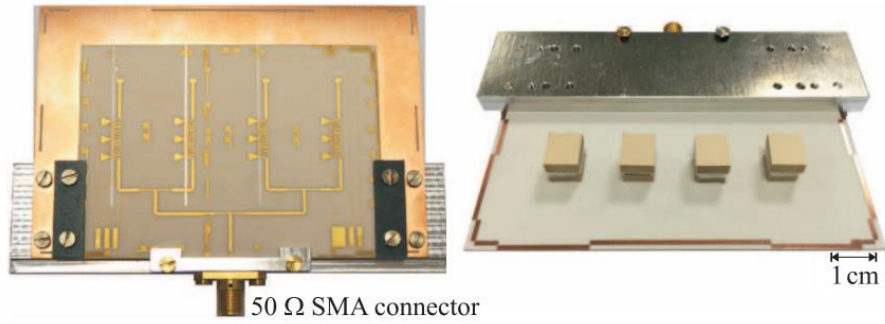
However, the multiband LWAs introduced in [36]-[40] have one shortfall: all the designs are based on the passive structures without control or tunability of the operating bands and the main beam direction. The electronically tunable LWA proposed in Chapter V can overcome this shortfall of most existing multiband LWA designs. In addition to have the dual-passband CRLH leaky-wave radiation characteristics, this electronically tunable LWA can realize the relatively independent tunability of the balanced point within the low passband while maintaining the CRLH backward-to forward leaky-wave radiation characteristics of the high passband. Thus, the proposed LWA can be used for the electronically controlled scanning within the low passband while keeping frequency scanning within the high passband.

### 3.4 Literature of Component Designs with BST Materials

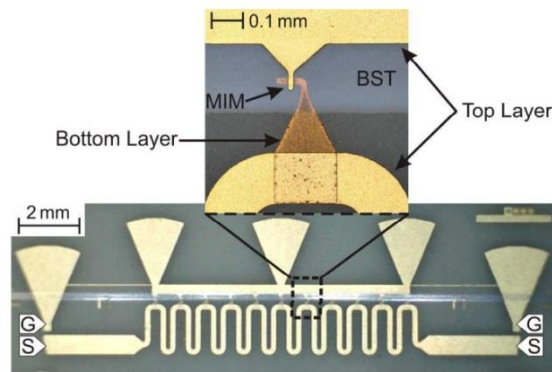
BST, as one of the most popular tunable materials for microwave frequency-agile

applications, has attracted extensive interest for both fundamental and applied research in recent years, due to its advantages, such as chemical stability, good temperature behavior, high electric-field-dependent permittivity, high tunability and the low loss tangent at microwave frequencies [41]. As an important category of FE materials, BST is known to exhibit a largely diversifiable ferroelectric/dielectric behavior that is influenced by a number of structural factors, such as lattice tetragonality [42].

Generally, the materials with low losses and low hysteretic effects are preferred for microwave applications. Therefore, BST materials in the paraelectric phase are usually desired for microwave applications. Depending on composition and fabrication of the BST materials, they can have a permittivity of a few hundreds to even thousand, which is favorable for miniaturization of antenna or component designs at microwave frequencies. Generally, the DC bias voltages of 2-8 V/ $\mu\text{m}$  are applied across the BST material, in order to tune its permittivity by up to 60% [43]. The BST varactors can be divided into two categories – parallel-plate type and planar type. Thus, the total DC bias voltages required to tune the capacitance of a BST varactor can be determined by the thickness of the BST layer for the parallel-plate type or the gap width for the planar type [43]. Some antenna and component designs with BST materials are briefly introduced as follows.



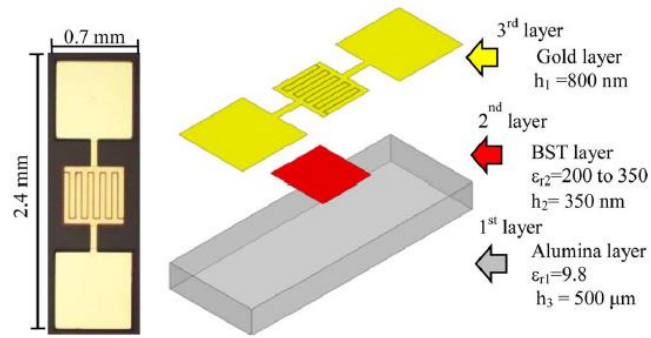
(a)



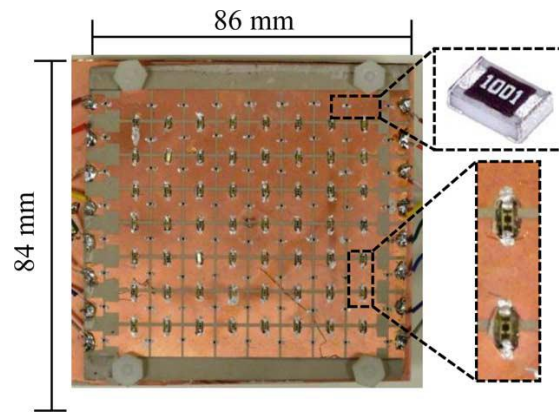
(b)

Figure 3.24 (a) Photograph of the fabricated phased array antenna; (b) layout of the loaded-line phase shifter with MIM BST varactors [44].

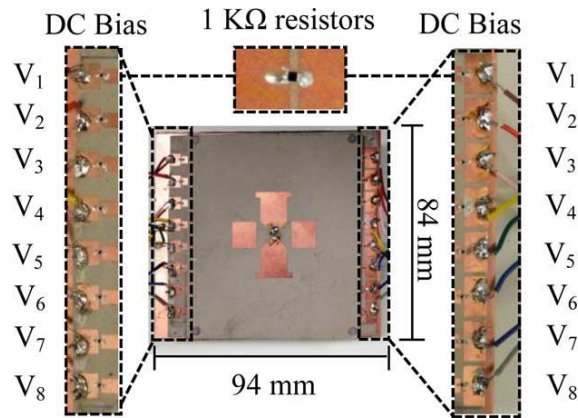
In [44], a beam-steerable dielectric resonator phased array antenna is presented based on inkjet-printed tunable loaded-line phase shifters using parallel-plate BST thick-film varactors. Figure 3.24(a) shows the photograph of the fabricated phase array antenna, and Figure 3.24(b) shows the layout of a loaded-line phase shifter. At 8 GHz, a relative tunability of 46% is achievable by applying 50 V DC bias voltages across the BST film with thickness of 1.2  $\mu\text{m}$ . The loaded-line phase shifter can achieve maximum  $260^\circ$  in measurement. The main beam of this phased array antenna can achieve  $\pm 30^\circ$  scanning angle using the loaded-line phase shifter with parallel-plate BST varactors.



(a)



(b)



(c)

Figure 3.25 (a) Photograph of one BST varactor; (b) top view of the tunable FSS with BST varactors; (c) photograph of the fabricated antenna [45].

In [45], a low-profile dipole antenna using a frequency selective surface (FSS) with interdigital BST varactors is designed to achieve a tunable frequency range from 2.23 GHz to 2.55 GHz. The interdigital BST varactors are shown in Figure 3.25(a), the top view of the tunable FSS with BST varactors is shown in Figure 3.25(b), and

the photograph of this antenna is shown in Figure 3.25(c). The fabricated interdigital BST varactors mounting on 500-um-thick alumina substrates can achieve a relative tunability of 33% by applying 90 V bias voltages, which are used for integration into the FSS structure. Thus, the antenna can be tuned over 2.33-2.55 GHz by electronically adjusting the capacitance of the BST varactors.

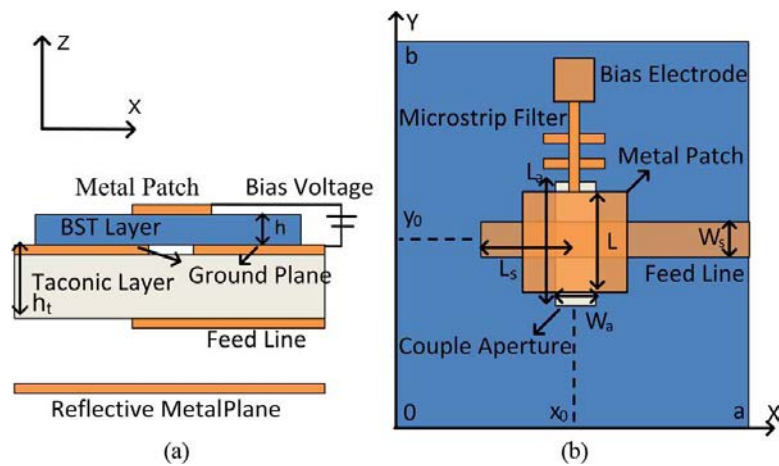


Figure 3.26 Configurations of the antenna with the BST layer, (a) side view; (b) top view [46].

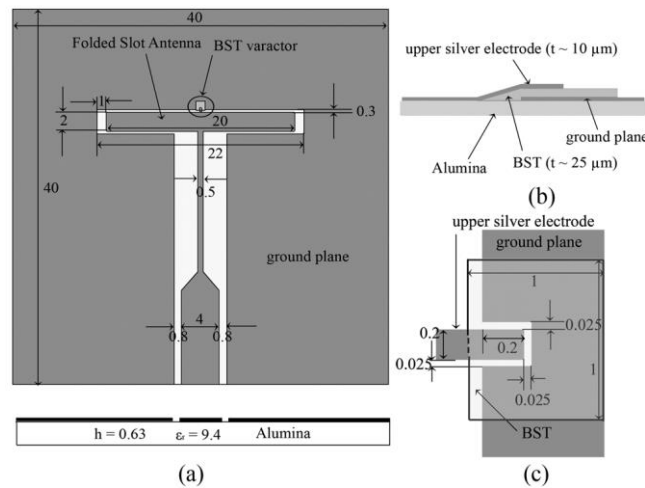


Figure 3.27 Antenna layout, (a) top view of the antenna; (b) side view of the BST varactor; (c) top view of the BST varactor. [47]

In [46], a reconfigurable microstrip antenna with integration of a BST layer is presented. The permittivity of this BST layer in this antenna structure is around 100,

and the thickness of this BST layer is 0.3  $\mu\text{m}$ . This BST layer is used as part of the substrate of the antenna. The configurations of this antenna are shown in Figure 3.26. The antenna can be continuously tuned from 13.3 GHz to 14.7 GHz as the DC bias voltages increase from 0 to 10 V/ $\mu\text{m}$ .

In [47], a frequency-reconfigurable folded slot antenna with a BST thick film is presented. The configuration of this antenna is shown in Figure 3.27. The parallel-plate BST varactor is integrated into the antenna structure. Alumina is used as the antenna substrate material. The thickness of this BST layer is 25  $\mu\text{m}$ . The permittivity of the BST film can be electronically tuned from 400 to 270 by applying the DC bias from 0 V to 200 V. Correspondingly, the parallel-plate BST varactor can be tuned from 1.5 pF to 1.05 pF, which achieves a relative tunability of 32%. Thus, this antenna can be tuned to work from 3.18 GHz to 3.29 GHz by applying the maximum DC bias voltages of 200 V.

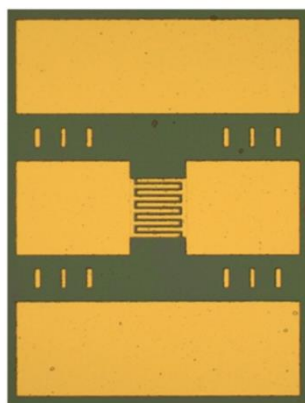


Figure 3.28 Configuration of the interdigital capacitor. [48]

In [48], an interdigital capacitor with a 0.273  $\mu\text{m}$  BST layer growing on a  $\text{LaAlO}_3$  substrate is presented. The configuration of the interdigital capacitor is shown in

Figure 3.28. This capacitor has a total length of 50  $\mu\text{m}$ , and has ten fingers with 5  $\mu\text{m}$  width and 1.5  $\mu\text{m}$  finger spacing. This capacitor has a Q factor of 200 at 1 GHz and has a capacitance of 0.33 pF with 0 V DC bias voltages. When 80 V DC bias voltages are applied to this capacitor, the Q factor is reduced to be 50 and the capacitance becomes around 0.18 pF. The relative tunability of this capacitor is 47%. The measured results of the Q factor for this capacitor also show that the Q factor will decrease when operating at higher frequencies.

In [49], a BST-based interdigital capacitor with 2  $\mu\text{m}$  finger width and 1  $\mu\text{m}$  finger spacing is proposed and analyzed. The BST layer, which is grown on a sapphire substrate, has 0.1  $\mu\text{m}$  thickness. The capacitance of this capacitor can be effectively tuned from 7 pF at 0 V DC bias to 3.8 pF at 90 V DC bias, and its relative tunability can achieve around 57%. According to the measured results, this capacitor can achieve quality factors of at least 20 from 1 GHz to 24 GHz. Furthermore, this BST interdigital capacitor is used in a phase shifter circuit at microwave frequencies. Finally, this phase shift circuit shows  $0^\circ$ - $110^\circ$  phase shifts at 20 GHz with the maximum insertion loss of 3.4 dB.

The FE BST material can enable flexibilities for antenna designs. The antennas with BST varactors can be designed to achieve miniaturization and a certain range of tunability. The brief information about the BST materials, and the antenna and component designs in [44]-[49] is further summarized in Table 3.4.

Most existing BST-based antenna designs mainly use an entire piece of the BST material, which may introduce unnecessary losses to degrade the antenna radiation

performance. An LWA design using discrete BST varactors, which will be presented in Chapter VI, can reduce the unnecessary losses from the BST materials compared to most existing antenna designs. In addition, tunable metamaterial-inspired antennas for microwave applications can be also realized by integrating BST materials into the antenna structure, due to the advantages of BST materials at microwave frequencies. The metamaterial-inspired antennas with BST materials can achieve the electronic control of the frequency response or the beam direction by adjusting the DC bias voltages applied to the BST varactors. Thus, tunable metamaterial-inspired antennas with the BST varactors are still an open and interesting topic for antenna research.

Table 3.4 Summary of the BST materials in [44]-[49].

	Ref. [44]	Ref. [45]	Ref. [46]	Ref. [47]	Ref. [48]	Ref. [49]
<b>BST Layer Thickness (um)</b>	1.2	0.35	300	25	0.273	0.1
<b>BST Permittivity Range (DC Bias)</b>	133 (0 V) – 70 (50 V)	350 (0 V) – 230 (90 V)	100 (0 V)	400 (0 V) – 270 (200 V)	0V – 80V	0V – 90 V
<b>Relative Tunability of BST</b>	23%	33%	Not Specify	40%	50%	57%
<b>Loss Evaluation</b>	BST's TanD: 0.07	Not Specify	Not Specify	BST's TanD: 0.05	Capacitor's Q: 200 (1 GHz)	Capacitor's Q: > 20 (1-24 GHz)
<b>BST Varactor Type</b>	Parallel-plate	Interdigital	Parallel-plate	Parallel-plate	Interdigital	Interdigital
<b>Substrate of BST Layer</b>	Al <sub>2</sub> O <sub>3</sub>	Alumina	Not Applicable	Alumina	LaAlO <sub>3</sub>	Sapphire
<b>Capacitance Range of BST Varactor</b>	Not Specify	1.4-1.0 pF	Not Specify	1.5-1.05 pF	0.33-0.18 pF	7-3.9 pF
<b>Function Realization</b>	Phase shift	Frequency reconfigurable	Frequency reconfigurable	Frequency reconfigurable	BST varactor	Phase shift
<b>Component Feature</b>	Antenna beam steering from -30° to +30°	Antenna frequency tuning from 2.33 to 2.55 GHz	Antenna frequency tuning from 13.3 to 14.7 GHz	Antenna frequency tuning from 3.18 to 3.29 GHz	Capacitance tuning	Phase shift from 0° to 110° at 20 GHz

### **3.5 Literature of Antenna Designs with Different Tuning Techniques**

Generally, tunable antennas are usually designed to overcome the limitations in conventional passive antennas, in order to support (1) more bandwidth or more operating bands; (2) minimization of the environment impact which may result in shifts of the operating bands [50]; (3) possible control of some other antenna properties, such as polarization and farfield patterns. The tuning functions of tunable antennas may be realized by different tuning techniques. Instead of FE BST materials, there are some other tuning techniques for tunable antenna designs, such as semiconductor varactors, liquid crystal, micro-electro-mechanical-system (MEMS) switches, and ferrite materials. Some examples of tunable antenna designs are briefly introduced as follows.

In [28], an electronically controlled LWA based on the CRLH TL structure with semiconductor varactors has been briefly introduced in Section 2.3. By supplying the uniform or non-uniform DC bias to the varactors in the antenna structure, this LWA can achieve the electronically controlled tunable radiation angle or the electronically controlled tunable beamwidth. In this tunable LWA design, silicon abrupt varactors are selected due to their low losses at microwave frequencies. The capacitance of the varactor is mainly controlled by the doping of the depletion layer. When the reverse DC bias applied to the P-N junction of the varactor increases, the depletion region also increases [51]. Because capacitance and dielectric capacitance are inversely related, the capacitance will decrease as the reverse voltage increases [51]. The

varactors have been evaluated to have the capacitance tuning range from 2.54 pF under 0 V DC bias to 0.7 pF under 20 V DC bias [28]. The insertion loss from a single varactor is also evaluated to be 0.94-0.99 dB depending on the reverse DC bias voltages and the operating frequencies.

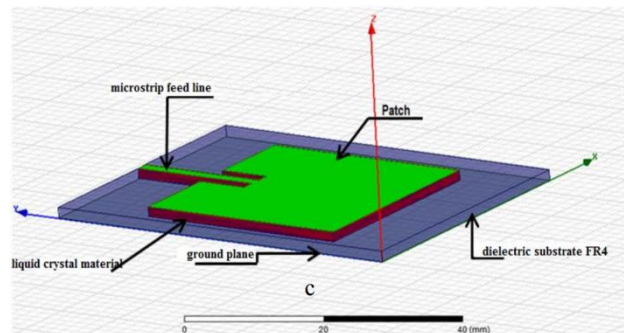


Figure 3.29 Configuration of a patch antenna on the liquid crystal substrate. [52]

In [52], a rectangular patch antenna using a liquid crystal substrate is designed for microwave applications. The liquid crystals are partly ordered materials between their solid and liquid phases, which have some advantageous features, such as low dielectric loss, low moisture absorption, light weight, mechanical stiffness, thermal stability and so on [52]. The configuration of this antenna is shown in Figure 3.29. In this antenna design, the liquid crystal can achieve the permittivity tuning range from 2.9 under 0 V DC bias to 2.13 under 15 V DC bias, so that this patch antenna can achieve the frequency tunability from 2.06 GHz to 2.64 GHz.

In [53], an RF-MEMS-integrated antenna is proposed for two-mode operations. The configurations of the antenna are shown in Figure 3.30. The RF MEMS switch can be modelled as a capacitor with 30 fF in the OFF state or a resistor with 1  $\Omega$  in the ON state. This antenna can operate at two different modes, depending on the operation



the SIW cavity of this antenna. This antenna can achieve the magnetically controlled frequency tunability of around 10% by changing the magnitude of bias magnetic fields between 0 T and 0.31 T. Meanwhile, the radiation patterns and gains of this antenna have little changes during the tuning.

Table 3.5 Summary of the tuning techniques for tunable antenna designs in [44], [28], [52]-[54].

	Ref. [44]	Ref. [28]	Ref. [52]	Ref. [53]	Ref. [54]
<b>Tuning Techniques</b>	BST	Silicon varactor	Liquid crystal	RF MEMS switch	Ferrite material
<b>Tunable Function</b>	Permittivity: 133 (0 V) – 70 (50 V)	Capacitance: 2.544 pF (0 V) – 0.7 (20 V)	Permittivity: 2.9 (0 V) – 2.13 (15 V)	ON-OFF states	Not Specify
<b>Relative Tunability</b>	23%	72%	26.5%	Not Applicable	14.9%
<b>Loss Evaluation</b>	BST's TanD: 0.07	Insertion Loss: 0.94-0.99 dB	Liquid crystal's TanD: 0.002	ON state (= 1 $\Omega$ )	Not Specify
<b>Tuning Type</b>	Parallel-plate	SMD	Substrate	SMD	Ferrite slabs
<b>Control Method</b>	DC bias voltages	DC bias voltages	DC bias voltages	Actuation voltage	Magnetic field
<b>Application</b>	Phased array	LWA	Patch antenna	Electrically small antenna	SIW slot antenna
<b>Antenna Features</b>	Antenna beam steering from -30° to +30°	Tunable radiation angle or tunable beamwidth	Frequency tunability over 2.06-2.64 GHz	ON state: 0.71 GHz with 20 MHz bandwidth OFF state: 4.96 GHz with 223 MHz bandwidth	Frequency tunability of 9.23-10.69 GHz

Different tuning techniques for tunable antenna designs have been briefly presented in [44], [28], [52]-[54], including BST materials, silicon varactors, crystal liquid, RF MEMS switch, and ferrite materials. The brief information of these tuning techniques is summarized and compared in Table 3.5.

Based on comparison of the tuning techniques for tunable antennas in Table 3.5, some conclusions can be draw as followings: (1) BST, ferrite, and crystal liquid are more

convenient to be integrated with antenna structures, compared to SMD varactors and MEMS switches; (2) The relative tunabilities of BST, ferrite, and crystal liquid seem worse than SMD varactors; (3) The losses of BST and crystal liquid are relatively low at microwave frequencies, while varactors may contribute more losses compared to the others.

### **3.6 Summary**

This chapter presents the literature review of artificial electromagnetic structures, BST materials and some tunable techniques applied to antenna designs. Most existing antenna designs based on artificial electromagnetic structures can have some performance improvement, such as bandwidth enhancement, radiation improvement, multiband leaky-wave radiation characteristics, and so on. The BST materials, as popular tunable materials, enable the frequency or pattern reconfigurability of antenna designs, due to its advantages at microwave frequencies. In addition, the literature of existing antenna designs using some other tuning techniques, i.e., silicon varactors, liquid crystal, MEMS switch, is reviewed and compared. However, these antennas suffer from some limitations, such as a limited number of operating resonances in the RA designs, the single passband in the CRLH-based LWAs, and non-frequency-reconfigurable or non-pattern-reconfigurable designs for the multiband LWA. The antenna designs proposed in the following chapters will present some advantages over most existing antenna designs, such as multiband and frequency tunable characteristics.

# CHAPTER IV

## OPEN-ENDED RESONANT ANTENNAS BASED ON EXTENDED COMPOSITE RIGHT/LEFT HANDED TRANSMISSION-LINE UNIT CELL STRUCTURE

### **4.1 Introduction**

The rapid development of novel wireless communication techniques encourages an increasing number of wireless services at different frequency bands. As an important component in wireless communication systems or mobile devices, the single or multiple antennas capable of operating at diverse commercial frequency bands while occupying small space are very necessary. The high demands for multiband or frequency-agile antennas have attracted great research interest in recent years.

The interesting properties of the CRLH structure make this artificial electromagnetic material very attractive for antenna designs. A group of antennas, which is called the metamaterial-inspired RAs, is formed by combining metamaterial-inspired structures with RA designs. The metamaterial-inspired RAs can be categorized into two types –

short-ended and open-ended [10]. In short-ended RAs, one or multiple metamaterial-inspired unit cell structures are usually used to form a radiated resonant structure with a termination connected to the main GP or the virtual GP. With a proper feeding approach, the intrinsic modes (i.e., the zeroth-order mode, negative-order modes and positive-order modes) of the resonant structure can be excited, thereby generating multiple operating resonances for radiation. One distinct feature of the RAs in this type is the zeroth-order mode ( $m = 0$ ) for radiation, due to the advantages of this mode, such as the size reduction [10]. Thus, these metamaterial-inspired RAs with this feature are also called ZOR antennas. On the other hand, RAs with an open end can be realized with one conventional open-ended antenna (e.g., monopole antenna) usually loaded with one metamaterial-inspired unit cell. The RAs can usually be designed with one unit cell with an open end at the termination. Compared with conventional open-ended antennas, metamaterial-inspired open-ended RAs mainly have two advantages [12]: (1) multiple operating resonances for multiband or wideband operations; (2) at least one operating resonance working at lower frequency compared to conventional monopole antennas.

Most existing metamaterial-inspired RA designs in both short-ended and open-ended types, which have been introduced in Section 3.2 of Chapter III, can usually generate a few operating resonances to cover a few frequency bands. In order to meet the needs of modern wireless services, metamaterial-inspired RAs should be designed to have multiple operating resonances working at as many commercial frequency bands as possible.

In this chapter, three open-ended RA designs based on one ECRLH unit cell structure are introduced as a novel class of metamaterial-inspired RAs for multiband or frequency-agile applications. The RAs include a short microstrip line as the feeding line and one ECRLH unit cell structure as the main radiation body. Due to the multiband properties of the ECRLH structure, these RAs can generate multiple operating resonances working at the chosen frequencies. The equivalent model of the proposed RAs is also developed in order to understand the antenna characteristics. In addition, the control of the operating resonances by changing the dimension of some parts in the antenna structure is summarized. The first RA is designed with SMD chip capacitors for the initial theoretical realization. The second RA is designed with interdigital structures (IDSs) in order to avoid the losses from the SMD chip capacitors. Based on exploration of the resonance control by important parts in the antenna structure, the third RA is designed with a GaAs semiconductor varactor as a tunable antenna, which can achieve the electronically controlled frequency tunability of one specific operating resonance over 0.7-0.96 GHz, while keeping the wideband coverage over 1.7-6 GHz formed by the other operating resonances. Therefore, the major advantages of metamaterial-inspired RAs in this class are summarized as below:

- (1) multiple operating resonances at chosen frequencies to achieve multiband or frequency-agile applications;
- (2) at least one operating resonance at lower frequencies in comparison with a conventional monopole antenna within similar space;

(3) electronically controlled tunability of one operating resonance at low frequency without destroying the wideband coverage formed by the other operating resonances in the tunable RA design.

This chapter is organized as follows. In Section 4.2, the resonant theory of an ECRLH structure will be explained by extending the resonant theory of a CRLH structure. A passive RA design with three SMD chip capacitors will be presented in Section 4.3. In Section 4.4, a passive RA design with three IDSs will be presented. Section 4.5 will introduce an electronically tunable RA design with one SMD GaAs semiconductor varactor. The summary will be given in Section 4.6.

## 4.2 Resonant Theory of ECRLH Structure

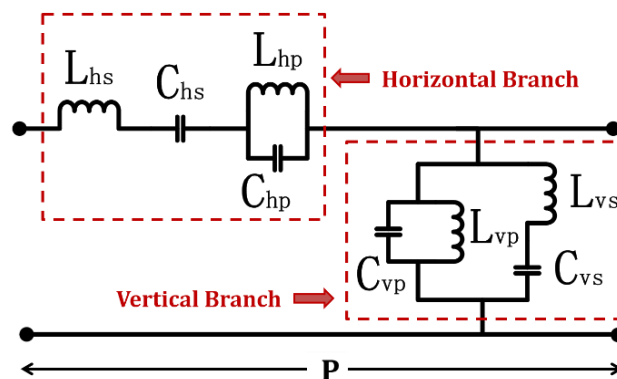


Figure 4.1 Equivalent circuit model of one ECRLH unit cell structure.

The introduction of the CRLH theory has been presented in Section 2.5 of Chapter II. The resonant theory of the ECRLH structure is developed based on that of the CRLH structure. The equivalent circuit model of one ECRLH unit cell structure is shown in Figure 4.1. An ECRLH resonant structure generally consists of one or multiple ECRLH unit cells. Theoretically, the ECRLH structure generates two pairs of LH and

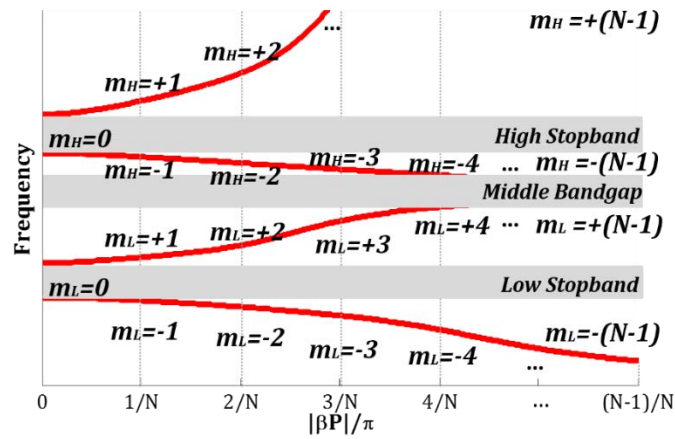
RH bands which can further form two CRLH bands respectively at low and high frequencies. One middle bandgap exists between two CRLH bands for separation. For a resonant structure with  $N$  ECRLH unit cells, a set of intrinsic harmonic modes exists in the low CRLH band ( $m_{Low}$ ), while another set of intrinsic modes ( $m_{High}$ ) exists in the high CRLH band. Within the low CRLH band, the modes can be positive for the RH band (i.e.,  $m_{Low} = +1, +2, \dots$ ) or negative for the LH band (i.e.,  $m_{Low} = -1, -2, \dots$ ) or even zero ( $m_{Low} = 0$ ) at the transition frequency area from the LH to RH band. Similarly, for the high CRLH band, it also has a set of intrinsic modes (i.e.,  $m_{High} = 0, m_{High} = -1, -2, \dots$  and  $m_{High} = +1, +2, \dots$ ).

As mentioned in Section 2.5 of Chapter II, the ECRLH structure has two operation conditions – unbalanced condition and balanced condition. The corresponding resonant modes of an ECRLH resonant structure with length  $L$  in both CRLH bands can be expressed as Eq. (4-1):

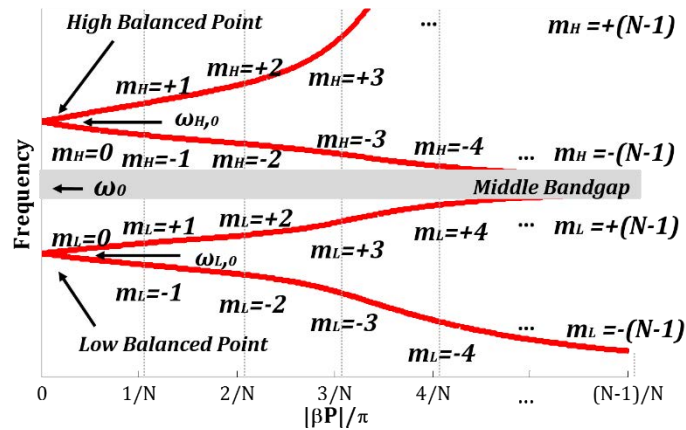
$$\beta_m P = \beta_m \frac{L}{N} = m \frac{\pi}{N} = m_{Low} \frac{\pi}{N} = m_{High} \frac{\pi}{N} \quad \text{Eq. (4-1)}$$

where  $P$  is the period of the unit cell,  $N$  is the number of unit cells,  $L = N \times P$ , and  $m_{Low}$  and  $m_{High}$  are the resonant modes for the low and high CRLH bands respectively, i.e.,  $m_{Low} = 0, \pm 1, \pm 2, \dots$ , and  $m_{High} = 0, \pm 1, \pm 2, \dots$ . Figure 4.2(a) and Figure 4.2(b) show the resonance spectrum of a resonant structure with  $N$  ECRLH unit cells for the unbalanced and balanced condition, respectively. In the unbalanced condition, an open stopband region exists in the transition area between the LH and RH band within each CRLH band. In the balanced condition, the open stopband

region originally in the unbalanced condition is closed and the balanced point is formed to achieve the smooth transition from the LH to RH band within each CRLH band. In this condition, as explained in [48],  $\omega_0$  is the resonant frequency of  $L_{hp}-C_{hp}$  and  $L_{vs}-C_{vs}$ , i.e.,  $\omega_0 = \omega_{hp} = \omega_{vs}$ , which is generally within the middle bandgap area.



(a)



(b)

Figure 4.2 Resonance spectrums of one ECRLH unit cell structure in different operation conditions, (a) the unbalanced condition; (b) the balanced condition.

Different operation conditions may have different effects on the frequency response of an RA. In [1], it has demonstrated that an open-ended RA with the unit cell in the

unbalanced condition can generate more operating resonances to work at the chosen frequency bands than one with the unit cell in the balanced condition. Thus, benefiting from the characteristics of the unbalanced condition, RAs are usually designed with one or multiple unit cells in this condition in order to generate multiple operating resonances working at the chosen frequency bands.

### 4.3 Passive RA Design with SMD Capacitors

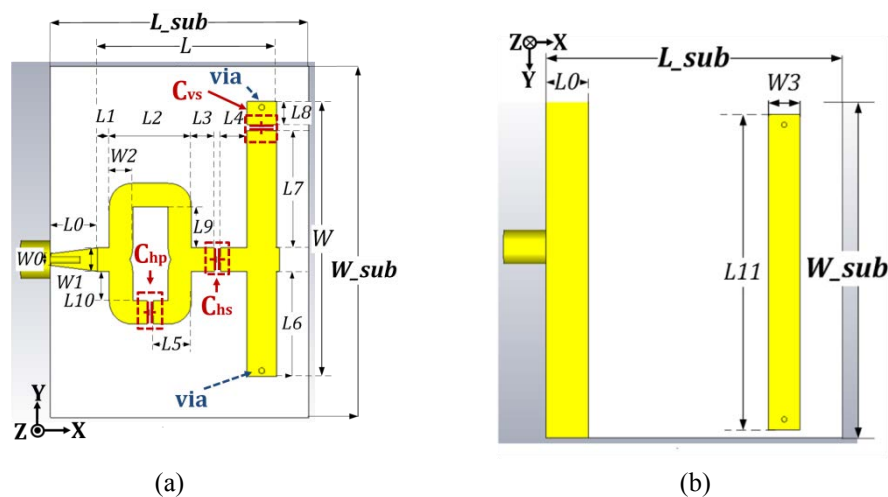


Figure 4.3 Configurations of the passive RA with SMD capacitors, (a) top view; (b) rear view.

In this section, the RA based on one ECRLH unit cell structure with SMD chip capacitors is designed for the initial theoretical realization. The design and analysis process for this RA is explained as the following steps: (1) the resonant structure are realized using the copper strips to model the ECRLH structure; (2) with a short microstrip line for feeding, the proposed RA generates multiple operating resonances for radiation; (3) after optimizing the dimensions of this RA, these operating resonances can work at the chosen frequencies; (4) the equivalent circuit model for this RA is developed and the parameter values in this model are extracted from the

full-wave simulated data; (5) the resonance control by the RA structure is discussed and summarized.

Table 4.1 Dimensions of the proposed passive RA with SMD chip capacitors and the capacitances of the SMD capacitors in this RA.

Symbol	Value	Symbol	Value
$L_{sub}$	47 mm	$W_{sub}$	55 mm
$L$	37 mm	$W$	51 mm
$L0$	7 mm	$W0$	2 mm
$L1$	5 mm	$W1$	4 mm
$L2$	16 mm	$W2$	4 mm
$L3$	5 mm	$W3$	5 mm
$L4$	5 mm	$L10$	8 mm
$L5$	7.5 mm	$L11$	53 mm
$L6$	26 mm		
$L7$	16 mm	Chs	0.5 pF
$L8$	4 mm	Chp	1.2 pF
$L9$	10 mm	Cvs	0.5 pF

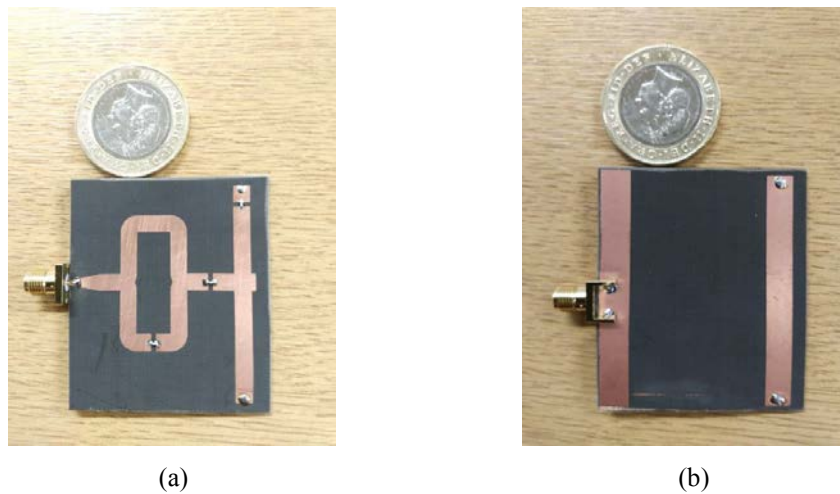


Figure 4.4 Photographs of the fabricated passive RA with SMD capacitors, (a) top view; (b) rear view.

The passive RA design is printed on a *Rogers RT/duroid 5880* substrate with dielectric constant of 2.2, loss tangent of 0.0009 and thickness of 1.575 mm. The configurations of the proposed RA with three SMD capacitors are shown in Figure 4.3. In this antenna structure,  $L_{hs}$ ,  $L_{hp}$ ,  $L_{vs}$  and  $L_{vp}$  are realized by the horizontal and vertical

copper strips, respectively. The parallel vertical copper strips are connected through two metalized vias. The metal strip at the bottom layer is modelled as the virtual ground of the ECRLH unit cell structure. This virtual ground is not directly connected to the main ground of the antenna. The ECRLH unit cell is properly excited by one microstrip feeding line.  $C_{hs}$ ,  $C_{hp}$  and  $C_{vs}$  are realized by the SMD *MURATA* 0402 capacitors while  $C_{vp}$  is modeled by parasitic capacitance between the parallel vertical copper strips. The information of *MURATA* 0402 capacitors is included in Appendix A. For example, the loop part with a SMD chip capacitor in the antenna structure is constructed to model  $L_{hp}$ - $C_{hp}$  in Figure 4.1; the vertical parallel strips on the top and bottom layers and one SMD chip capacitor are used to model  $L_{vp}$ - $C_{vp}$  and  $L_{vs}$ - $C_{vs}$  in Figure 4.1. The proposed RA is open-ended at the termination of the structure. The detailed dimensions of the proposed RA are listed in Table 4.1. The overall size of the proposed RA in the unbalanced condition is  $47 \text{ mm} \times 55 \text{ mm} \times 1.575 \text{ mm}$  (i.e.,  $0.11\lambda_0 \times 0.13\lambda_0 \times 0.0037 \lambda_0$ , where  $\lambda_0$  is the free-space wavelength of the lowest operating frequency of 0.707 GHz). The prototypes of the fabricated RA with an ECRLH unit cell structure are shown in Figure 4.4.

### 4.3.1 Measurement and Simulation

Figure 4.5 presents the full-wave simulated (purple dash line) and measured (blue solid line)  $S_{11}$  results of the proposed RA. Clearly, the proposed RA generates multiple operating resonances and has the triple-band feature of one narrow band at 0.707 GHz and two wide bands of 1.7-3.0 GHz and 4.5-6.0 GHz, working at LTE, WIFI 2.4 GHz and 5 GHz bands. The simulated (blue crossing) and measured (red

triangle) gains of this RA are shown in Figure 4.6.

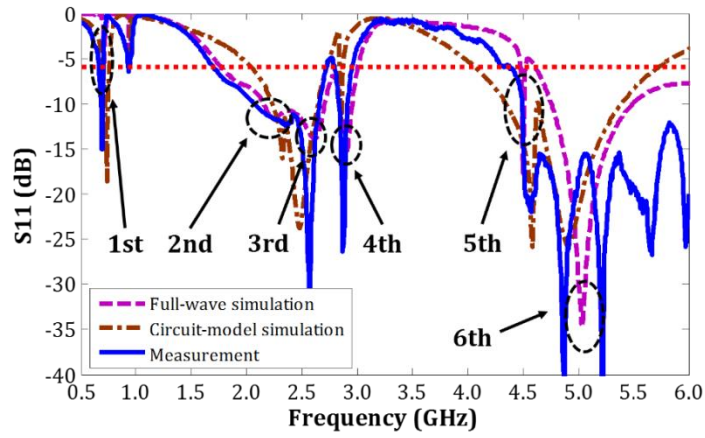


Figure 4.5 Full-wave simulated, circuit-model simulated and measured S11 results of the proposed RA.

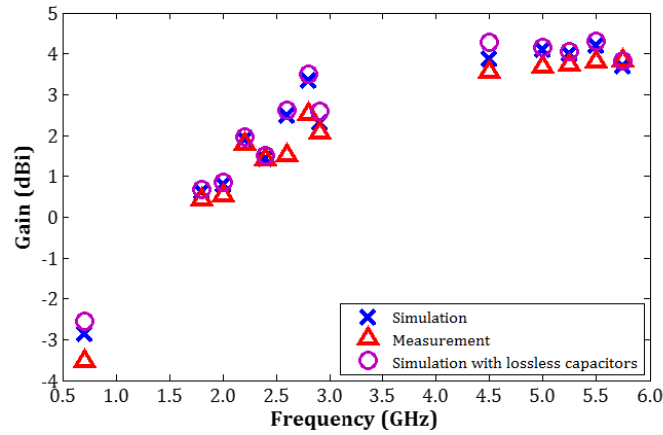


Figure 4.6 Full-wave simulated and measured gains of the proposed RA with SMD capacitors.

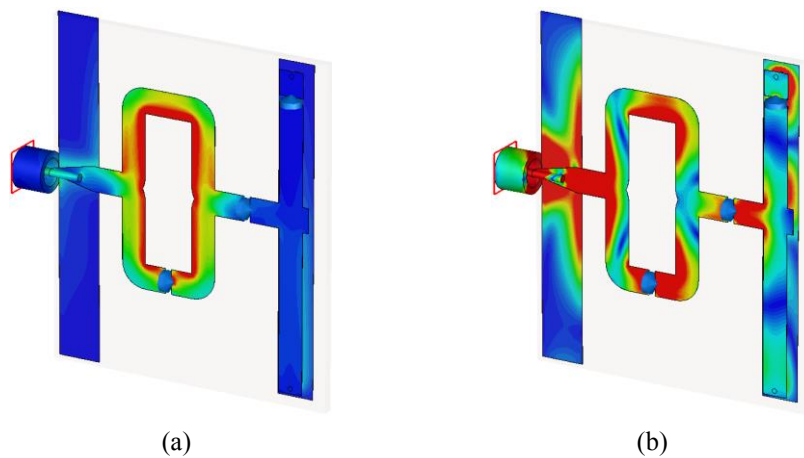
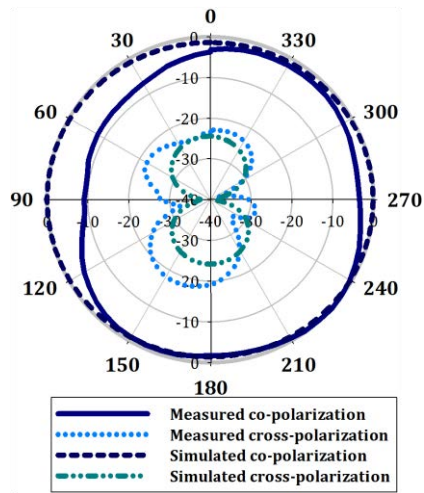
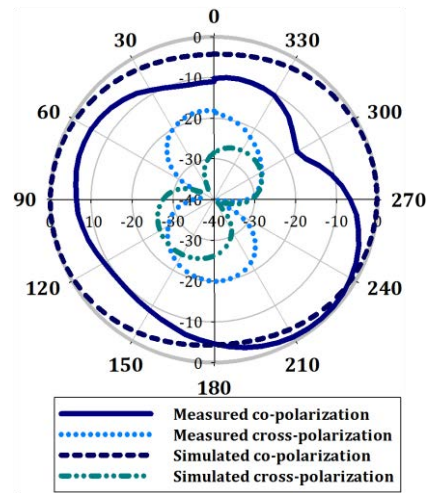


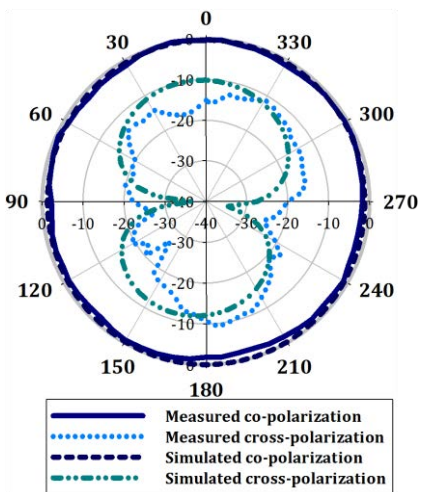
Figure 4.7 Current distributions of this RA, (a) 0.707 GHz; (b) 5.5 GHz.



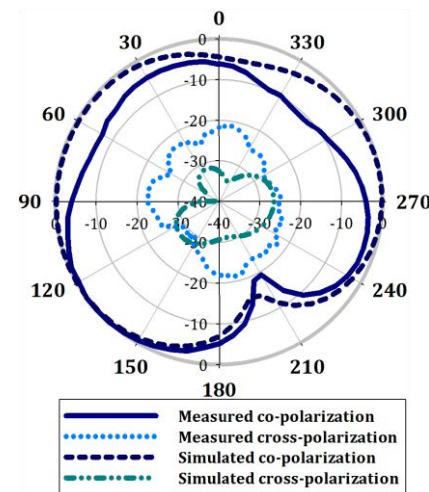
(a)



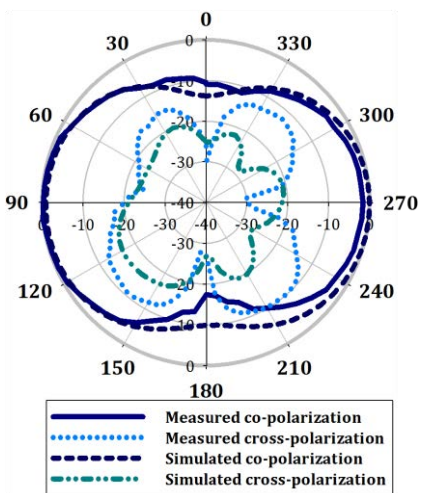
(b)



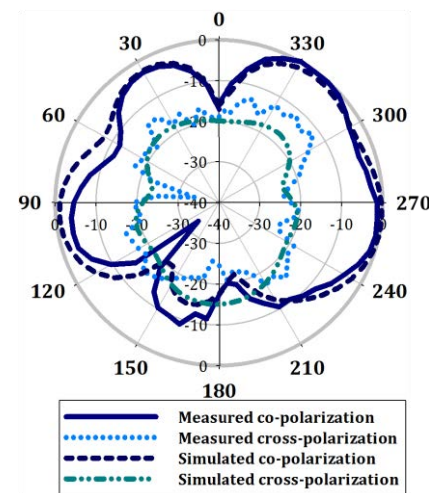
(c)



(d)



(e)



(f)

Figure 4.8 Measured and simulated normalized farfield patterns of the RA for co-polarization and cross-polarization, (a) YOZ plane at 0.707 GHz; (b) XOY plane at 0.707 GHz; (c) YOZ plane at 2.4 GHz; (d) XOY plane at 2.4 GHz; (e) YOZ plane at 5.5 GHz; (f) XOY plane at 5.5 GHz.

This proposed RA suffers from low gain at 0.707 GHz, which is due to the electrically small size of the loop part in the antenna structure. At the resonant frequency of 0.707 GHz, the current mainly flows around the loop part, which is shown in Figure 4.7(a). This results in the low radiation efficiency and low gain. However, the radiation efficiency and antenna gain of this operating resonance will be further improved at higher frequencies according to simulations. In addition, the SMD chip capacitors introduce a certain amount of loss to degrade the antenna gain. Figure 4.6 also presents the simulated gains of the antenna structure with the ideal lossless capacitors (purple circle). After comparing two simulated results (i.e., blue crossings and purple circles) in Figure 4.6, it shows that the SMD capacitors introduce around 0.1-0.4 dB loss for the antenna gain degradation depending on frequencies.

The simulated and measured normalized farfield radiation patterns at the YOZ and XOY planes for 0.707, 2.4, and 5.5 GHz are shown in Figure 4.8. Figure 4.8 shows that this antenna has the omnidirectional farfield patterns at 0.707 GHz and 2.4 GHz, but the non-omnidirectional patterns at 5.5 GHz due to a combination of multiple radiation parts in the antenna structure shown in Figure 4.7(b).

The differences between the full-wave simulated and measured results in Figure 4.5, Figure 4.6 and Figure 4.8 mainly come from two reasons:

- (1) the fabrication and measurement deviations;
- (2) the loss resulting from soldering;

### 4.3.2 Analysis of passive RA with SMD chip capacitors

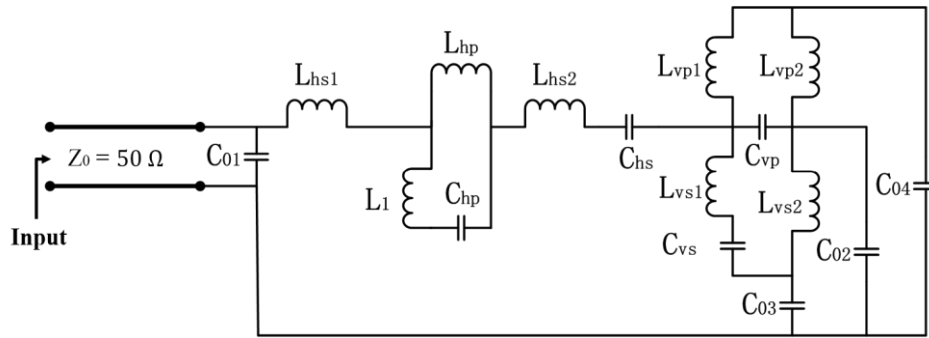


Figure 4.9 Equivalent circuit model of the proposed RA with SMD capacitors.

Table 4.2 Component values in the equivalent circuit model of this RA with SMD chip capacitors.

Symbol	Values (pF)	Symbol	Values (nH)
C <sub>01</sub>	0.42	L <sub>hs1</sub>	1.64
C <sub>02</sub>	0.38	L <sub>hs2</sub>	3.1
C <sub>03</sub>	0.33	L <sub>hp</sub>	9.8
C <sub>04</sub>	0.29	L <sub>1</sub>	8.3
C <sub>hp</sub>	1.2	L <sub>vs1</sub>	4.3
C <sub>hs</sub>	0.5	L <sub>vs2</sub>	11.4
C <sub>vs</sub>	0.5	L <sub>vp1</sub>	13.7
C <sub>vp</sub>	0.71	L <sub>vp2</sub>	15.3

In order to analyze the antenna characteristics, the equivalent circuit model of the proposed RA is developed, which is shown in Figure 4.9. In this model, the microstrip feeding line is modelled as a 50  $\Omega$  TL. C<sub>01</sub>, C<sub>02</sub>, C<sub>03</sub>, and C<sub>04</sub> are used to model the equivalent capacitors between different parts of the ECRLH unit cell structure and the main ground of the antenna. The component values in this equivalent model are listed in Table 4.2, which are extracted in the following steps:

- (1) each part of this RA structure is analyzed using the full-wave simulations, so that the approximate values can be assigned to the components in the model. Specifically, through the full-wave simulation of each metal strip segment, the S

parameters of this strip can be obtained. Thus, the total inductance can be approximately derived using the equation of  $L = \text{Im}(1/Y_{11})/\omega$ , where  $\omega$  is the angular frequency and  $Y_{11}$  is an element in Y parameters [55].

- (2) In addition to the known capacitances of the chip capacitors, the parallel-plate capacitance  $C_{vp}$  can be approximately calculated using the equation of  $C = \epsilon_0 \epsilon A/d$ , where  $\epsilon_0$  is the permittivity in free space,  $\epsilon$  is the permittivity of the dielectrics between the plates,  $A$  is the overlapping area of two plates, and  $d$  is the distance between two plates.
- (3) After assigning the approximate values to the components in this model, final optimizations are implemented in order to make the circuit-model simulated results close to the full-wave simulated ones.

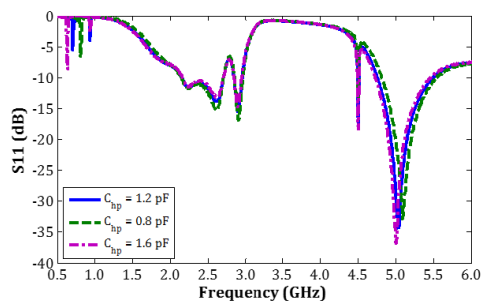
The circuit-model simulated S11 (brown dot dash line) is also presented in Figure 4.5. The circuit-model and full-wave simulated results have differences because this equivalent circuit does not fully take into account all coupling effects among the RA structure. However, the equivalent circuit approach could not only provide an insight into the frequency response of the proposed RA, but also provide a fast tool for an initial approximation of the RA in terms of the frequency response.

Furthermore, different parts in the RA structure have some effects on these operating resonances. Figure 4.10 shows the effects on these operating resonances by changing the dimension of each part of the antenna structure. As examples, the effects on the frequency response of the RA by changing the capacitance of  $C_{hp}$ ,  $C_{hs}$ , and  $C_{vs}$  are shown in Figure 4.10(a), Figure 4.10(b), and Figure 4.10(c), respectively.

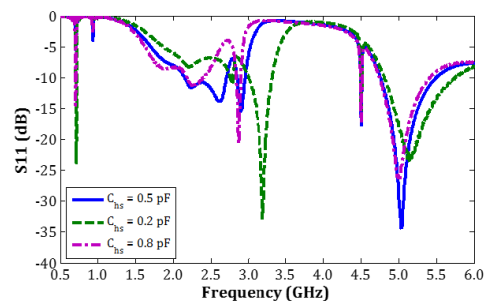
Figure 4.10(a) shows that the capacitance changing of  $C_{hp}$  mainly shifts the 1st operating resonances without obviously affecting other operating resonances. Figure 4.10(b) shows that the capacitance changing of  $C_{hs}$  mainly affects 2nd, 3rd, 4th and 6th operating resonances. Figure 4.10(c) shows that the capacitance changing of  $C_{vs}$  mainly affects 3rd, 4th, and 5th operating resonances. Table 4.3 summarizes the important parts of the antenna structure and the operating resonances correspondingly controlled by each part. From this summary, the effects shown in Figure 4.10(a) may be used to design a tunable antenna, because only one operating resonance at the low frequency will be affected by the capacitance of  $C_{hp}$ .

Table 4.3 Some parts of the RA with SMD chip capacitors and the operating resonances correspondingly controlled by each part.

Symbol	No. of Operating Resonances Controlled
$C_{hp}$	1st
$C_{hs}$	2nd, 3rd, 4th, and 6th
$C_{vs}$	3rd, 4th, and 5th
$L10$	1st, 3rd, 4th, 5th, and 6th
$L9$	1st, 4th, and 6th
$L6$	2nd, 3rd, 4th, and 5th
$L7$	2nd, 3rd, 4th, and 5th
$L1$	2nd, 3rd, and 6th
$L2$	2nd, 3rd, 4th, and 6th



(a)



(b)

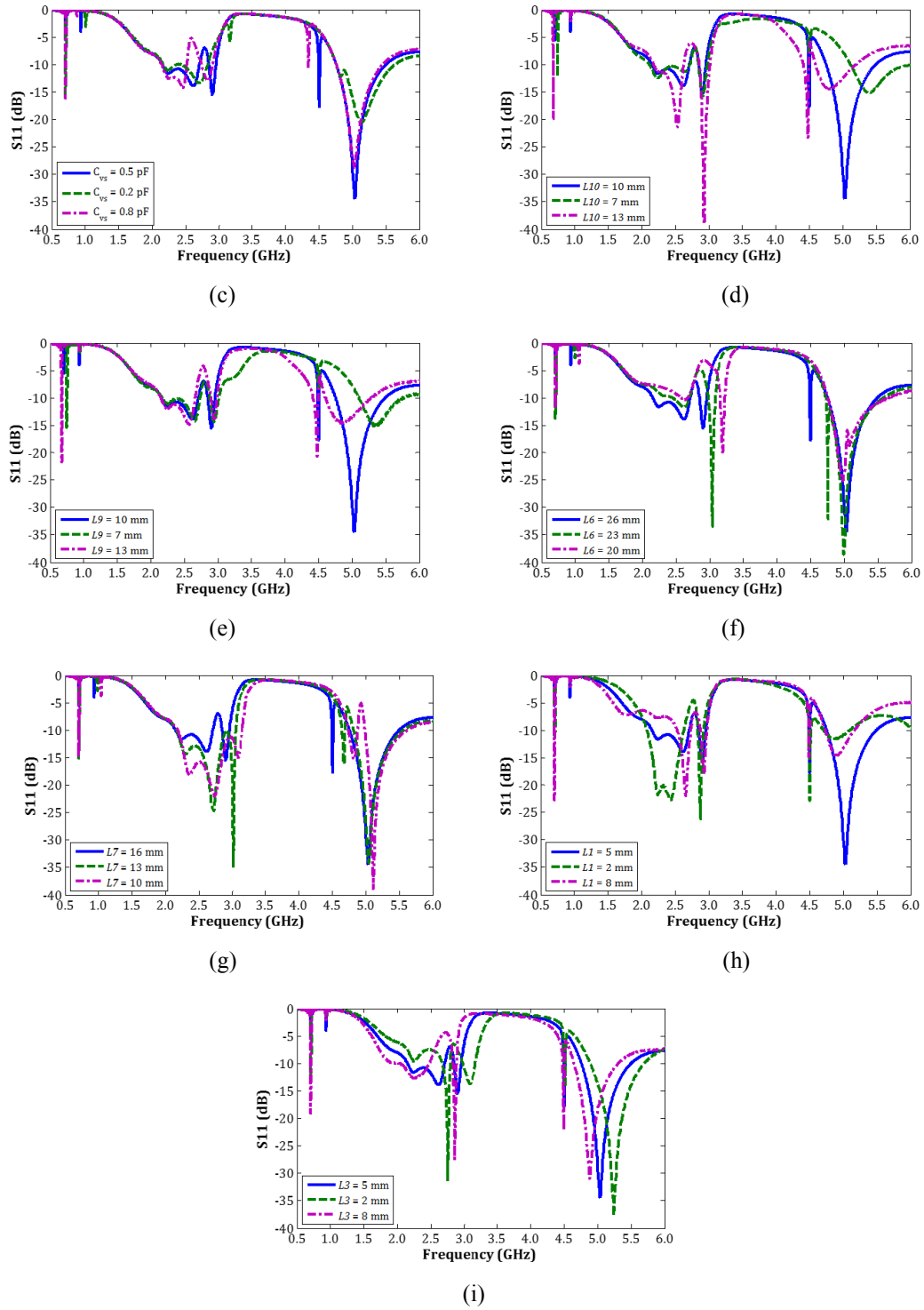


Figure 4.10 Effects of the dimension changing of the part of the antenna structure on the frequency response of this RA, (a)  $C_{hp}$ ; (b)  $C_{hs}$ ; (c)  $C_{vs}$ ; (d)  $L_{10}$ ; (e)  $L_9$ ; (f)  $L_6$ ; (g)  $L_7$ ; (h)  $L_1$ ; (i)  $L_3$ .

## 4.4 Passive RA Design with IDSs

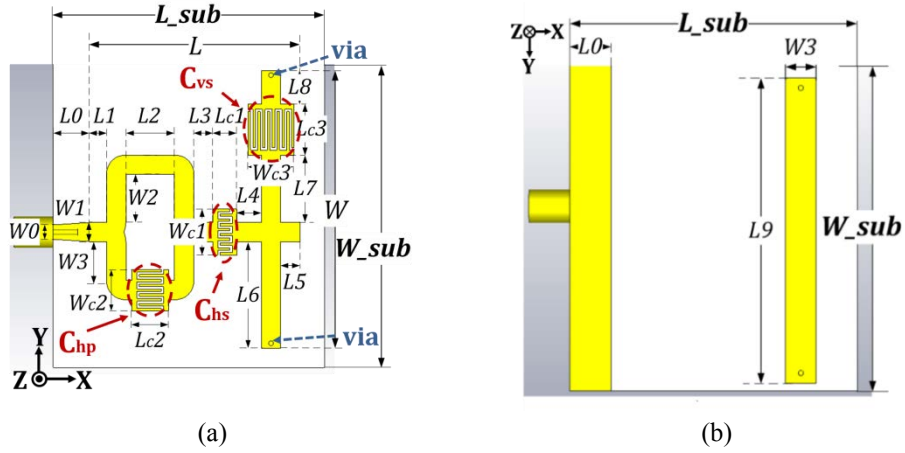


Figure 4.11 Configurations of the passive RA with IDSs, (a) top view; (b) rear view.

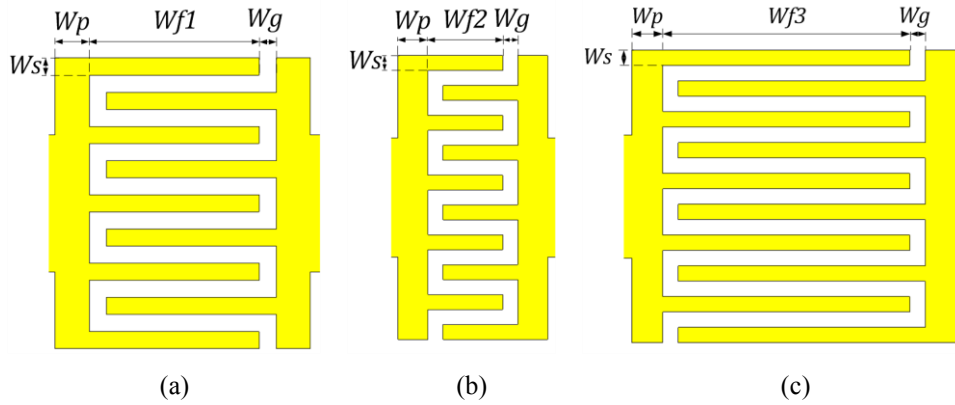


Figure 4.12 IDSs in the proposed antenna structure, (a)  $C_{hp}$ ; (b)  $C_{hs}$ ; (c)  $C_{vs}$ .

Table 4.4 Dimensions of the proposed passive RA with IDSs.

Symbol	Dimension (mm)	Symbol	Dimension (mm)
$L_{sub}$	56	$W_{sub}$	64
$L$	43	$W$	57.5
$L0$	8	$W0$	3
$L1$	3	$W1$	4
$L2$	5	$W2$	10
$L3, L5$	4	$W3$	8
$L4$	5	$W4$	6
$L6$	22	$Wp$	1
$L7$	14	$Wg, Ws$	0.5
$L8$	7	$Wf1$	5
$L9$	59.5	$Wf2$	2.5
$Lc1$	5	$Wf3$	8
$Lc2$	7.5	$Wc1, Wc3$	9.5
$Lc3$	10.5	$Wc2$	8.5

In this section, the RA with IDSs are designed, in order to avoid the losses from the SMD chip capacitors used in the RA design of Section 4.3. The design and analysis process for this RA are similar as the one in Section 4.3. In addition, this RA is compared to a conventional reference monopole, in order to demonstrate that this RA can have one operating resonance working at lower frequencies than this monopole.

The passive design of the RA with IDSs is shown in Figure 4.11, which is realized on a *Rogers RT/duroid 5880* substrate with dielectric constant of 2.2, loss tangent of 0.0009 and thickness of 1.575 mm. The main radiator of this RA is an ECRLH unit cell with three IDSs. These three IDSs are respectively used to realize  $C_{hs}$ ,  $C_{hp}$ , and  $C_{vs}$ , which are shown in Figure 4.12. Similarly,  $C_{vp}$  is achieved by the parasitic capacitance of the vertical parallel copper strips. These vertical paralleled strips are respectively placed on the top and bottom layers and are connected through two metalized vias.  $L_{hs}$ ,  $L_{hp}$ ,  $L_{vp}$  and  $L_{vs}$  are realized by the horizontal and vertical copper strips. The copper strip at the bottom layer is used to model the ground of the ECRLH TL unit cell structure, which is not directly connected to the main ground of the proposed RA. The overall size of the proposed RA is  $56 \text{ mm} \times 64 \text{ mm} \times 1.575 \text{ mm}$  (i.e.,  $0.16\lambda_0 \times 0.18\lambda_0 \times 0.004\lambda_0$ , where  $\lambda_0$  is the wavelength of the lowest operating frequency of 0.887 GHz). The detailed dimensions of the proposed RA and the IDSs are listed in Table 4.4. The prototypes of the fabricated antenna are presented in Figure 4.13.

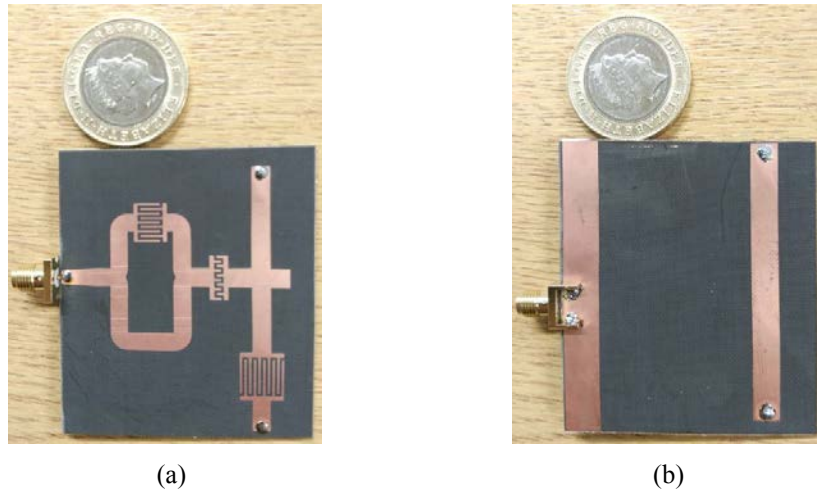


Figure 4.13 Prototypes of the fabricated RA with IDSs, (a) front view; (b) rear view.

#### 4.4.1 Measurement and Simulation

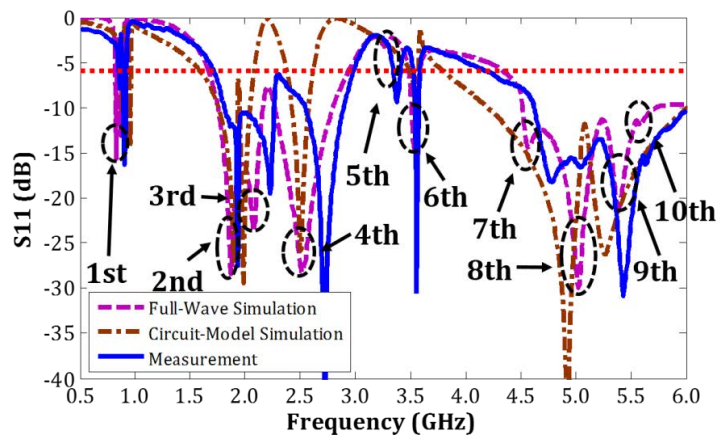


Figure 4.14 Full-wave simulated, circuit-model simulated and measured S11 results of the proposed RA with the IDSs.

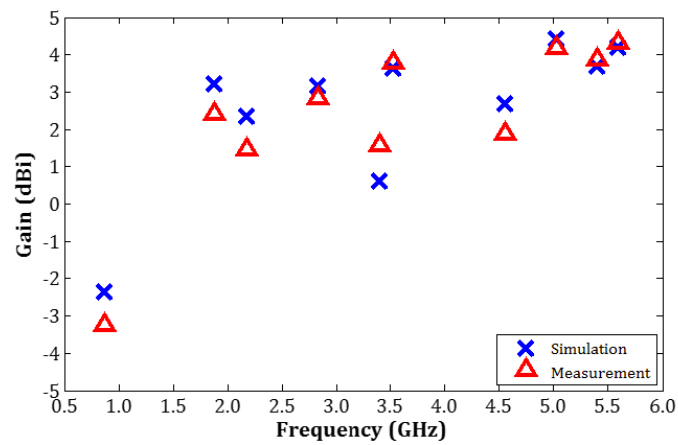


Figure 4.15 Simulated and measured gains of the proposed RA at resonant frequencies.

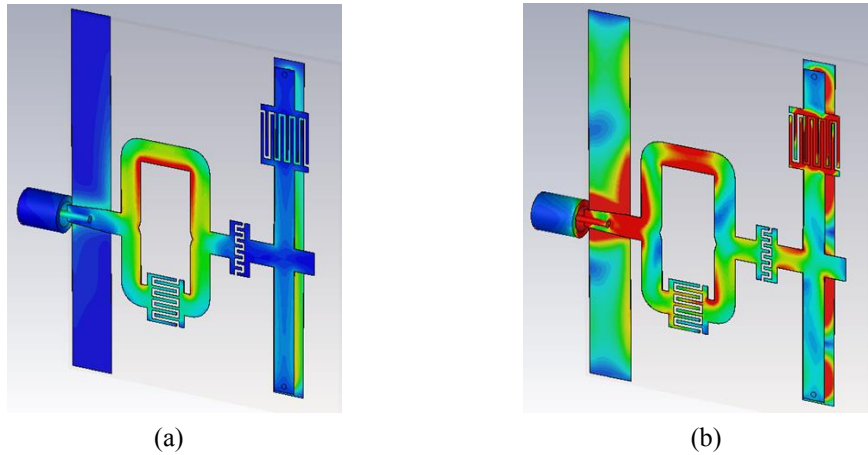
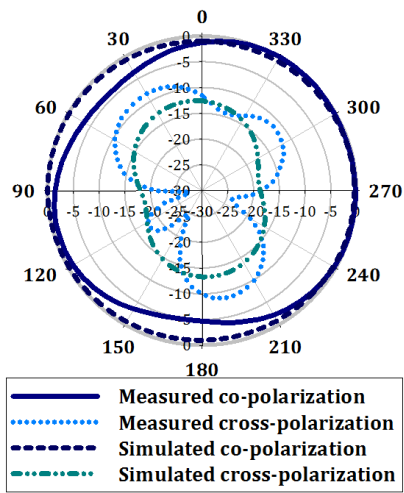


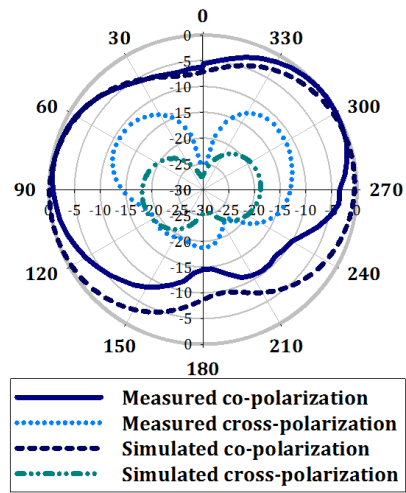
Figure 4.16 Current distribution of this RA, (a) 0.887 GHz; (b) 5.5 GHz.

The full-wave simulated (purple dash line) and measured (blue solid line) S11 results of the proposed RA are presented in Figure 4.14. The simulated and measured S11 results have a close agreement, with respect to the -6 dB bandwidth. In the full-wave simulated S11, the proposed RA has ten operating resonances over 0.5-6.0 GHz working at GSM-850, DCS, PCS, UMTS, Bluetooth, WiFi (2.4 GHz and 5 GHz), TD-2500 and WiMAX (2500-2690 MHz, 3400-3690 MHz, and 5250-5280 MHz).

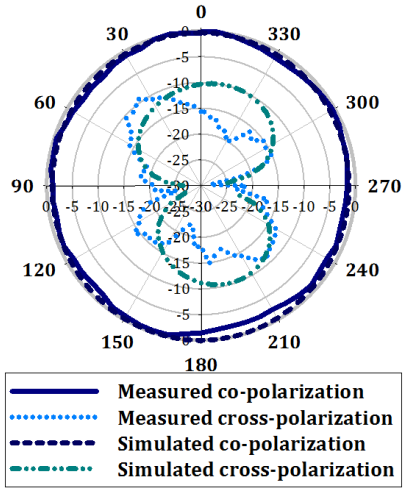
Figure 4.15 shows the measured and simulated gains of this antenna. At 0.887 GHz, the simulated gain is -2.358 dBi, whereas the measured gain is -3.38 dBi. The antenna gain is low at 0.887 GHz, due to the electrically small size of the loop part in the RA structure. At 0.887 GHz, the current mainly flows around this loop part, which is shown in Figure 4.16(a). This results in low radiation efficiency and low gain. However, according to the simulations, the antenna gain and the radiation efficiency will be improved at higher frequencies. According to the simulation, the antenna gain using this operating resonance will be improved to be -1.7 dB at 0.96 GHz.



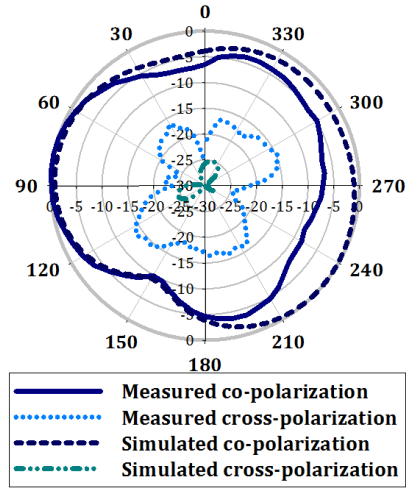
(a)



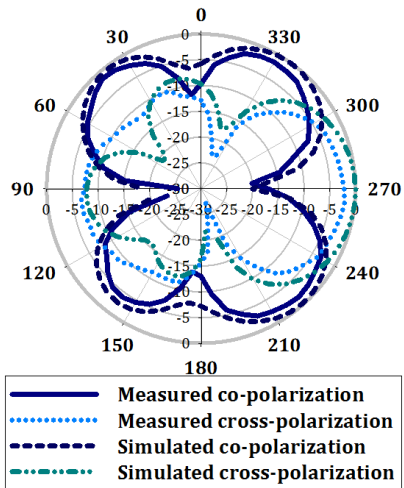
(b)



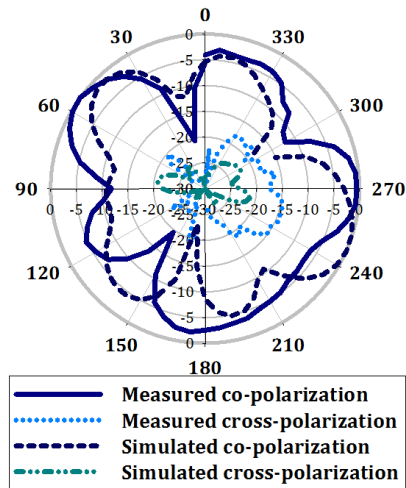
(c)



(d)



(e)



(f)

Figure 4.17 Measured and simulated normalized farfield patterns of this RA for co-polarization and cross-polarization, (a) YOZ plane at 0.887 GHz; (b) XOY plane at 0.887 GHz; (c) YOZ plane at 2.4 GHz; (d) XOY plane at 2.4 GHz; (e) YOZ plane at 5.5 GHz; (f) XOY plane at 5.5 GHz.

Figure 4.17 presents the simulated and measured normalized farfield radiation patterns at the YOZ and XOY planes for 0.887, 2.4, and 5.5 GHz. Similarly, the proposed antenna presents the omnidirectional patterns at 0.887 GHz and 2.4 GHz. At 5.5 GHz, the patterns are not omnidirectional, due to a combination of multiple radiation parts in the RA structure, which is shown in Figure 4.16(b).

The differences between the simulated and measured results in Figure 4.14, Figure 4.15 and Figure 4.17 can be mainly summarized as the following reasons:

- (1) The fabrication and measurement deviations;
- (2) the loss resulting from soldering;

#### 4.4.2 Analysis of passive RA with IDSs

Table 4.5 Component values in the equivalent circuit model of this RA with IDSs.

Symbol	Values (pF)	Symbol	Values (nH)
C01	0.35	Lhs1	1.2
C02	0.32	Lhs2	2.8
C03	0.25	Lhp	9.3
C04	0.27	L1	7.8
Chp	1.7	Lvs1	6.2
Chs	0.48	Lvs2	10.8
Cvs	1.9	Lvp1	11.1
Cvp	0.85	Lvp2	13.6

Similarly, the equivalent circuit model of the proposed RA with IDSs can also be represented as the model shown in Figure 4.9, but with different component values.

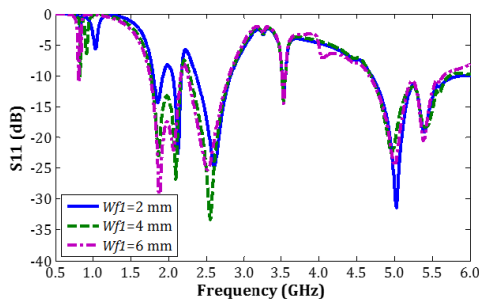
The component values in this model are listed in Table 4.5. The component values in this equivalent model are extracted by the similar steps as the ones in Section 4.3. In addition, the capacitance for one IDS can be derived using the full-wave simulation.

After getting the full-wave simulated S parameters of an IDS, the total capacitance can be approximately derived using the equation of  $C = -1/[\omega \cdot \text{Im}(Y_{11})]$ , where  $\omega$  is the angular frequency and  $Y_{11}$  is an element in Y parameters [55].

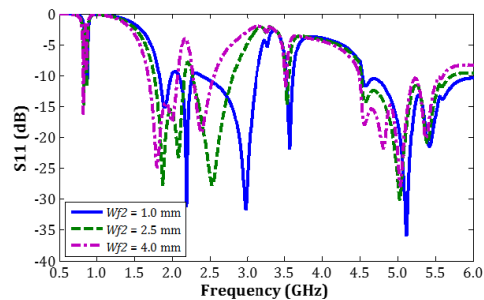
The circuit-model simulated S11 (brown dot dash line) is also presented in Figure 4.14. The differences between the circuit-model and full-wave simulated results are due to the same reasons as the case in Section 4.3. Besides, the parasitic inductance in each IDS is not taken into consideration in this equivalent model, which may contribute to the differences.

Table 4.6 Some parts of the RA with IDSs and the operating resonances correspondingly controlled by each part.

Symbol	No. of Operating Resonances Controlled
$Wf1$	1st and 2nd
$Wf2$	2nd, 3rd, 4th, and 7th
$Wf3$	3rd, 4th, 5th, 6th, 9th, and 10th
$L1$	2nd, 3rd, 4th, 7th, 8th, and 9th
$L3$	2nd, 3rd, 4th, 6th, 8th, and 9th
$L6$	3rd, 4th, 6th, 8th, 9th, and 10th
$L7$	1st, 2nd, 3rd, 6th, 9th, and 10th
$W2$	1st, 4th, 7th, 8th, 9th, and 10th
$W3$	1st, 5th, 7th, 8th, and 10th



(a)



(b)

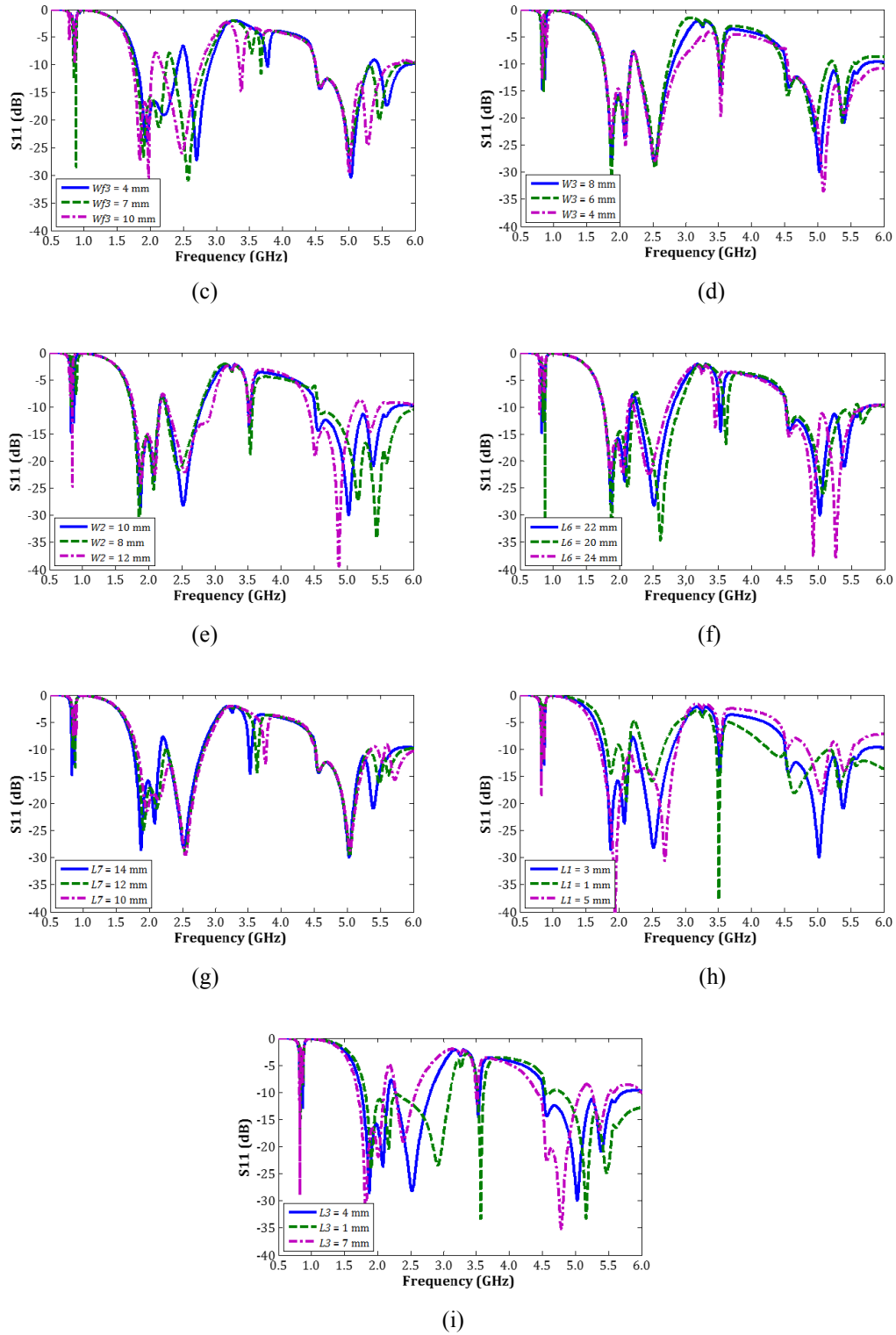


Figure 4.18 Effects of the dimension changing of the part of the antenna structure on the frequency response of the antenna, (a)  $Wf1$ ; (b)  $Wf2$ ; (c)  $Wf3$ ; (d)  $W3$ ; (e)  $W2$ ; (f)  $L6$ ; (g)  $L7$ ; (h)  $L1$ ; (i)  $L3$ .

In this RA, different parts of the antenna structure have different effects on the frequency response of this antenna. The effects on the frequency response by

changing some important parts of the structure (e.g.,  $Wf1$ ,  $Wf2$ , and  $Wf3$ ) are shown in Figure 4.16. As examples, Figure 4.16(a) shows that the dimension changing of the finger length for the IDS of  $C_{hp}$  (i.e.,  $Wf1$ ) mainly affects the 1st and 2nd operating resonances. Figure 4.16(b) shows that the dimension changing of the finger length for the IDS of  $C_{hs}$  (i.e.,  $Wf2$ ) mainly affects 2nd, 3rd, 4th, and 7th operating resonances. However, the changing of  $Wf2$  does not destroy the frequency coverage from 4.5 GHz to 6 GHz. In Figure 4.16(c), it shows that the dimension changing of the finger length for the IDS of  $C_{vs}$  (i.e.,  $Wf3$ ) mainly affects 3rd, 4th, 5th, 6th, 9th, and 10th operating resonances. However, the dimension changing of  $Wf3$  does not affect the frequency coverage of 1.71-2.69 GHz and 4.5-6 GHz. The summary of the operating resonances controlled by some important parts of the antenna structure is presented in Table 4.6. According to this summary, it may be possible to design a tunable RA using the phenomenon in Figure 4.18(a), in order to realize the frequency tunability of one operating resonance at the low frequency without destroying the wideband coverage formed by the other operating resonances.

#### **4.4.3 Comparison with A Conventional Monopole Antenna**

For comparison, a conventional monopole antenna within similar space is realized on the same substrate material. The configuration of this monopole antenna is shown in Figure 4.19, and the detailed dimensions of this monopole antenna are listed in Table 4.7. Figure 4.20 presents the comparison between full-wave simulated S11 results of the RA with IDSs and this monopole antenna. The lowest working frequency of the RA is at 0.887 GHz, while that of the conventional monopole

antenna is 1.1 GHz. Thus, the proposed RA can work at a lower frequency compared to this conventional monopole antenna within the similar space. Furthermore, this RA has ten operating resonances to achieve multiband coverage. However, this conventional monopole antenna only has three operating resonances over 0.5-6 GHz.

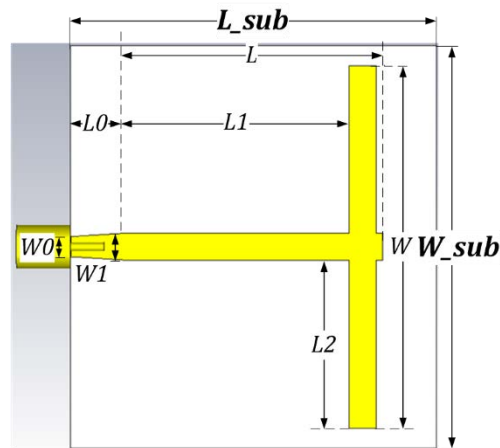


Figure 4.19 Configuration of a conventional monopole antenna.

Table 4.7 Dimensions of a conventional monopole antenna.

Symbol	Dimension (mm)	Symbol	Dimension (mm)
$L_{sub}$	56	$W_{sub}$	64
$L$	43	$W$	60
$L0$	8	$W0$	3
$L1$	38	$W1$	4
$L2$	28		

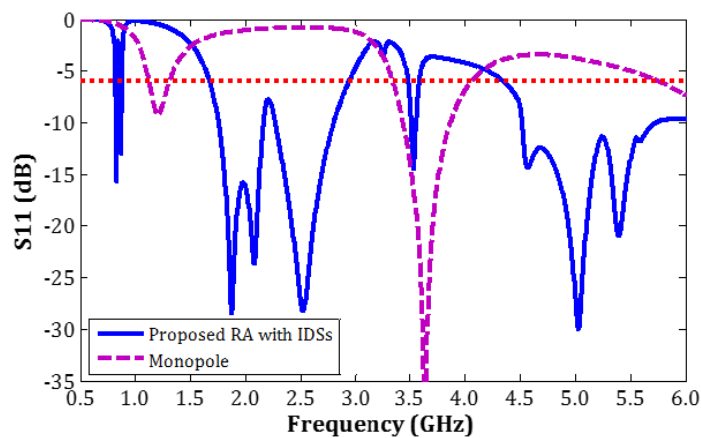


Figure 4.20 Comparison of S11 results between the RA with IDSs and this monopole antenna.



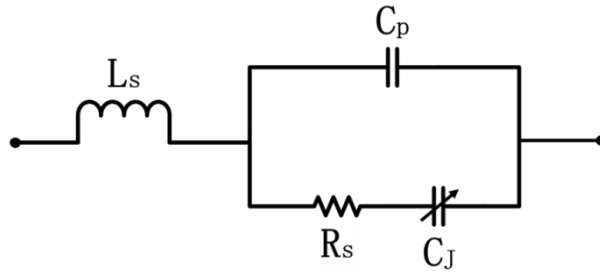
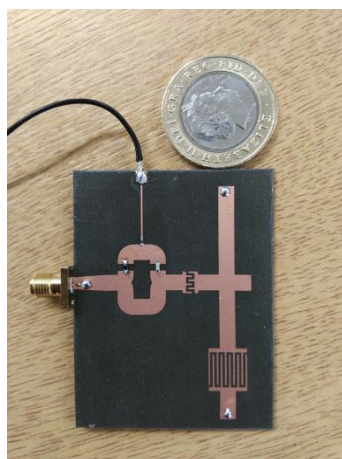


Figure 4.22 Equivalent circuit model of *MICROSEMI MV34002* semiconductor varactor.

Table 4.8 Dimensions of the tunable antenna with one varactor.

Symbol	Dimension (mm)	Symbol	Dimension (mm)
$L_{sub}$	45	$W_{sub}$	60
$L$	36	$W$	57.5
$L0$	6	$W0$	3
$L1$	3	$W1$	4
$L2$	10	$W2$	4
$L3$	4	$W3$	6
$L4$	4	$Lc1$	4
$L5$	10	$Lc3$	10.5
$L6$	22	$Wg$	0.5
$L7$	14	$Ws$	0.5
$L8$	7	$Wp$	1
$L9$	2	$Wf2$	1.5
$L10$	3.5	$Wf3$	8
$L11$	58.5		



(a)



(b)

Figure 4.23 Configurations of the tunable RA with one varactor, (a) top view; (b) rear view.

Same as the previous RAs, this proposed RA is also designed on a *Rogers RT/duroid 5880* substrate with dielectric constant of 2.2, loss tangent of 0.0009 and thickness of 1.575 mm. Figure 4.20 shows the configurations of this RA. In this antenna structure,  $C_{hs}$  and  $C_{vs}$  are realized by the IDSs, which are shown in Figure 4.21(c) and Figure 4.21(d), respectively. In order to achieve the frequency tunability of one operating resonance,  $C_{hp}$  is chosen as the tuning element and is realized by a combination of one SMD GaAs semiconductor varactor and one DC block 0603 10 pF chip capacitor. This semiconductor varactor used in the structure for  $C_{hp}$  is *MICROSEMI MV34002*. The equivalent circuit model of this varactor is briefly presented in Figure 4.22. In this circuit model,  $L_s$  and  $C_p$  represent the parasitic inductance and capacitance resulting from the packaging, respectively, and  $R_s$  is used to represent the equivalent resistance mainly resulting from the semiconductor [56].  $C_J$  represents the tunable capacitance for the tuning function of the varactor [56]. The brief information of *MICROSEMI MV34002* semiconductor varactor and the relationship between  $C_t$  and the reverse voltage are included in Appendix B. The varactor is biased by one DC bias line with one 0402 1 M $\Omega$  resistor as the RF block. In experiments, a bias Tee is used to connect with the feed line in order to supply the negative “-” bias voltage, while the positive “+” bias voltage is supplied through a DC bias line. The overall size of the proposed antenna is 45 mm  $\times$  60 mm  $\times$  1.575 mm. The detailed dimensions of this tunable antenna and its two IDSs are listed in Table 4.8. The photographs of this fabricated tunable antenna are shown in Figure 4.23.

### 4.5.1 Simulation and Measurement

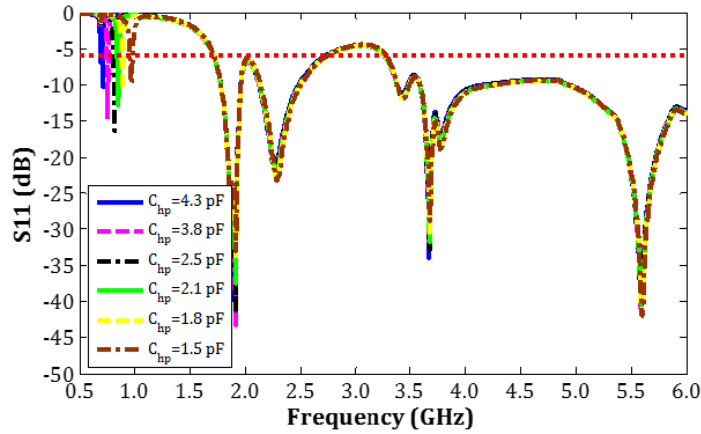


Figure 4.24 Simulated S11 of the RA with different capacitances of  $C_{hp}$ .

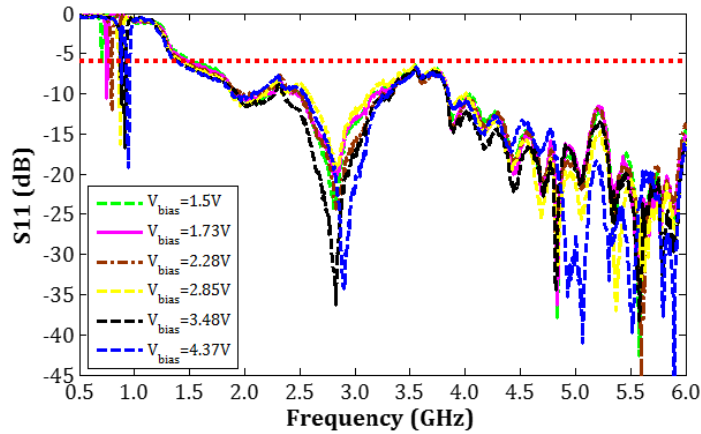


Figure 4.25 Measured S11 of the RA by applying different DC bias voltages to the varactor.

Figure 4.24 presents the full-wave simulated S11 of the RA by changing the capacitance of  $C_{hp}$  from 4.3 pF to 1.5 pF, which shows that one operating resonance at the low frequency can be tuned to cover the entire 4G LTE low band from 0.7 GHz to 0.96 GHz without affecting the wideband coverage over 1.7-6.0 GHz formed by the other operating resonances. In simulations,  $C_{hp}$  represents  $C_J$  in the equivalent circuit model shown in Figure 4.22. According to Appendix B, the other component values used in simulations are  $R_s \approx 1.415 \Omega$ ,  $L_s = 0.45 \text{ nH}$ , and  $C_p = 0.1 \text{ pF}$ , respectively.

Figure 4.25 presents the measured S11 results of this tunable RA, which demonstrates that the 4G LTE low band over 0.7-0.96 GHz is covered by one electronically tunable operating resonance at the low frequency with different DC bias of 1.5-4.37 V applied to the varactor for  $C_{hp}$ . A wide frequency band covering 1.7-6.0 GHz is formed by the other operating resonances, with respect to the -6 dB bandwidth. The measured results show that the electronic tunability of one operating resonance over 0.7-0.96 GHz does not destroy the frequency coverage of the wide band of 1.7-6 GHz. Thus, this antenna has potentials for 4G LTE applications for most modern commercial frequency bands.

The measured and simulated normalized farfield patterns at 0.7 GHz with 1.5 V bias voltages, 0.85 GHz with 2.85 V bias voltages and 0.96 GHz with 4.37 V bias voltages are shown in Figure 4.26, respectively. Figure 4.26 shows that the measured farfield patterns at 0.7 GHz, 0.85 GHz, and 0.96 GHz are quasi-omnidirectional and are close to omnidirectional. Figure 4.27 shows the measured and simulated normalized farfield patterns of the tunable antenna with 2.85 V bias for 2.4 GHz and 5.5 GHz as examples. Based on the results, this tunable antenna presents the quasi-omnidirectional patterns at the low frequencies over 0.7-0.96 GHz, and the omnidirectional patterns at 2.4 GHz, but the non-omnidirectional patterns at the high frequencies, e.g., 5.5 GHz. The non-omnidirectional patterns at the high frequencies result from a combination of the multiple radiation parts in the antenna structure.

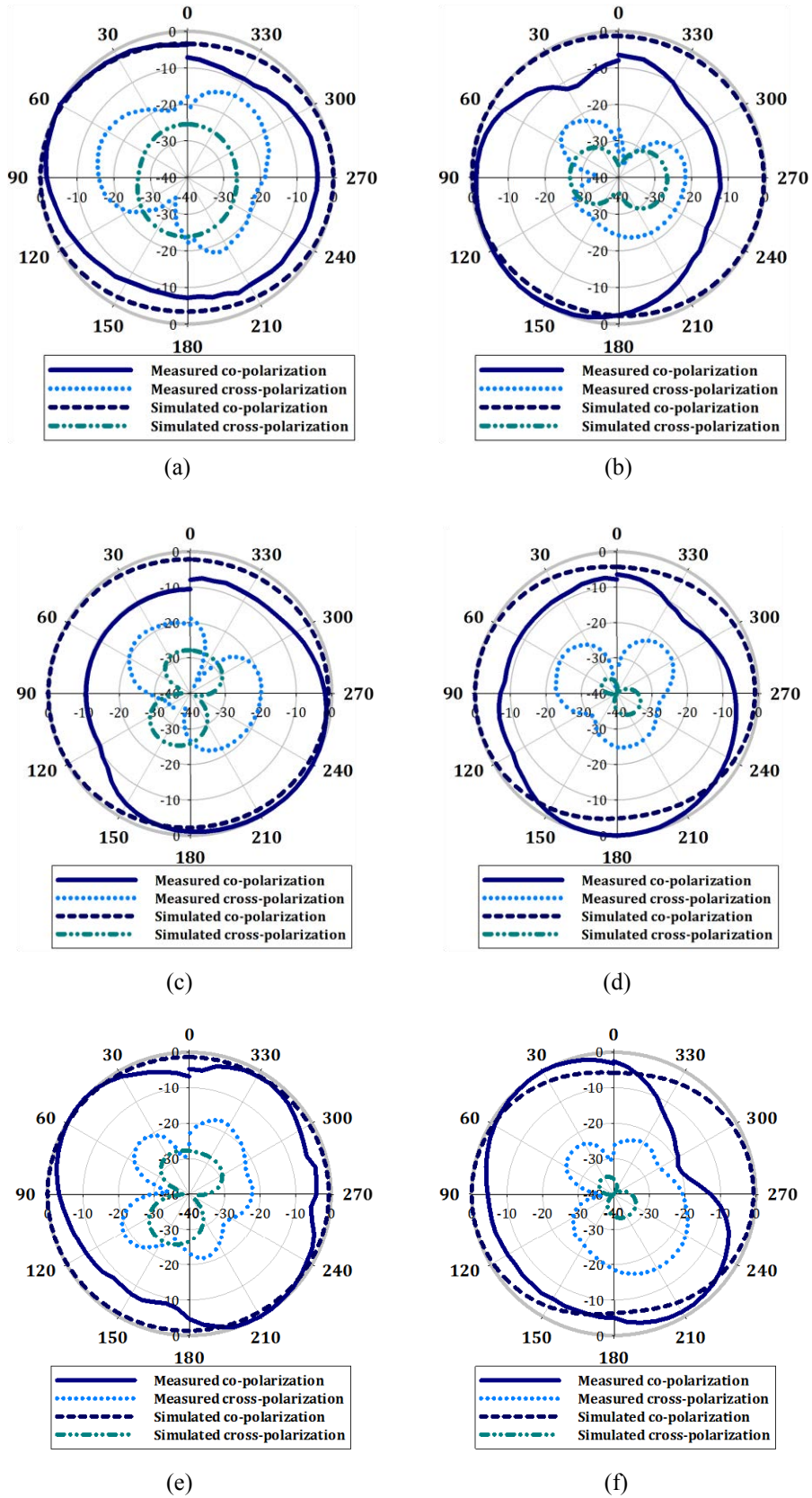


Figure 4.26 Measured and simulated normalized patterns of the tunable RA for co-polarization and cross-polarization, (a) YOZ plane at 0.7 GHz with 1.5 V; (b) XOY plane at 0.7 GHz with 1.5 V; (c) YOZ plane at 0.85 GHz with 2.85 V; (d) XOY plane at 0.85 GHz with 2.85 V; (e) YOZ plane at 0.96 GHz with 4.37 V; (f) XOY plane at 0.96 GHz with 4.37 V.

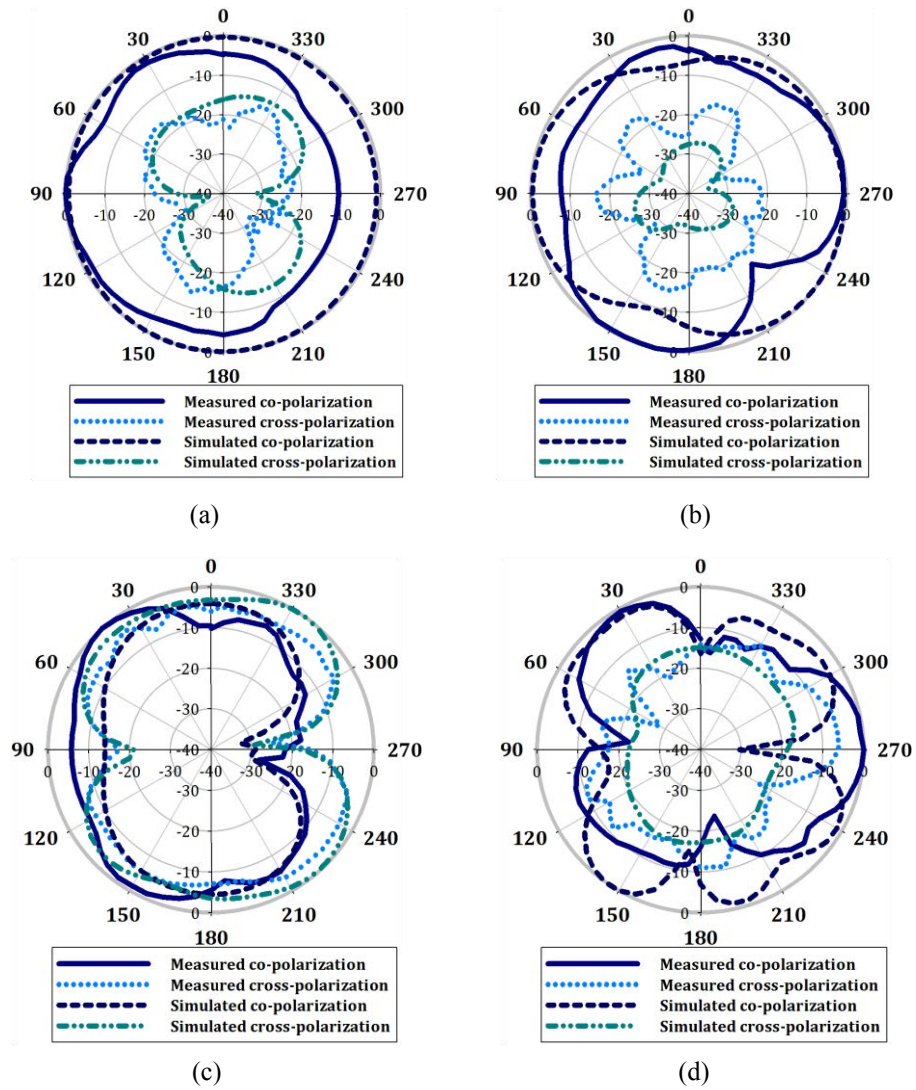


Figure 4.27 Measured and simulated normalized patterns of the tunable RA with 2.85 V bias voltage for co-polarization and cross-polarization, (a) YOZ plane at 2.4 GHz; (b) XOY plane at 2.4 GHz; (c) YOZ plane at 5.5 GHz; (d) XOY plane at 5.5 GHz.

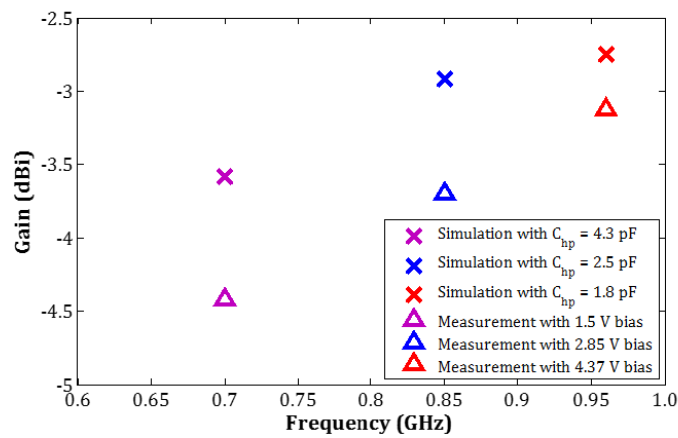


Figure 4.28 Simulated and measured gains of the tunable RA with different bias voltages at 0.7 GHz, 0.85 GHz, and 0.96 GHz.

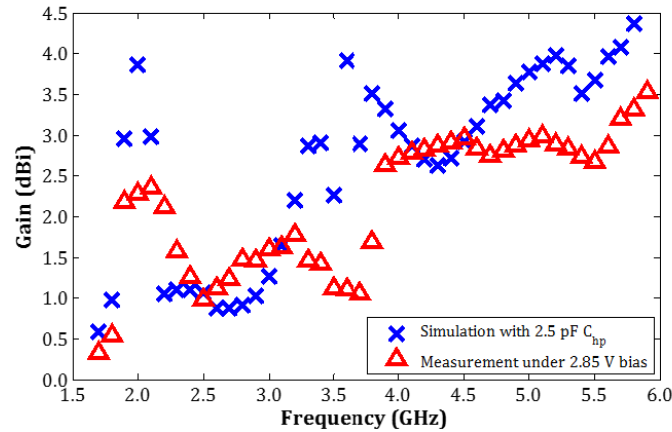


Figure 4.29 Simulated and measured gains of the tunable RA over 1.7-6.0 GHz with 2.85 V DC bias.

The measured and simulated gains of this antenna with 1.5 V, 2.85 V and 4.37 V bias voltages at 0.7 GHz, 0.85 GHz, and 0.96 GHz are presented in Figure 4.28. This RA suffers from low gain at low frequency, e.g. 0.7 GHz, which is due to the same reason as two previous RA designs, i.e., the electrically small size of the loop part in the antenna structure. According to the simulated and measured results, antenna gains are improved at higher frequencies, e.g., 0.96 GHz. Figure 4.29 shows the measured and simulated gains of this tunable RA over 1.7-6.0 GHz under 2.85 V DC bias voltages as an example. The differences between the measured and simulated results for this active RA mainly come from four reasons:

- (1) the measurement deviations;
- (2) the loss resulting from soldering;
- (3) the parasitic effects and losses from the SMD components, such as the resistor and the varactor, particularly the varactor. Some parasitic effects and losses from the varactor are the main contributor to the differences in the full-wave simulated and measured S parameters, gains and farfield patterns.

## 4.5.2 Loss Analysis of Varactor

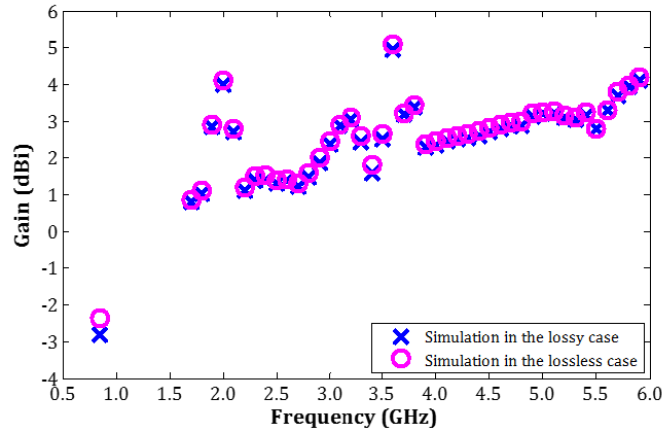


Figure 4.30 Comparison of the simulated gains of the tunable RA with a lossy and lossless equivalent circuit model of the varactor with  $C_{hp}$  of 2.5 pF.

The SMD *MICROSEMI MV34002* semiconductor varactor, as a lossy component in this RA design, introduces a certain amount of losses to degrade the antenna radiation performance. The losses introduced by this varactor are evaluated in simulations by comparing the antenna gains in the lossy and lossless case. The case of this tunable RA with  $C_{hp}$  of 2.5 pF is taken as an example. In the lossy case, the antenna is simulated with the equivalent model of the varactor shown in Figure 4.22. In this equivalent model,  $R_s$  is used to represent the equivalent resistance mainly resulting from the semiconductor [56], and  $R_s \approx 1.415 \Omega$  according to Appendix B. In the lossless case, this equivalent resistance (i.e.,  $R_s$ ) in the equivalent model of the varactor is removed, in order to avoid any losses in the model. Thus, this equivalent model of the varactor becomes the lossless and ideal in this case. Figure 4.30 presents the comparison of the simulated gains of this tunable RA with the lossy (blue crossing) and lossless (pink circle) equivalent model of the varactors. It shows that the antenna gains achieve -2.36 dBi at 0.85 GHz, 1.52 dBi at 2.4 GHz, and 2.7 dBi at 5.5 GHz in

the lossless case. For comparison, the antenna gains are -2.82 dBi at 0.85 GHz, 1.4 dBi at 2.4 GHz, and 2.8 dBi at 5.5 GHz. Thus, it can be estimated that this semiconductor varactor introduces around 0.1-0.8 dB losses to degrade the antenna radiation performance depending on frequencies.

## 4.6 Summary

Table 4.9 Summary of the RAs in this chapter.

	<b>RA with SMD Capacitors</b>	<b>RA with IDSs</b>	<b>RA with One Varactor</b>
Antenna Dimensions	47 mm × 55 mm × 1.575 mm	56 mm × 64 mm × 1.575 mm	45 mm × 60 mm × 1.575 mm
Frequency Coverage	0.707 GHz; 1.7~3 GHz; 4.5~6 GHz	0.887 GHz; 1.7~3 GHz; 3.3~3.4 GHz; 3.52~3.59 GHz 4.5~6 GHz	0.7~0.96 GHz; 1.7~6 GHz
Measured Gain Range	-3.55~3.42 dB	-3.38~4.2 dB	-4.32~3.5 dB
Pattern Type	Omnidirectional at 0.707 and 2.4 GHz; Non-omnidirectional at 5.5 GHz	Omnidirectional at 0.887 and 2.4 GHz; Non-omnidirectional at 5.5 GHz	Omnidirectional at 0.7~0.96 GHz and 2.4 GHz; Non-omnidirectional at 5.5 GHz
Antenna Characteristics	Tri-band characteristics	Multiband characteristics	Electronic tunability of a narrow band over 0.7~0.96 GHz; A broad band over 1.7~6 GHz

A class of the open-ended RAs based on one ECRLH unit cell structure is presented for multiband or frequency-agile applications. The RAs can generate multiple operating resonances with excitation by a short microstrip feeding line. The passive RAs can achieve multiband properties. In addition, compared to one conventional monopole antenna occupying similar space, the passive RA with IDSs has at least one operating resonance working at lower frequency. Based on the explorations of the resonance control by the part of  $C_{hp}$  in the RA structures, an electronically tunable RA with one semiconductor varactor is designed to achieve the frequency tunability over

0.7-0.96 GHz by one operating resonance at the low frequency and maintain the wideband coverage over 1.7-6.0 GHz formed by the other operating resonances. The summary of the RAs in this chapter is listed in Table 4.9. Compared to most existing RA designs introduced in Section 3.2 of Chapter III, the RAs in this class can generate more operating resonances working at the chosen frequency bands. In addition to the multiband properties, the tunable RA design achieves the electronically controlled frequency tunability of one operating resonance at low frequency while keeping the wideband coverage formed by the other operating resonances.

# CHAPTER V

## DUAL-BAND LEAKY WAVE ANTENNAS BASED ON METAMATERIAL-INSPIRED TRANSMISSION-LINE STRUCTURES

### 5.1 Introduction

In past decades, LWAs have attracted significant research interest due to their advantageous features: (1) the main beam steered by the variation of the operation frequency; (2) relatively low profile; (3) low cost for fabrication; (4) single or multiple high directivity beams depending on feeding methods.

Since the theory of the metamaterial CRLH structure was proposed in [8], many LWAs have been designed based on metamaterial-inspired structures. In recent years, LWAs with multiband properties have aroused a lot of research interest. A conventional approach for metamaterial-inspired LWAs to achieve multiband properties is to use different intrinsic harmonic modes of the antenna structure. However, the disadvantage of this approach is that the multiple passbands of the LWA cannot be controlled independently. Specifically, when one passband shifts, the other

passbands will shift as well. The ECRLH structure [12] can enable LWAs to achieve the multiband properties. The equivalent model of the ECRLH structure has been shown in Figure 4.1. There are four L-C resonators in the model with adding one parallel L-C resonator in the horizontal branch and one series L-C resonator in the vertical branch of the conventional CRLH unit cell structure. Theoretically, the ECRLH structure can generate two pairs of LH and RH bands. The component designs can utilize combinations of these LH and RH bands in different operation conditions (i.e., balanced and unbalanced conditions) for dual-band, tri-band, quad-band or even multiband applications.

In [36], a SIW LWA based on the ECRLH structure composing of 1-D cascaded unit cells is presented for dual-band applications with simultaneous filtering characteristics. This LWA utilizes the balanced condition of the ECRLH structure to achieve two distinct passbands. The main beam of this antenna would be scanned from the backward (LH band) to forward (RH band) direction through broadside smoothly. The main advantages of this LWA can be summarized as followings: (1) two distinct complete passbands can be generated respectively at low and high frequencies with separation of one middle bandgap; (2) the CRLH backward-to-forward leaky-wave radiation characteristics can be found in both passbands. However, notably, the CRLH radiation characteristics happen at the low edge of the passband at high frequencies. This will easily result in the unexpected disappearance of the CRLH characteristics within this passband and the loss of the backward-to-forward leaky-wave radiation characteristics within this passband, if the LWA design is inappropriate.

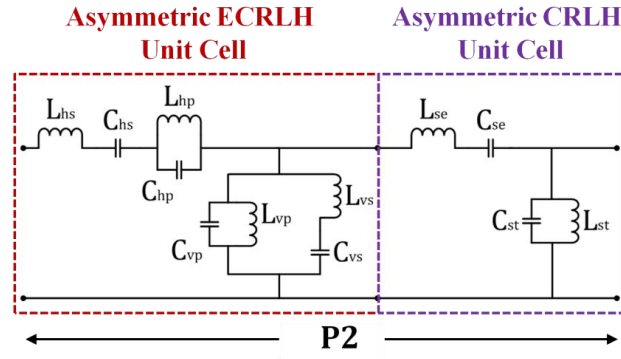


Figure 5.1 Simplified equivalent circuit model of one *Supercell\_v1* structure.

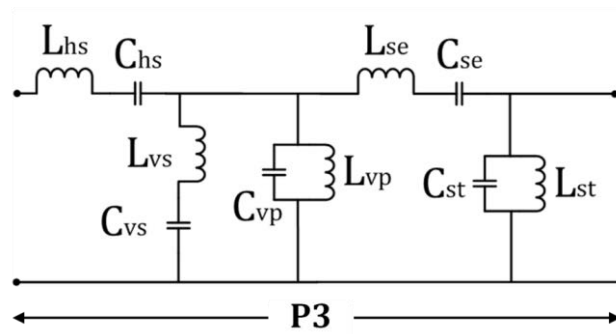


Figure 5.2 Simplified equivalent circuit model of one *Supercell\_v2* structure.

In this chapter, four LWA designs based on metamaterial-inspired structures are presented to achieve the dual-passband characteristics. The first LWA is designed based on the ECRLH structure with SMD chip capacitors. This LWA design demonstrates the phenomenon that the conventional CRLH backward-to-forward leaky-wave radiation characteristic disappears within its high passband. According to the observation that this LWA does not achieve the CRLH backward-to-forward leaky-wave radiation characteristics within its high passband, two LWAs respectively based on the *Supercell\_v1* and *Supercell\_v2* structure are proposed to improve this leaky wave radiation status and achieve the CRLH backward-to-forward leaky-wave radiation characteristics within both passbands. The simplified equivalent models of one single *Supercell\_v1* and *Supercell\_v2* structure are shown in Figure 5.1 and

Figure 5.2, respectively. The *Supercell\_v2* structure is developed from the *Supercell\_v2* structure by removing the  $L_{hp}$ - $C_{hp}$  resonator. In addition, an electronically tunable LWA based on the *Supercell\_v2* structure is proposed to achieve the relatively independent tunability of the low balanced point while keeping the frequency position of the high balanced point and maintaining the CRLH backward-to-forward leaky-wave radiation characteristics within its high passband.

This chapter is organized as follows. In Section 5.2, a microstrip LWA based on 14 cascaded ECRLH unit cells with SMD chip capacitors is presented. In Section 5.3, by following the analysis of the metamaterial-inspired *Supercell\_v1* structure using the TL approach, a microstrip LWA based on 6 cascaded *Supercell\_v1* structures is presented. In Section 5.4, a microstrip LWA based on 7 cascaded *Supercell\_v2* structures with SMD chip capacitors is introduced for the initial theoretical demonstration; an electronically tunable LWA based on the *Supercell\_v2* structure with integration of SMD silicon semiconductor varactors is proposed to investigate its frequency tunability in this section. Finally, the summary is given in Section 5.5.

## **5.2 Passive LWA Design Based On ECRLH Structure**

In this section, a microstrip LWA is designed based on the ECRLH structure with SMD chip capacitors. The substrate material is *Rogers RT/duroid 5880* with dielectric constant of 2.2, loss tangent of 0.0009 and thickness of 1.575 mm. The ECRLH TL structure is composed of 14 cascaded ECRLH unit cells. The configuration of one

ECRLH unit cell structure is shown in Figure 5.3. In this unit cell structure,  $C_{hs}$ ,  $C_{hp1}$ ,  $C_{hp2}$ ,  $C_{vs}$ , and  $C_{vp}$  are realized by the SMD *MURATA 0402* chip capacitors, which are 3.8 pF, 20 pF, 4.1 pF, 1.5 pF, and 0.1 pF, respectively. The information of *MURATA 0402* chip capacitors is shown in Appendix A. The dimensions of this unit cell structure are listed in Table 5.1. This antenna is simulated in the software *CST Microwave Studio* and then fabricated for antenna measurements. A photograph of the fabricated LWA with 14 cascaded ECRLH unit cells is shown in Figure 5.4. The total length and width of this LWA are 280.4 mm and 50 mm, respectively.

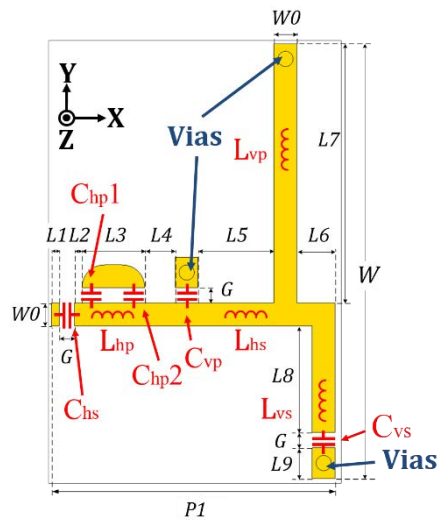


Figure 5.3 Configuration of one asymmetric ECRLH unit cell structure.

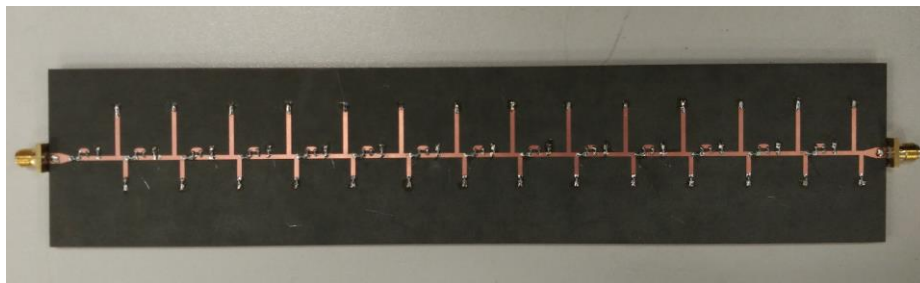


Figure 5.4 Photograph of the fabricated LWA with 14 ECRLH unit cells.

Table 5.1 Dimensions of one ECRLH unit cell structure.

Symbol	Dimension (mm)	Symbol	Dimension (mm)
$P1$	18.6	$W$	28.5
$L1$	0.5	$W0$	1.5
$L2$	0.5	$G$	1
$L3$	4.1	$L7$	17
$L4$	2	$L8$	7
$L5$	5	$L9$	2
$L6$	2.5		

### 5.2.1 Measurement Results

The simulated and measured results of S11 and S21 of this LWA are shown in Figure 5.5. It shows that two distinct passbands at the low and high frequencies are formed separated by a middle bandgap. These two passbands at the low and high frequencies are called the low and high passbands, respectively. With respect to the -6 dB bandwidth, the low passband is over 0.6-1.55 GHz, while the high passband is over 3.1-6.5 GHz.

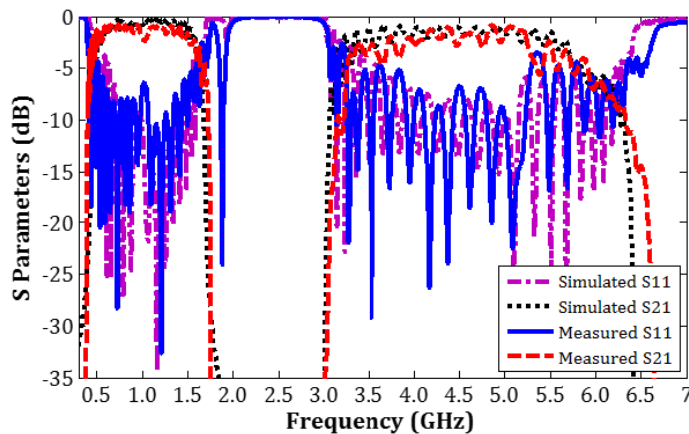


Figure 5.5 Simulated and measured S11 and S21 of the passive LWA with 14 ECRLH unit cells.

The leaky-wave radiation characteristics of this LWA within the low and high passband are further investigated. Figure 5.6 shows the measured and simulated normalized co-polarized farfield leaky-wave radiation patterns at the XOZ plane of

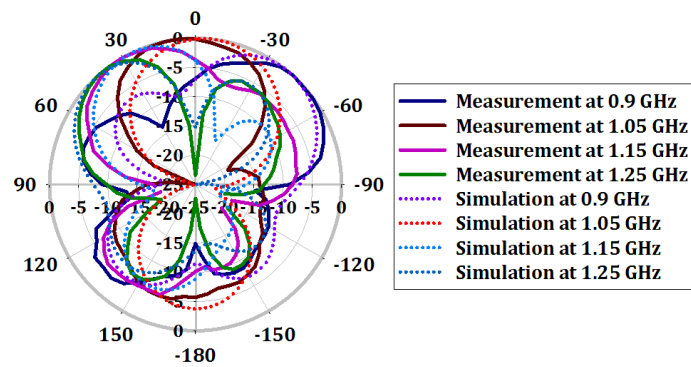
this LWA within the two passbands. Figure 5.6(a) shows, within the low passband, the main beam scans from  $-42^\circ$  to  $+36^\circ$  over 0.9-1.25 GHz. However, the farfield leaky-wave radiation characteristics within the high passband are different from the low passband. The forward (RH band) leaky-wave radiation happens in the low-edge region of the high passband, while the backward (LH band) leaky-wave radiation happens in the high-edge region of the high passband. The simulated and measured co-polarized normalized farfield leaky-wave radiation patterns within the high passband are shown in Figure 5.6(b) and Figure 5.6(c), respectively. Figure 5.6(b) shows the leaky-wave radiation of this antenna is from  $+12^\circ$  to  $+60^\circ$  over 3.1-3.6 GHz, which is at the low edge of the high passband. In Figure 5.6(c), the main beam scans from  $-80^\circ$  to  $-24^\circ$  over 5.7-6.2 GHz, which happens at the high edge of the high passband. There is no smooth transition from the backward to forward direction through broadside with the high passband. Within the high passband, there is a stopband area between these two leaky-wave regions, so there is no leaky wave radiation in this area. The reason for this will be explored in Section 5.2.2.

The measured and simulated gains of this antenna at the leaky-wave regions are shown in Figure 5.7. In experiments, this LWA achieves the peak gain of -10.2 dBi within the low passband. Within the high passband, the measured peak gains of -1.8 dBi and 8.5 dBi are achieved at the RH and LH leaky-wave regions, respectively.

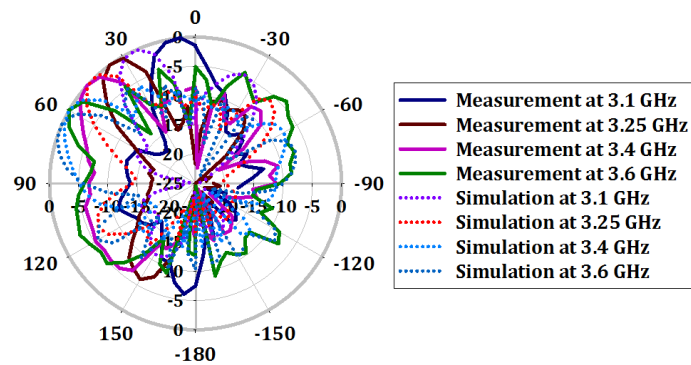
The differences between the full-wave simulated and measured results in Figure 5.5, Figure 5.6, and Figure 5.7 are summarized as the following reasons:

(1) the fabrication and measurement deviations;

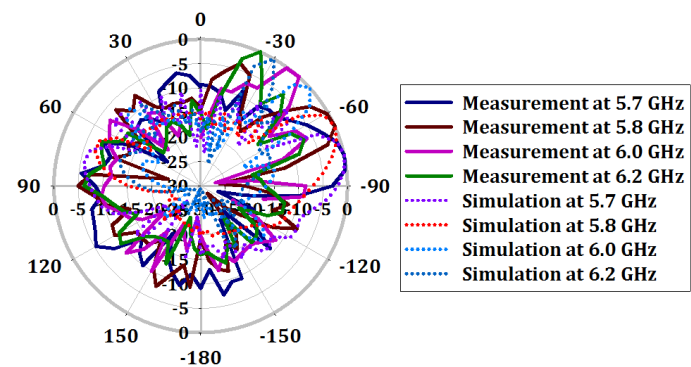
(2) the loss resulting from soldering;



(a)



(b)



(c)

Figure 5.6 Normalized simulated and measured co-polarized farfield leaky-wave radiation patterns at the XOZ plane within two passbands, (a) 0.9-1.25 GHz; (b) 3.1-3.6 GHz; (c) 5.7-6.2 GHz.

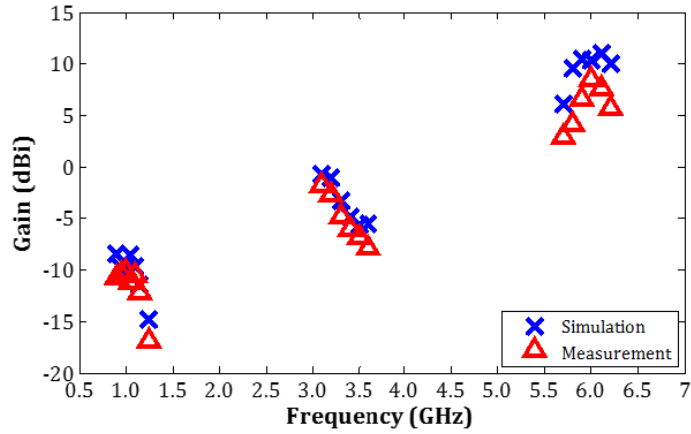


Figure 5.7 Simulated and measured gains in dBi of this passive LWA at the leaky-wave regions.

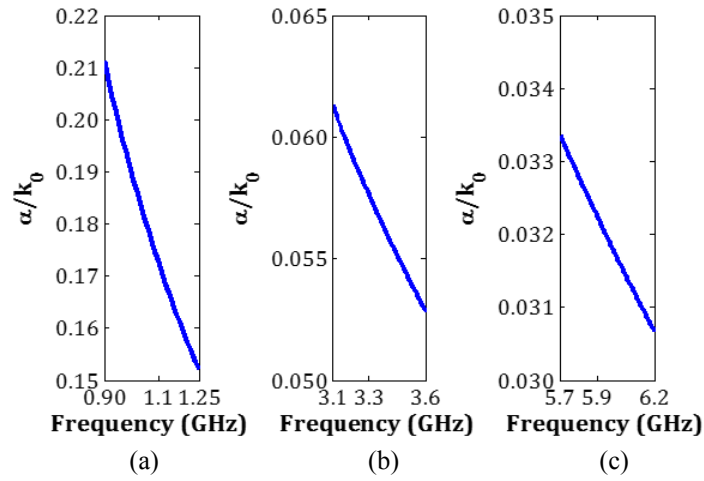


Figure 5.8 Leakage rates of this LWA at the leaky-wave regions, (a) 0.9-1.25 GHz; (b) 3.1-3.6 GHz; (c) 5.7-6.2 GHz.

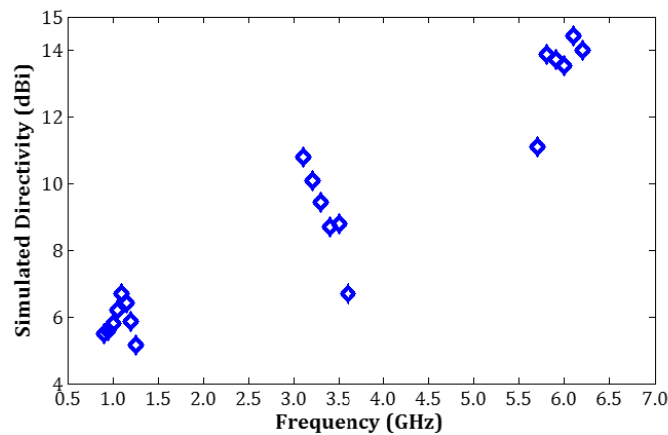


Figure 5.9 Simulated directivities of this LWA at the leaky-wave regions within both passbands.

According to the results shown in Figure 5.7, this LWA suffers from low gains, particularly at low frequencies, because most of the accepted power by this antenna is

absorbed by an absorption load at one end of the LWA structure, and just a small amount of power is radiated. This is due to the limitation of the printed circuit board (PCB) size which results in an ineffective antenna aperture and high leakage rates [4].

The leakage rates of this LWA can be approximately calculated by

$$\alpha/k_0 \approx (0.18\lambda_0)/L \quad \text{Eq. (5-1)}$$

where  $L$  is the entire physical length of the LWA,  $L = N \cdot P1$ ,  $P1$  is the period of the ECRLH unit cell,  $N$  is the number of the unit cells in the LWA structure,  $k_0$  is the wave-number in the free space, and  $\lambda_0$  is the wavelength in free space. The leakage rates of this LWA at the leaky-wave regions are shown in Figure 5.8. The antenna gains could be improved by cascading more ECRLH unit cells in the structure. In simulations, a LWA with 50 ECRLH unit cells can achieve the peak gains of 1.2 dBi within the low passband, and 10.2 dBi and 17.5 dBi respectively for the RH and LH leaky wave regions within the high passband. The simulated directivities of this LWA are presented in Figure 5.9.

### 5.2.2 Analysis of One ECRLH TL Unit Cell

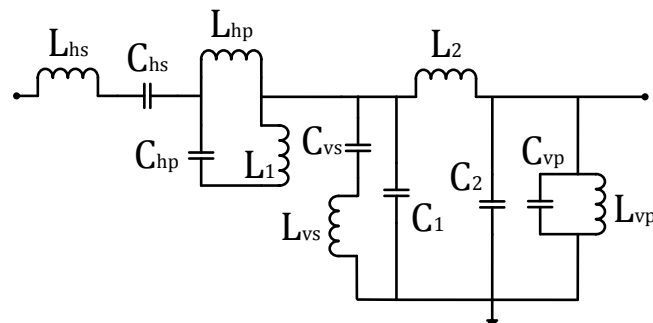
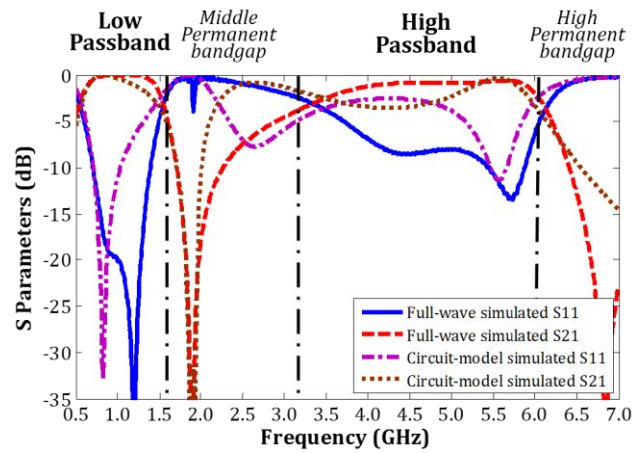


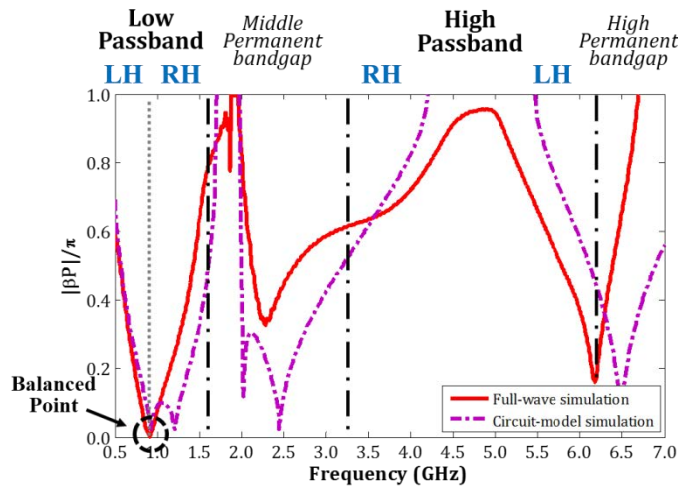
Figure 5.10 Equivalent circuit model of one ECRLH unit cell structure.

Table 5.2 Component values used in the equivalent circuit model of one ECRLH unit cell structure.

Symbol	Values (pF)	Symbol	Values (nH)
$C_{hp}$	3.4	$L_{hs}$	2.6
$C_{hs}$	3.8	$L_{hp}$	0.7
$C_{vs}$	1.5	$L_{vs}$	4.5
$C_{vp}$	0.1	$L_{vp}$	5.4
$C_1$	1.3	$L_1$	1.1
$C_2$	1.4	$L_2$	1.4



(a)



(b)

Figure 5.11 Full-wave and circuit-model simulated performances of one ECRLH unit cell in the antenna structure, (a) the frequency response; (b) the dispersion diagram.

The dispersion relation of one unit cell can be used to investigate the leaky-wave radiation characteristics of the LWA. The equivalent circuit model of one ECRLH unit cell structure is developed in Figure 5.10. Compared to the model in Figure 4.1, the

equivalent model in Figure 5.10 considers the parasitic effects among the antenna structure, such as the parasitic capacitances between the top-layer metal and the main GP. In this model, parasitic capacitances and inductances (i.e.,  $C_1$ ,  $C_2$ ,  $L_1$  and  $L_2$ ) are included. The component values in this equivalent circuit model are listed in Table 5.2. They are extracted from the full-wave simulations using the same steps as introduced in Chapter IV. The dispersion relation can be derived using Eq. (2-51). The full-wave and circuit-model simulated frequency responses and dispersion diagrams of one ECRLH unit cell structure are shown in Figure 5.11(a) and Figure 5.11(b), respectively. The full-wave simulated S parameters (blue solid line and red dash line) in Figure 5.11(a) show that the low passband over 0.7-1.4 GHz and the high passband over 3.5-5.7 GHz are formed, with respect to the -6 dB bandwidth.

In the full-wave simulated dispersion diagram (red solid line) in Figure 5.11(b), there is one balanced point at the transition frequency point from the LH to RH band within the low passband. Thus, the LWA scans from the backward to forward direction through broadside smoothly within the low passband. However, there is no balanced point within the high passband. Instead, there is one RH band at the low edge and one LH band at the high edge, respectively. There is a stopband existing between the RH and LH band. The conventional CRLH characteristics within the high passband are destroyed mainly by the parasitic capacitor  $C_1$ , which is the parasitic capacitance between the branch of  $L_{vs}$  and the main GP. Thus, the forward (RH band) frequency scanning is at the low edge and the backward (LH band) frequency scanning happens at the high edge of the high passband.

There are some differences between the full-wave and circuit-model simulated results. The equivalent model in Figure 5.10 does not fully consider all the coupling effects among the ECRLH unit cell structure. However, this model can provide a fast and convenient way to analyze and understand the characteristics of the ECRLH unit cell in this LWA structure.

### 5.2.3 Loss of SMD Chip Capacitors

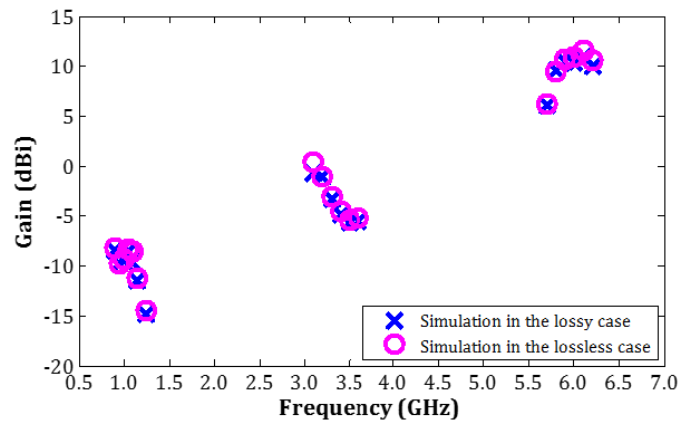


Figure 5.12 Comparison of the simulated gains of this passive LWA at the leaky-wave regions in the lossy and lossless case.

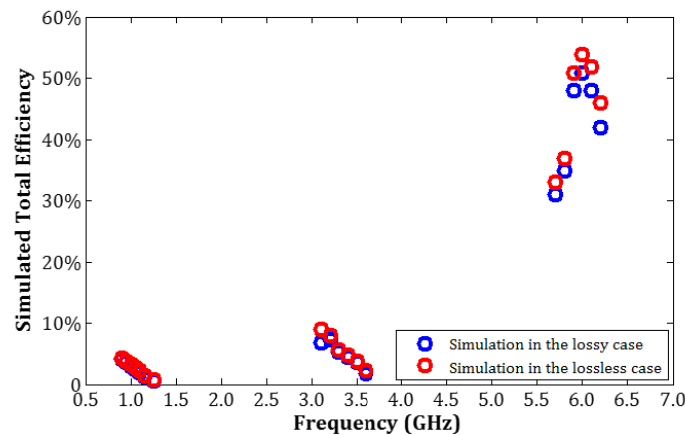


Figure 5.13 Comparison of the simulated total efficiencies of this passive LWA at the leaky-wave regions in the lossy and lossless case.

The chip capacitors used in this LWA introduce some losses to degrade the antenna radiation performance. The losses introduced by chip capacitors can be evaluated by

replacing them with ideal lossless capacitors in simulations. In the lossy case, the LWA simulated with SMD chip capacitors and ideal lossless capacitors are labelled as the lossy and lossless case, respectively. The comparisons between the simulated gains and total efficiencies of the LWA within the leaky-wave regions in the lossy and lossless case are shown in Figure 5.12 and Figure 5.13, respectively. Figure 5.12 shows that the gain degradations resulting from the losses of the SMD capacitors are around 0.2-1.4 dBi over 0.9-1.25 GHz, 0.1-0.4 dBi over 3.1-3.6 GHz, and 0.2-0.6 dBi over 5.7-6.2 GHz, respectively. Figure 5.13 shows that the simulated total efficiencies of the LWA are decreased by the losses from the chip capacitors with 0.2%-0.3% over 0.9-1.25 GHz, 0.4%-2% over 3.1-3.6 GHz, and 2%-4% over 5.7-6.2 GHz, respectively.

### 5.3 Passive LWA Design Based On *Supercell\_v1* Structure

#### 5.3.1 Analysis Using TL Approach

The simplified equivalent model of the *Supercell\_v1* structure has been shown in Figure 5.1. It is composed of six L-C resonators totally. The total impedance of the horizontal branch and the total admittance of the vertical branch in the asymmetric ECRLH unit cell are expressed in Eq. (5-2) and Eq. (5-3), respectively:

$$Z_H = j\omega L_{hs} + \frac{1}{j\omega C_{hs}} + 1/(j\omega C_{hp} + \frac{1}{j\omega L_{hp}}) \quad \text{Eq. (5-2)}$$

$$Y_V = j\omega C_{vp} + \frac{1}{j\omega L_{vp}} + 1/(j\omega L_{vs} + \frac{1}{j\omega C_{vs}}) \quad \text{Eq. (5-3)}$$

Similarly, the total impedance of the horizontal branch and the total admittance of the

vertical branch in the asymmetric CRLH unit cell are respectively expressed by

$$Z_{se} = j\omega L_{se} + \frac{1}{j\omega C_{se}} \quad \text{Eq. (5-4)}$$

$$Y_{st} = j\omega C_{st} + \frac{1}{j\omega L_{st}} \quad \text{Eq. (5-5)}$$

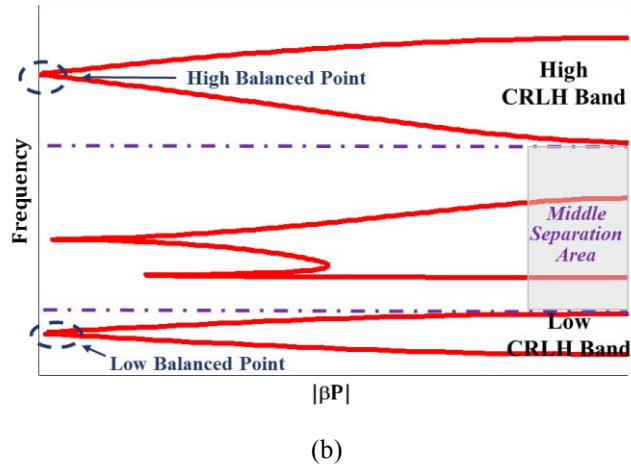
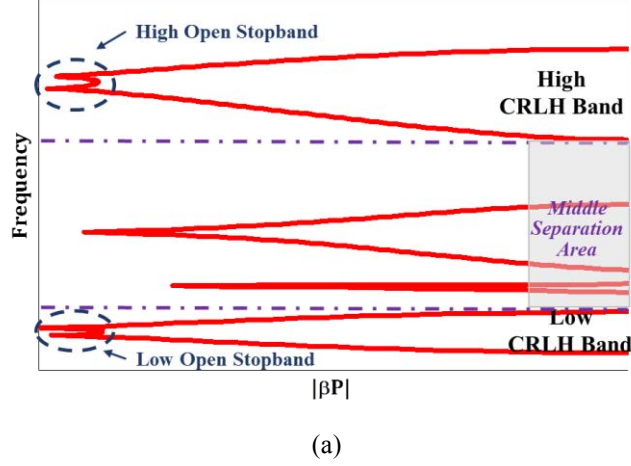


Figure 5.14 Dispersion diagrams of a *Supercell\_v1* structure in different conditions, (a) the unbalanced condition; (b) the balanced condition.

The transmission ABCD matrix of a *Supercell\_v1* structure is expressed by

$$\begin{aligned} \begin{bmatrix} A & B \\ C & D \end{bmatrix} &= \begin{bmatrix} A_1 & B_1 \\ C_1 & D_1 \end{bmatrix} \begin{bmatrix} A_2 & B_2 \\ C_2 & D_2 \end{bmatrix} \\ &= \begin{bmatrix} 1 + Z_H Y_V & Z_H \\ Y_V & 1 \end{bmatrix} \begin{bmatrix} 1 + Z_{se} Y_{st} & Z_{se} \\ Y_{st} & 1 \end{bmatrix} \quad \text{Eq. (5-6)} \end{aligned}$$

The expressions for the coefficients “A”, “B”, “C” and “D” are obtained respectively:

$$A = 1 + Z_H Y_V + Z_{se} Y_{st} + Z_H Y_V Z_{se} Y_{st} + Z_H Y_{st} \quad \text{Eq. (5-7)}$$

$$B = Z_{se} + Z_{se}Z_H Y_V + Z_H \quad \text{Eq. (5-8)}$$

$$C = Y_V + Y_V Z_{se} Y_{st} + Y_{st} \quad \text{Eq. (5-9)}$$

$$D = Y_V Y_{st} + 1 \quad \text{Eq. (5-10)}$$

Multiple *Supercell\_v1* structures can be cascaded to model an effectively homogenous TL, if the period meets the homogeneity condition [8]. The condition requires that the period of one *Supercell\_v1* structure should be much smaller than the guided wavelength, i.e.,  $P2 \ll \lambda_g$ . Then the dispersion relation of the *Supercell\_v1* structure can be derived based on the Bloch-Floquet theorem [8]:

$$\beta \cdot P2 = \cos^{-1}\left(\frac{A+D}{2}\right) \quad \text{Eq. (5-11)}$$

where  $\beta$  is the phase constant and  $P2$  is the period of a *Supercell\_v1* structure.

Similarly, the *Supercell\_v1* structure has two operation conditions – the unbalanced and balanced conditions. The dispersion relations of the *Supercell\_v1* structure can be derived using Eq. (5-11). Figure 5.14(a) and Figure 5.14(b) show the dispersion diagrams of the *Supercell\_v1* structure in the unbalanced and balanced condition, respectively. Figure 5.14(a) shows that there is an open stopband at the transition area from the LH band to the RH band within each passband. The two passbands are separated by one middle separation area. In contrast, Figure 5.13(b) shows that, in the balanced condition of the *Supercell\_v1* structure, the open stopband within each passband is closed and one balanced point is formed at the transition frequency point from the LH to RH band within each passband.

### 5.3.2 Antenna Design

The full configuration of a *Supercell\_v1* structure is shown in Figure 5.15. In one *Supercell\_v1* structure, seven SMD MURATA 0402 chip capacitors are integrated at the positions of  $C_{hs}$ ,  $C_{hp1}$ ,  $C_{hp2}$ ,  $C_{vs}$ ,  $C_{vp}$ ,  $C_{se}$ , and  $C_{st}$ , respectively, which are illustrated in Figure 5.15. The detailed equivalent circuit model of this *Supercell\_v1* structure with considerations of the parasitic capacitances and inductances among the *Supercell\_v1* structure is shown in Figure 5.16, and the component values in this circuit model are listed in Table 5.3. The component values are extracted in the same way as introduced in Chapter IV.

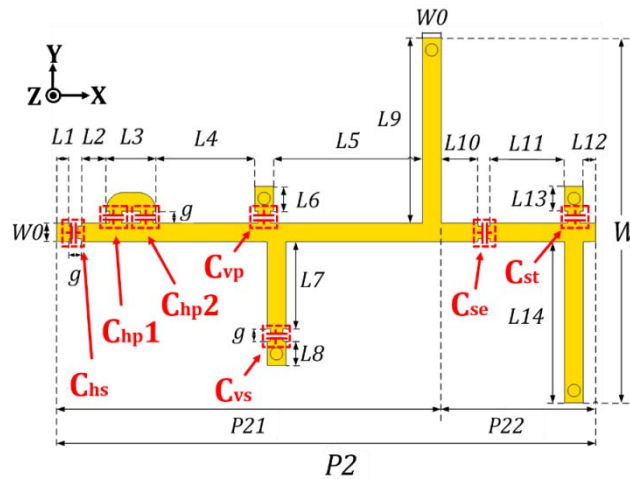


Figure 5.15 Configuration of one *Supercell\_v1* structure.

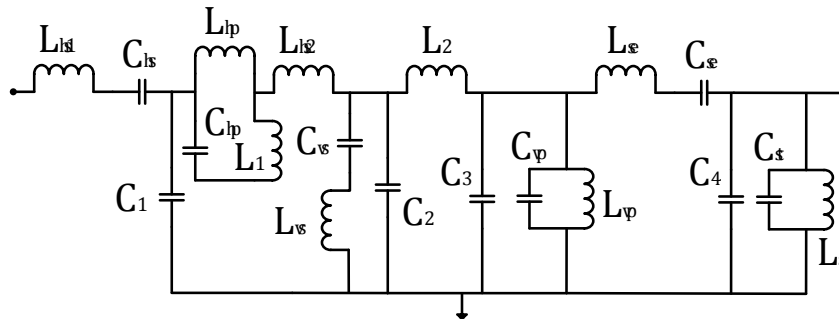


Figure 5.16 Equivalent circuit model of one *Supercell\_v1* structure.

The proposed LWA is composed of 6 cascaded *Supercell\_v1* structures, which is

printed on a *Rogers RT/duroid 5880* substrate with dielectric constant of 2.2, loss tangent of 0.0009 and thickness of 1.575 mm. This LWA employs the *Supercell\_v1* structures to work in the balanced condition. Table 5.4 lists the detailed dimensions of a *Supercell\_v1* structure in the balanced condition. The SMD capacitors used for  $C_{hs}$ ,  $C_{hp1}$ ,  $C_{hp2}$ ,  $C_{vs}$ ,  $C_{vp}$ ,  $C_{se}$ , and  $C_{st}$ , are 8.0 pF, 20.0 pF, 3.0 pF, 1.7 pF, 0.2 pF, 2.0 pF, and 0.2 pF, respectively. The physical length of a *Supercell\_v1* structure is 43.5 mm. A photograph of the fabricated LWA with 6 cascaded *Supercell\_v1* structures is shown in Figure 5.17. The total length and width of the LWA are 281 mm and 50 mm, respectively.

Table 5.3 Component values in the equivalent circuit model of one *Supercell\_v1* structure.

Symbol	Values (pF)	Symbol	Values (nH)
$C_{hp}$	2.6	$L_{hs1}$	1.67
$C_{hs}$	8.0	$L_{hs2}$	2.59
$C_{vs}$	1.7	$L_{hp}$	1.16
$C_{vp}$	0.1	$L_{vs}$	6.9
$C_{se}$	2.0	$L_{vp}$	11.2
$C_{st}$	0.2	$L_{se}$	4.4
$C_1$	0.42	$L_{st}$	7.0
$C_2$	0.72	$L_1$	0.92
$C_3$	0.61	$L_2$	4.64
$C_4$	0.69		

Table 5.4 Dimensions of one *Supercell\_v1* structure.

Symbol	Dimension (mm)	Symbol	Dimension (mm)
$P2$	43.5	$P21$	31
$L1$	1	$P22$	12.5
$L2$	2	$W$	29.5
$L3$	4	$W0$	1.5
$L4$	8	$g$	1
$L5$	12	$L10$	3
$L6$	2	$L11$	6
$L7$	7	$L12$	12
$L8$	2	$L13$	2
$L9$	15	$L14$	13

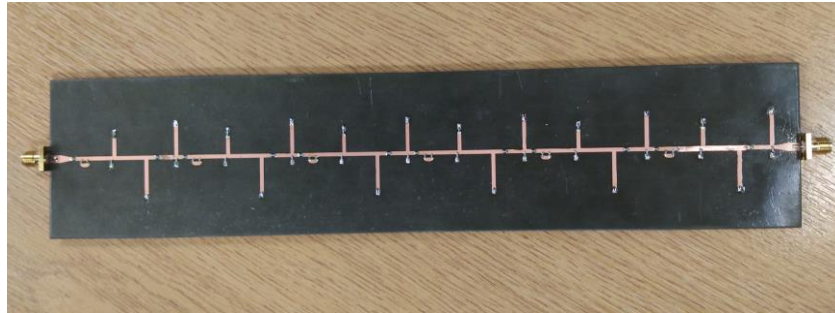
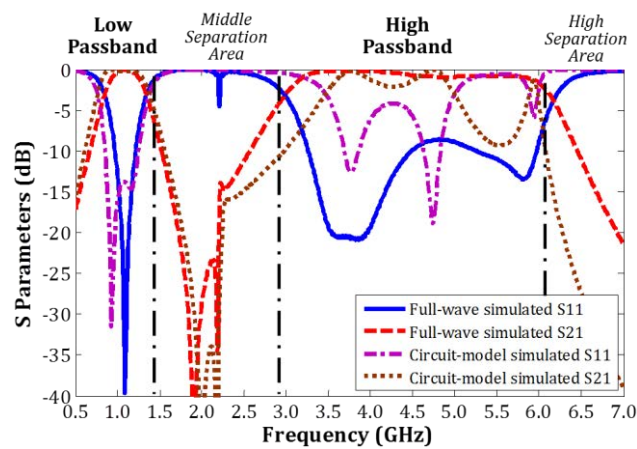
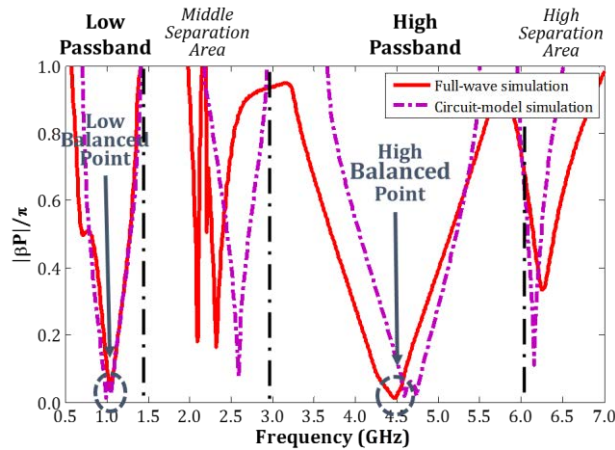


Figure 5.17 Photograph of the fabricated LWA with 6 *Supercell\_v1* structures.

### 5.3.3 Analysis of *Supercell\_v1* Structure



(a)



(b)

Figure 5.18 Full-wave and circuit-model simulated performances of a *Supercell\_v1* structure, (a) the frequency response; (b) the dispersion diagram.

The full-wave and circuit-model simulated results of the frequency response of a single *Supercell\_v1* structure in the LWA are shown in Figure 5.18(a). The full-wave

simulated results (blue solid line and red dash line) in Figure 5.18(a) show that this *Supercell\_v1* structure has two distinct passbands respectively at the low and high frequencies separated by a middle separation area. The full-wave simulated dispersion diagram (red solid line) in Figure 5.18(b) shows the corresponding dispersion diagram of this structure and shows that there is a CRLH band and a balanced point within each passband. Thus, this *Supercell\_v1* structure operates in the balanced condition.

There are some differences between the full-wave and circuit-model simulated results. The equivalent circuit model in Figure 5.16 does not fully consider all the coupling effects among the *Supercell\_v1* structure. But the equivalent circuit model can provide a fast and convenient way to analyze and understand the characteristics of the *Supercell\_v1* structure.

### 5.3.4 Measurement Results of LWA

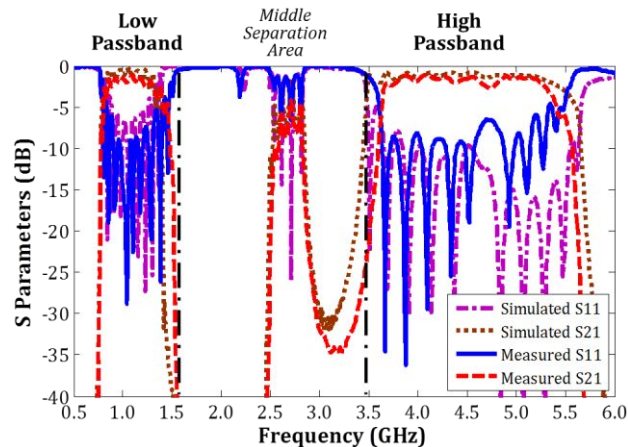
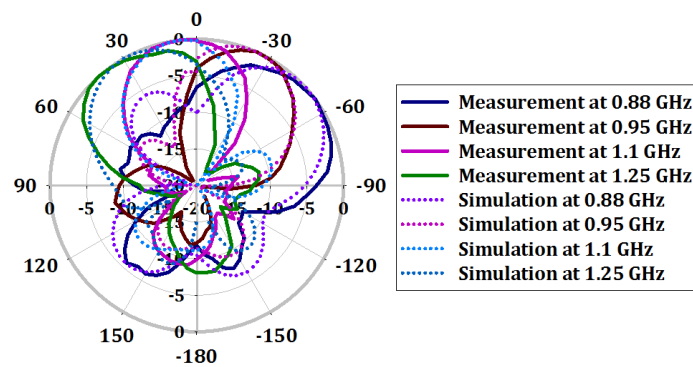


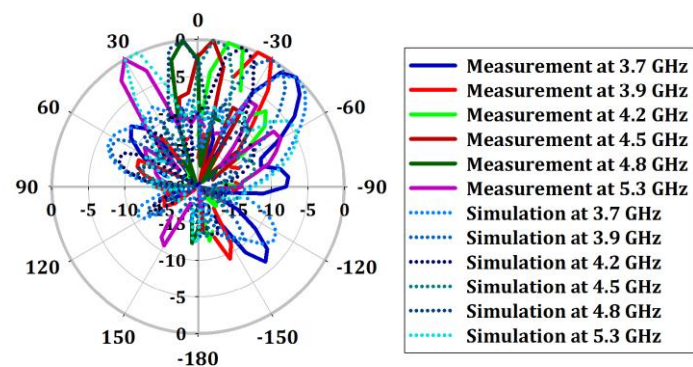
Figure 5.19 Full-wave simulated and measured S11 and S21 of the passive LWA with 6 *Supercell\_v1* structures.

Figure 5.19 shows the full-wave simulated and measured results of S11 and S21 of the LWA with 6 cascaded *Supercell\_v1* structures. Figure 5.19 shows that the low

passband over 0.8-1.45 GHz and the high passband over 3.55-5.4 GHz are formed with respect to the -6 dB bandwidth. These two passbands are separated by a middle separation area. In this area, there is an unmatched passband over 2.5-2.8 GHz. For this LWA, the leaky-wave radiation characteristics within the low and high passband are the main focus, thus this unmatched passband is neglected here. The balanced points within the low and high passbands are at 1.1 GHz and 4.65 GHz, respectively. Compared to the results of the single *Supercell\_v1* structure, the operating frequencies of these two balanced points have a small shift, due to the inter-cell coupling effects among these cascaded *Supercell\_v1* structures in the LWA.



(a)



(b)

Figure 5.20 Co-polarized simulated and measured normalized farfield leaky-wave radiation patterns at the XOZ plane within two passbands, (a) 0.88-1.25 GHz; (b) 3.7-5.3 GHz.

The simulated and measured normalized farfield leaky-wave radiation patterns at the XOZ plane within both passbands are shown in Figure 5.20. The measured results show that the main beam scans from  $-42^\circ$  to  $+36^\circ$  over 0.88-1.25 GHz for the low passband and scans from  $-42^\circ$  to  $+30^\circ$  over 3.7-5.3 GHz for the high passband, respectively. Thus, the desired CRLH leaky-wave radiation characteristics are demonstrated within both passbands.

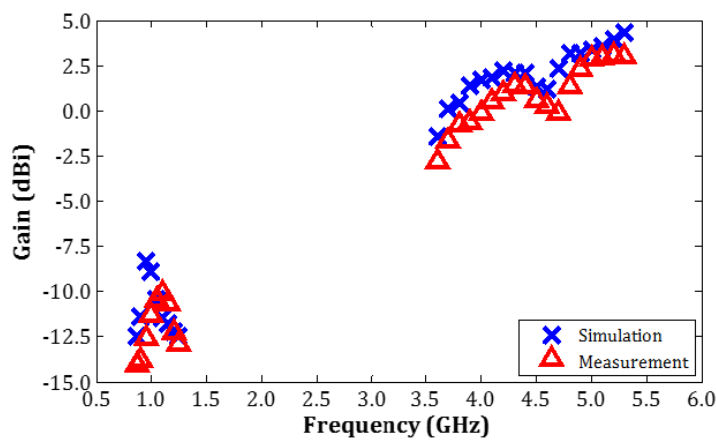


Figure 5.21 Simulated and measured gains at the leaky-wave regions within both passbands.

The simulated and measured gains of this LWA at the leaky-wave regions within both passbands are shown in Fig. 5.21. The measured peak gain within the low passband is  $-10.1$  dBi, whereas the measured peak gain within the high passband is  $2.14$  dBi. This LWA also suffers from low gain, particularly at the low frequencies, due to the same reason as the LWA in Section 5.2. The leakage rates at the leaky-wave regions of this LWA are calculated using Eq. (5-11), which are shown in Figure 5.22. In simulations, a LWA with 25 cascaded *Supercell\_v1* structures can achieve an improved gain of  $0.85$  dBi peak gain within the low passband. The simulated directivities of this LWA are shown in Figure 5.23.

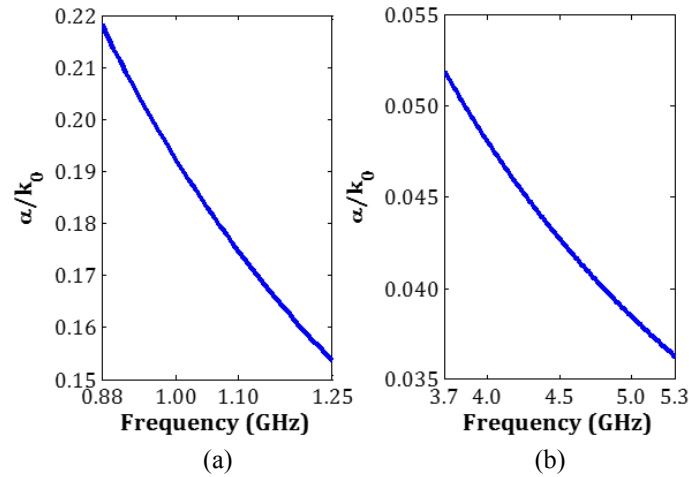


Figure 5.22 Leakage rates of this LWA at the leaky-wave regions, (a) 0.8-1.25 GHz; (b) 3.7-5.3 GHz.

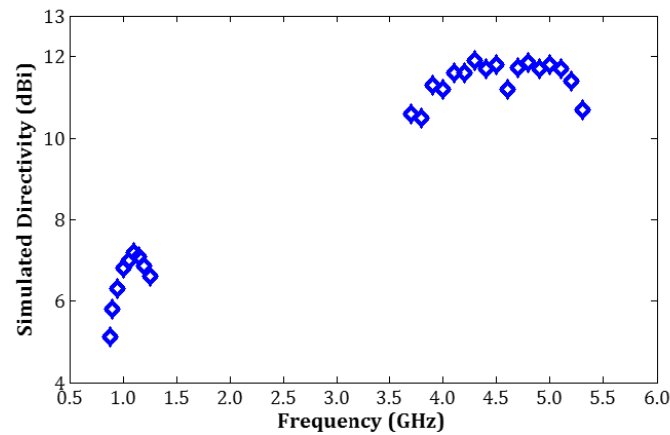


Figure 5.23 Simulated directivities of this LWA at the leaky-wave regions within both passbands.

The differences between the full-wave simulated and measured results in Figure 5.19, Figure 5.20, and Figure 5.21 are summarized as the following reasons:

- (1) the fabrication and measurement deviations;
- (2) the loss resulting from soldering;

### 5.3.5 Loss of SMD Chip Capacitors

The losses of all SMD chip capacitors are evaluated by replacing the real SMD chip capacitors with the ideal lossless capacitors in simulations. Similarly, the simulated gains and total efficiencies of this LWA at the leaky-wave regions within both

passbands in the lossy and lossless case are compared in Figure 5.24 and Figure 5.25, respectively. Figure 5.24 shows that all SMD chip capacitors degrade the antenna gains of around 0.2-0.8 dBi over 0.88-1.25 GHz and 0.1-1.0 dBi over 3.7-5.3 GHz, respectively. Figure 5.25 shows that the simulated total efficiencies are reduced by the losses of all chip capacitors with 0.2%-0.4% over 0.88-1.25 GHz and 0.2%-1.2% over 3.7-5.3 GHz, respectively.

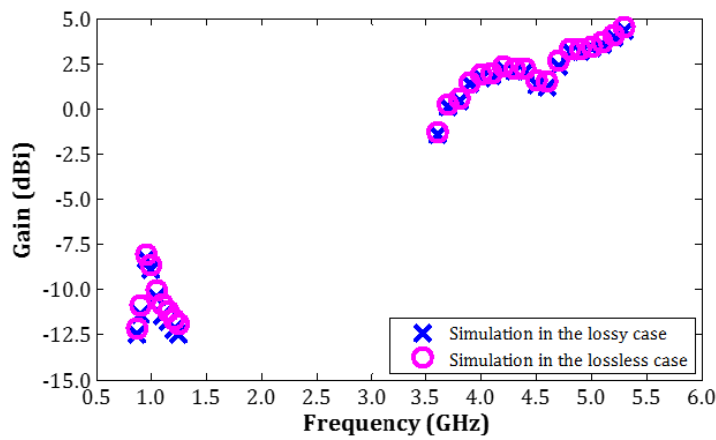


Figure 5.24 Comparison of the simulated gains of this passive LWA at the leaky-wave regions within both passbands in the lossy and lossless case.

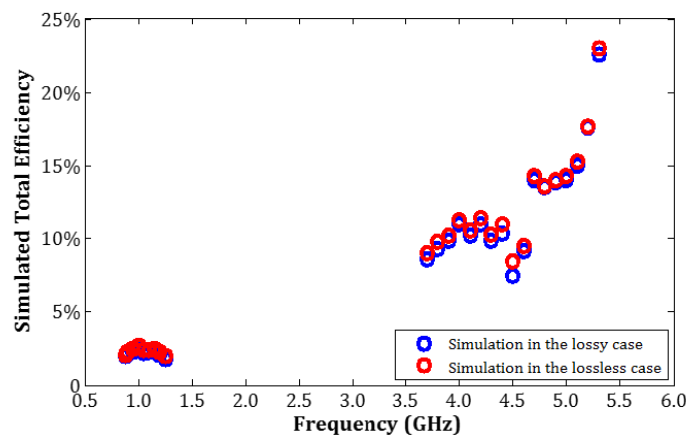


Figure 5.25 Comparison of the simulated total efficiencies of this passive LWA at the leaky-wave regions within both passbands in the lossy and lossless case.

## 5.4 LWA Designs Based On *Supercell\_v2* Structure

### 5.4.1 Analysis of *Supercell\_v2* Structure Using TL Approach

As shown in Figure 5.2, the simplified model of the *Supercell\_v2* structure mainly contains five L-C resonators totally. The *Supercell\_v2* structure is improved compared with the *Supercell\_v1* structure by removing the  $L_{hp}$ - $C_{hp}$  resonator. Similar as the *Supercell\_v1* structure, the *Supercell\_v2* structure also enables two distinct passbands at the low and high frequencies with a middle separation area. The physical length of a *Supercell\_v2* structure is represented by P3. The total impedances of the first and second horizontal branches and the total admittances of the first and second vertical branches are respectively expressed by the following equations:

$$Z_1 = j\omega L_{hs} + \frac{1}{j\omega C_{hs}} \quad \text{Eq. (5-12)}$$

$$Z_2 = j\omega L_{se} + \frac{1}{j\omega C_{se}} \quad \text{Eq. (5-13)}$$

$$Y_1 = j\omega C_{vp} + \frac{1}{j\omega L_{vp}} + 1/(j\omega L_{vs} + \frac{1}{j\omega C_{vs}}) \quad \text{Eq. (5-14)}$$

$$Y_2 = j\omega C_{st} + \frac{1}{j\omega L_{st}} \quad \text{Eq. (5-15)}$$

The transmission ABCD matrix of a *Supercell\_v2* structure is expressed in Eq. (5-16):

$$\begin{aligned} \begin{bmatrix} A & B \\ C & D \end{bmatrix} &= \begin{bmatrix} A_1 & B_1 \\ C_1 & D_1 \end{bmatrix} \begin{bmatrix} A_2 & B_2 \\ C_2 & D_2 \end{bmatrix} \\ &= \begin{bmatrix} 1 + Z_1 Y_1 & Z_1 \\ Y_1 & 1 \end{bmatrix} \begin{bmatrix} 1 + Z_2 Y_2 & Z_2 \\ Y_2 & 1 \end{bmatrix} \end{aligned} \quad \text{Eq. (5-16)}$$

The expressions for the coefficients ‘‘A’’, ‘‘B’’, ‘‘C’’ and ‘‘D’’ are obtained respectively:

$$A = 1 + Z_1 Y_1 + Z_2 Y_2 + Z_1 Y_1 Z_2 Y_2 + Z_1 Y_2 \quad \text{Eq. (5-17)}$$

$$B = Z_2 + Z_2 Z_1 Y_1 + Z_1 \quad \text{Eq. (5-18)}$$

$$C = Y_1 + Y_1 Z_2 Y_2 + Y_2 \quad \text{Eq. (5-19)}$$

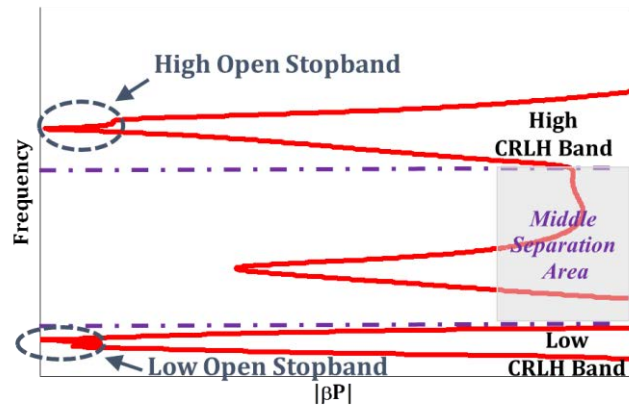
$$D = Y_1 Y_2 + 1 \quad \text{Eq. (5-20)}$$

The period of the *Supercell\_v2* structure is much smaller than the guided wavelength (i.e.,  $P3 \ll \lambda_g$ ) for electromagnetic homogeneity [8]. Thus, multiple periodic *Supercell\_v2* structures can be cascaded together to model an effectively homogenous TL structure. Based on the Bloch-Floquet theorem [8], the dispersion relation of this *Supercell\_v2* structure can be derived using the coefficients of “A” and “D” in Eq. (5-21):

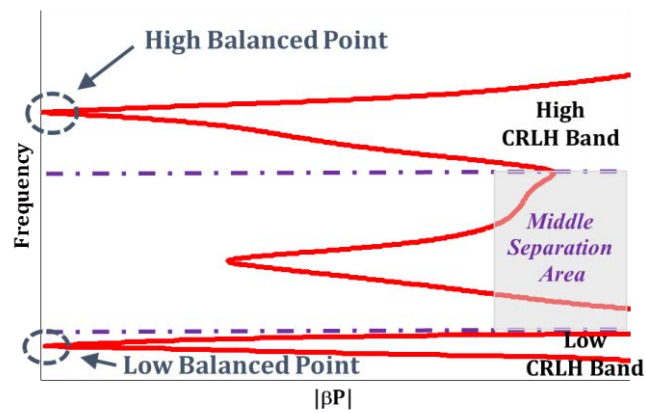
$$\beta \cdot P3 = \cos^{-1}\left(\frac{A+D}{2}\right) \quad \text{Eq. (5-21)}$$

where  $\beta \cdot P3$  is the phase shift of the single *Supercell\_v2* structure, and  $\beta$  is the propagation constant.

Similar to the *Supercell\_v1* structure, the *Supercell\_v2* structure also has two operation conditions – unbalanced condition and balanced condition. The dispersion relations of the *Supercell\_v2* structure in the unbalanced and balanced condition are derived from Eq. (5-21). Figure 5.26(a) and Figure 5.26(b) present the dispersion diagram of a *Supercell\_v2* structure in the unbalanced and balanced condition, respectively. In the unbalanced condition shown in Figure 5.26(a), there is an open stopband existing at the transition frequency area between the LH and RH band within each passband. In the balanced condition, the open stopband is closed to form a balanced point at the transition frequency point from the LH band to the RH band within each passband.



(a)



(b)

Figure 5.26 Dispersion diagrams of one *Supercell\_v2* structure in different conditions, (a) the unbalanced condition; (b) the balanced condition.

## 5.4.2 Passive LWA Design Based On *Supercell\_v2* Structure

### 5.4.2.1 Passive antenna design

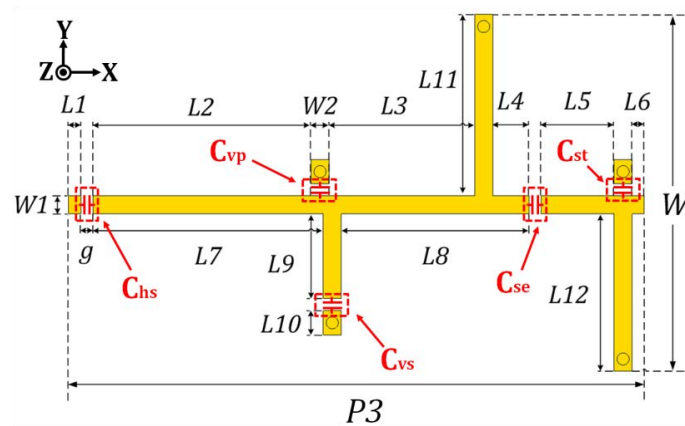


Figure 5.27 Configuration of a *Supercell\_v2* structure.

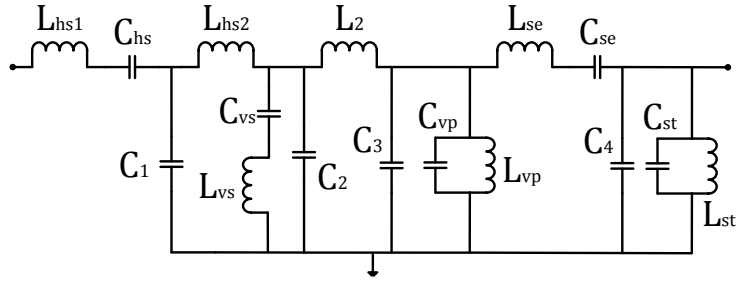


Figure 5.28 Detailed equivalent circuit model of one *Supercell\_v2* structure.

Table 5.5 Component values in the equivalent circuit model of one *Supercell\_v2* structure.

Symbol	Values (pF)	Symbol	Values (nH)
C <sub>hs</sub>	4.9	L <sub>hs1</sub>	2.2
C <sub>vs</sub>	1.2	L <sub>hs2</sub>	5.0
C <sub>vp</sub>	0.1	L <sub>vs</sub>	5.9
C <sub>se</sub>	1.4	L <sub>vp</sub>	23.2
C <sub>st</sub>	0.1	L <sub>se</sub>	5.6
C <sub>1</sub>	0.65	L <sub>st</sub>	5.1
C <sub>2</sub>	0.43	L <sub>1</sub>	8.3
C <sub>3</sub>	0.78		
C <sub>4</sub>	0.75		

Table 5.6 Dimensions of one *Supercell\_v2* structure.

Symbol	Value (mm)	Symbol	Value (mm)
L1	1.0	P3	47.5
L2	18.0	W	29.5
L3	12.0	W1	1.5
L4	3.0	W2	1.5
L5	6.0	g	1.0
L6	1.0		
L7	19.0	L10	2.0
L8	15.5	L11	15.0
L9	7.0	L12	13.0

A passive microstrip LWA is designed with 7 cascaded *Supercell\_v2* structures. The antenna layout is printed on the substrate of *Taconic TLY-5* laminate with thickness of 1.575 mm, permittivity of 2.2, and loss tangent of 0.0009. The configuration of a *Supercell\_v2* structure is shown in Figure 5.27. The corresponding equivalent circuit

model with considering parasitic capacitances and inductances among this *Supercell\_v2* structure is shown in Figure 5.28, and the extracted component values in this circuit model are listed in Table 5.5. The steps for extracting these component values are same as the ones introduced in Chapter IV. The detailed dimensions of one *Supercell\_v2* structure are listed in Table 5.6. In each *Supercell\_v2* structure, the capacitors of  $C_{hs}$ ,  $C_{vp}$ ,  $C_{vs}$ ,  $C_{se}$ , and  $C_{st}$  shown in Figure 5.27 are realized by SMD *MURATA* 0402 chip capacitors with the capacitance of 4.9 pF, 0.1 pF, 1.2 pF, 1.4 pF, and 0.1 pF, respectively. The photograph of the fabricated LWA with 7 cascaded *Supercell\_v2* structures is shown in Figure 5.29. The whole length and width of the fabricated LWA are 352.5 mm and 45 mm, respectively.

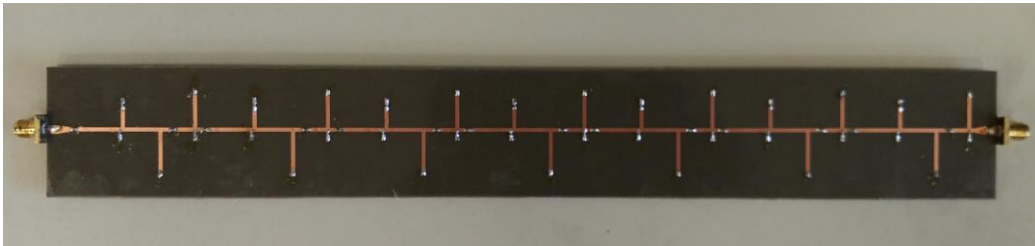
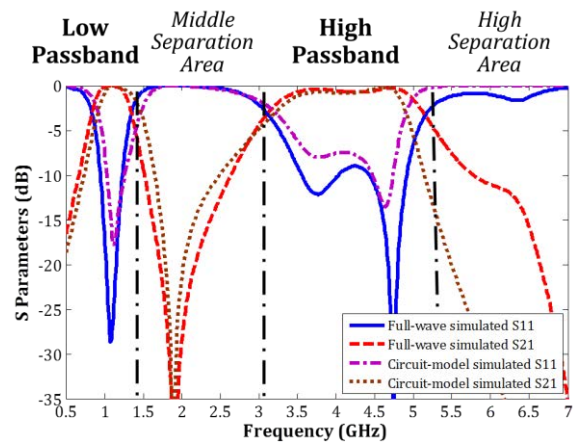


Figure 5.29 Photograph of the passive LWA with 7 cascaded *Supercell\_v2* structures.

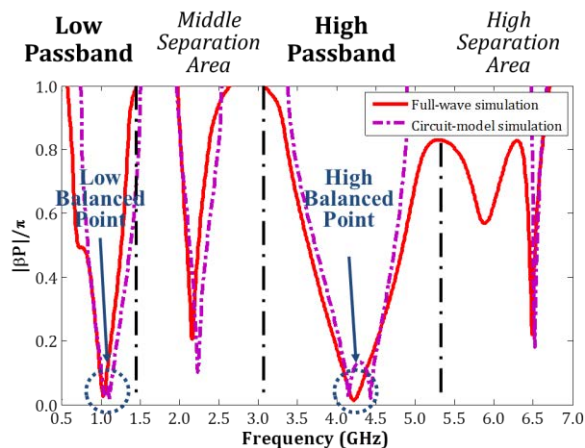
#### 5.4.2.2 Analysis of *Supercell\_v2* structure

Figure 5.30(a) presents the full-wave (blue solid line and red dash line) and circuit-model simulated results of  $S_{11}$  and  $S_{21}$  of a *Supercell\_v2* structure. This *Supercell\_v2* structure forms two distinct passbands respectively at the low and high frequencies with separated by a middle separation area as well, which is similar to the *Supercell\_v1* structure. The dispersion relation of a *Supercell\_v2* structure can be derived using Eq. (5-21). Figure 5.30(b) shows the full-wave and circuit-model simulated dispersion diagrams of this *Supercell\_v2* structure. The full-wave simulated

dispersion diagram (red solid line) shows that this *Supercell\_v2* structure has a full CRLH band with a balanced point at the transition frequency point from the LH to RH band within each passband.



(a)



(b)

Figure 5.30 Full-wave and circuit-model simulated performances of a *Supercell\_v2* structure, (a) the frequency response; (b) the dispersion diagram.

There are some differences between the full-wave and circuit-model simulated results. The equivalent circuit model in Figure 5.28 does not fully consider all the coupling effects among the *Supercell\_v2* structure. However, the equivalent circuit model can provide a fast and convenient way to analyze and understand the characteristics of the *Supercell\_v2* structure.

### 5.4.2.3 Measurement results

The simulated and measured results of S11 and S21 of the fabricated LWA with 7 cascaded *Supercell\_v2* structures are shown in Figure 5.31. The measured results show that this LWA has two distinct passbands at the low and high frequencies separated by a middle separation area. With respect to the -6 dB bandwidth, the low CRLH passband has the bandwidth from 0.88 GHz to 1.56 GHz, whereas the high CRLH passband has the bandwidth from 3.65 GHz to 5.3 GHz.

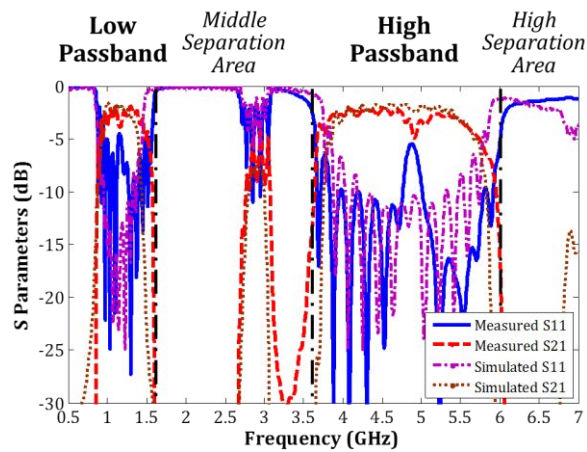
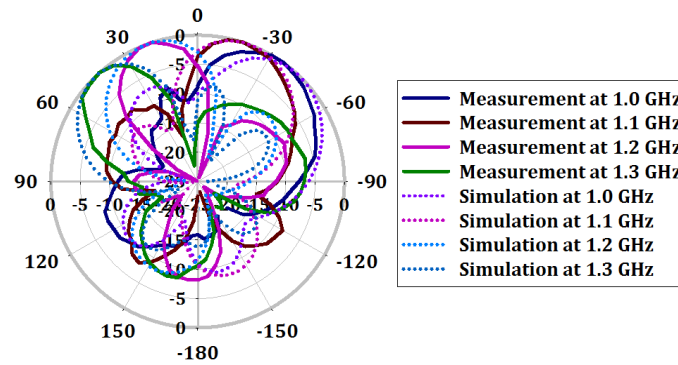


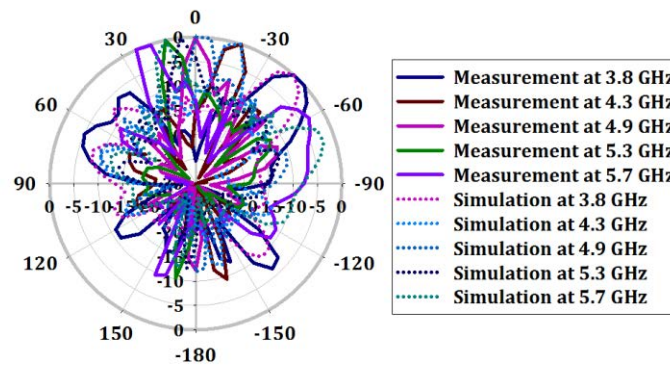
Figure 5.31 Measured and simulated S11 and S21 of the passive LWA with 7 *Supercell\_v2* structures.

The normalized co-polarized farfield patterns at the XOZ plane at the leaky-wave radiation regions within two CRLH passbands are shown in Figure 5.32(a) and Figure 5.32(b), respectively. Figure 5.32(a) shows that the main beam of this LWA scans between  $-42^\circ$  to  $+48^\circ$  over 0.9-1.3 GHz within the low passband, whereas Figure 5.29(a) shows that the main beam of this LWA scans between  $-42^\circ$  to  $+24^\circ$  over 3.8-5.7 GHz within the high passband. Within both passband, the LWA has the leaky-wave radiation from the backward to forward direction. The measured and simulated gains of this LWA at the leaky-wave regions within both passbands are

presented in Figure 5.33. The peak gains of -8.5 dBi and 3.9 dBi are observed within the low and high passbands, respectively.



(a)



(b)

Figure 5.32 Co-polarized simulated and measured normalized farfield leaky-wave radiation patterns at the XOZ plane within two passbands, (a) 1.0-1.3 GHz; (b) 3.8-5.7 GHz.

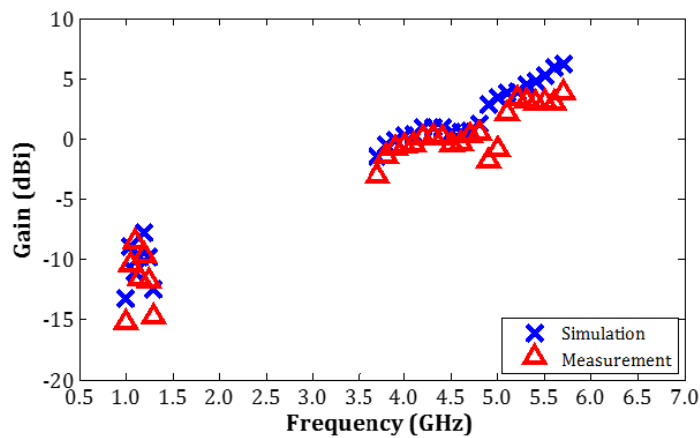


Figure 5.33 Simulated and measured gains of this LWA at the leaky-wave regions within both passbands.

The differences between the full-wave simulated and measured results in Figure 5.31, Figure 5.32, and Figure 5.33 are summarized as the following reasons:

- (1) the fabrication and measurement deviations;
- (2) the loss resulting from soldering.

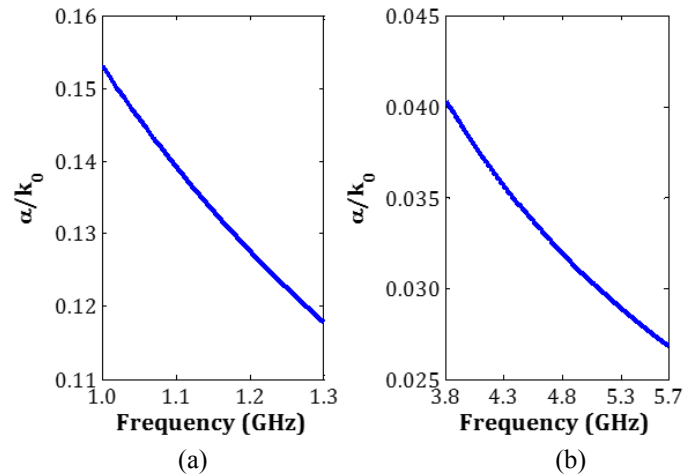


Figure 5.34 Leakage rates of this LWA at the leaky-wave regions, (a) 1.0-1.3 GHz; (b) 3.8-5.7 GHz.

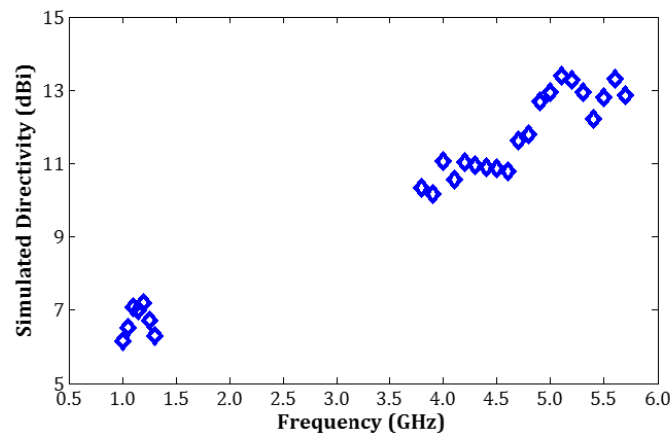


Figure 5.35 Simulated directivities of this LWA at the leaky-wave regions within both passbands.

This LWA also suffers from low gain, particularly for the low passband, due to the limited PCB size which results in that most of the accepted power by this LWA is absorbed by an absorption load at one end of the antenna and just a small amount of the power is radiated. The leakage rates can be used to reflect this phenomenon. The

leakage rates derived from Eq. (5-21) are shown in Figure 5.34. This LWA has high leakage rates at the leaky wave regions within both passbands. Similarly, the antenna gains will be improved if the LWA is designed with more cascaded *Supercell\_v2* structures. According to the simulations, a LWA with 25 cascaded *Supercell\_v2* structures can achieve a peak gain of 0.88 dBi within the low passband. The simulated directivities of this LWA are presented in Figure 5.35.

#### 5.4.2.4 Loss of SMD chip capacitors

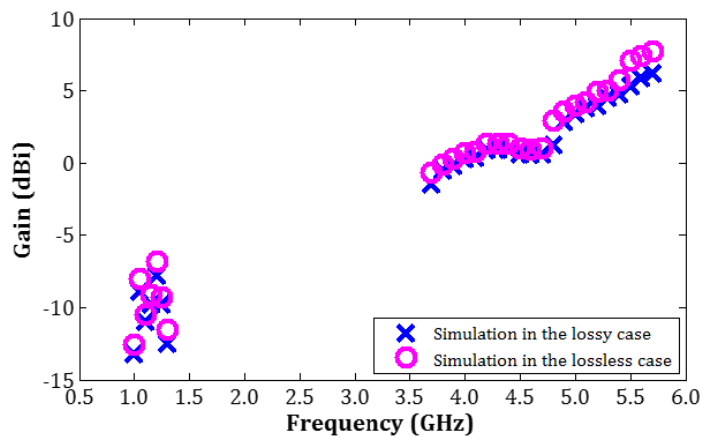


Figure 5.36 Comparison of the simulated gains of this passive LWA at the leaky-wave regions in the lossy and lossless case.

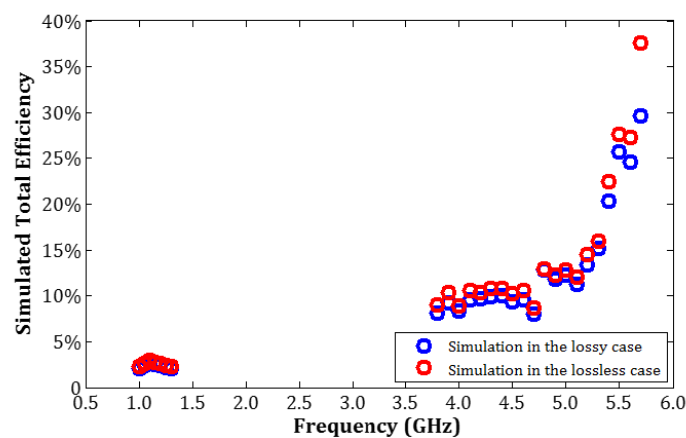


Figure 5.37 Comparison of the simulated total efficiencies of this passive LWA at the leaky-wave regions in the lossy and lossless case.

In the same way, the losses introduced by the SMD chip capacitors in the LWA structure can be evaluated by replacing the real chip capacitors with the ideal lossless capacitors in simulation. The comparisons of the simulated gains and total efficiencies of the LWA in the lossy and lossless cases are shown in Figure 5.36 and Figure 5.37, respectively. Figure 5.36 shows that the losses of 0.5-1.0 dBi over 1.0-1.3 GHz and 0.5-2.0 dBi over 3.8-5.7 GHz are introduced by all real chip capacitors. Figure 5.37 shows that the total efficiencies are decreased by all real chip capacitors with 0.2%-0.9% dBi over 1.0-1.3 GHz and 0.3%-8% over 3.8-5.7 GHz, depending on frequencies.

#### **5.4.2.5 Influence of capacitors on dispersion relation of *Supercell\_v2* structure**

The influence of the capacitance of different capacitors (i.e.,  $C_{hs}$ ,  $C_{vp}$ ,  $C_{vs}$ ,  $C_{se}$ , and  $C_{st}$ ) on the dispersion relation of the *Supercell\_v2* structure is investigated. Figure 5.38 presents the comparisons of dispersion diagrams of the *Supercell\_v2* structure with different capacitances of each SMD chip capacitor.

Figure 5.38(a) shows the capacitance of  $C_{hs}$  has almost no obvious influence on both the low and high CRLH passbands and the operation condition of each CRLH passband. Figure 5.38(b) and Figure 5.38(c) show that the capacitance of  $C_{se}$  and  $C_{vs}$  mainly affects the operation condition of the low CRLH passband and secondarily has little influence on the operation condition of the high CRLH passband as well. Thus,  $C_{se}$  and  $C_{vs}$  can be used to tune the frequency position of the low balanced point while almost keeping the position of the high balanced point without destroying the CRLH

leaky-wave radiation characteristics of the high CRLH passband simultaneously. In Figure 5.33(d) and Figure 5.33(e), the capacitance of  $C_{vp}$  and  $C_{st}$  only affects the operation condition of the high CRLH passband without affecting the balanced condition of the low CRLH passband at all. Thus,  $C_{vp}$  and  $C_{st}$  can be used to achieve independent control of the operation condition of the high CRLH passband.

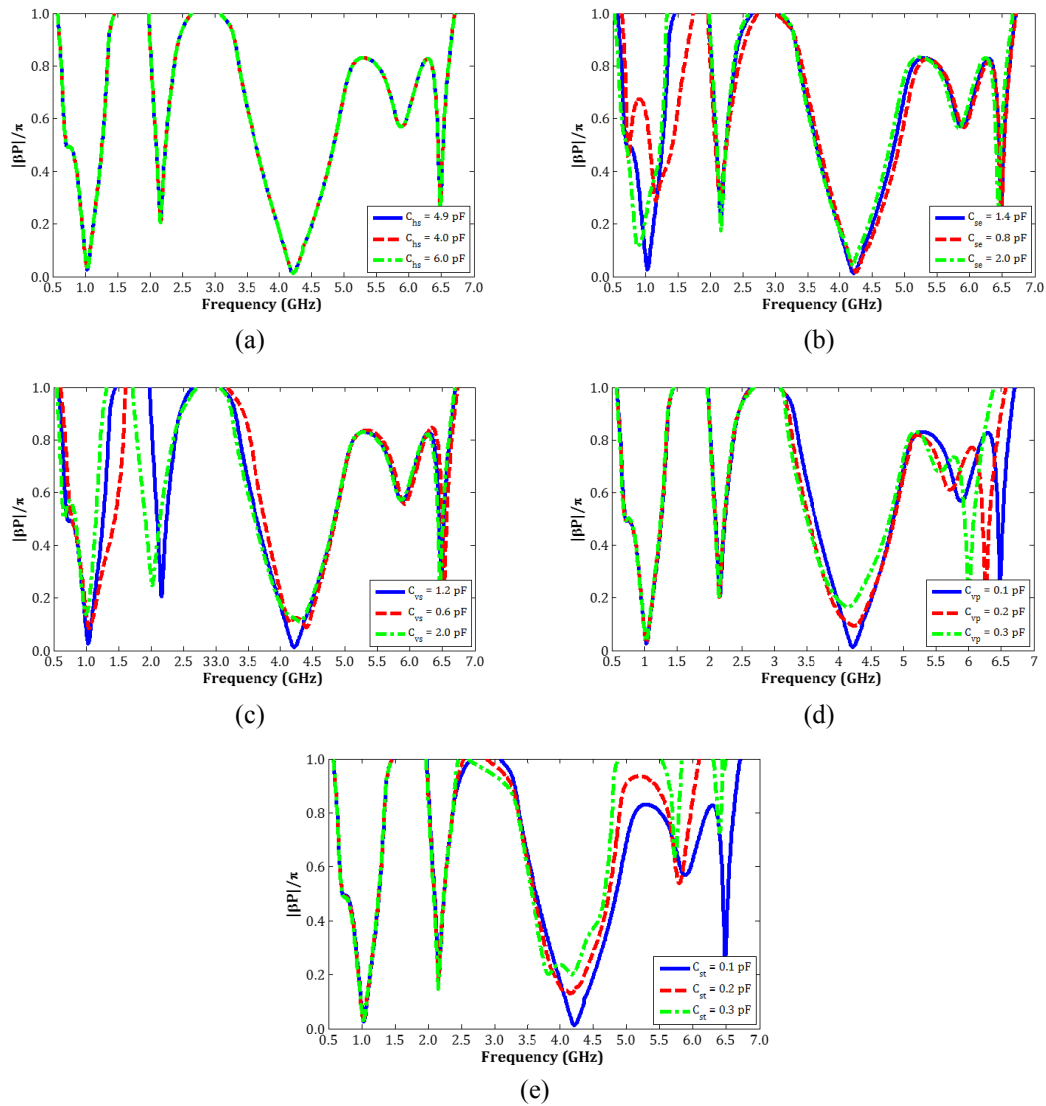


Figure 5.38 Comparison of dispersion diagrams with different capacitances of each capacitor, (a)  $C_{hs}$ ; (b)  $C_{se}$ ; (c)  $C_{vs}$ ; (d)  $C_{vp}$ ; (e)  $C_{st}$ .

In summary, four major capacitors (i.e.,  $C_{se}$ ,  $C_{vs}$ ,  $C_{vp}$ , and  $C_{st}$ ) can be used to achieve relatively independent tunability of the balanced point of the low CRLH passband.

Simultaneously, the effects on the high CRLH passband resulting from the capacitance changing of  $C_{se}$  and  $C_{vs}$  can be slightly compensated by adjusting the capacitances of  $C_{vp}$  and  $C_{st}$ .

### 5.4.3 Tunable LWA Design Based On *Supercell\_v2* Structure

#### 5.4.3.1 Tunable antenna design

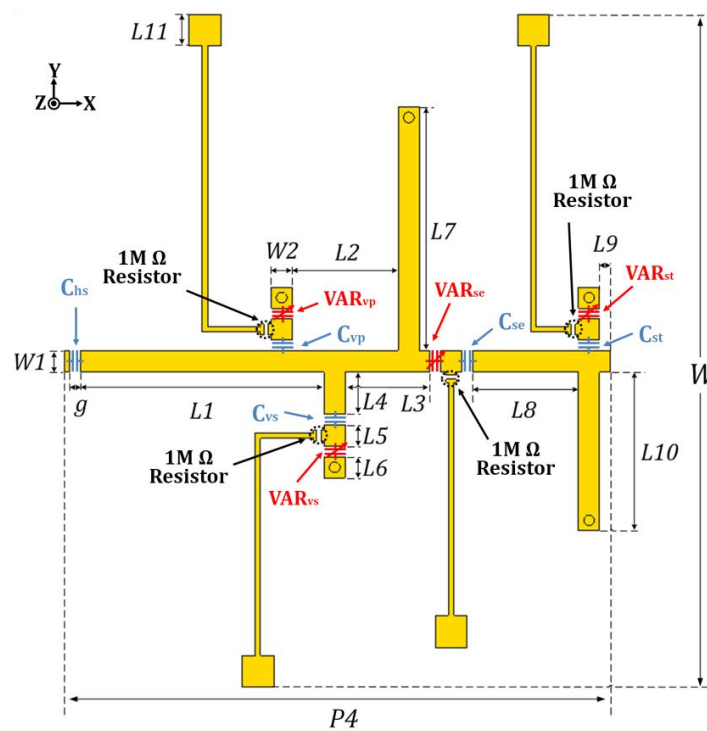


Figure 5.39 Configuration of a tunable *Supercell\_v2* structure.

Table 5.7 Dimensions of one tunable *Supercell\_v2* structure.

Symbol	Value (mm)	Symbol	Value (mm)
$L1$	22	$P4$	53.5
$L2$	10	$W$	60
$L3$	8	$W1$	2
$L4$	4	$W2$	2
$L5$	2	$g$	1
$L6$	2	$L9$	1
$L7$	23	$L10$	15
$L8$	10	$L11$	3

Following by the influence investigations of each capacitor in Figure 5.38, an electronically tunable LWA is designed with SMD silicon semiconductor varactors. The configuration of a tunable *Supercell\_v2* structure is shown in Figure 5.39. The detailed dimensions of this tunable *Supercell\_v2* structure are listed in Table 5.7. In a single *Supercell\_v2* structure shown in Figure 5.39,  $C_{hs}$  is realized by a SMD *MURATA* 0402 chip capacitor with a fixed capacitance of 4.9 pF.  $C_{se}$ ,  $C_{vs}$ ,  $C_{vp}$ , and  $C_{st}$  are also realized as the DC blocks by *MURATA* 0402 chip capacitors with 3.6 pF, 2.4 pF, 0.2 pF, and 0.2 pF, respectively.

SMD *SKYWORKS SMV1234-040LF* silicon semiconductor varactors are integrated into the *Supercell\_v2* structure to realize  $VAR_{se}$ ,  $VAR_{vs}$ ,  $VAR_{vp}$ , and  $VAR_{st}$ . The equivalent model of a *SKYWORKS SMV1234-040LF* varactor can be also represented by the one in Figure 4.22, but with a different set of parameter values. The information of this *SKYWORKS SMV1234-040LF* varactor is included in Appendix C. The tuning capacitance range of a varactor is from 9.63 pF with 0 V DC bias to 1.32 pF with 15 V bias. The capacitance of the DC block capacitor also affects the total capacitance tuning range in the corresponding branch.  $VAR_{se\_final}$ ,  $VAR_{vs\_final}$ ,  $VAR_{vp\_final}$ , and  $VAR_{st\_final}$  are used to represent the total capacitance tuning range of the varactor combined with the corresponding DC block capacitor in different branches, respectively. Thus, the final tuning ranges of  $VAR_{se\_final}$ ,  $VAR_{vs\_final}$ ,  $VAR_{vp\_final}$ , and  $VAR_{st\_final}$  are 2.62-0.97 pF, 1.92-0.86 pF, 0.196-0.174 pF, and 0.196-0.174 pF from 0 V bias to 15 V bias, respectively.

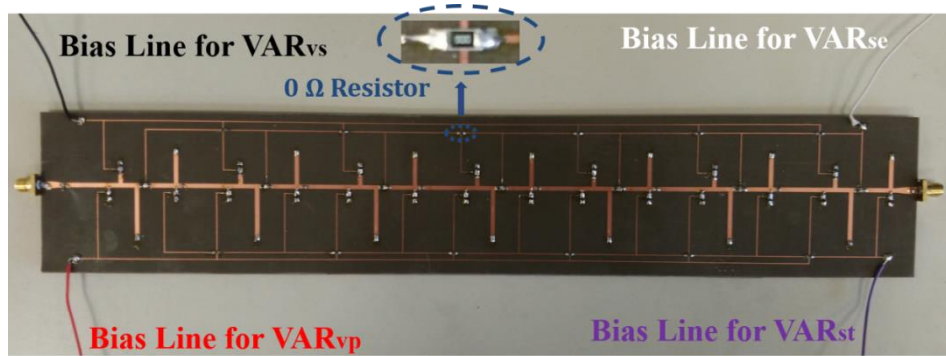


Figure 5.40 Photograph of this tunable LWA with 7 cascaded *Supercell\_v2* structures.

In addition, SMD 0402 1 M $\Omega$  resistors are used as the RF blocks in this *Supercell\_v2* structure. In order to electronically tune the capacitance of the varactors, the positive (“+”) DC bias are applied to this tunable *Supercell\_v2* structure through bias lines. The photograph of this fabricated tunable LWA with all SMD components is shown in Figure 5.40. This tunable LWA structure consists of 7 cascaded *Supercell\_v2* structures. In the bias network, in order to avoid overlapping of these bias lines on the same metal layer, the SMD 0805 0  $\Omega$  resistors are used as jumpers in this antenna structure. The total length and width of the fabricated LWA are 384.5 mm and 70 mm, respectively.

### 5.4.3.2 Frequency responses

#### (1) Initial state

In the initial state of this LWA, the DC bias applied to VAR<sub>se</sub>, VAR<sub>vs</sub>, VAR<sub>vp</sub>, and VAR<sub>st</sub> are 3 V, 0 V, 0 V, and 14.5 V, respectively. Figure 5.41 presents the measured and simulated results of S11 and S21 of this LWA in the initial state over 0.5-5.0 GHz. In simulations, the equivalent model of this varactor  $R_s = 0.8 \Omega$ ,  $L_s = 0.45 \text{ nH}$ ,  $C_p = 1.15 \text{ pF}$ , and  $C_j = 3.8 \text{ pF}$  is used in the initial state. Figure 5.41 shows that this

tunable LWA has two distinct passbands at the low and high frequencies separated by a middle separation area. Within this middle separation area, there is an unmatched passband over 2.2-2.5 GHz. Because two CRLH passbands are the main interest in this LWA design, this unmatched passband is not discussed here. In measurements, the -6 dB bandwidth of the low and high passband is 0.79-1.41 GHz and 2.8-4.3 GHz, respectively. The measured results show that there is a small open-stopband area existing at around 1.08 GHz within the low CRLH passband.

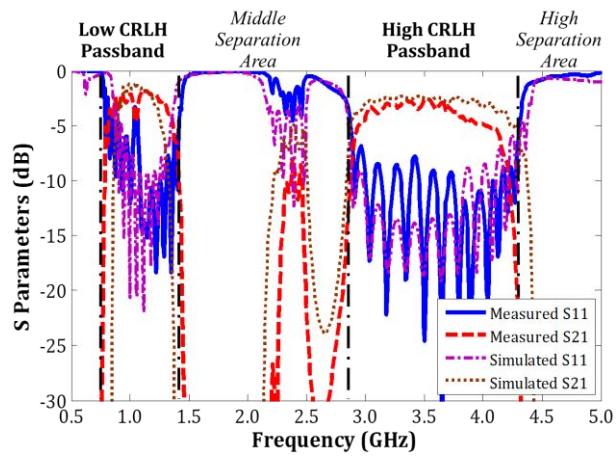


Figure 5.41 Measured and simulated results of S11 and S21 of this tunable LWA in the initial state.

## (2) Tuning and controlling states

Table 5.8 List of all states with different sets of DC bias voltages.

	DC Bias Voltages to VAR <sub>sc</sub> (V)	DC Bias Voltages to VAR <sub>vs</sub> (V)	DC Bias Voltages to VAR <sub>vp</sub> (V)	DC Bias Voltages to VAR <sub>st</sub> (V)
<i>Initial State</i>	3.0	0	0	14.5
<i>2nd State</i>	5.3	4.0	0	14.5
<i>3rd State</i>	7.6	8.0	0	14.5
<i>4th State</i>	8.4	14.5	0	14.5
<i>5th State</i>	3.0	0	14.5	14.5
<i>6th State</i>	3.0	0	14.5	0

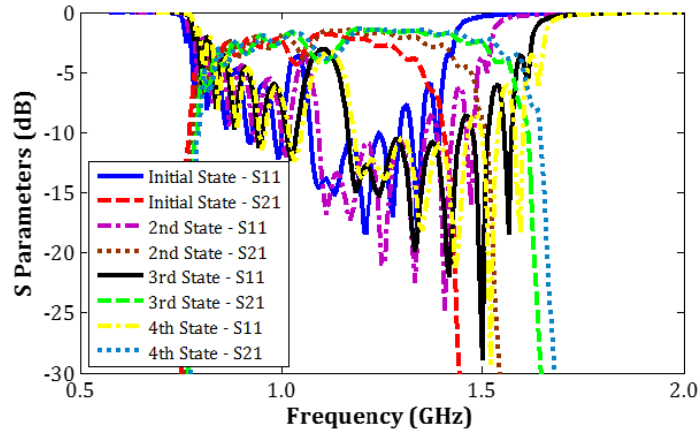


Figure 5.42 Comparison of the measured results of S11 and S21 of the low CRLH passband between the initial state and the tuning states.

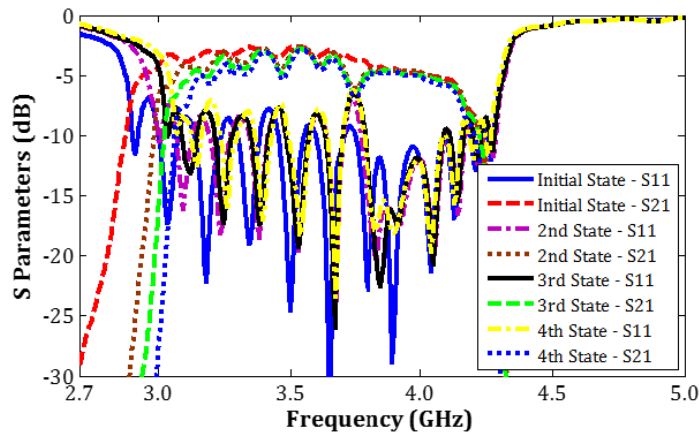


Figure 5.43 Comparison of the measured results of S11 and S21 of the high CRLH passband between the initial state and the tuning states.

Table 5.8 lists all the states with different applied DC bias voltages. The 2nd, 3rd and 4th state are defined as the tuning states, whereas the 5th and 6th state are defined as the controlling states. For this LWA, the balanced points within the low and high CRLH passband are labelled as the low and high balanced point, respectively. For the tuning states, the relatively independent tunability of the low balanced point is achieved by applying different sets of DC bias voltages to  $VAR_{se}$  and  $VAR_{vs}$  with little effects on the operation condition and the band coverage of the high CRLH passband. For the controlling states, the operation condition of the high CRLH passband is

adjusted without obvious effects on the balanced condition of the low CRLH passband by applying different sets of DC bias voltages to  $VAR_{vp}$  and  $VAR_{st}$ .

The tuning states (i.e., the 2nd, 3rd, and 4th states) are mainly used to explain the relatively independent tunability of the low CRLH passband by applying different sets of DC bias voltages to  $VAR_{se}$  and  $VAR_{vs}$ . Figure 5.42 shows the comparison of the measured results of S11 and S21 for the low CRLH passband between the initial state and the tuning states. In Figure 5.42, the low balanced point is electronically tuned upwards from the initial state to the 4th state in terms of the operating frequency. In the 4th state, the low CRLH passband has the -6 dB bandwidth of 0.81-1.64 GHz. Figure 5.43 presents the comparison of the measured results of S11 and S21 for the high CRLH passband of this LWA between the initial state and the tuning states. The compared results show that the band coverage of the high CRLH passband is affected and the operation condition of the high CRLH passband is also affected slightly. In the 4th state, the -6 dB bandwidth coverage of the high CRLH passband is 3.0-4.3 GHz. A small open stopband appears at 3.8 GHz in the 4th state. Therefore, different sets of the bias voltages applied to  $VAR_{se}$  and  $VAR_{vs}$  and the fixed DC bias to  $VAR_{vp}$  and  $VAR_{st}$  can mainly achieve the relatively independent tunability of the low CRLH passband and have some small effects on the band coverage and operation condition of the high CRLH passband. However, the CRLH characteristics within the high CRLH passband are maintained even though its band coverage is slightly affected.

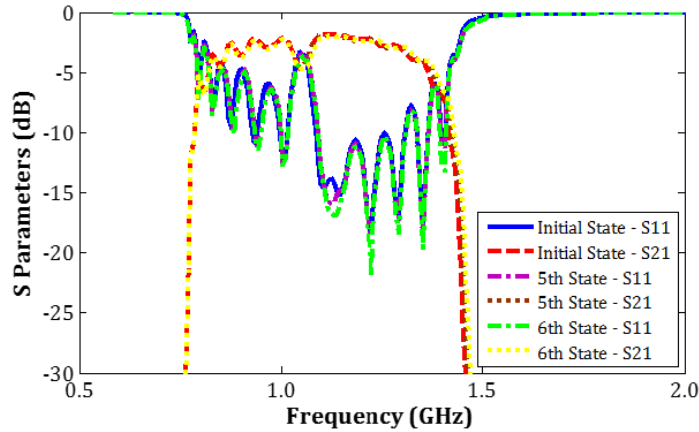


Figure 5.44 Comparison of the measured results of S11 and S21 of the low CRLH passband between the initial state and the controlling states.

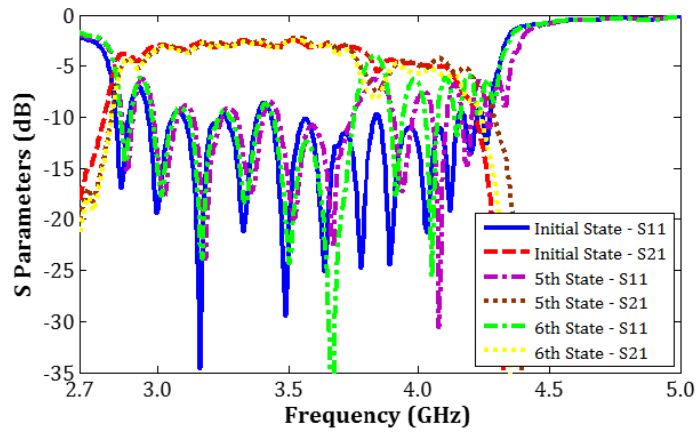


Figure 5.45 Comparison of the measured results of S11 and S21 of the high CRLH passband between the initial state and the controlling states.

The effects of different sets of the bias voltages to  $VAR_{vp}$  and  $VAR_{st}$  with the fixed bias voltages to  $VAR_{se}$  and  $VAR_{vs}$  are investigated by comparing the initial state and the controlling states. Figure 5.44 shows that the comparison of the measured results of S11 and S21 for the low CRLH passband between the initial state and the controlling states. The results show that the low CRLH passband is not clearly affected in the initial, 5th, and 6th states. Figure 5.45 shows that the comparison of the measured results of S11 and S21 for the high CRLH passband between the initial state and the controlling states. Figure 5.45 shows that the operation condition of the high

CRLH passband changes from the balanced condition in the initial state to the slightly unbalanced condition in the 6th state. In the 6th state, a small open stopband between the LH and RH band within the high CRLH passband appears at 3.8 GHz. Therefore, different sets of the bias voltages applied to  $\text{VAR}_{\text{vp}}$  and  $\text{VAR}_{\text{st}}$  and the fixed DC bias to  $\text{VAR}_{\text{se}}$  and  $\text{VAR}_{\text{vs}}$  can mainly affect the operation condition of the high CRLH passband without affecting the performance of the low CRLH passband.

In summary, the capacitance tuning of  $\text{VAR}_{\text{se}}$  and  $\text{VAR}_{\text{vs}}$  by supplying different DC bias voltages enables relatively independent tunability of the low balanced point. Simultaneously, the capacitance tuning of  $\text{VAR}_{\text{se}}$  and  $\text{VAR}_{\text{vs}}$  has effects on the band coverage of the high CRLH passband and has slight effects on its operation condition. However, the conventional CRLH characteristics of the high CRLH passband are maintained during the capacitance changing of  $\text{VAR}_{\text{se}}$  and  $\text{VAR}_{\text{vs}}$ . The capacitance tuning of  $\text{VAR}_{\text{vp}}$  and  $\text{VAR}_{\text{st}}$  is mainly used to adjust the operation condition of the high CRLH passband.

### 5.4.3.3 Dispersion relations

The corresponding dispersion relation of this tunable *Supercell\_v2* structure can be derived using Eq. (5-22):

$$\beta \cdot P4 = \cos^{-1}\left(\frac{A+D}{2}\right) \quad \text{Eq. (5-22)}$$

Figure 5.46 shows the comparison of the simulated dispersion diagrams of this tunable *Supercell\_v2* structure in the initial and 4th states. It proves the phenomenon discovered in Figure 5.42 and Figure 5.43. The low CRLH passband is relatively

independently tuned from the initial state to the 4th state with slight effects on the operation condition of the high CRLH passband. It is obvious that the low balanced point is tuned from 1.03 GHz in the initial state to 1.12 GHz in the 4th state, which achieves a relative tunability of around 8.9%. Simultaneously, the operation condition of the high CRLH passband is transferred from the balanced condition to the slightly unbalanced condition.

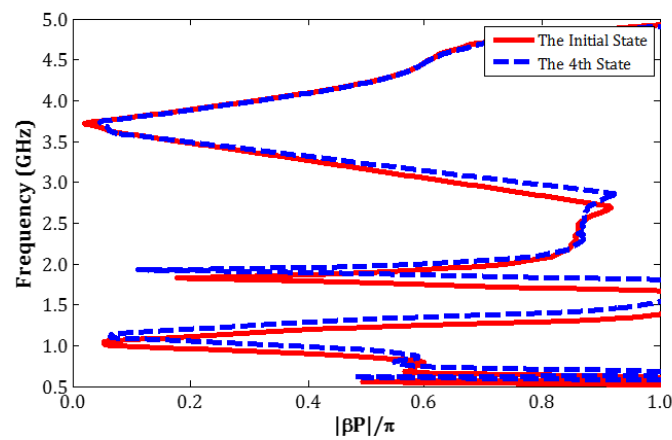


Figure 5.46 Comparison of the simulated dispersion diagrams of the single tunable *Supercell\_v2* structure between the initial state and the 4th state.

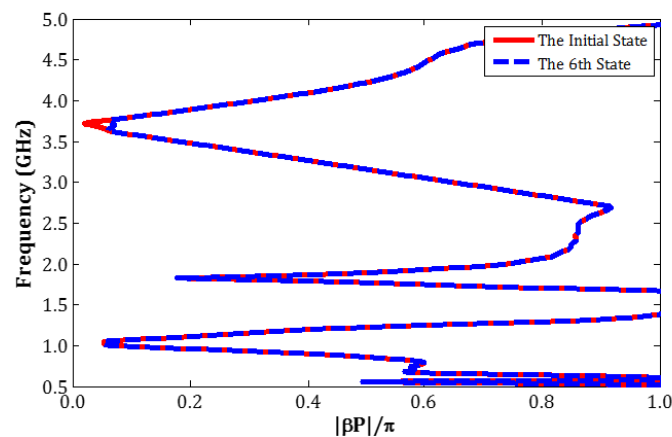


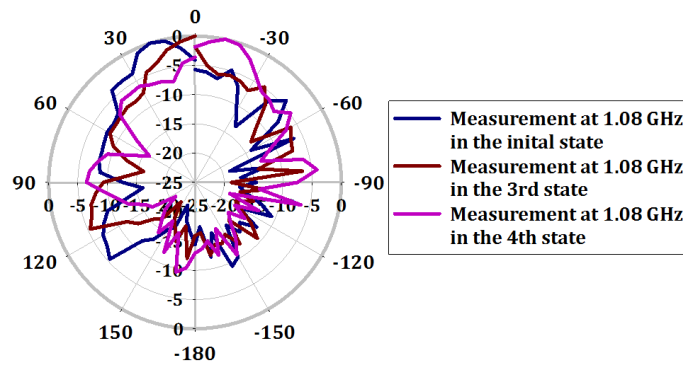
Figure 5.47 Comparison of the simulated dispersion diagrams of the single tunable *Supercell\_v2* structure between the initial state and the 6th state.

Figure 5.47 shows the comparison of the simulated dispersion diagrams of this tunable *Supercell\_v2* structure in the initial and 6th states. It shows that there is no

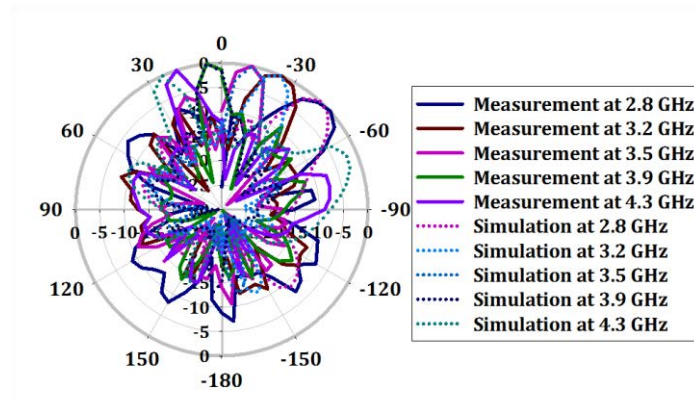
obvious change within the low CRLH passband between the initial and the 4th states.

However, the high CRLH passband in the 6th state has an open stopband appearing between the LH and RH band in comparison with the high CRLH passband in the initial state.

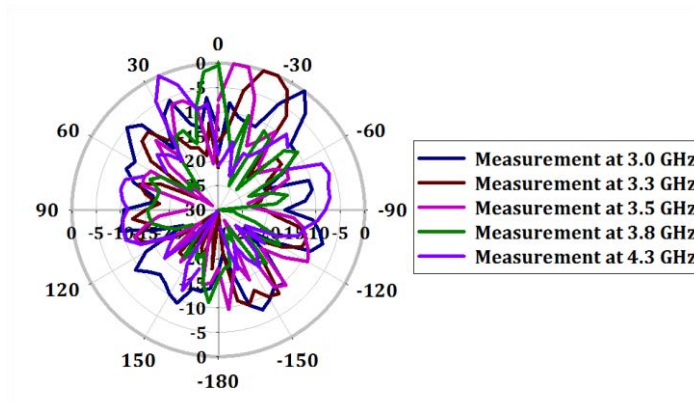
#### 5.4.3.4 Farfield patterns



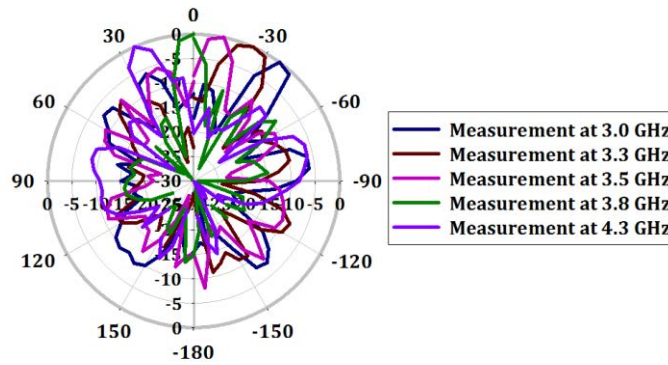
(a)



(b)



(c)



(d)

Figure 5.48 Co-polarized normalized farfield patterns of the tunable LWA at the XOZ plane, (a) the measured results at 1.08 GHz in the initial, 3rd, and 4th states; (b) the measured and simulated results over 2.8-4.3 GHz in the initial state; (c) the measured results over 3.0-4.3 GHz in the 3rd state; (d) the measured results over 3.0-4.3 GHz in the 4th state.

This tunable LWA achieves electronically controlled steering of the main beam at a fixed frequency within the low CRLH passband while simultaneously maintaining the conventional frequency scanning within the high CRLH passband. For the low CRLH passband, the measured normalized co-polarized farfield patterns at the XOZ plane for the main beam steering within the low CRLH passband are shown in Figure 5.48(a). It shows that the main beam of this LWA is electronically steered between  $+18^\circ$  in the initial state and  $-12^\circ$  in the 4th state at a fixed frequency of 1.08 GHz. For the high CRLH passband, the conventional frequency scanning characteristics of the main beam are maintained in the initial, 3rd and 4th state. The measured normalized co-polarized farfield patterns at the XOZ plane within the high CRLH passband in the initial, 3rd and 4th state are shown in Figure 5.48(b), Figure 5.48(c), and Figure 5.48(d), respectively. Figure 5.48(b) shows that the main beam scans from  $-48^\circ$  at 2.8 GHz to  $+24^\circ$  at 4.3 GHz in the initial state. Due to the effects from the capacitance changing of  $VAR_{se}$  and  $VAR_{vs}$  on the band coverage of the high

CRLH passband, Figure 5.48(c) shows that the main beam of this antenna scans from  $-36^\circ$  at 3.0 GHz to  $+24^\circ$  at 4.3 GHz in the 3rd state, and Figure 5.48(d) shows that the main beam of scans from  $-36^\circ$  at 3.0 GHz to  $+24^\circ$  at 4.3 GHz in the 4th state as well.

#### 5.4.3.5 Gains and directivities

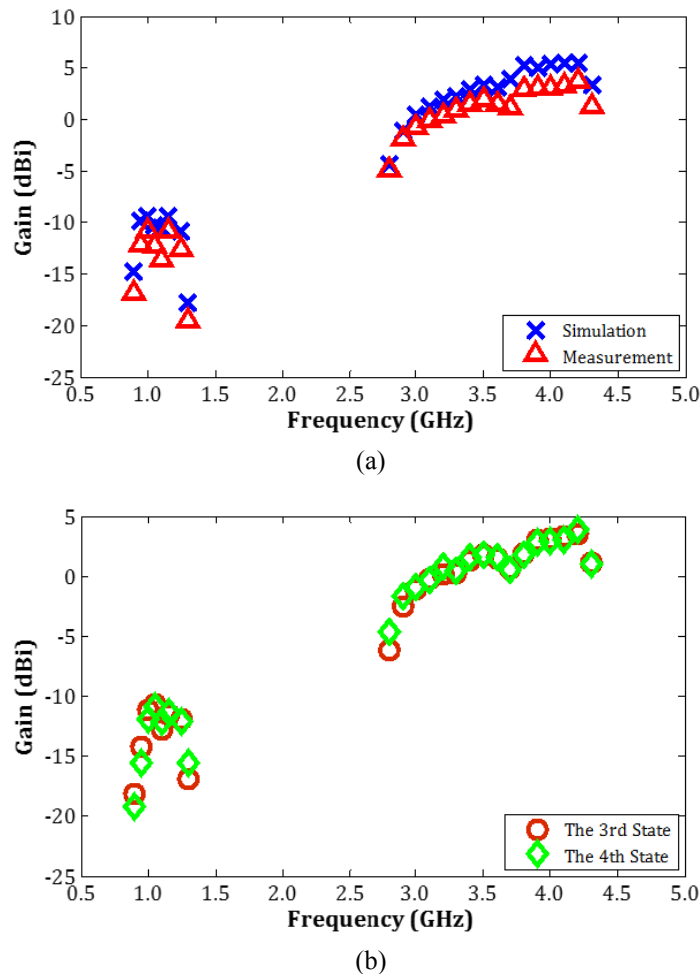


Figure 5.49 Gains of this tunable LWA, (a) the simulated and measured results in the initial state; (b) the measured results in the 3rd and 4th states.

Figure 5.49(a) presents the measured and simulated gains of this LWA in the initial state as an example. The measured peak gains within the low and high CRLH passband are -10 dBi and 3.67 dBi, respectively. Figure 5.49(b) presents the measured gains of the LWA in the 3rd and 4th state. Figure 5.49(b) shows that the measured

gains of this LWA in the 3rd and 4th states are almost the same as the gains in the initial state. The simulated directivities of this LWA are shown in Figure 5.50.

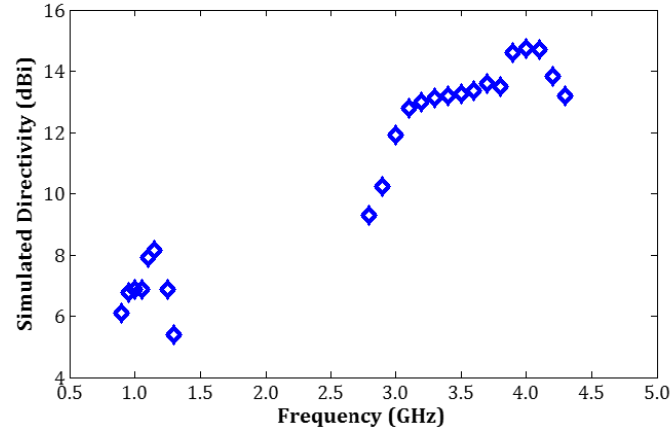


Figure 5.50 Simulated directivities of this tunable LWA at the leaky-wave regions with both passbands.

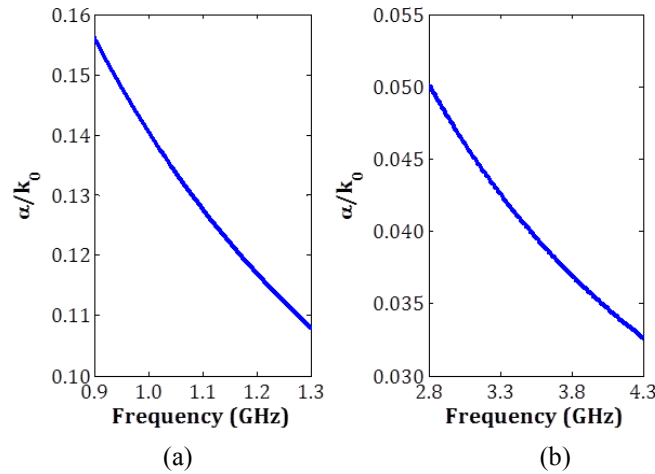


Figure 5.51 Leakage rates of this tunable LWA in the initial state at the leaky wave regions with both CRLH passbands, (a) 0.9-1.3 GHz; (b) 2.8-4.3 GHz.

The differences between the full-wave simulated and measured results are summarized as the following reasons:

- (1) the fabrication and measurement deviations;
- (2) the loss resulting from soldering;
- (3) the parasitic effects and losses from the SMD components, particularly the semiconductor varactors and the 1 M $\Omega$  and 0  $\Omega$  resistors.

Similarly, this tunable LWA also suffers from low gain, particularly for the low passband, due to the same reasons that the limited size of the PCB and the antenna aperture is ineffective at the low frequencies. The most of the accepted power by this LWA is absorbed by an absorption load at one end of the antenna and just a small amount of the power is radiated, which results in high leakage rates. The leakage rates of this tunable LWA at the leaky wave regions within both CRLH passbands in the initial state are also calculated in the same way, which are shown in Figure 5.51. The gains of this tunable antenna can be improved by cascading more *Supercell\_v2* structures. In simulation, a LWA with 25 *Supercell\_v2* structures can achieve the peak gains of -1.7 dBi and 9.7 dBi within the low and high CRLH passband, respectively.

#### **5.4.3.6 Loss of varactors and chip capacitors**

The SMD components (e.g., varactors, chip capacitors, 1 M $\Omega$  resistors and 0  $\Omega$  resistors) in this structure introduce some losses to degrade the antenna radiation performance. The detailed information of the *SKYWORKS SMV1234-040LF* silicon semiconductor varactor can be found in Appendix C, and the *MURATA* 0402 chip capacitors can be found in Appendix A.

The losses introduced by all SMD components adversely affect the antenna radiation performance. Thus, the losses introduced by the varactors and the chip capacitors are evaluated in two scenarios in the simulation. The LWA in the initial state is taken as an example for the loss evaluation. In the 1st lossless scenario, the equivalent resistance (i.e.  $R_s$ ) in the equivalent model of the varactor is removed; in the 2nd

lossless scenario, the SMD chip capacitors are replaced by the lossless capacitors, in addition to the 1st scenario of the removal of  $R_s$ .

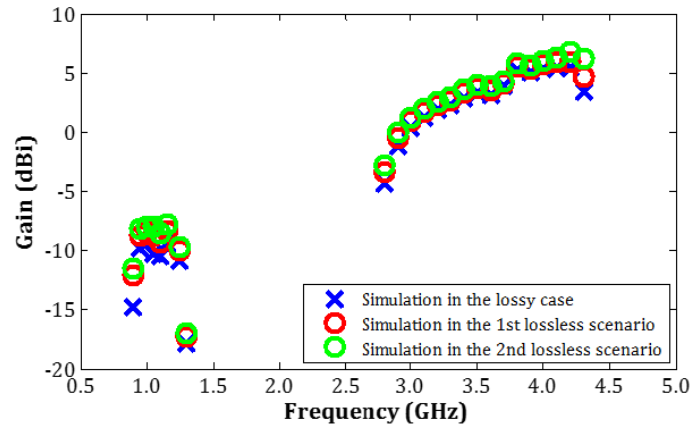


Figure 5.52 Comparison of the simulated gains the leaky-wave regions within both CRLH passbands in the lossy, and the 1st and 2nd lossless scenario.

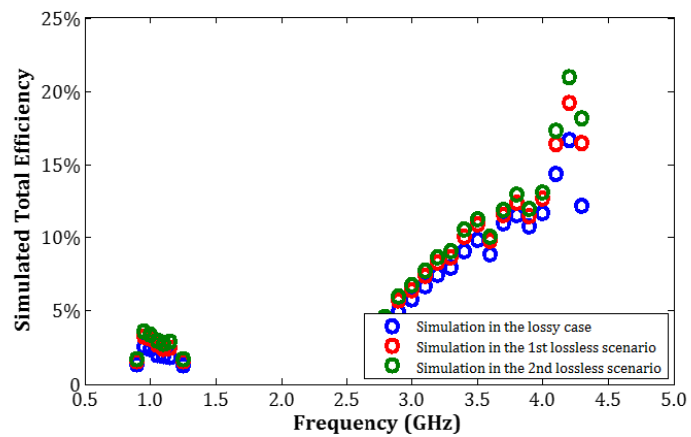


Figure 5.53 Comparison of the simulated total efficiencies at the leaky-wave regions within both CRLH passbands in the lossy, and the 1st and 2nd lossless scenario.

The comparisons of the simulated gains and total efficiencies of this LWA in the lossy case, and the 1st and 2nd lossless scenario are presented in Figure 5.52 and Figure 5.53, respectively. After comparing the simulated gain results, it is observed that the varactors and chip capacitors introduce the loss of 0.8-2.6 dBi and 0.3-0.8 dBi to degrade the antenna gain at the low leaky-wave region, respectively. For the high

leaky-wave region, 0.3-1.4 dBi and 0.2-0.7 dBi gain degradations are introduced by the varactors and capacitors, respectively. In terms of the total efficiency, it is observed that the varactors and chip capacitors result in the decrease of the total efficiencies with 0.2%-1.2% within the low CRLH passband and 0.8-4.5% within the high CRLH passband, depending on the operating frequencies.

## 5.5 Summary

Table 5.9 Summary of the LWAs in this chapter.

	<b>Passive ECR LH LWA</b>	<b>Passive Supercell_v1 LWA</b>	<b>Passive Supercell_v2 LWA</b>	<b>Tunable Supercell_v2 LWA</b>
Antenna Dimensions	280.4 mm × 50 mm × 1.575 mm	281 mm × 50 mm × 1.575 mm	325 mm × 45 mm × 1.575 mm	384 mm × 70 mm × 1.575 mm
Passband Coverage	0.6~1.55 GHz; 3.1~6.5 GHz	0.8~1.55 GHz; 3.1~6.5 GHz	0.88~1.56 GHz; 3.65~5.3 GHz	0.79~1.41 GHz (Initial State); 2.8~4.3 GHz (Initial State)
Leaky Wave Regions	0.9~1.25 GHz; 3.1~3.6 GHz; 5.7~6.2 GHz	0.88~1.25 GHz; 3.7~5.3 GHz	0.9~1.3 GHz; 3.8~5.7 GHz	Around 1.08 GHz (Initial State); 2.8~4.3 GHz (Initial State)
Antenna Characteristics	(1) CRLH in the low passband; (2) RH at the low edge of the high passband; (3) RH at the low edge of the high passband	(1) CRLH in the low passband; (2) CRLH in the high passband;	(1) CRLH in the low passband; (2) CRLH in the high passband;	(1) CRLH in the low passband; (2) CRLH in the high passband; (3) Tunability of the low balanced point with retaining the high balanced point
Peak Gain of Each Leaky Wave Region	(1) -10.2 dBi; (2) -1.2 dBi; (3) 8.5 dBi	(1) -10.1 dBi; (2) 2.14 dBi	(1) -8.5 dBi; (2) 3.9 dBi	(1) -10 dBi (Initial State); (2) 3.67 dBi (Initial State)
Scanning Angles	(1) -42° ~ +36° ; (2) +10° ~ +60° ; (3) -80° ~ -25°	(1) -45° ~ +35° ; (2) -45° ~ +30°	(1) -40° ~ +45° ; (2) -45° ~ +20°	(1) -12° ~ +18° (4th State ~ Initial State); (2) -48° ~ +24° (Initial State)

In this chapter, four microstrip dual-band LWAs are presented with step-by-step

advances in different leaky-wave radiation characteristics. The LWA based on the ECRLH structure with SMD chip capacitors achieves the backward-to-forward frequency scanning at the low passband, the forward frequency scanning at the low edge of the high passband, and the backward frequency scanning at the high edge of the high passband, respectively. The LWAs based on the cascaded *Supercell\_v1* and *Supercell\_v2* structures with SMD chip capacitors achieve the backward-to-forward frequency scanning within both the low and high passbands. Furthermore, an electronically tunable LWA with SMD semiconductor varactors achieves relatively independent tunability of the low balanced point while maintaining the frequency position of the high balanced point and the backward-to-forward CRLH leaky-wave characteristics within the high CRLH passband. The summary of the LWAs presented in this chapter is listed in Table 5.9. Compared to most existing designs, the LWAs based on the *Supercell\_v1* and *Supercell\_v2* structures have the following advantages:

- (1) two distinct CRLH passbands and the CRLH backward-to-forward leaky-wave radiation characteristics within both passbands;
- (2) for the tunable design, the relative independent tunability of the low balanced point with maintaining the frequency position of the high balanced point and the CRLH backward-to-forward leaky-wave radiation characteristics within the high passbands.

# CHAPTER VI

## UNCERTAINTY ANALYSIS OF DETERMINATION IN PERMITTIVITY OF FERROELECTRIC MATERIALS AND IMPLICATIONS FOR DESIGN OF A CRLH-BASED LEAKY WAVE ANTENNA

### 6.1 Introduction

The FE BST material is one of the most popular tunable materials for microwave applications, due to its properties, such as the high electric-field-dependent dielectric permittivity and the relatively low dielectric loss tangent at microwave frequencies [43]. Depending on the composition and fabrication techniques of BST materials, the dielectric permittivity can generally achieve a few hundreds or even thousand, which is favorable for miniaturization of antenna or component designs at microwave frequencies. Typically, the DC bias voltages of 2-8 V/ $\mu\text{m}$  are applied across the BST material in order to tune its permittivity by up to 60% [43]. The DC bias voltage needed for BST materials is determined by the thickness of the BST layer for a

parallel-plate varactor or the gap width in the metallization for a planar varactor [47]. The typical thickness of the BST layer is around 0.4-1.0  $\mu\text{m}$  or the gap width is around 10-50  $\mu\text{m}$ . The FE BST materials have been applied to many component designs at microwave frequencies, such as tunable antennas and phased arrays based on BST varactors [44]-[47], phase shifters [57], [58], and tunable filters [59], [60].

This chapter is organized as follows. The FE BST material is briefly introduced in Section 6.2. In Section 6.3, a microstrip LWA based on the CRLH structure with integration of discrete BST interdigital varactors is described. In Section 6.4, the uncertainty analysis in determination of permittivity of the BST material is presented. The summary is given in Section 6.5. This work was undertaken as a side project to the main work of the thesis and was published in the proceedings of 2015 Joint IEEE International Symposium on the Applications of Ferroelectric (ISAF) [61].

## **6.2 Background of BST Material**

Two quantities are generally used to describe the electric-field-dependent permittivity. The complex expression of a complex quantity is  $\epsilon_r = \epsilon_r' - j\epsilon_r''$ .  $\epsilon_r'$  is the real part of the complex permittivity, which expresses the stored energy in the dielectric medium and generally referred to as the relative permittivity or dielectric constant; and  $\epsilon_r''$  is the imaginary part of the complex permittivity, which expresses the dissipated energy in the dielectric medium. The tunability ( $n$ ) is defined as the ratio of  $\epsilon_r'$  under zero electric-field bias (0) to  $\epsilon_r'$  under a non-zero electric-field bias (E)

[43]. The relative tunability ( $n_r$ ) is defined the ratio of the change in  $\epsilon_r'$  between the zero and a defined electric-field bias with respect to  $\epsilon_r'$  under the zero electric-field bias [43]. The tunability and the relative tunability are expressed in Eq. (6-1) and Eq. (6-2), respectively:

$$n = \epsilon_r'(0) / \epsilon_r'(E) \quad \text{Eq. (6-1)}$$

$$n_r = [\epsilon_r'(0) - \epsilon_r'(E)] / \epsilon_r'(E) \quad \text{Eq. (6-2)}$$

The loss tangent ( $\tan\delta$ ) of the BST film is defined as the ratio the imaginary and real parts of the dielectric permittivity [43], which is shown in Eq. (6-3):

$$\tan\delta = \frac{\text{Im}(\epsilon_r)}{\text{Re}(\epsilon_r)} = \frac{\epsilon_r''}{\epsilon_r'} \quad \text{Eq. (6-3)}$$

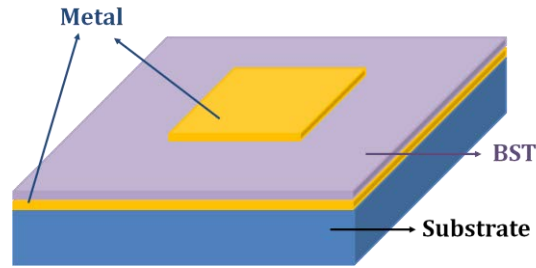
The quality factor, i.e.,  $Q = 1/\tan\delta$ , is another way to describe the loss of the material [43].

The FE BST film varactors normally can be constructed in two different types – parallel-plate type and co-planar type. Illustrations of a parallel-plate and planar BST varactor are shown in Figure 6.1(a) and Figure 6.1(b), respectively.

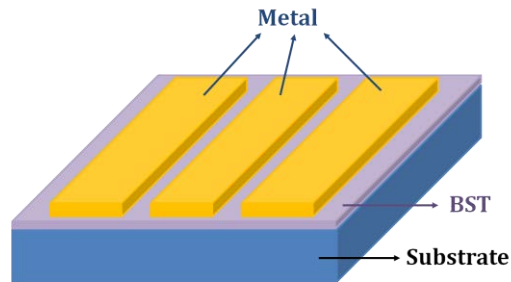
The commutation quality factor (CQF) is an important parameter to measure the performance of the FE BST varactor, which is expressed in Eq. (6-4) [43]:

$$\text{CQF} = (n - 1)^2 / (n \cdot \tan\delta_1 \cdot \tan\delta_2) \quad \text{Eq. (6-4)}$$

where  $n$  is the tunability defined in Eq. (6-1),  $\tan\delta_1$  and  $\tan\delta_2$  are the loss tangents of the FE BST varactor under the zero and non-zero DC bias voltages, respectively.



(a)



(b)

Figure 6.1 Types of the BST varactors, (a) parallel-plate type; (b) planar type.

Table 6.1 Comparison of BST with GaAs and MEMS techniques [43].

	<b>BST</b>	<b>GaAs</b>	<b>MEMS</b>
<i>Tunability (n)</i>	~2-4:1	~2-6:1	~1.5-3:1
<i>Q Value</i>	~20-100	~20-50	Very high
<i>Control Voltage</i>	< 15 V (Parallel-plate)	< 15 V	< 50 V
<i>Tuning Speed</i>	~ 10 <sup>-9</sup> s	~10 <sup>-6</sup> s	~10 <sup>-5</sup> s
<i>Reliability</i>	Good	Good	Poor
<i>Cost</i>	Low	High	High
<i>Power Handling</i>	Good	Poor	Good

The desired parameters of the BST thin-film varactors at microwave frequencies have been briefly summarized: (1) low loss tangent, i.e.,  $\tan\delta < 0.01$ ; (2) high tunability, i.e.,  $n > 2$  or  $n_r > 50\%$ ; (3) low loss of production on inexpensive substrates; (4) reliability and reproducibility [43]. A comparison of the BST varactor with other two types of varactor technologies, i.e., GaAs semiconductor varactors and micro-electrical mechanical systems varactors, is presented in Table 6.1 [34].

Obviously, compared to GaAs and MEMS varactors, the varactors with BST materials are a very good option for tunable component designs at microwave frequencies.

### 6.3 CRLH-Based LWA with BST Varactors

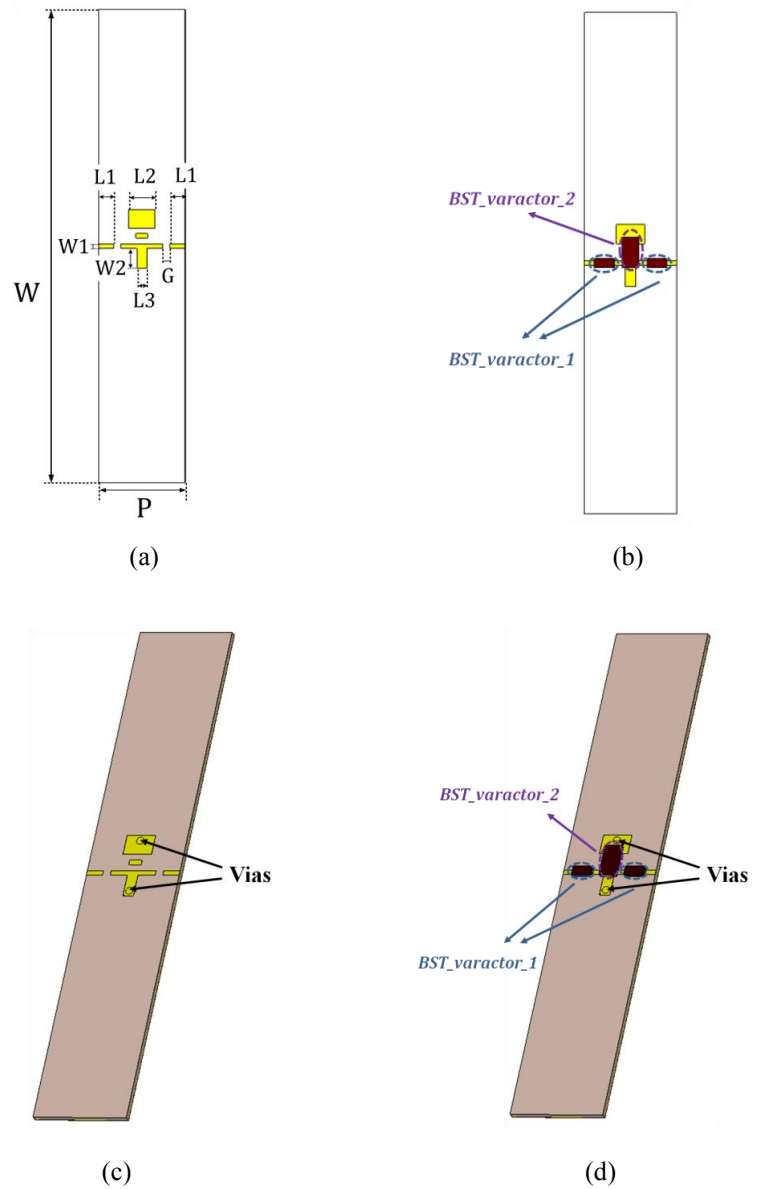


Figure 6.2 Expanded views of the CRLH unit cell with and without BST varactors, (a) top view without BST varactors; (b) top view with BST varactors; (c) perspective view without BST varactors; (d) perspective view with BST varactors.

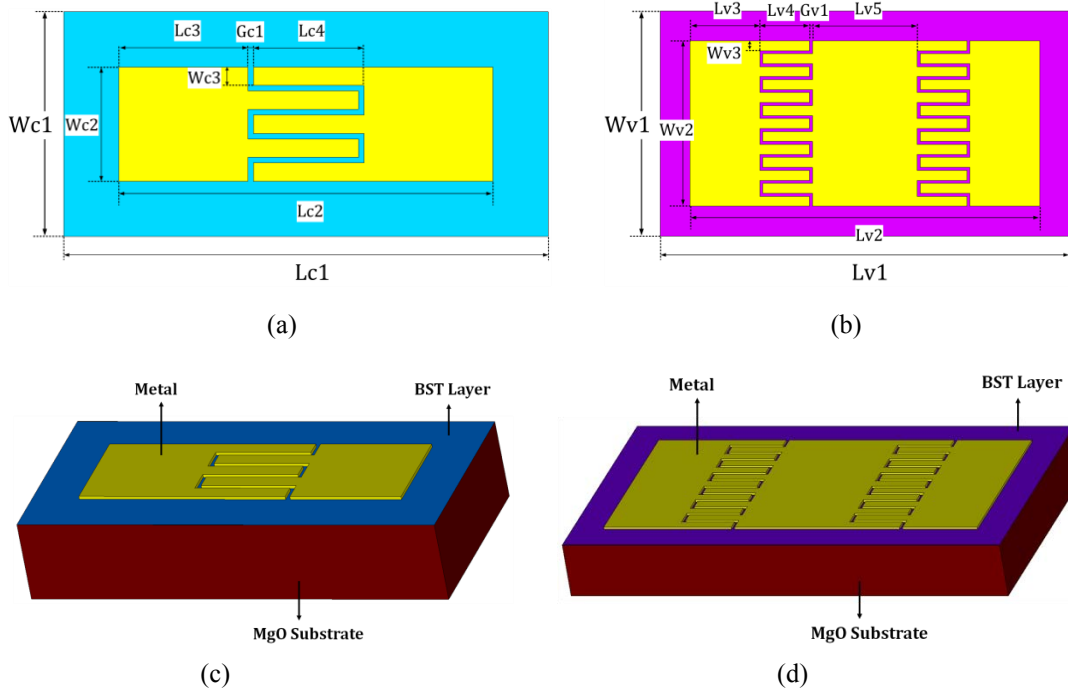


Figure 6.3 Expanded views of the discrete BST varactors, (a) top view of *BST\_varactor\_1*; (b) top view of *BST\_varactor\_2*; (c) perspective view of *BST\_varactor\_1*; (d) perspective view of *BST\_varactor\_2*.

A microstrip LWA based on the CRLH structure with discrete FE BST interdigital varactors has been simulated in the software *CST Microwave Studio*. This antenna structure is composed of multiple cascaded CRLH unit cells with discrete BST varactors. The discrete BST varactors are integrated with the antenna structure in a flip-chip way. This antenna is simulated on *Rogers RT/duroid 6002* of thickness 0.762 mm, permittivity 2.94, and loss tangent 0.0012. Expanded views of one CRLH unit cell without the BST varactors and with the BST varactors are shown in Figure 6.2(a), Figure 6.2(b), Figure 6.2(c), and Figure 6.2(d), respectively. In this unit cell structure, three BST varactors are used as discrete tuning elements. Two identical BST varactors are represented as *BST\_varactor\_1*, while the other one is represented as *BST\_varactor\_2*. Expanded views of *BST\_varactor\_1* and *BST\_varactor\_2* are presented in Figure 6.3. The detailed dimensions of the CRLH unit cell,

$BST\_varactor\_1$  and  $BST\_varactor\_2$  are listed in Table 6.2.

Table 6.2 Dimensions of one CRLH unit cell and BST varactors.

Symbol	Value (mm)	Symbol	Value (mm)	Symbol	Value (mm)
P	12.32	Lc1	2.63	Lv1	4.11
L1	2.15	Lc2	2.03	Lv2	3.51
L2	3.80	Lc3	0.70	Lv3	0.70
L3	1.40	Lc4	0.60	Lv4	0.50
W	67.00	Wc1	1.22	Lv5	1.05
W1	0.62	Wc2	0.62	Wv1	2.06
W2	2.84	Wc3	0.10	Wv2	1.66
G	1.03	Gc1	0.03	Wv3	0.10
				Gv1	0.03

For  $BST\_varactor\_1$  and  $BST\_varactor\_2$ , the BST layers used in the varactors are assumed to have the thickness of 600 nm. The BST films are grown on MgO substrates with thickness of around 0.5 mm, which was suggested by Dr M. M. Kechik and Dr T. J. Jackson [61]. The relative permittivity of MgO is 9.9. The gold layer is grown on the BST layer. For design purpose, the parameters closely to the BST layer at microwave frequencies were taken from typical literature values. Table 6.3 lists some parameters of the BST varactors in the antenna design in the simulation.

Table 6.3 Some parameters of the BST varactors in the LWA design in the simulation.

Symbol	Value	Explanation
$\epsilon_r'$ (0 V)	400	Permittivity of the BST layer under 0 V DC bias voltages
$n_r$	50%	Relative tunability of the permittivity of the BST layer
$\tan\delta$	0.02	Loss tangent of the BST layer
E	5 V/ $\mu\text{m}$	DC bias voltages applied to the BST layer per $\mu\text{m}$
$E_{\text{max}}$	150 V	Maximum DC bias voltages applied to tune each BST varactor

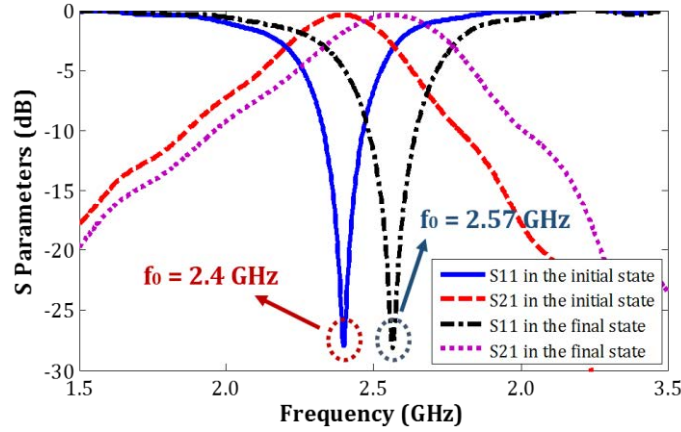


Figure 6.4 Simulated S11 and S21 of the CRLH unit cell in the initial and final state.

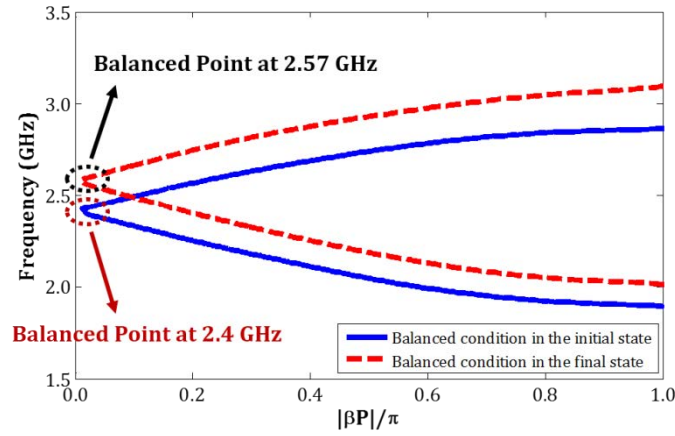


Figure 6.5 Simulated dispersion diagram of the CRLH unit cell in the initial and final state.

In the initial state, Figure 6.4 shows the simulated S11 and S21 of one CRLH unit cell with BST varactors under the 0 V DC bias voltages. The corresponding dispersion diagram can be derived using Eq. (3-26), which is shown in Figure 6.5. In the initial state that the 0 V bias is applied to both *BST\_varactor\_1* and *BST\_varactor\_2*, i.e.,  $\epsilon_r'$  of both BST films is 400, the resonant frequency of the single CRLH TL unit cell is at 2.4 GHz. Figure 6.5 shows that a balanced point exists at the transition frequency point of 2.4 GHz from the LH band to the RH band.

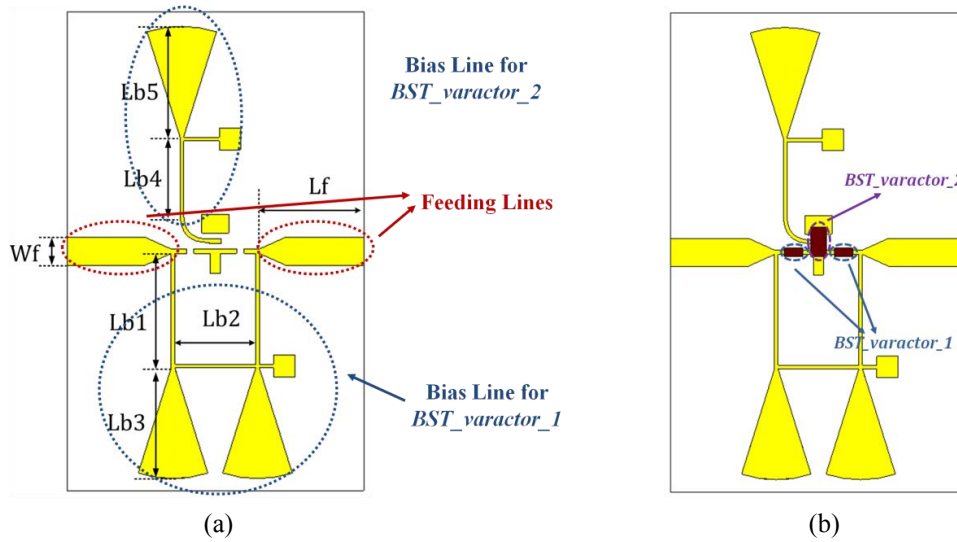


Figure 6.6 Configurations of the unit cell with feeding lines and bias lines, (a) without BST varactors; (b) with BST varactors.

Table 6.4 Dimensions of the feeding lines and bias lines.

Symbol	Value (mm)	Symbol	Value (mm)	Symbol	Value (mm)
Wf	3.9	Lb1	15.99	Lb3	14.94
Lf	14.6	Lb2	11.32	Lb4	10.00
				Lb5	14.94

In the final state, it is assumed that  $\epsilon_r'$  of *BST\_varactor\_1* and *BST\_varactor\_2* can be electronically tuned from 400 to 200 and from 400 to 250, respectively, i.e., the tunability of 50% and 37.5%, respectively. The resonant frequency of the unit cell is tuned by 7.1% totally. The simulated S parameters and corresponding dispersion diagram of the unit cell in the final state are also shown in Figure 6.4 and Figure 6.5, respectively. Figure 6.4 shows the resonant frequency shifts upwards by 170 MHz. Figure 6.5(b) shows the balanced point of this unit cell is at 2.57 GHz.

The configurations of the single unit cell with the feeding lines and bias lines are shown in Figure 6.6(a), and the complete unit cell with BST varactors is shown in Figure 6.6(b). The dimensions of the feeding lines and bias lines are listed in Table 6.4.

The bias lines are mainly composed of a quarter-wavelength ( $\lambda/4$ ) microstrip line and a radial stub. The bias lines are used to supply “+” DC bias voltages to all BST varactors in order to tune the permittivity of the BST films.

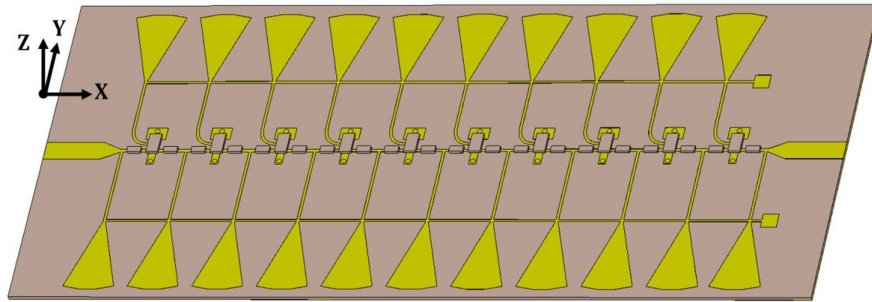


Figure 6.7 Complete configuration of the LWA with BST varactors.

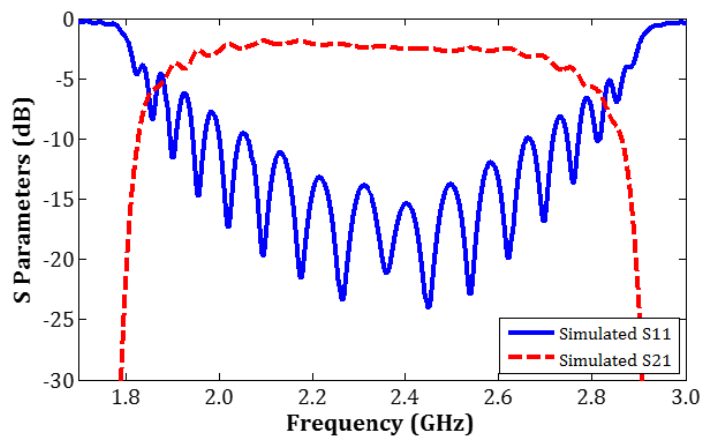


Figure 6.8 Simulated S parameters of the LWA in the initial state.

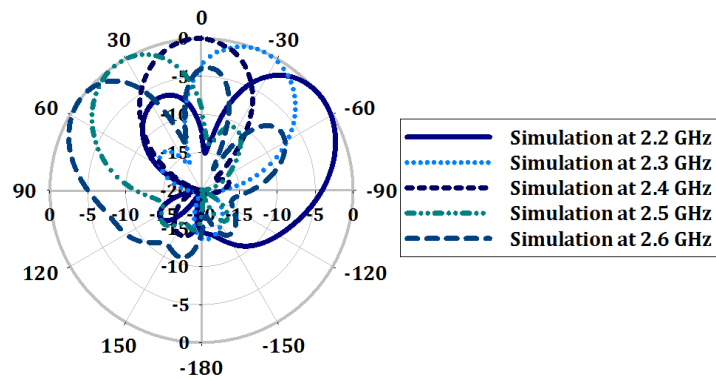


Figure 6.9 Simulated farfield patterns of the LWA over 2.2-2.6 GHz in the initial state.

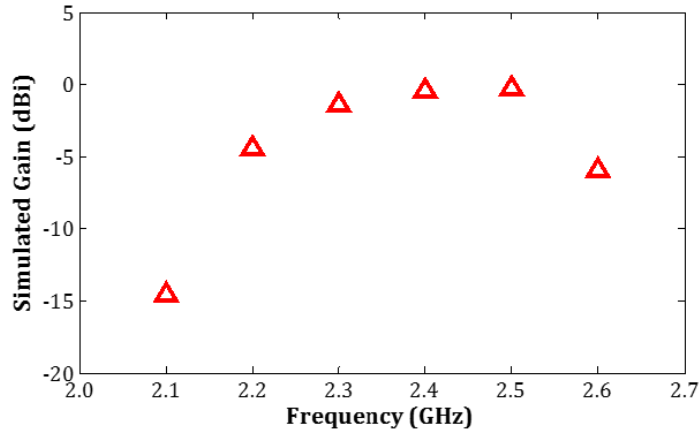


Figure 6.10 Simulated gains in dBi of the LWA over 2.1-2.6 GHz in the initial state.

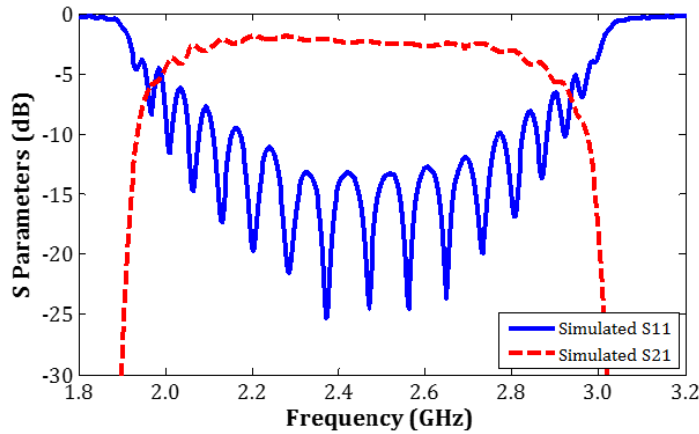


Figure 6.11 Simulated S parameters of the LWA in the final state.

The complete configuration of the proposed LWA with discrete BST varactors is shown in Figure 6.7. In this antenna structure, 10 CRLH unit cells with discrete BST varactors are cascaded together as the main antenna aperture. The simulated S parameters of this LWA in the initial state are presented in Figure 6.8. The operating frequency of the LWA is at 2.4 GHz in the initial state. The -6 dB bandwidth of this operating band is from 1.9 GHz to 2.7 GHz. The simulated normalized farfield patterns at the XOZ plane over 2.2-2.6 GHz at the leaky-wave regions are plotted in Figure 6.9. This LWA scans from  $-50^\circ$  to  $+55^\circ$  over 2.2-2.6 GHz. The simulated gains in dBi of this LWA at the leaky-wave radiation regions are presented in Figure 6.10.

The simulated peak gain at the leaky-wave regions is -0.3 dBi at 2.5 GHz. The gain can be improved by cascading more unit cells in the LWA structure.

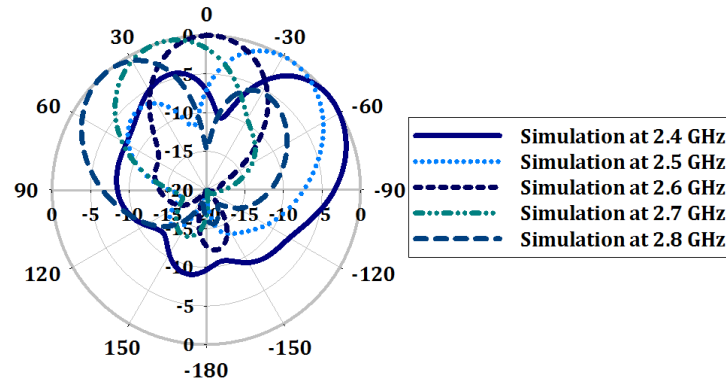


Figure 6.12 Simulated farfield patterns of the LWA over 2.4-2.8 GHz in the final state.

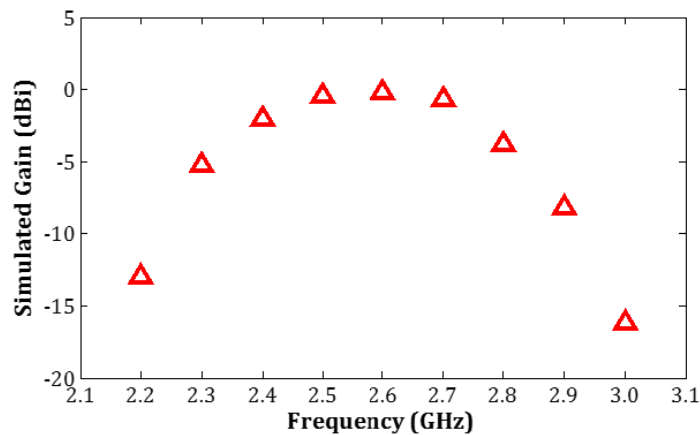


Figure 6.13 Simulated gains in dBi of the LWA over 2.2-3.0 GHz in the final state.

The simulated S parameters, the normalized farfield patterns at the XOZ plane, and the simulated farfield gains of this tunable LWA in the final state are shown in Figure 6.11, Figure 6.12, and Figure 6.13, respectively, using the same BST parameters for the single tunable unit cell. The balanced frequency point of the LWA in the final state is at 2.5 GHz. With respect to the -6 dB bandwidth, this antenna works from 2.0 GHz to 2.9 GHz. The operation frequency of the LWA shifts from 2.4 GHz to 2.6 GHz with a tunability of 4.1%. In this state, the main beam of the antenna scans from  $-55^\circ$  to

+45° over 2.4-2.8 GHz. The simulated peak gain of the LWA within the leaky-wave radiation region is -0.1 dBi at 2.6 GHz.

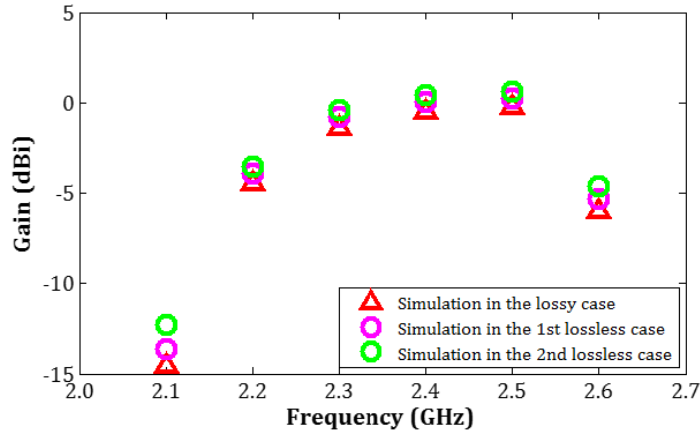


Figure 6.14 Comparison of the simulated gains in dBi of the LWA in the lossy and lossless cases under 0 V DC bias voltages.

The losses introduced by the BST materials in the LWA structure can be analyzed by comparing the lossy case and the lossless cases. In this 1st lossless case that the loss tangent of the BST films is set to be zero, i.e.,  $\tan\delta = 0$ , the simulated gains of LWA with the lossless BST materials under the 0 V DC bias voltages are shown in Figure 6.14. In the 2nd lossless case that the entire varactors are assumed to be lossless, the simulated gains with the entire lossless varactors under the 0 V DC bias voltages are also shown in Figure 6.14. After comparing the simulated gain results in Figure 6.14, around 0.5-0.8 dBi gain differences for the 1st lossless case and 0.9-2.3 dBi gain differences for the 2nd lossless case are observed, respectively. Thus, the BST materials in the antenna structure introduce around 0.5-0.8 dBi and all the varactors introduce around 0.9-2.3 dBi gain degradation for the LWA radiation performance.

## 6.4 Uncertainty Analysis

Table 6.5 Some parameters used in the uncertainty analysis.

Symbol	Value	Explanation
$c$	$3 \times 10^8$ m/s	Light speed in free space
$\epsilon_0$	$8.854 \times 10^{-12}$ F/m	Permittivity of free space
$Z_0$	$50 \Omega$	$50 \Omega$ characteristic impedance
$w$	0.05 mm	Width of the signal line
$s$	0.025 mm	Gap width between ground plane and signal line
$w_g$	0.25 mm	Width of the ground plane
$t$	0.005 mm	Thickness of the metal layer
$L_{CPW}$	2.5 mm	Entire length of the CPW TL
$H_2$	0.5 mm	Thickness of the MgO substrate
$\epsilon_{r\_sub}$	9.9	Permittivity of the MgO substrate
$\tan\delta_{sub}$	0.0001	Loss tangent of the MgO substrate
$H_1$	$0.6 \times 10^{-3}$ mm	Thickness of the BST layer
$\tan\delta_{BST}$	0.02	Loss tangent of the BST layer

In this section, the uncertainty in the determination of the BST permittivity is analyzed. It can be imagined that the “known” value is actually an expected value with a standard deviation which describes the probability that a particular varactor’s permittivity will be within a certain range around the expected value. The expected value is obtained from a characterization process. The uncertainty the determination of the BST permittivity will influence the initial capacitance (i.e., under 0 V DC bias voltages), which will further affect the initial state of the proposed LWA in Section 6.3. Specifically, the proposed LWA in the initial state was designed to work under the balanced condition. However, if the permittivity of BST materials is sufficiently different from the expected value, then there may result in a deviation from the balanced condition, causing an open stopband to exist between the LH and RH band.

Thus, the uncertainty analysis the determination of the BST permittivity can help us consider the uncertainty in the design. In this section, the uncertainty analysis of the calculation of the permittivity from the materials' characterization process is the main focus.  $\epsilon_{r\_BST}$  is the effective permittivity of the BST layer that we expect to calculate using the conformal mapping method.

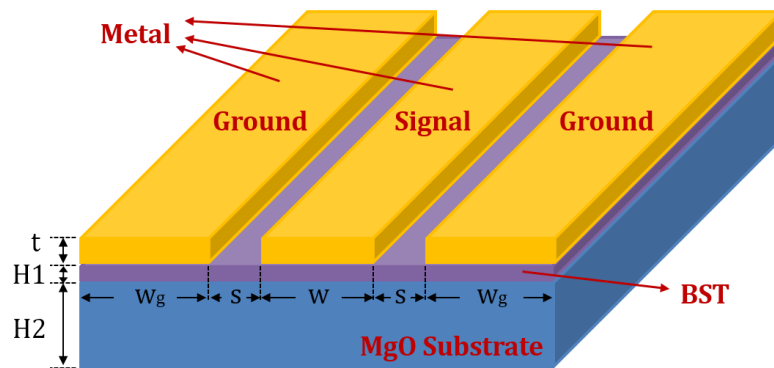


Figure 6.15 Two-layer CPW TL model.

The analysis is based on a two-layer CPW TL model in order to characterize the BST permittivity. The two-layer CPW model is presented in Figure 6.15. The dimensions of this CPW model are also represented in Figure 6.15. The BST layer is in the middle between the metal layer and the MgO substrate. Table 6.5 lists some parameters used in the uncertainty analysis.

The S parameters can be obtained from the full-wave simulations of this CPW model. For the analysis, the data are provided using the software SONET EM simulation [61]. Then, the transmission ABCD matrix can be obtained from the S parameters using the following equations:

$$A = \frac{(1+S_{11})(1-S_{22})+S_{12}S_{21}}{2S_{21}} \quad \text{Eq. (6-5)}$$

$$B = Z_0 \frac{(1+S_{11})(1+S_{22})-S_{12}S_{21}}{2S_{21}} \quad \text{Eq. (6-6)}$$

$$C = \frac{1}{Z_0} \frac{(1-S_{11})(1-S_{22})-S_{12}S_{21}}{2S_{21}} \quad \text{Eq. (6-7)}$$

$$D = \frac{(1-S_{11})(1+S_{22})+S_{12}S_{21}}{2S_{21}} \quad \text{Eq. (6-8)}$$

The complex propagation constant ( $\gamma$ ) of this CPW TL structure is expressed by

$$\gamma = \alpha + j\beta \quad \text{Eq. (6-9)}$$

where  $\alpha$  is the attenuation constant and  $\beta$  is the phase constant.

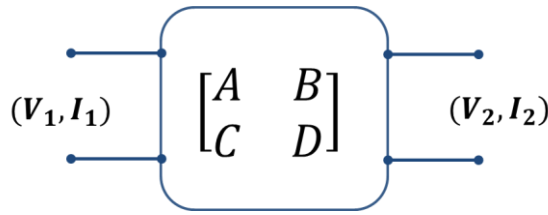


Figure 6.16 Two-port network in the transmission ABCD matrix.

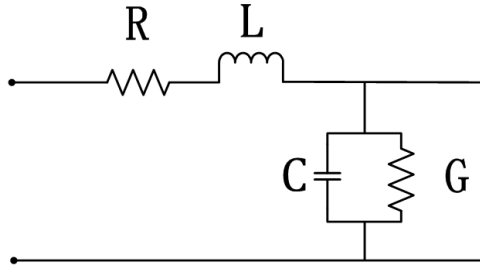


Figure 6.17 Equivalent circuit model of the CPW TL structure.

The two-port network, which is shown in Figure 6.16, can be expressed in terms of the ABCD matrix. For a lossy TL, the ABCD matrix can be re-written as below [61]:

$$A = \cosh(\gamma L_{CPW}) \quad \text{Eq. (6-10)}$$

$$B = Z_0 \sinh(\gamma L_{CPW}) \quad \text{Eq. (6-11)}$$

$$C = \frac{1}{Z_0} \sinh(\gamma L_{CPW}) \quad \text{Eq. (6-12)}$$

$$D = \cosh(\gamma L_{CPW}) \quad \text{Eq. (6-13)}$$

Thus, Eq. (6-9) can be re-expressed in terms of the elements “A” and “D”:

$$\gamma = \frac{1}{L_{CPW}} \operatorname{acosh}\left(\frac{A+D}{2}\right) \quad \text{Eq. (6-14)}$$

The attenuation constant ( $\alpha$ ) and the phase constant ( $\beta$ ) can be further derived using Eq. (6-14) and Eq. (6-9). The characteristic impedance of this CPW TL is expressed using the elements “B” and “C” in Eq. (6-15):

$$Z_c = \sqrt{\frac{B}{C}} \quad \text{Eq. (6-15)}$$

The equivalent circuit model of this CPW TL is shown in Figure 6.17. The propagation constant and the characteristic impedance of this TL can be written in Eq. (6-16) and Eq. (6-17), respectively:

$$\gamma = \alpha + j\beta = \sqrt{(R + j\omega L)(G + j\omega C)} \quad \text{Eq. (6-16)}$$

$$Z_c = \sqrt{\frac{R + j\omega L}{G + j\omega C}} \quad \text{Eq. (6-17)}$$

The “R”, “L”, “G”, and “C” in the equivalent circuit model can be calculated using the following equations:

$$R = \operatorname{Re}(\gamma \cdot Z_c) \quad \text{Eq. (6-18)}$$

$$L = \frac{1}{\omega} \operatorname{Im}(\gamma \cdot Z_c) \quad \text{Eq. (6-19)}$$

$$G = \operatorname{Re}(\gamma / Z_c) \quad \text{Eq. (6-20)}$$

$$C = \frac{1}{\omega} \operatorname{Im}(\gamma / Z_c) \quad \text{Eq. (6-21)}$$

In [62], the effective permittivity of the complete CPW structure is shown to be calculated using Eq. (6-22):

$$\varepsilon_{eff} = 1 + q_1(\varepsilon_{r_{BST}} - \varepsilon_{r_{sub}})/2 + q_2(\varepsilon_{r_{sub}} - 1)/2 \quad \text{Eq. (6-22)}$$

where the filling factors  $q_1$  and  $q_2$  can be respectively calculated by

$$q_1 = \frac{K(k_1) K(k'_0)}{K(k'_1) K(k_0)} \quad \text{Eq. (6-23)}$$

$$q_2 = \frac{K(k_2)K(k'_0)}{K(k'_2)K(k_0)} \quad \text{Eq. (6-24)}$$

$K(k_i)$  and  $K(k'_i)$  are the complete elliptic integrals of the first kind with  $k'_i = \sqrt{1 - k_i^2}$ ,  $i = 0,1,2, \dots$ . The complete elliptic integrals of the first kind can be found in [9]. In the above expressions, the parameters  $k_0$ ,  $k_1$ , and  $k_2$  are closely related to the dimensions shown in Figure 6.15, which are expressed in Eq. (6-25), Eq. (6-26), and Eq. (6-27), respectively [62]:

$$k_0 = \frac{w/2}{w/2+s} \quad \text{Eq. (6-25)}$$

$$k_1 = \frac{\sinh\left(\frac{\pi w/2}{2H_1}\right)}{\sinh\left[\frac{\pi\left(\frac{w}{2}+s\right)}{2H_1}\right]} \quad \text{Eq. (6-26)}$$

$$k_2 = \frac{\sinh\left(\frac{\pi w/2}{2H}\right)}{\sinh\left[\frac{\pi\left(\frac{w}{2}+s\right)}{2H}\right]} \quad \text{Eq. (6-27)}$$

where  $H$  is the total thickness of the two-layer substrate, i.e.,  $H = H_1 + H_2$ . The parameters  $k'_0$ ,  $k'_1$ , and  $k'_2$  are calculated by  $k'_0 = \sqrt{1 - k_0^2}$ ,  $k'_1 = \sqrt{1 - k_1^2}$ , and  $k'_2 = \sqrt{1 - k_2^2}$ , respectively.

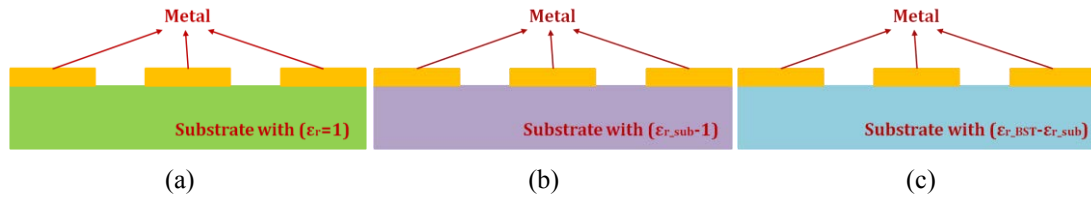


Figure 6.18 Equivalent models, (a) the equivalent CPW with air filling, i.e.,  $\epsilon_r = 1$ ; (b) the equivalent CPW model with permittivity of  $(\epsilon_{r\_sub} - 1)$ ; (c) the equivalent CPW model with permittivity of  $(\epsilon_{r\_BST} - \epsilon_{r\_sub})$ .

In the conformal mapping method, in order to get the permittivity of the BST film material, the CPW model is mapped to three equivalent models – the model of the CPW with air filling, the equivalent CPW model with  $(\epsilon_{r\_sub} - 1)$  permittivity, and the equivalent CPW model with  $(\epsilon_{r\_BST} - \epsilon_{r\_sub})$  permittivity, which are shown in

Figure 6.18(a), Figure 6.18(b), and Figure 6.18(c), respectively [62]. The total capacitance of the main CPW model ( $C_{tot}$ ) is the sum of the capacitances of three equivalent CPW models [62]:

$$C_{tot} = C_0 + C_2 + C_1 \quad \text{Eq. (6-28)}$$

where  $C_0$ ,  $C_2$ , and  $C_1$  are calculated by

$$C_0 = 4\varepsilon_0 \frac{K(k_0)}{K(k'_0)} \quad \text{Eq. (6-29)}$$

$$C_2 = 2\varepsilon_0(\varepsilon_{r\_sub} - 1) \frac{K(k_2)}{K(k'_2)} \quad \text{Eq. (6-30)}$$

$$C_1 = 2\varepsilon_0(\varepsilon_{r\_BST} - \varepsilon_{r\_sub}) \frac{K(k_1)}{K(k'_1)} \quad \text{Eq. (6-31)}$$

$C_{tot}$  can also be calculated in Eq. (6-32):

$$C_{tot} = 4\varepsilon_0 \varepsilon_{eff} \frac{K(k_0)}{K(k'_0)} \quad \text{Eq. (6-32)}$$

In this conformal mapping process, it is assumed that the total capacitance of the main CPW model is equivalent to the “C” in Figure 6.17, i.e.,  $C_{tot} = C$ . Thus, the effective permittivity of the structure is calculated by

$$\varepsilon_{eff} = \frac{C \cdot K(k'_0)}{4\varepsilon_0 \cdot K(k_0)} \quad \text{Eq. (6-33)}$$

The permittivity of the BST film material is further calculated in Eq. (6-34):

$$\varepsilon_{r\_BST} = \frac{2(\varepsilon_{eff}-1)+q_2+(q_1-q_2)\varepsilon_{r\_sub}}{q_1} \quad \text{Eq. (6-34)}$$

In measurement, three key parameters (i.e.,  $w/2$ ,  $s$ , and  $H_1$ ) are considered as the major contributors to the uncertainty in the extracted permittivity of the BST material using the conformal mapping method [61], due to the experiences from [62] and [63] that the thickness of the BST film and the dimensions of the signal line and gap width of the CPW TL are the major factors considered in the uncertainty analysis. These parameters with different sets of the corresponding standard deviations will trigger

uncertainty in the derived  $\epsilon_{r\_BST}$ . The standard deviations come from the process for deposition and lithography of the films and are determined from multiple measurements assumed to follow a normal distribution. The uncertainty ratio ( $U_i$ ) in percentage are used to express the uncertainty influence, which is calculated by [61]

$$U_i = \frac{\sigma_i^2}{\sigma_{tot}^2}, \quad i = 1, 2, \dots \quad \text{Eq. (6-35)}$$

where  $\sigma_{tot}^2 = \sum \sigma_i^2$ ,  $i = 1, 2, \dots$ .

Table 6.6 The first case of the key parameters with corresponding standard deviation.

Parameter	Expected Value	Standard Deviation
$w/2$	25 $\mu\text{m}$	2 $\mu\text{m}$
$s$	25 $\mu\text{m}$	2 $\mu\text{m}$
$H_1$	0.6 $\mu\text{m}$	0.03 $\mu\text{m}$

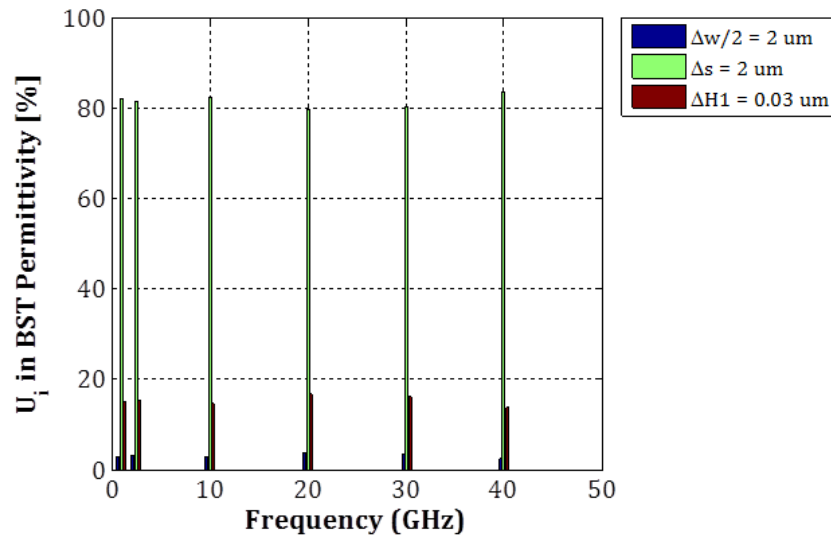


Figure 6.19 Distribution of uncertainties in BST permittivity in the first case.

The software MATLAB is used for analysis of the uncertainty influence and calculation of the uncertainty ratio. The Gaussian distributions of values of  $w/2$ ,  $s$ , and  $H_1$  are generated by the MATLAB codes which are shown in Appendix B. Then,

one distribution of relative permittivity of the BST film at the chosen target frequencies are generated for each key parameter [61]. The standard deviation of the extracted permittivity distribution (i.e.,  $\sigma_i$ ,  $i = 1, 2, \dots$ ) for three key parameters respectively are used in calculation of the uncertainty index (i.e.,  $U_i$ ) using Eq. (6-35).

Table 6.7 The second case of the key parameters with corresponding standard deviation.

Parameter	Expected Value	Standard Deviation
$w/2$	25 $\mu\text{m}$	1 $\mu\text{m}$
$s$	25 $\mu\text{m}$	1 $\mu\text{m}$
$H_i$	0.6 $\mu\text{m}$	0.03 $\mu\text{m}$

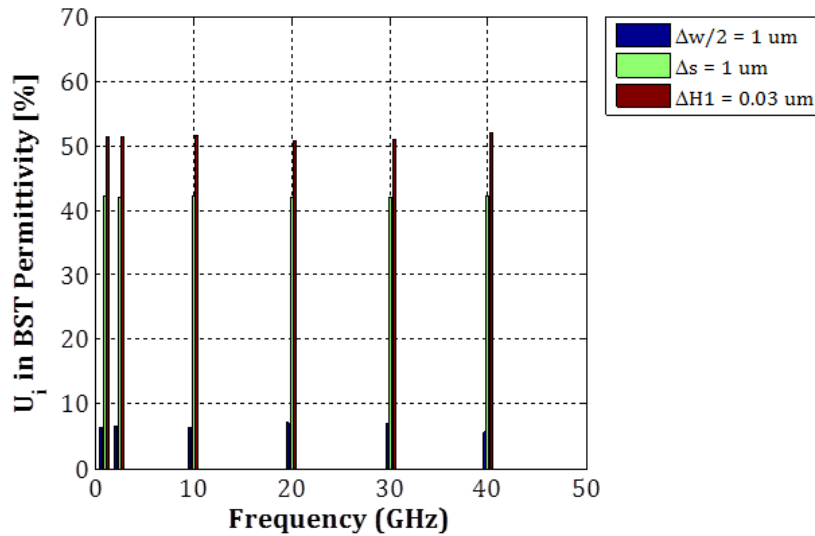


Figure 6.20 Distribution of uncertainties in BST permittivity in the second case.

The first case of the key parameters and their corresponding standard deviations is listed in Table 6.6. In this case, the standard deviation for each key parameter came from the examination of the CPW TL in the scanning electron microscope and experience of reproducibility of the thickness measurements by a stylus profiler [61].

The distributions of the uncertainties at 1, 2.5, 10, 20, 30, and 40 GHz are calculated and shown in Figure 6.19. Figure 6.19 shows that the uncertainty ratio in  $\epsilon_{r\_BST}$  is primarily dominated by the standard deviation of the gap width ( $\Delta s$ ), and is secondarily dominated by the standard deviation of thickness of the BST material ( $\Delta H_1$ ).

The key parameters in the second case have smaller standard deviations from lithography, as listed in Table 6.7. In this case, the distributions of the uncertainties are shown in Figure 6.20. In this case, the uncertainty ratio in  $\epsilon_{r\_BST}$  is primarily dominated by thickness of the BST material ( $\Delta H_1$ ), and is secondarily dominated by the standard deviation of the gap width ( $\Delta s$ ).

After comparing the uncertainty ratio in two cases, the conclusions can be drawn as follows: (1) different values of the standard deviations in the key parameters show different presentations of the uncertainty ratio of the BST permittivity; (2) the uncertainty ratio remains almost same at different frequencies. Therefore, the parameters that dominate the uncertainty ratio should be carefully considered in the design.

## 6.5 Summary

In this chapter, an electronically tunable LWA based on the CRLH structure with discrete FE BST interdigital varactors was presented. The BST varactors integrated into the LWA structure enable the frequency tunability of the CRLH-based LWA. This

LWA provides a good way to integrate the antenna structure with BST materials. Most existing BST-based antenna designs use an entire piece of the BST layer in antenna designs, which can introduce unnecessary losses to degrade the antenna radiation performance. With discrete BST varactors in the LWA structure, the losses from the BST materials can be reduced, so that the antenna radiation performance may be improved. In addition, the uncertainty analysis for the BST material is investigated using the conformal mapping method. The uncertainty ratios show different proportions with different sets of the standard deviation of the parameters and remain almost same at different frequencies. The uncertainty analysis can help us carefully consider the influence from the geometric deviations in the design, thereby helping us further optimize the design.

In principle, one could use the uncertainty in  $\epsilon'$  to find uncertainty in the capacitance values of *BST\_varactor\_1* and *BST\_varactor\_2*, and then use multiple CST simulations to find an uncertainty in the predicted the frequency of the balanced point, gain, etc. In the paper, we assumed the “worst-case” value of  $\epsilon_r'$  and looked at how those affected the antenna. If one knows such limits, it is then possible to say whether a design can be realized with high yield in practice, or whether a fabricated antenna is performing as well as can be expected given the reliability of the input data. If it is worse than you would predict the process of manufacturing the antenna might be suspect. Alternatively, the design can aim for designs robust against the uncertainties in the input parameters.

# CHAPTER VII

## CONCLUSIONS AND FUTURE RESEARCH

### 7.1 Conclusions

In this thesis, metamaterial-inspired RAs and LWAs have been presented for multiband or frequency-agile applications. The open-ended RAs based on one ECRLH unit cell structure achieve the multiband or frequency tunable characteristics. The microstrip LWAs based on the metamaterial-inspired structures (i.e., *Supercell\_v1* and *Supercell\_v2*) achieve the dual-passband features with the CRLH leaky-wave characteristics within both passband. An electronically tunable LWA based on the *Supercell\_v2* structure achieves the relatively independent control of the low balanced point with keeping the frequency position of the high balanced point and maintaining the backward-to-forward leaky-wave radiation characteristics within the high passband. Besides, as additional research, a microstrip LWA with discrete BST varactors has been demonstrated in simulations. Furthermore, the uncertainty in the determination of the BST permittivity has been analyzed in order to provide design clues and optimize the design process.

### **7.1.1 Class of Metamaterial-Inspired RAs**

The class of three open-ended metamaterial-inspired RAs based on one ECRLH unit cell structure has been proposed in Chapter IV for multiband or frequency-agile applications. As an extension of conventional metamaterial-inspired RAs, the ones in this class can generate multiple operating resonances working at the chosen frequencies. The passive RAs with chip capacitors and IDSs achieve multiband properties and support diverse wireless frequency bands over 0.5-6.0 GHz. An electronically tunable RA with one semiconductor varactor achieves the frequency tunability of one operating resonance at the low frequency without destroying the wideband coverage formed by the other operating resonances. This class of the RAs has great potentials and is a good reference to design the small antennas for multiband applications. The investigation of the multiband or frequency-tunable characteristics in these designs enables new structures of small antennas with supporting a variety of commercial frequency bands in modern cellular wireless communication systems.

### **7.1.2 Class of Dual-Passband LWAs**

The dual-passband LWAs based on the ECRLH and new metamaterial-inspired supercell structures have been presented and investigated in Chapter V. According to the observation that the presented LWA based on the ECRLH structure does not have the backward-to-forward leaky-wave radiation characteristics within its high passband, the LWAs based on the metamaterial-inspired *Supercell\_v1* and *Supercell\_v2* structures have been proposed to realize the backward-to-forward leaky-wave radiation characteristics within both passbands. Furthermore, a microstrip

electronically tunable LWA based on multiple cascaded *Supercell\_v2* structures has been designed to achieve the relatively independent tunability of the low balanced point while keeping the frequency position of the high balanced point and maintaining the backward-to-forward leaky-wave radiation characteristics within the high CRLH passband. The dual-passband LWAs with the backward-to-forward leaky-wave radiation characteristics can be used for dual-band high-directivity or communication applications. The investigation of the supercell structures may be used as references to design different kinds of antennas.

### **7.1.3 Class of BST-Based Antennas**

In Chapter VI, a microstrip CRLH-based LWA with discrete BST thin-film flip-chip varactors has been designed and demonstrated in the simulation. Its balanced point is demonstrated to achieve relative frequency tunability of 4.1% in the simulation. Due to the importance of the BST permittivity for tunable antenna designs, the uncertainty analysis in the determination of the FE BST permittivity has been performed. The uncertainty ratios relate the standard deviations in the geometric parameters to the uncertainty in the BST permittivity. Moreover, the uncertainty ratios remain similar at different frequencies. The LWA design with discrete BST varactors provides a good way to integrate the antenna structure with BST materials. Furthermore, the uncertainty analysis in determination of the BST permittivity can provide useful clues when we are designing a BST-based antenna. The analysis results can tell us which geometric parameters affect the BST permittivity. We need to take the permittivity deviation into consideration about its influence on the antenna performance

(e.g., frequency response and beam direction) or appropriately reduce the expectation about the accuracy requirement on the antenna performance.

Based on the above statements, the antenna characteristics, achievements, meanings and studies of three classes of the antennas in this thesis are summarized in Table 7.1.

Table 7.1 Summary of the antenna characteristics, achievements, meanings and studies of three classes of antennas in this thesis.

	<b>Class of Metamaterial-Inspired RAs</b>	<b>Class of Metamaterial-Inspired LWAs</b>	<b>Class of Tunable LWA With BST Varactors</b>
Characteristics	<ul style="list-style-type: none"> <li>(1) One ECRLH unit cell used as the resonant structure;</li> <li>(2) Open-ended structure;</li> <li>(3) Multi-band or wideband applications;</li> <li>(4) Relatively independent tunability of one specific operating resonance</li> </ul>	<ul style="list-style-type: none"> <li>(1) Dual-passband feature;</li> <li>(2) Triple leaky-wave regions for the ECRLH LWA, while dual CRLH leaky-wave region for both <i>Supercell_v1</i> and <i>Supercell_v2</i> LWAs</li> <li>(3) Relatively independent tunability of low balanced point with retaining the frequency position of the high balanced point for active <i>Supercell_v2</i> LWA</li> </ul>	<ul style="list-style-type: none"> <li>(1) Integration of a CRLH LWA with discrete BST varactor for electronic tunability;</li> <li>(2) Effects on the permittivity determination of BST material from the uncertainty analysis</li> </ul>
Achievements	<ul style="list-style-type: none"> <li>(1) Performance investigation of the novel open-ended RAs with one ECRLH unit cell structure;</li> <li>(2) Discussion of the control of the important parts of the RA structure;</li> <li>(3) Investigation of the tunability of the active RA for frequency reconfigurability</li> </ul>	<ul style="list-style-type: none"> <li>(1) Investigation of the LWA design based on the ECRLH unit cells;</li> <li>(2) Proposal of two supercells, i.e., <i>Supercell_v1</i> and <i>Supercell_v2</i>, and investigation of the LWA designs based on these two supercells;</li> <li>(3) Investigation of tunability of the low balanced point for the active <i>Supercell_v2</i> LWA</li> </ul>	<ul style="list-style-type: none"> <li>(1) Investigation of tunability of a CRLH LWA design with discrete BST flip-chip varactors;</li> <li>(2) Uncertainty analysis in determination of permittivity of BST material for optimization of the design process</li> </ul>
Meanings	<ul style="list-style-type: none"> <li>(1) Provide new ideas for the small antenna design;</li> <li>(2) Use for multiband or wideband applications;</li> <li>(3) Use for frequency agility</li> </ul>	<ul style="list-style-type: none"> <li>(1) Use for dual-band scanning or communication applications;</li> <li>(2) Use for beam steering at a fixed frequency for the active design</li> </ul>	<ul style="list-style-type: none"> <li>(1) Provide a new integration method of LWA with discrete BST varactors;</li> <li>(2) Steer the main beam of the LWA at a fixed frequency;</li> <li>(3) Provide clues for component designs with BST varactors;</li> <li>(4) Optimize the design process of component with BST varactors</li> </ul>
Studies & Obtains	<ul style="list-style-type: none"> <li>(1) Understand the background theory of metamaterial-inspired RAs;</li> <li>(2) Understand the multiband function and radiation characteristics of RAs;</li> <li>(3) Study the tunability of the active RA;</li> <li>(4) Study that the operating resonance at low frequency can be improved by better exciting or working at higher frequencies</li> </ul>	<ul style="list-style-type: none"> <li>(1) Understand the background theory of conventional and metamaterial-inspired LWAs;</li> <li>(2) Use the dispersion diagram for analysis of frequency response and leaky-wave radiation characteristics;</li> <li>(3) Study that the LWA gain is closely related to the number of unit cells and the losses introduced by all SMD components</li> </ul>	<ul style="list-style-type: none"> <li>(1) Understand the property of BST material and the design of BST varactors;</li> <li>(2) Study integration approaches of antenna with BST varactors;</li> <li>(3) Learn the method to extract the permittivity of BST film;</li> <li>(4) Study effects of uncertainties on determination of effective permittivity of BST</li> </ul>

## 7.2 Future Research

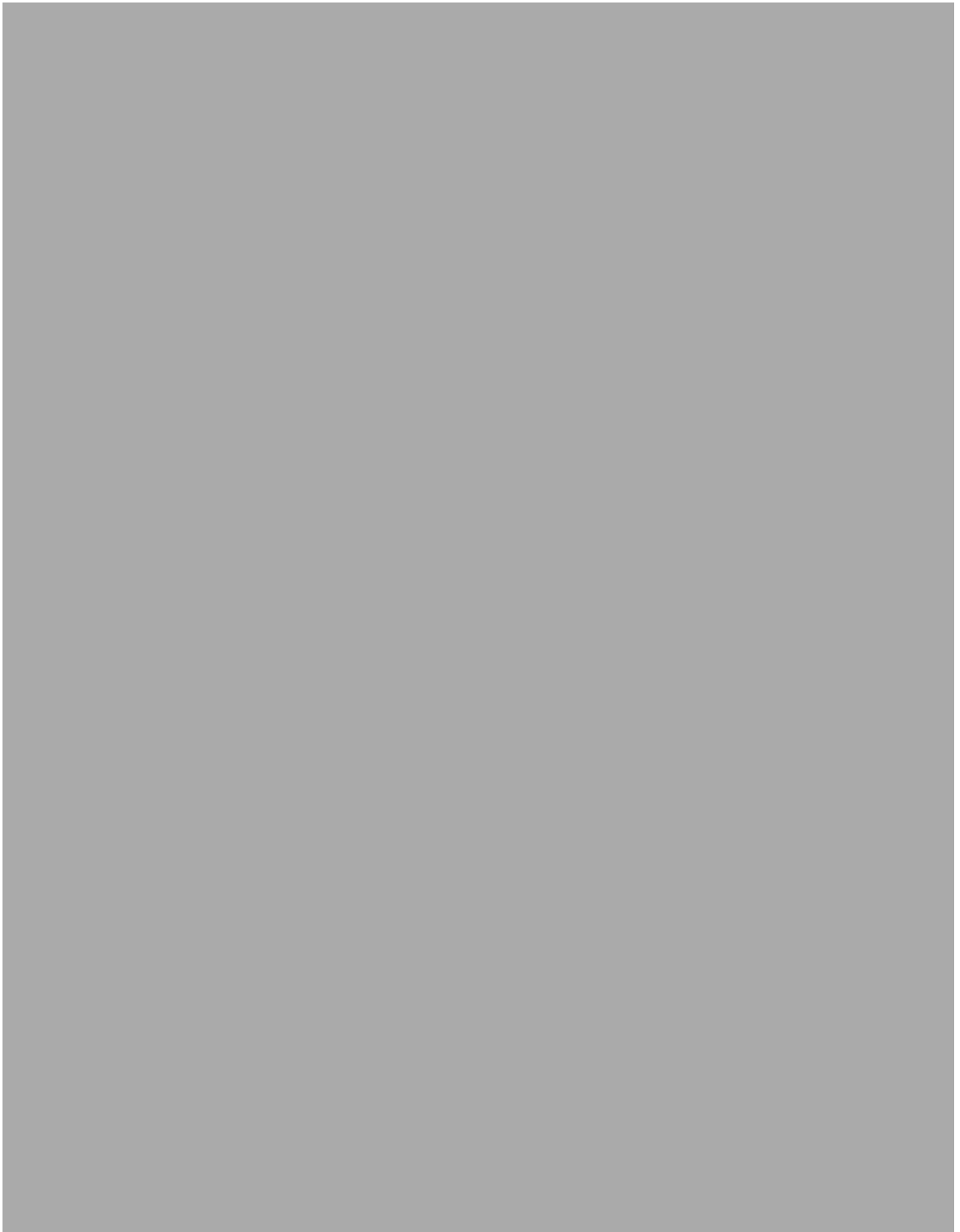
In this thesis, antenna designs based on different metamaterial-inspired structures for

multiband or frequency-agile applications have been presented. The combinations of different metamaterial-inspired structures with antenna designs are still a hot on-going open research topic. Thus, the future research directions of antenna designs based on different metamaterial-inspired structures can be summarized as follows:

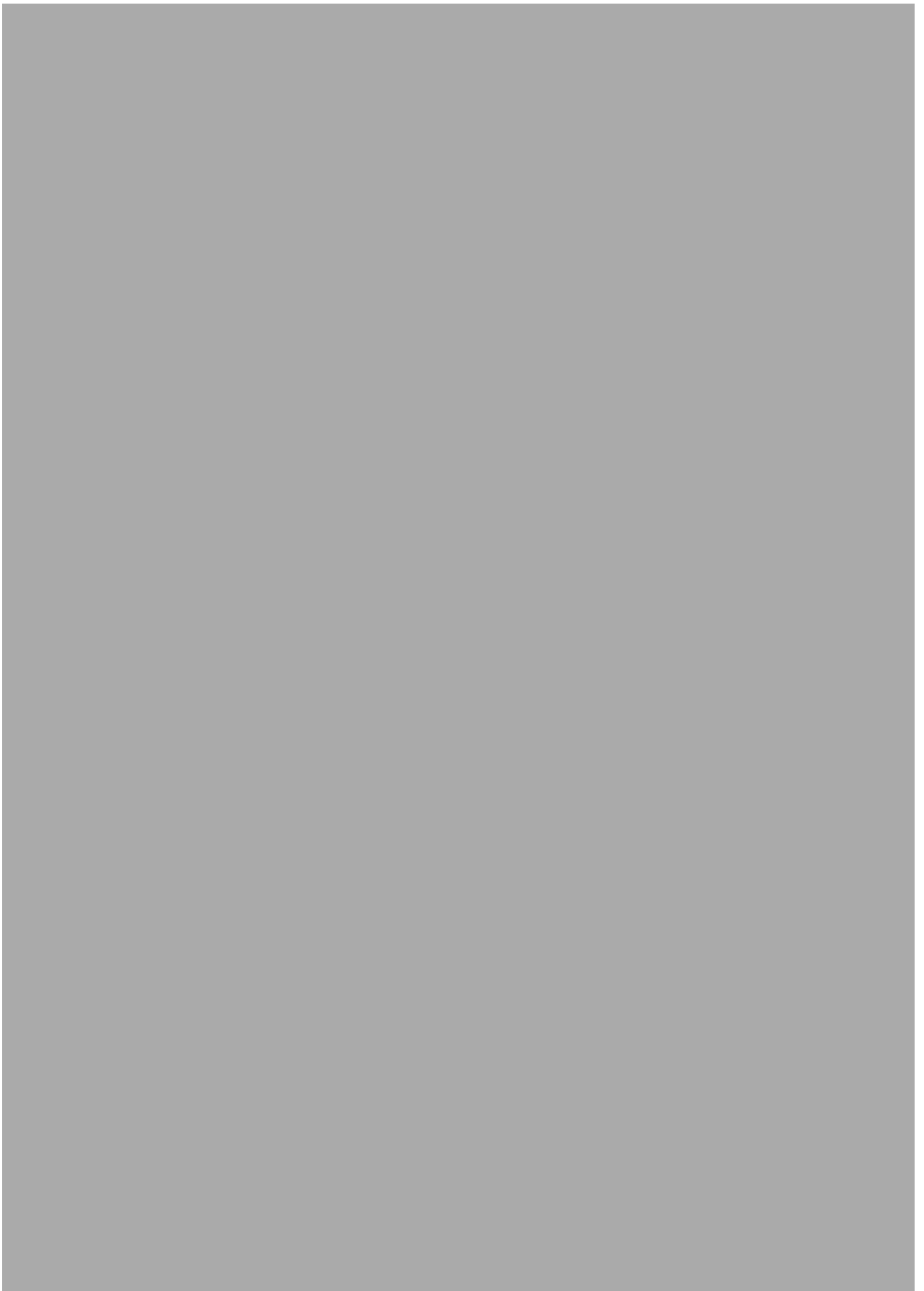
- (1) For metamaterial-inspired RAs, there are two major future research directions:
  - a. Investigate the antenna characteristics of open-ended RA designs with multiple ECRLH unit cells;
  - b. Investigate the antenna characteristics of short-ended RA designs with one or multiple ECRLH unit cells.
- (2) For metamaterial-inspired LWAs, there are two major future research directions as well:
  - a. Develop a LWA design with 2-D multi-layer frequency selective surfaces based on the proposed metamaterial-inspired structures for high-directivity and high-gain applications;
  - b. Develop novel metamaterial-inspired supercell structures with new characteristics, and apply them to LWA designs.
- (3) For BST-based antennas, there are two major future research directions:
  - a. Fabricate the LWA using discrete BST varactors introduced in Chapter VI for practical demonstration;
  - b. Design a phased array with BST materials for electronically controlled beam steering functions.

# Appendix A

## Brief Datasheet of *MURATA* 0402 Chip Capacitor



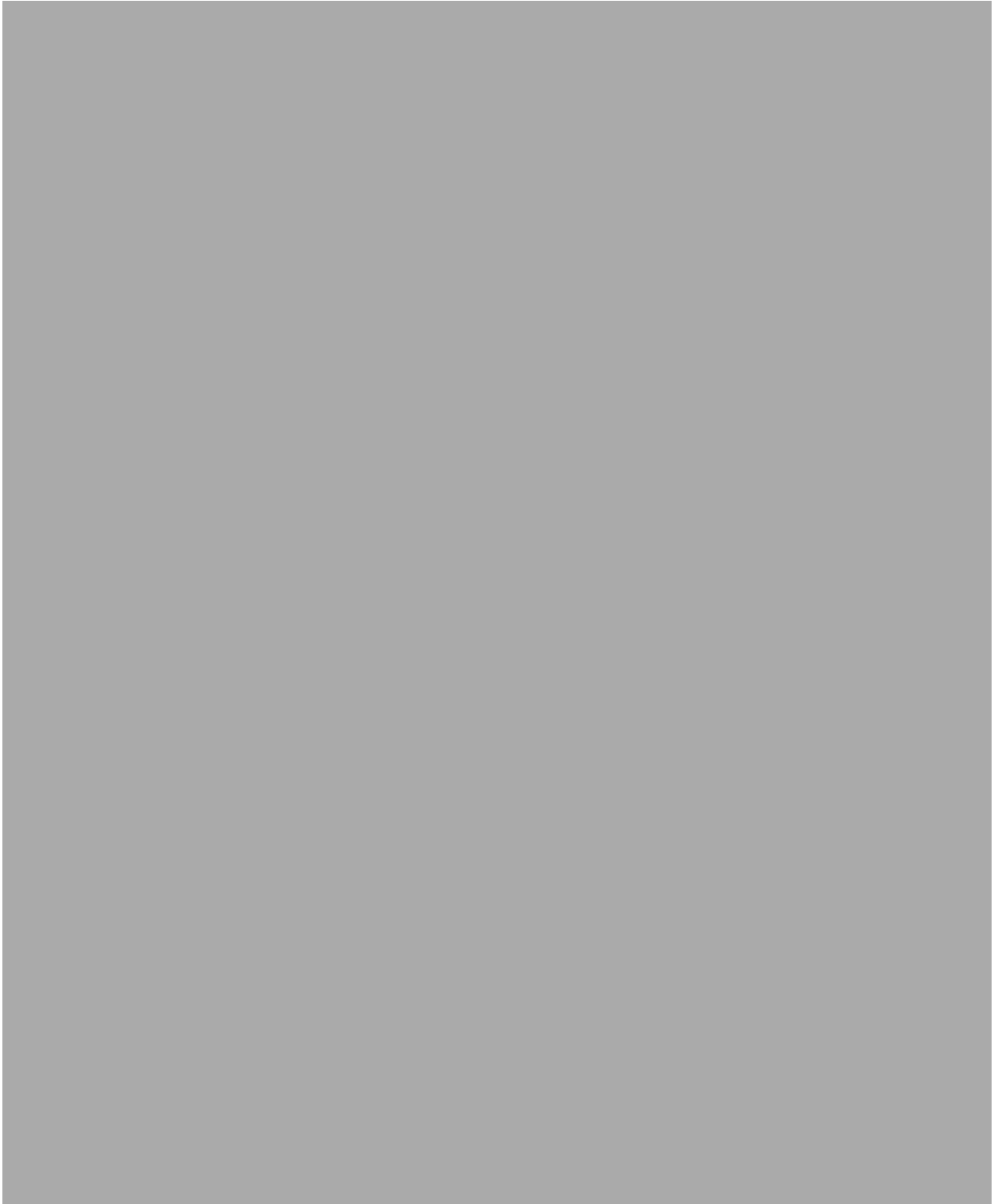






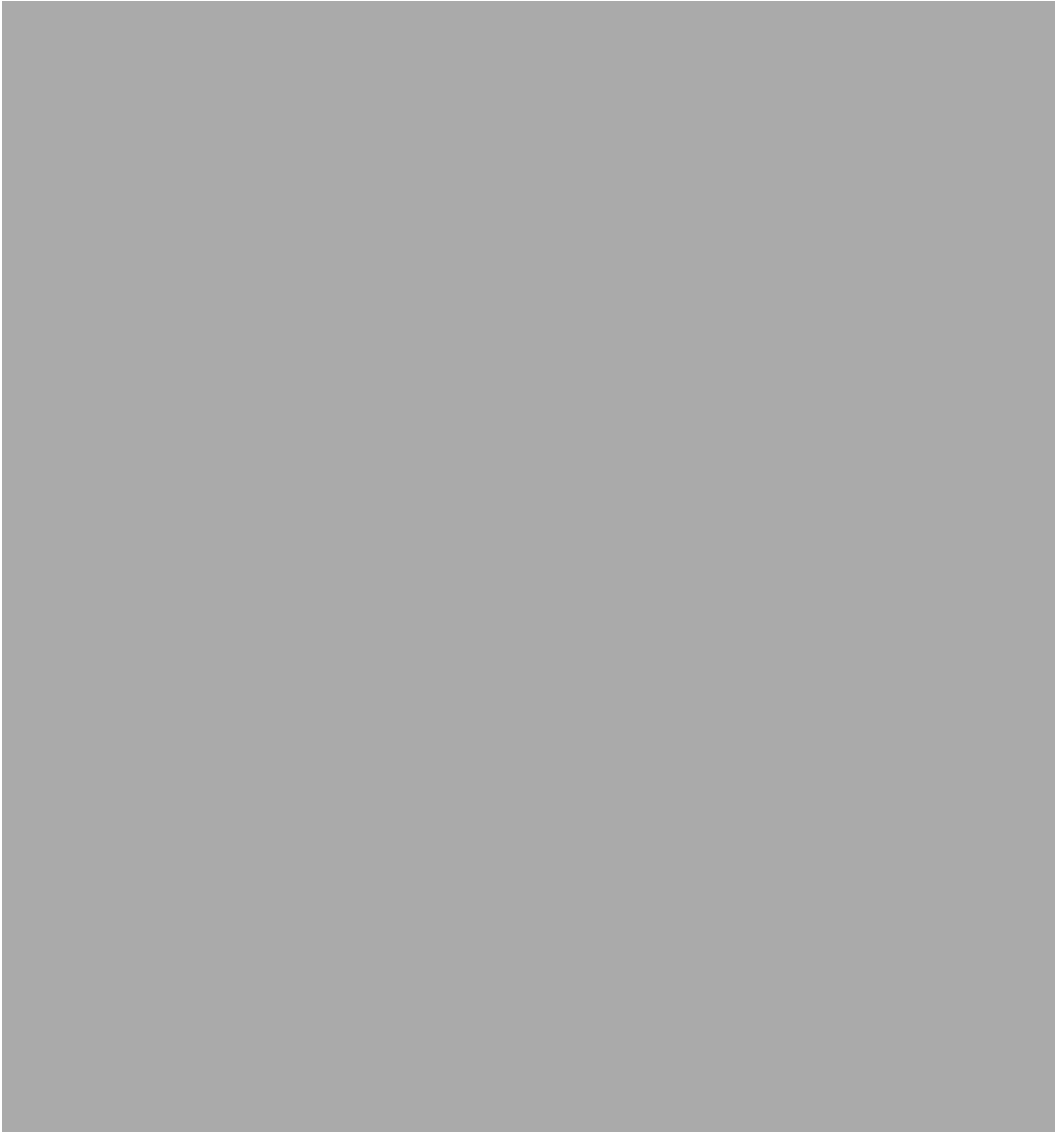
# Appendix B

Datasheet of *MICROSEMI MV34002* Semiconductor Varactor

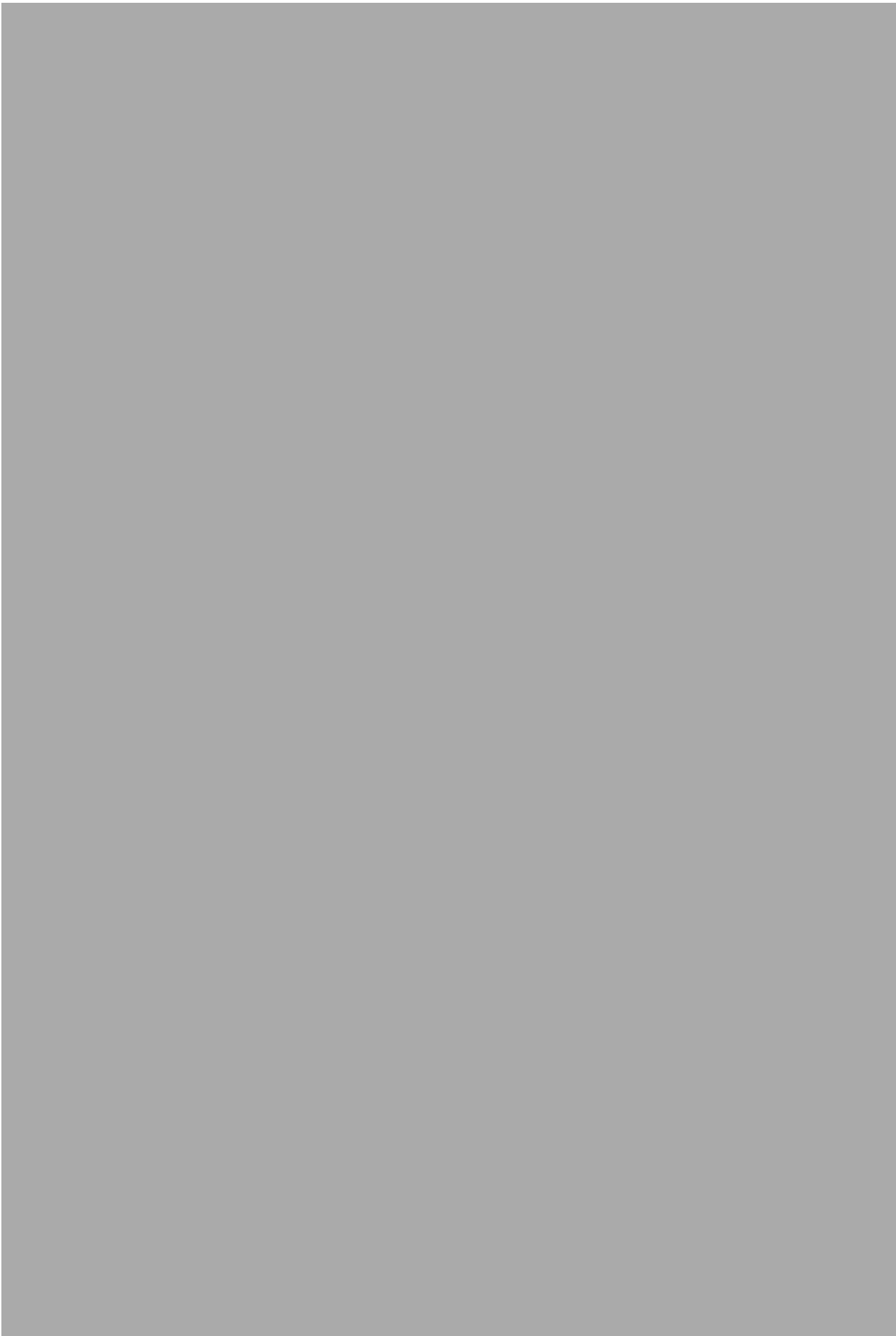


# Appendix C

Datasheet of *SKYWORKS SMV1234-040LF* Silicon Semiconductor Varactor







# Appendix D

## MATLAB Function 1

```
function
[f_c,er1_BST_c]=Conformal_Mapping_BST_20150311(Tdata,par,flag,f_p)

Z = 50;
c0=3e8;
e0=8.854e-12;
l = 2500e-6;           % Length of transmission line
H2=500e-6;           % Thickness of substrate
gpw=250e-6;          % ground plane width
Target_Er_sub=9.9;   % Permittivity of substrate in measurement

Er2=Target_Er_sub;

if (flag==1)
    s=par/2*1e-6; % half width of centre conductor
    g=25e-6; % gap width
    H1=0.6e-6; % thickness of substrate
elseif (flag==2)
    s=25e-6; % half width of centre conductor
    g=par*1e-6; % gap width
    H1=0.6e-6; % thickness of substrate
elseif (flag==3)
    s=25e-6; % half width of centre conductor
    g=25e-6; % gap width
    H1=par*1e-6; % thickness of substrate
end

H=H1+H2;           % Entire Thickness of two-layer substrate

%% Reading S parameters Data from the data table
f = Tdata(:,1).*1e9; % frequency vector - first column of Tdata
S11_real = Tdata(:,2) .* cos( Tdata(:,3) * pi/180);
S11_img = Tdata(:,2) .* sin( Tdata(:,3) * pi/180);
S11      = S11_real + 1i*S11_img;
S21_real = Tdata(:,4) .* cos( Tdata(:,5) * pi/180);
S21_img = Tdata(:,4) .* sin( Tdata(:,5) * pi/180);
S21      = S21_real + 1i*S21_img;
```

```

S22_real = Tdata(:,8) .* cos( Tdata(:,9) * pi/180);
S22_img   = Tdata(:,8) .* sin( Tdata(:,9) * pi/180);
S22      = S22_real + 1i*S22_img;
S12_real = Tdata(:,6) .* cos( Tdata(:,7) * pi/180);
S12_img  = Tdata(:,6) .* sin( Tdata(:,7) * pi/180);
S12      = S12_real + 1i*S12_img;

f_c=f(f_p,1);

%% Extracting ABCD parameters from Scattering parameters
Aa = (1./(2.*S21)) .* ( ((1+S11).*(1-S22))+(S21.*S12) );
Bb = (1./(2.*S21)) .* ( Z .* ( ((1+S11).*(1+S22))-(S12.*S21) ));
Cc = (1./(2.*S21)) .* ( 1/Z .* ( ((1-S11).*(1-S22))-(S12.*S21) ));
Dd = (1./(2.*S21)) .* ( ((1-S11).*(1+S22))+(S12.*S21) );
% A_c=Aa(f_p,1);
% B_c=Bb(f_p,1);
% C_c=Cc(f_p,1);
% D_c=Dd(f_p,1);

%% Extracting propagation constant gamma
gamma = (1/l).*(acosh((Aa+Dd)./2));
% gamma = 1/l*(acosh((A_c+D_c)/2));
alpha = real(gamma); %this has units of 'Neper'
beta  = imag(gamma); %this has units of rads per metre
phi_gamma = atan(beta/alpha); %this is the phase of gamma

%% Creating continuous beta from discontinuous beta due to standing waves
beta_s = unwrap(beta,pi/l);

%% gamma correction
gamma_shifted = alpha + 1i.*beta_s;

%% Conformal mapping definitions for BST thin film
k0=s/(s+g);
k0p=sqrt(1-k0^2);

k1=sinh(pi*s/(2*H1))/sinh(pi*(s+g)/(2*H1));
k1p=sqrt(1-k1^2);

k2=sinh(pi*s/(2*H))/sinh(pi*(s+g)/(2*H));
k2p=sqrt(1-k2^2);

% The elliptic integrals of the first kind for k0,k1,k2
Elliptic_Ratio_k0=ellipke(k0p)/ellipke(k0);

```

```

Elliptic_Ratio_k2=ellipke(k2p)/ellipke(k2);
Elliptic_Ratio_k1=(2/pi)*log(4/k1);      % Version 1

q1=Elliptic_Ratio_k0/Elliptic_Ratio_k1;
q2=Elliptic_Ratio_k0/Elliptic_Ratio_k2;

%% Impedance Calculation
Z0_BC = (Bb./Cc).^0.5;
phi_z = atan(imag(Z0_BC)./real(Z0_BC));

%% Calculation of RLGC paramters
R = real(Z0_BC.*gamma_shifted);
L = imag(Z0_BC.*gamma_shifted)/(2*pi*f_c);
C = imag(gamma_shifted./Z0_BC)/(2*pi*f_c);
G = real(gamma_shifted./Z0_BC);

%% Permittivity calculation - effective permittivity
eps_eff=(C./(4*e0)).*Elliptic_Ratio_k0;

%% Thin Film Permittivity calculation - er1_BST and loss tangent
er1_BST=(2.*(eps_eff-1)+q2+(q1-q2).*Er2)./q1;

end

```

## MATLAB Function 2

```

clear all;
close all;
clc;

%% Global Parameters
filename='CPW21.xls';
Tdata = xlsread(filename);

H2=500e-6;          % Thickness of substrate
H1=0.6e-6;         % Thickness of BST thin film
s=25e-6;           % Half width of centre conductor
g=25e-6;           % Gap width
gpw=250e-6;       % Ground plane width
Length=2500e-6;   % length of transmission line
t=500e-9;          % Thickness of metal conductor

```

```

H=H1+H2; % Entire Thickness of two-layer substrate

Target_Er_BST=400; % Permittivity of BST in measurement
Target_TanD_BST=0.02; % Tangent loss of BST in measurement
Target_Er_sub=9.9; % Permittivity of substrate in measurement
Target_TanD_sub=0.0001; % Tangent loss of substrate in measurement

%% Parameter Deviation Setting
Para_array=[2*s, g, H1]*1e6;
Mean_array=Para_array;
StdVar_array=[1, 1, 0.03];
%Step_array=[0.1, 0.2, 0.01];
Num_Para=length(Para_array);

factor=1; % The standard deviation of the normal
distribution is factor*StdVar_array(i)
Num_Samples=61;
X1=Mean_array(1)+factor*StdVar_array(1)*randn(1,Num_Samples);
X2=Mean_array(2)+factor*StdVar_array(2)*randn(1,Num_Samples);
X3=Mean_array(3)+factor*StdVar_array(3)*randn(1,Num_Samples);
X_array=[X1;X2;X3];

%% Conformal Mapping for calculation of Eps at
1GHz,2.5GHz,10GHz,20GHz,30GHz,40GHz.
TargetFre_array=[1,2.5,10,20,30,40]; % Frequency unit: GHz
TargetFrePos_array=[1,31,181,381,481,581];
length_TargetFre=length(TargetFrePos_array);
length_par=Num_Samples;
fre_value_array=zeros(length_TargetFre,length_par);
Er_array=zeros(length_TargetFre,length_par);

max_value_DiffSq=zeros(Num_Para,length_TargetFre);
max_pos_DiffSq=zeros(Num_Para,length_TargetFre);
Target_std_deviation=zeros(Num_Para,length_TargetFre);

for i=1:Num_Para % 3 parameters
% for i=1:1
    for m=1:length_TargetFre % 6 frequency points
% for m=1:1
        TargetF_pos=TargetFrePos_array(m); % The sequence of target
frequency point (GHz)
        for n=1:length_par % 61 sample points
            par_value=X_array(i,n);

```

```

[fre,Er]=Conformal_Mapping_BST_20150209(Tdata,par_value,i,TargetF_pos
);
    fre_value_array(m,n)=fre;
    Er_array(m,n)=Er;
    end
end
Diff=Er_array-Target_Er_BST;
Diff_square=Diff.^2;
for z=1:length_TargetFre

[max_value_DiffSq(i,z),max_pos_DiffSq(i,z)]=max(Diff_square(z,:));
    %Target_std_deviation(i,z)=Diff(z,max_pos_DiffSq(i,z));
    end
end

Uncertainty_Ratio_Table=zeros(Num_Para,length_TargetFre);
sum_array=zeros(1,length_TargetFre);
for y=1:length_TargetFre
    sum_array(1,y)=sum(max_value_DiffSq(:,y));

Uncertainty_Ratio_Table(:,y)=max_value_DiffSq(:,y)/sum_array(1,y);
end
Uncertainty_Ratio_Table2=Uncertainty_Ratio_Table';

figure(1);
bar(TargetFre_array,Uncertainty_Ratio_Table2);
grid;
ylabel('U_i in BST Permittivity [%]','FontSize', 16);
xlabel('Frequency (GHz)','FontSize', 16);
%title('Distribution of Uncertainty in BST Permittivity');
legend('\Deltaw/2','\Deltas','\DeltaH1',-1);
set(gca,'YTickLabel',{'0','10','20','30','40','50','60','70','80','90',
'','100'});

```

## References

- [1] Amr A. Ibrahim, Amr M. E. Safwat, and Hadia El-Hennawy, "Triple-Band Microstrip-Fed Monopole Antenna Loaded With CRLH Unit Cell," *IEEE Antennas Wireless Propag. Lett.*, vol. 10, pp. 1547–1550, 2011.
- [2] Jeongpyo Kim, Giho Kim, Wonmo Seong, and Jaehoon Choi, "A Tunable Internal Antenna With an Epsilon Negative Zeroth Order Resonator for DVB-H Service," *IEEE Trans. Antennas Propag.*, vol. 57, no. 12, pp. 4014–4017, Sep. 2009.
- [3] Miguel Durán-Sindreu, Jun Choi, Jordi Bonache, Ferran Martín, and Tatsuo Itoh, "Dual-band leaky wave antenna with filtering capability based on extended-composite right/left-handed transmission lines," *Microwave Symposium Digest (IMS), 2013 IEEE MTT-S International*, pp. 1-4, Jun. 2013.
- [4] Debabrata K. Karmokar, and Karu P. Esselle, "Periodic U-Slot-Loaded Dual-Band Half-Width Microstrip Leaky-Wave Antennas for Forward and Backward Beam Scanning," *IEEE Trans. Antennas Propag.*, vol. 63, no. 12, pp. 5372–5381, Dec. 2015.
- [5] David R. Jackson, Christophe Caloz, and Tatsuo Itoh, "Leaky Wave Antenna," *Proc. Of The IEEE*, vol. 100, no. 7, Jul. 2012.
- [6] A. A. Oliner, and D. R. Jackson, "Leaky-wave antennas," in *Antenna Engineering Handbook*, J. L. Volakis, Ed. New York: McGraw-Hill, 2007.
- [7] Simone Paulotto, Paolo Baccarelli, Fabrizio Frezza, and David R. Jackson, "A Novel Technique for Open-Stopband Suppression in 1-D Periodic Printed Leaky-Wave Antennas," *IEEE Trans. Antennas Propag.*, vol. 57, no. 7, pp. 1894–1906, Jul. 2009.
- [8] C. Caloz, and T. Itoh, *Electromagnetic Metamaterials Transmission Line Theory and Microwave Applications*. New York: Wiley, 2006.
- [9] Paolo Baccarelli, Simone Paulotto, David R. Jackson, and Arthur A. Oliner, "A New Brillouin Dispersion Diagram for 1-D Periodic Printed Structures," *IEEE Trans. Microw. Theory Tech.*, vol. 55, no. 7, pp. 1484-1495, Jul. 2007.
- [10] Christophe Caloz, Tatsuo Itoh and Andre Rennings, "CRLH metamaterial leaky-wave and resonant antennas," *IEEE Antennas Propog. Magazine*, vol. 50, iss. 5, pp. 25-39, Nov. 2008.
- [11] Gonghan Wang, and Quanyuan Feng, "A Novel Coplanar Waveguide Feed Zeroth-Order Resonant Antenna With Resonant Ring," *IEEE Antennas Wireless Propag. Lett.*, vol. 13, pp. 774–777, 2014.
- [12] A. Rennings, S. Otto, J. Mosig, C. Caloz and I. Wolff, "Extended composite right/left-handed (E-CRLH) metamaterial and its application as quad-band quarter-wavelength transmission line," *Proceedings of Asia-Pacific Microwave Conference 2006*, pp. 1405–1408, Dec. 2006.
- [13] G.V. Eleftheriades, "Design of generalized negative-refractive-index transmission lines for

- quad-band applications”, *IET Microw. Antennas Propag.*, vol. 4, pp. 977–981, 2010.
- [14] Lai. A., Itoh. T., and Caloz. C., “Composite right/left-handed transmission line metamaterials,” *IEEE Microw. Mag.*, vol. 5, no. 3, pp. 34–50, Oct. 2004.
- [15] A. Sanada, M. Kimura, I. Awai, C. Caloz, and T. Itoh, “A Planar Zeroth-Order Resonator Antenna Using a Left-Handed Transmission Line,” *Microwave Conference, 34th European*, vol. 3, pp. 1341-1344, 2004.
- [16] Jae-Hyun Park, Young-Ho Ryu, Jae-Gon Lee, and Jeong-Hae Lee, “Epsilon Negative Zeroth-Order Resonator Antenna,” *IEEE Trans. Antennas Propag.*, vol. 55, no. 12, pp. 3710–3712, Dec. 2007.
- [17] Jae-Gon Lee, and Jeong-Hae Lee, “Zeroth Order Resonance Loop Antenna,” *IEEE Trans. Antennas Propag.*, vol. 55, no. 3, pp. 994-997, Mar. 2007.
- [18] Jeong Keun Ji, Gi Ho Kim, and Won Mo Seong, “Bandwidth Enhancement of Metamaterial Antennas Based on Composite Right/Left-Handed Transmission Line,” *IEEE Antennas Wireless Propag. Lett.*, vol. 9, pp. 36–39, 2010.
- [19] Hong-Min Lee, “A Compact Zeroth-Order Resonant Antenna Employing Novel Composite Right/Left-Handed Transmission-Line Unit-Cells Structure,” *IEEE Antennas Wireless Propag. Lett.*, vol. 10, pp. 1377–1380, 2011.
- [20] Pei-Ling Chi, and Yi-Sen Shih, “Compact and Bandwidth-Enhanced Zeroth-Order Resonant Antenna,” *IEEE Antennas Wireless Propag. Lett.*, vol. 14, pp. 285–288, 2015.
- [21] Long Li, Zhen Jia, Feifei Huo, and Weiqiang Han, “A Novel Compact Multiband Antenna Employing Dual-Band CRLH-TL for Smart Mobile Phone Application,” *IEEE Antennas Wireless Propag. Lett.*, vol. 12, pp. 1688–1691, 2013.
- [22] Hakjune Lee, Duk-Jae Woo, and Sangwook Nam, “Compact and Bandwidth-Enhanced Asymmetric Coplanar Waveguide (ACPW) Antenna Using CRLH-TL and Modified Ground Plane,” *IEEE Antennas Wireless Propag. Lett.*, vol. 15, pp. 810–813, 2016.
- [23] Gonghan Wang, and Quanyuan Feng, “A Novel Coplanar Waveguide Feed Zeroth-Order Resonant Antenna With Resonant Ring,” *IEEE Antennas Wireless Propag. Lett.*, vol. 13, pp. 774–777, 2014.
- [24] W. W. Hansen, “Radiating electromagnetic waveguide,” U.S., Patent 2.402.622, 1940.
- [25] C. Caloz, and T. Itoh, “Novel microwave devices and structures based on the transmission line approach of meta-materials,” *Microwave Symposium Digest, 2003 IEEE MTT-S International*, vol. 1, pp. 195-198, 2003.
- [26] Simone Paulotto, Paolo Baccarelli, Fabrizio Frezza, and David R. Jackson, “Full-Wave Modal Dispersion Analysis and Broadside Optimization for a Class of Microstrip CRLH Leaky-Wave Antennas,” *IEEE Trans. Microw. Theory Tech.*, vol. 56, no. 12, pp. 2826–2837, Dec. 2008.
- [27] P. Baccarelli, C. Di Nallo, S. Paulotto, and D. R. Jackson, “A full-wave numerical approach for modal analysis of 1-D periodic microstrip structures,” *IEEE Trans. Microw. Theory Tech.*,

- vol. 54, no. 4, pp. 1350–1362, Apr. 2006.
- [28] Sungjoon Lim, Christophe Caloz, and Tatsuo Itoh, “Metamaterial-Based Electronically Controlled Transmission-Line Structure as a Novel Leaky-Wave Antenna with Tunable Radiation Angle and Beamwidth,” *IEEE Trans. Microw. Theory Tech.*, vol. 52, no. 12, pp. 2678–2690, Dec. 2004.
- [29] Francisco P. Casares-Miranda, Carlos Camacho-Peñalosa, and Christophe Caloz, “High-Gain Active Composite Right/Left-Handed Leaky-Wave Antenna,” *IEEE Trans. Antennas Propag.*, vol. 54, no. 8, pp. 2292–2300, Aug. 2006.
- [30] Romain Siragusa, Etienne Perret, Pierre Lemaître-Auger, Hoang Van Nguyen, Smaïl Tedjini, and Christophe Caloz, “A Tapered CRLH Interdigital/Stub Leaky-Wave Antenna With Minimized Sidelobe Levels,” *IEEE Antennas Wireless Propag. Lett.*, vol. 11, pp. 1214–1217, 2012.
- [31] Nasimuddin, Zhi Ning Chen, and Xianming Qing, “Multilayered Composite Right/Left-Handed Leaky-Wave Antenna With Consistent Gain,” *IEEE Trans. Antennas Propag.*, vol. 60, no. 11, pp. 5056–5062, Nov. 2012.
- [32] Gerard Zamora, Simone Zuffanelli, Ferran Paredes, Francisco Javier Herraiz-Martinez, Ferran Martin, and Jordi Bonache, “Fundamental-Mode Leaky-Wave Antenna (LWA) Using Slotline and Split-Ring-Resonator (SRR)-Based Metamaterials,” *IEEE Antennas Wireless Propag. Lett.*, vol. 12, pp. 1424–1427, 2013.
- [33] Wenquan Cao, Zhi Ning Chen, Wei Hong, Bangning Zhang, and Aijun Liu, “A Beam Scanning Leaky-Wave Slot Antenna With Enhanced Scanning Angle Range and Flat Gain Characteristic Using Composite Phase-Shifting Transmission Line,” *IEEE Trans. Antennas Propag.*, vol. 62, no. 11, pp. 5871–5875, Nov. 2014.
- [34] Ali Pourghorban Saghati, Mir Mojtaba Mirsalehi, and Mohammad Hassan Neshati, “A HMSIW Circularly Polarized Leaky-Wave Antenna With Backward, Broadside, and Forward Radiation,” *IEEE Antennas Wireless Propag. Lett.*, vol. 13, pp. 451–454, 2014.
- [35] Tomas Zvolensky, Juha Ala-Laurinaho, Constantin R. Simovski, and Antti. V. Räsänen, “A Systematic Design Method for CRLH Periodic Structures in the Microwave to Millimeter-Wave Range,” *IEEE Trans. Antennas Propag.*, vol. 62, no. 8, pp. 4153–4161, Aug. 2014.
- [36] Miguel Durán-Sindreu, Jun Choi, Jordi Bonache, Ferran Martín, and Tatsuo Itoh, “Dual-band leaky wave antenna with filtering capability based on extended-composite right/left-handed transmission lines,” *Microwave Symposium Digest (IMS), 2013 IEEE MTT-S International*, pp. 1-4, Jun. 2013.
- [37] Cheng Jin, and Arokiaswami Alphones, “Leaky-Wave Radiation Behavior From a Double Periodic Composite Right/Left-Handed Substrate Integrated Waveguide,” *IEEE Trans. Antennas Propag.*, vol. 60, no. 4, pp. 1727–1735, Apr. 2012.
- [38] Debabrata K. Karmokar, and Karu P. Esselle, “Periodic U-Slot-Loaded Dual-Band

- Half-Width Microstrip Leaky-Wave Antennas for Forward and Backward Beam Scanning,” *IEEE Trans. Antennas Propag.*, vol. 63, no. 12, pp. 5372–5381, Dec. 2015.
- [39] Jan Machac, Milan Polivka, and Kirill Zemlyakov, “A Dual Band Leaky Wave Antenna on a CRLH Substrate Integrated Waveguide”, *IEEE Trans. Antennas Propag.*, vol. 61, no. 7, pp. 3876–3879, Jul. 2013.
- [40] Roy B. V. B. Simorangkir, and Yongshik Lee, “A Planar Dual-Band Periodic Leaky-Wave Antenna Based on a Mu-Negative (MNG) Transmission Line,” *IEEE Trans. Antennas Propag.*, vol. 63, no. 5, pp. 2370–2374, May 2015.
- [41] Y.-H. Chun, J.-S. Hong, P. Bao, T.J. Jackson, M.J. Lancaster, “Tunable slotted ground structured bandstop filter with BST varactors,” *IET Microw. Antennas Propag.*, Vol. 3, Iss. 5, pp. 870-876, 2009.
- [42] Zhou, Xiaoyuan, “Dielectric properties of barium strontium titanate (BST) thin films and phase shifters based on BST thin films,” *The Hong Kong Polytechnic University*, PhD Dissertation, 2008.
- [43] P. Bao, T. J. Jackson, X. Wang, and M. J. Lancaster, “Barium Strontium Titanate Thin Film Varactors for Room-Temperature Microwave Device Applications,” *J. Phys. D: Appl. Phys.* 41 (2008) 063001, Feb. 2008.
- [44] M. Nikfalazar, A. Mehmood, M. Sohrabi, M. Mikolajek, A. Wiens, H. Maune, C. Kohler, J. R. Binder, and R. Jakoby, “Steerable Dielectric Resonator Phased-Array Antenna Based on Inkjet-Printed Tunable Phase Shifter With BST Metal-Insulator-Metal Varactors,” *IEEE Antennas Wireless Propag. Lett.*, vol. 15, pp. 877-880, 2016.
- [45] David Cure, Thomas M. Weller, Tony Price, Félix A. Miranda, and Frederick W. Van Keuls, “Low-Profile Tunable Dipole Antenna Using Barium Strontium Titanate Varactors,” *IEEE Trans. Antennas Propag.*, vol. 62, no. 3, pp. 1185–1193, Mar. 2014.
- [46] Yelong Wang, Yang Liu, Honglei Du, Chunheng Liu, Qian Xue, Xiaoyang Gao, Shandong Li, and Yueguang Lu, “A Frequency Reconfigurable Microstrip Antenna Based on Substrate,” *IEEE Trans. Antennas Propag.*, vol. 63, no. 2, pp. 770–775, Feb. 2015.
- [47] Vamsi Krishna Palukuru, Mikko Komulainen, Timo Tick, Jani Peräntie, and Heli Jantunen, “Low-Sintering-Temperature Ferroelectric-Thick Films: RF Properties and an Application in a Frequency-Tunable Folded Slot Antenna,” *IEEE Antennas Wireless Propag. Lett.*, vol. 7, pp. 461-464, 2008.
- [48] Cedric J. G. Meyers, Christopher R. Freeze, Susanne Stemmer, and Robert A. York, “(Ba,Sr)TiO<sub>3</sub> tunable capacitors with RF commutation quality factors exceeding 6000,” *Appl. Phys. Lett.* 109, 112902 (2016), 2016.
- [49] Yu Liu, Amit S. Nagra, Erich G. Erker, Padmini Periaswamy, Troy R. Taylor, James Speck, and Robert A. York, “BaSrTiO<sub>3</sub> Interdigitated Capacitors for Distributed Phase Shifter Applications,” *IEEE Microw. Guided Wave Lett.*, vol. 10, no. 11, pp. 448–450, Nov. 2000.
- [50] Guangli Yang , Hao Wang , and Li Yang, “Tunable Antenna Introductions, Challenges and

- Opportunities,” *Progress In Electromagnetics Research Symposium Proceedings*, Guangzhou, China, pp. 2201-22014, 2014.
- [51] P. Penfield and R. P. Rafuse, *Varactor Applications*. Cambridge, MA: MIT Press, 1962.
- [52] Sihem Missaoui, Sayed Missaoui, and Mohsen Kaddour, “Tunable microstrip patch antenna based on liquid crystals,” *Direct and Inverse Problems of Electromagnetic and Acoustic Wave Theory (DIPED)*, 2016 XXIst International Seminar/Workshop on, pp. 88-91, Dec. 2016.
- [53] A. Zohur, H. Mopidevi, D. Rodrigo, M. Unlu, L. Jofre, and Bedri A. Cetiner, “RF MEMS Reconfigurable Two-Band Antenna,” *IEEE Antennas Wireless Propag. Lett.*, vol. 12, pp. 72-75, 2013.
- [54] Li-Rong Tan, Rui-Xin Wu, Cong-Yi Wang, and Yin Poo, “Ferrite-Loaded SIW Bowtie Slot Antenna With Broadband Frequency Tunability,” *IEEE Antennas Wireless Propag. Lett.*, vol. 13, pp. 325-328, 2014.
- [55] Runiu Fang, Min Miao, and Yufeng Jin, “Investigation of Parasitic Effects Induced by the Ground on LTCC Passive Components,” *Progress In Electromagnetics Research Symposium Proceedings, Taipei*, pp. 1102-1106, 2013.
- [56] K. E. Mortenson, *Variable capacitance diodes: the operation and characterization of varactor, charge storage and PIN diodes for RF and microwave applications*, 1974.
- [57] Mohsen Sazegar, Yuliang Zheng, Holger Maune, Christian Damm, Xianghui Zhou, Joachim Binder, and Rolf Jakob, “Low-Cost Phased-Array Antenna Using Compact Tunable Phase Shifters Based on Ferroelectric Ceramics,” *IEEE Trans. Microw. Theory Tech.*, vol. 59, no. 5, pp. 1265-1273, May 2011.
- [58] Mohsen Sazegar, Yuliang Zheng, Holger Maune, Christian Damm, Xianghui Zhou, and Rolf Jakob, “Compact Tunable Phase Shifters on Screen-Printed BST for Balanced Phased Arrays,” *IEEE Trans. Microw. Theory Tech.*, vol. 59, no. 12, pp. 3331-3337, Dec. 2011.
- [59] Jayesh Nath, Dipankar Ghosh, Jon-Paul Maria, Angus I. Kingon, Wael Fathelbab, Paul D. Franzon, and Michael B. Steer, “An Electronically Tunable Microstrip Bandpass Filter Using Thin-Film Barium–Strontium–Titanate (BST) Varactors,” *IEEE Trans. Microw. Theory Tech.*, vol. 53, no. 9, pp. 2707-2712, Dec. 2005.
- [60] Jennifer Sigman, Christopher D. Nordquist, Paul G. Clem, Garth M. Kraus, and Patrick S. Finnegan, “Voltage-Controlled Ku-Band and X-Band Tunable Combline Filters Using Barium Strontium Titanate,” *IEEE Microw. Wireless Compon. Lett.*, vol. 18, no. 9, pp. 593-595, Sep. 2008.
- [61] X. Gao, T. J. Jackson, P. Gardner, M. M. Kechik, B. Jancar, O. Ochar, and A. Belous, “Influence of uncertainty in dielectric properties on the design performance of a tunable composite right/left handed leaky wave antenna,” *2015 Joint IEEE International Symposium on the Applications of Ferroelectric (ISAF)*, pp. 182-185, May 2015.
- [62] U. Arz, M. D. Janezic, and W. Heinrich, “Wideband relative permittivity extraction based on

CPW phase constant measurements”, *ARFTG Microwave Measurement Conference*, pp. 37-39, 2011.

- [63] P. K. Petrov, Y. Pan, B. Zou, and M. McN, Alford, “Dielectric constant and loss tangent of thin ferroelectric films at microwave frequencies – how accurately can we evaluate them?” *Integrated Ferroelectrics: An International Journal*, vol. 97, no. 1, pp. 27-37, 2008.